

H24/3118

**MONASH UNIVERSITY**  
THESIS ACCEPTED IN SATISFACTION OF THE  
REQUIREMENTS FOR THE DEGREE OF  
DOCTOR OF PHILOSOPHY

ON..... 7 December 2001 .....

.....  
for Sec. Research Graduate School Committee

Under the copyright Act 1968, this thesis must be used only under the normal conditions of scholarly fair dealing for the purposes of research, criticism or review. In particular no results or conclusions should be extracted from it, nor should it be copied or closely paraphrased in whole or in part without the written consent of the author. Proper written acknowledgement should be made for any assistance obtained from this thesis.

# Improved modelling of zonal currents and SST in the tropical Pacific

Thesis submitted for the degree of Doctor of Philosophy

Noel S. Keenlyside

B.Sc., Hon.

May 2001

Cooperative Research Centre for Southern Hemisphere Meteorology

Department of Mathematics and Statistics

Monash University

# Contents

Summary . . . . .	v
Statement . . . . .	vii
Acknowledgements . . . . .	ix
<b>1 Introduction</b>	<b>1</b>
<b>2 Observations</b>	<b>7</b>
2.1 Introduction . . . . .	7
2.2 Dynamic height and thermocline depth . . . . .	8
2.3 Zonal and meridional equatorial currents . . . . .	11
2.4 Vertical velocity . . . . .	37
2.5 Sea Surface Temperature . . . . .	40
2.6 Concluding Remarks . . . . .	44
<b>3 Dynamical Ocean Model</b>	<b>47</b>
3.1 Introduction . . . . .	47
3.2 Model formulation . . . . .	48
3.3 Implementation . . . . .	67
3.4 Simulation of the annual mean . . . . .	70
3.5 Modal convergence . . . . .	79
3.6 Summary . . . . .	86
<b>4 Annual cycle of zonal currents</b>	<b>89</b>
4.1 Introduction . . . . .	89
4.2 Annual cycle . . . . .	91
4.3 Analysis and Discussion . . . . .	96
4.4 Sensitivity studies . . . . .	104
4.5 Summary . . . . .	107
<b>5 Interannual variability of zonal currents</b>	<b>109</b>
5.1 Background . . . . .	111
5.2 Modelled interannual zonal currents . . . . .	115
5.3 Analysis . . . . .	122
5.4 Sensitivity studies . . . . .	131
5.5 Summary and discussion . . . . .	133
<b>6 Modelling Sea Surface Temperature</b>	<b>137</b>
6.1 Model . . . . .	139
6.2 Simulation of SST anomalies . . . . .	146
6.3 Sensitivity studies . . . . .	149
6.4 SST budget . . . . .	153
6.5 The 1990's . . . . .	158
6.6 Discussion and summary . . . . .	160

<b>7</b>	<b>Concluding remarks and other work</b>	<b>163</b>
7.1	ICM . . . . .	164
7.2	Main findings . . . . .	165
7.3	Additional work, and other avenues of research . . . . .	167
7.4	Summary . . . . .	169
	<b>Appendix A: Approximations</b>	<b>171</b>
A.1	Stratification . . . . .	171
A.2	Scale analysis of advective terms . . . . .	175
	<b>Appendix B: SST model development</b>	<b>179</b>
B.1	Thermocline depth anomalies . . . . .	179
B.2	Subsurface temperature parametrisation . . . . .	184
	<b>References</b>	<b>189</b>

## Errata

- p V para 3, second sentence: Replace "These are the first data to provide" with "The TAO/TRITON array provides the first"
- p 10, figure 2.1: The units in (a) are dynamic centimeters and in (b) are meters.
- p 21 para 4, last sentence: Replace "griding" with "gridding"
- p 28 para 3, third sentence: Replace "A phenomenon that is referred to" with "This phenomenon is referred to"
- p 40 para 3, first line: Replace " data sets. For example" with "data sets, for example,"
- p 103 last para, third last sentence: Replace "but there sum" with "but their sum"
- p 112 para 3, last sentence: Replace "So to" with "So, too"
- p 113 para 1, second sentence: Replace " are sensitivity to" with "are sensitive to"
- p 138, first line: Replace "So to" with "So, too"
- p 189, reference for Bryden and Brady [1985]: Replace "*J. Climate*" with "*J. Mar. Res*"
- p 192, reference for Moore and Philander [1977]: Delete "correct reference"

## Summary

Intermediate complexity models (ICM) of the El Niño Southern Oscillation (ENSO) have focused on modelling thermocline-induced SST changes. Zonal advection has been largely neglected. Although ICMs have had remarkable success, recent studies suggest zonal advection controls interannual SST variability in the central Pacific; a region believed to be critical to atmosphere-ocean coupling (e.g., Picaut and Delcroix [1995]).

This study is an investigation of zonal current variability in the tropical Pacific, and the role of zonal currents in controlling SST. The main results are obtained with an ICM, which is developed here. The model is an extension of the McCreary [1981] baroclinic mode model, and includes effects for varying stratification and nonlinearity. Non-linear terms have been widely neglected in earlier ICM studies, so this model provides a useful tool to assess their neglect.

Observations, particularly current data from the TAO/TRITON array of moored buoys [Yu and McPhaden, 1999b], are important to this study. These are the first data to provide reliable measurements of interannual zonal current variability along the equator in the Pacific.

The ICM simulates the annual cycle of zonal currents well. Taking advantage of the simplicity of the model, a mechanism for the annual cycle of the equatorial undercurrent (EUC) is identified. The annual cycle of the EUC is the result of meridional advection of the annual cycle north of the equator onto the equator. The annual cycle of zonal currents north of the equator is determined by linear dynamics.

The model also realistically simulates interannual zonal current variability in the central Pacific. This is the region where atmospheric coupling is important, and SST is controlled by zonal advection. Non-linear terms are identified to be important in the eastern equatorial Pacific. In particular, they control the magnitude of linear zonal current variability. Also, the neglect of non-linearity explains the deficiencies in satellite-derived geostrophic currents in the eastern equatorial Pacific. Elsewhere

satellite currents match in-situ observations well.

Finally, through the addition of a SST component to the ICM, the impact of improved current simulation on modelling SST variability is assessed. The SST component differs from other ICMs primarily in its parameterisation of subsurface temperature. The parameterisation used here is based on the inversion of the SST equation using observations and model data. With the realistic simulation of zonal currents in the central Pacific, the model is able to simulate SST realistically across the Pacific. The impact of improved zonal current simulation on SST simulation during the 1997-98 ENSO event is also investigated.

## Statement

I hereby certify that this thesis contains no material which has been accepted for the award of any other degree or diploma in any university or other institution and, to the best of my knowledge, contains no material previously published or written by another person, except where due reference is made in the text of the thesis.



Noel Keenlyside

May 2001

## Acknowledgements

Most of all, I must thank my supervisors for their support, encouragement, and understanding. In particular, Professor David Karoly for always taking an interest in my study, and ensuring its continued progress; and Dr Richard Kleeman for his guidance, his enthusiasm in our work, and for his continued supervision, even after moving overseas. Without them this study would not have been possible.

I would also like to thank Dr Tony Hirst, for his help during periods when Dr Kleeman was overseas, and for his ongoing interest in my study.

This study was funded by the Cooperative Research Centre (CRC) for Southern Hemisphere Meteorology. I recognise the central role that the CRC played in my study, and my life in Melbourne. It gave me the opportunity to come to Melbourne, and work in the area of my interest. The many friends I have made through the CRC helped my studies significantly, and made all my time in Melbourne enjoyable.

I must also thank my wife Mandy, for her support, patience, and understanding. With her love this study was possible. I thank my daughter Yola, for helping me to focus on life. I am also deeply thankful of my parents, for their strong encouragement and support.

# Chapter 1

## Introduction

This thesis describes a study of the dynamics of equatorial zonal currents and their role in controlling sea surface temperature (SST) in the equatorial Pacific. The background for this study, a discussion of its relevance, and an outline of the thesis are now presented.

The El Niño Southern Oscillation (ENSO) is the dominant mode of interannual climate variability and is driven by the interaction between the ocean and atmosphere in the equatorial Pacific (e.g., Philander [1990]). The cold (La Niña) and warm (El Niño) phases of this phenomenon are associated with large changes in the equatorial currents, the thermal structure of the ocean, and atmospheric circulation (e.g., McPhaden et al. [1998]). The changes in the atmospheric circulation affect weather around the world (e.g., Glantz et al. [1991]), having large economic and social impact, and thus, make understanding and forecasting this phenomenon important [Philander, 1990].

There has been a significant effort to understand the ENSO since the early 1980s, and much progress has been made [McPhaden et al., 1998]. However, as evidenced by the poor ENSO forecasts of the 1990s [Ji et al., 1996; Barnston et al., 1999], important aspects of this phenomenon remain poorly understood.

It is generally accepted that the ENSO is the result of a coupled ocean-atmosphere instability. Observations have served to show a number of elements of this instability (e.g., see Philander [1990]). During an El Niño event, westerly wind anomalies

associated with anomalous convection are seen at the date line. These wind anomalies are followed by the spread of 28°C SST across the Pacific. In the ocean, there is also a coincident relaxation of the equatorial circulation. During a La Niña, there is a converse set of events.

The relation between these events that results in a coupled ocean-atmosphere instability is still not fully understood. However, it is generally accepted that on interannual time scales the ocean forces the atmosphere through SST-controlled latent heating, and that the atmosphere forces the ocean through zonal wind-stress anomalies that are generated by the SST-driven convection (e.g., Stockdale et al. [1998]).

Earlier studies focused on mechanisms associated with the large SST anomalies in the eastern Pacific (e.g., the delayed action oscillator [Schopf and Suarez, 1988; Battisti, 1988]). However, there is now strong evidence that the SST anomalies in the central Pacific are more important to ENSO than the larger anomalies in the east. Observations show that the largest anomalies in convection and zonal wind occur in the central Pacific, and that they are strongly correlated with the underlying SST anomalies [Fu et al., 1986; Delcroix, 1998; Shu and Clarke, 2000]. Further, these quantities are strongly related to the Southern Oscillation [Picaut and Delcroix, 1995; Shu and Clarke, 2000; Picaut et al., 2001], implying a direct link between ENSO and the ocean-atmosphere coupling in the central Pacific.

The mechanisms controlling SST in the equatorial Pacific are still not fully understood. Observational studies are limited by data quality (e.g., Wang and McPhaden [2000]). Results from modelling studies are also less than conclusive, since the mechanisms controlling SST are model [Miller et al., 1993], and wind field [Harrison et al., 1990] dependent. However, it is generally agreed that, on interannual time scales, SST is controlled by entrainment processes in the eastern Pacific (e.g., Battisti [1988]; Wang and McPhaden [2000]), and by zonal advection in the central Pacific (e.g., Delcroix et al. [2000]; Picaut et al. [2001]; Wang and McPhaden [2000]).

Intermediate complexity models (ICMs) and ocean general circulation models

(OGCMs) have proved useful in the simulation of SST [Stockdale et al., 1998], and in the forecasting of ENSO [Latif et al., 1998]. The abilities of these models to simulate SST is related to the degree to which the above two mechanisms controlling SST are represented. In general, OGCMs simulate SST anomalies best in the central equatorial Pacific, whereas ICMs simulate SST anomalies best in the far eastern Pacific [Miller et al., 1993]. This behaviour can be understood as follows. In traditional ICMs, entrainment processes are well represented, but zonal advection is poor [Shu and Clarke, 2000]. The converse occurs in OGCMs. The poor performance of OGCMs in the eastern Pacific may be related to difficulties in simulating the mean thermal structure. ICMs avoid these problems by specifying the background thermal structure [Stockdale et al., 1998].)

Since many earlier studies focused on the SST anomalies in the eastern Pacific, the modelling of interannual zonal current variability has been neglected. Another reason for this was the lack of available data (chapter 2, McPhaden et al. [1998]). However, given the importance of SST in the central Pacific to ENSO, and the role of zonal advection in controlling SST there, it is important to understand and simulate the dynamics of zonal currents.

The dynamics of zonal current variability are not well understood. Two examples of this, which are investigated in this thesis, are the annual cycle of the equatorial undercurrent (EUC), and the interannual variability of surface zonal currents. Due to lack of data, there are no observational studies analysing the annual cycle of the EUC, and only the annual cycle of depth integrated flow has been investigated [Yu and McPhaden, 1999b]. Modelling studies have also had difficulty explaining the annual cycle of the EUC (e.g., Yu et al. [1997]), and have not provided a satisfactory explanation.

Recent studies of interannual variability of zonal currents have focused on explaining the different processes responsible for anomalous zonal currents in the central Pacific (e.g., boundary reflections, non-local wind forcing); their aim was to shed light on the mechanism controlling ENSO [Delcroix et al., 1994; 2000; Shu and Clarke, 2000; Picaut et al., 2001]. There has been little investigation of the dynamics

of interannual variability of zonal currents, particularly in the eastern Pacific. Observational studies have been limited to only analysing the depth integrated zonal momentum balance [Yu and McPhaden, 1999a].

Using OGCMs to understand dynamics of zonal current variability (as well as SST variability) is difficult, because of the complexity of these models. ICMs are of little use, since, as mentioned above, they model zonal current variability poorly. Thus, our lack of understanding of the dynamics of zonal current variability is due to both a lack of data, and a suitable analysis tool. OGCMs are too complex, and ICMs are not sufficiently realistic.

This study is aimed at

1. Developing a more realistic ICM for better understanding zonal current variability
2. Improve our understanding of two aspects of zonal current variability: the annual cycle of the EUC, and interannual variability of surface zonal currents
3. Better understanding the role of zonal current variability in controlling SST.

The ICM developed here improves on traditional ICMs, and is better able to simulate zonal currents. Similar to other ICMs, the model developed here consists of two components: a dynamical ocean model, and a SST model. The SST component is very similar to that of other ICMs, except that a new formulation for subsurface temperature is used. The most significant changes are in the dynamical component. The dynamical component of traditional ICMs generally consist of single baroclinic-mode model plus a surface mixed layer (e.g., Zebiak and Cane [1987]; Kleeman [1993]). The model here is a McCreary [1981] type modal model, modified to include a surface mixed layer and a simplified model of the residual non-linear equations.

The advantage of ICMs over an OGCMs is that their simplicity allows them to be used for mechanism analysis. This is well recognised, and other efforts have been made to improve the simulation of zonal currents and SST in ICMs [Shu and Clarke,

2000; Dewitte, 2000]. The improvements in these models have been achieved only by the addition of high order baroclinic modes. These models, since they neglect non-linear terms in the zonal momentum balance, are less realistic than the model developed here.

In summary, an ICM is developed here to study the dynamics of zonal currents, and their role in controlling SST. The background and justification for this study is as follows: (1) it is important to understand the dynamics of zonal currents, because they are important to SST variability, particularly in the central Pacific, and to ENSO. (2) Dynamics of zonal current variability are poorly understood, because of lack of data, and a suitable model. (3) An ICM is developed here, because its simplicity allows it to be used to analyse the dynamics of zonal currents.

The structure of the thesis is as follows. In the next chapter, observations, which are used through out the thesis to evaluate the model's performance, are presented. There is special attention given to describe available current data.

In chapter 3 the dynamical ocean model is formulated, and its annual mean simulation is compared with observations. In chapter 4 the model's simulation of the annual cycle of zonal currents is investigated. The focus is on explaining the poorly understood annual cycle of the equatorial undercurrent. The model's design allows a simple mechanism to be deduced. Chapter 5 presents an analysis of the model's simulation of interannual zonal current variability. Model results show that non-linear effects are highly significant in the eastern Pacific. The importance of non-linearity in the east explains the less accurate satellite-inferred and linear model currents there.

In chapter 6 the SST component of the model is formulated, and its simulation of SST anomalies is compared to observations. The simulation in the central Pacific is improved over traditional ICMs, and is now comparable to OGCMs. The improved simulation of zonal currents in the central Pacific is identified as the reason for the more accurate simulation of SST anomalies. The interesting result of this chapter is the identification that zonal advection is not the only significant processes controlling

SST variability in the central Pacific.

In the final chapter, a brief overview of the study is given, summarising the main results. Several areas of future work are also identified. The study concludes with two appendices, which provide additional material on the dynamical and SST components of the model.

## Chapter 2

### Observations

#### 2.1 Introduction

Interannual variability of the equatorial Pacific ocean is an important aspect of the El Niño Southern Oscillation (ENSO) phenomenon. The significance of ENSO to world weather means it is important to understand the interannual variability of the equatorial Pacific. Accurate observations are critical to gaining a good understanding, as they allow precise statistical and dynamical relations to be found. Dynamical relations are important when data are limited, and they also allow predictions to be made.

Observations of the equatorial Pacific, excluding sea surface temperature (SST), are in general poor prior to the mid 1980's. However, significant efforts have been made since the 1980's to improve observations in this region (e.g., TAO/TRITON (Tropical Atmosphere Ocean, Triangle Trans-Ocean Buoy Network) array, and Drifter data). One exciting aspect of the recent observations is a better understanding of the equatorial circulation, an area where modelling studies have played an important role, but in which model testing has been limited. There are now sufficient amounts of data for current measurements to play a useful role in ocean model development [Reverdin et al., 1994; Yu and McPhaden, 1999b]. Describing these relatively new observations is the focus of this chapter.

The chapter presents a survey of the available observations of the equatorial

Pacific, an observational description of interannual variability of SST and associated variables, and observations relevant to obtaining a realistic dynamical ocean model. A intermediate complexity ocean model is developed in subsequent chapters and used to understand certain aspects of the observations presented here.

The chapter is structured into four sections: Dynamic height and thermocline depth, zonal and meridional equatorial currents, vertical velocity, and SST. The length and detail of each section varies as relevant.

## 2.2 Dynamic height and thermocline depth

To first order, much of the ocean's circulation is explained by geostrophic theory, even zonal currents in the equatorial region [Lukas and Firing, 1984; Yu et al., 1995]. Thus, variables that measure horizontal pressure variation are important to ocean model testing. Surface dynamic height and sea level are the most widely used, since these records are relatively long and of good quality [McPhaden et al., 1998]. Thermocline depth, because of the two-layer nature of the tropical Pacific [Philander, 1990], is also useful for model testing. Thermocline depth and 20-degree isotherm depth will be used inter-changeably throughout this study.

The focus of this section is on presenting thermocline depth observations, since this variable is also strongly related to SST variability in the east [Wang and McPhaden, 2000]. The quality and availability of the data are not discussed (see [McPhaden et al., 1998] for a general overview).

### 2.2.1 Data

The observations presented here are primarily from Levitus [1982] mean temperature and salinity climatology; Levitus et al. [1994] monthly temperature climatology; and measurements from the TAO/TRITON array [Yu and McPhaden, 1999b]. Mean and annual variations in the depth of 20-degree isotherm are calculated via cubic spline interpolation of the Levitus mean and monthly mean climatologies. Monthly mean

20-degree isotherm observations were kindly provided by the TAO project office, Dr. Michael J. McPhaden, Director, and were calculated from linear-interpolated daily average profiles centred at noon GMT. Interannual thermocline depth anomalies are calculated by first subtracting the annual cycle, and then subtracting the residual long term mean. The latter adjusts the anomalies to have zero mean. Although it is not necessary for the anomalies to have zero mean over finite data, in practice, the results are more consistent, particularly in the central eastern Pacific.

### 2.2.2 Annual Mean

Figure 2.1a shows the mean surface dynamic height of the tropical Pacific ocean. Over the whole equatorial region, 20°S to 20°N, surface dynamic height slopes downward from west to east. In the west, surface dynamic height is 40-50 Dyn cm higher than in the east. This is equivalent to a sea surface height difference of 40-50cm. Superimposed on this are strong meridional gradients, indicating surface geostrophic zonal currents. In the west, between 15 to 20°N, and between 15 to 20°S, peaks in dynamic height indicate the respective centres of the northern and southern subtropical cells. Closer to the equator, the trough in dynamic height between 7 to 10°N divides the North Equatorial Countercurrent (NECC) from the North Equatorial Current (NEC). The trough in the east between 3°N to 16°S, indicates the South Equatorial Current (SEC).

The annual mean 20-degree isotherm depth is shown in figure 2.1b. The two layer nature of the ocean is reflected in the horizontal variations of the 20-degree isotherm depth. From west to east the 20-degree isotherm slopes up, from 180m to 40m. It is deepest in the centres of the subtropical gyres, and displays all the troughs and ridges seen in surface dynamic height. Only in the position of the southern subtropical gyre, is any departure from the two layer approximation noticeable.

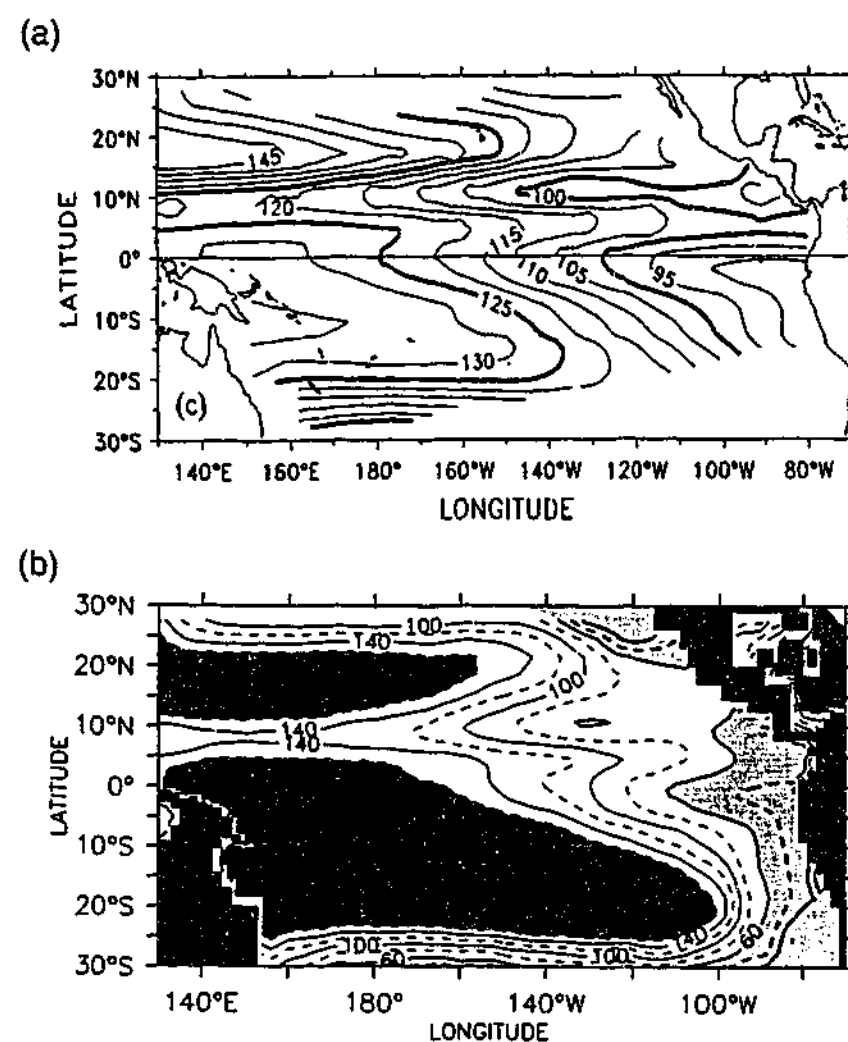


Figure 2.1: (a) annual mean dynamic height (0/450 dbar) calculated from expendable bathythermograph measurements (collected between 1979 and 1995), and using local mean T-S curves from Levitus et al. [1994]. The figure is taken from Delcroix [1998]. (b) annual mean 20-degree isotherm depth calculated from Levitus [1982] mean temperature observations.

### 2.2.3 Annual Cycle

The annual cycle of 20-degree isotherm depth on the equator, at 5°S, and 5°N are shown in figure 2.2. Annual variability at all three latitudes is greatest in the central eastern Pacific. At 5°S and 5°N the phase of the annual cycle propagates westward. On the equator the phase of the annual cycle is not marked by distinctive phase propagation. It is sometimes westward propagating in the west, and sometimes eastward propagating in the east, but overall, the direction of phase propagation is not distinctive.

The annual cycle of surface dynamic height resembles that of the 20-degree

isotherm depth. A complete description, both observational and dynamical, of the annual cycle of surface dynamic height, 20-degree isotherm depth, and zonal current is given by Yu and McPhaden [1999b]. This work indicates that linear wave dynamics control the annual cycle of these three variables.

### 2.2.4 Interannual variability

Interannual anomalies of the 20-degree isotherm depth are shown in figure 2.3. The magnitude of the anomalies shows that variations in the depth of the 20-degree isotherm are primarily interannual. The variability is strongest on the equator, but still significant off the equator at 5°N and 5°S. The figure also illustrates the well known ENSO variations in the east-west slope of the thermocline. During the strong El Niño events of 1982-83 and 1997-98, the thermocline on the equator is depressed in the east by up to 80m from its climatological value, and raised in the west by more than 40m. During these events the thermocline is effectively level across the equatorial Pacific. Similar, but weaker variations are also evident during the 1986-87 El Niño event and for the El Niño events of the early 1990's. Converse anomalies are also seen during the 1988-89 and 1998-99 La Niña events.

## 2.3 Zonal and meridional equatorial currents

A description of the annual mean, and annual and interannual variability of equatorial currents is now given. The focus is on zonal currents, as this study is an investigation of the influence of zonal currents on equatorial SST. An account of the mean meridional circulation is also given; meridional currents are described in this section, and vertical velocity is described in the next. Due to lack of data, there are large uncertainties in the annual and interannual variability of both meridional and vertical velocity. Thus, neither are discussed in detail. A summary of current measurements in the equatorial Pacific is given. It highlights issues associated with data quality and availability.

Further accounts of the mean equatorial circulation can be found in Tomczak and

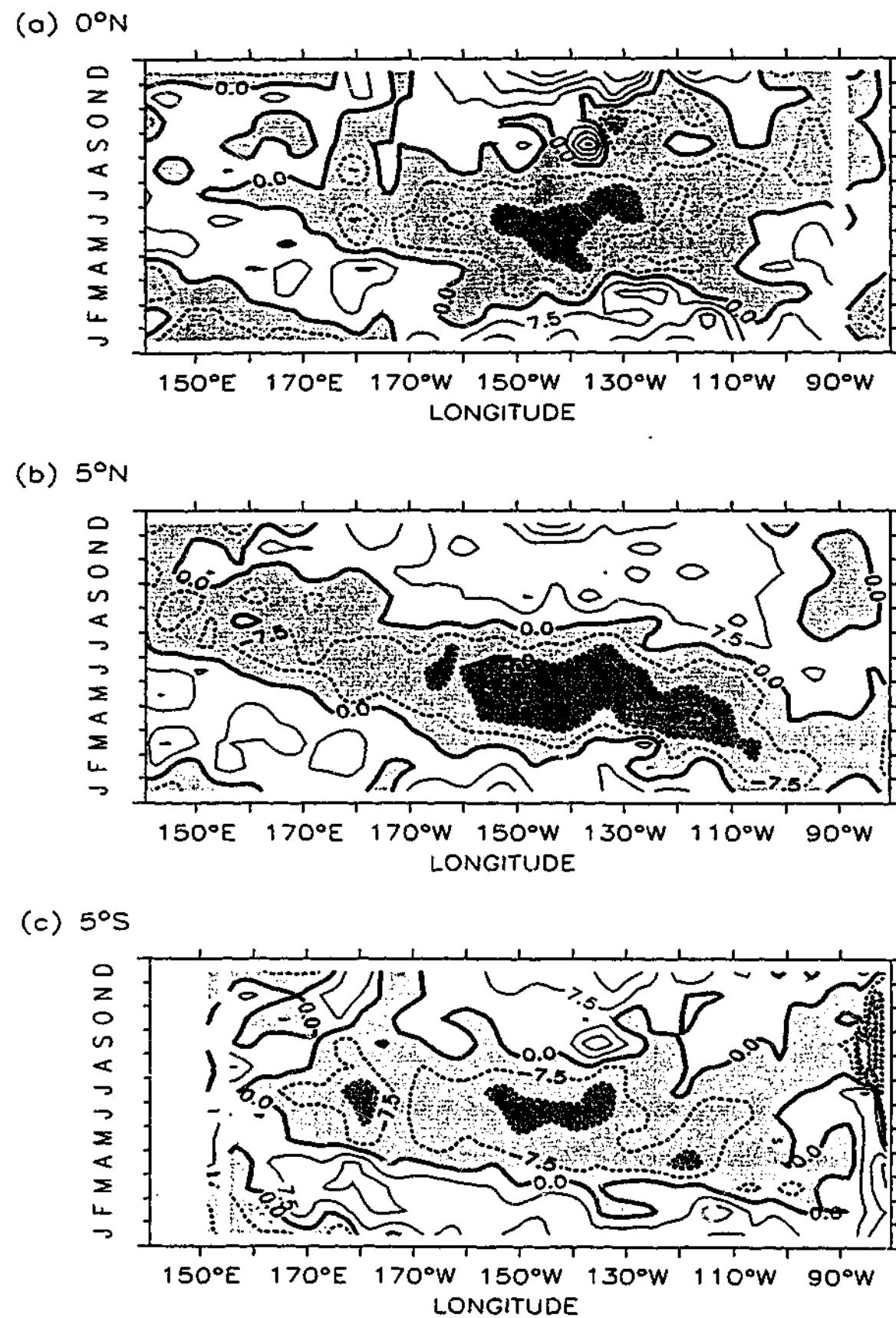


Figure 2.2: The annual cycle of 20-degree isotherm depth (a) on the equator, (b) 5°N, and (c) 5°S are plotted in terms of anomalies about the annual mean. Units are meters. Negative anomalies are shaded, and the contour interval is 7.5m. (The plots are constructed from the Levitus et al. [1994] monthly temperature climatology.)

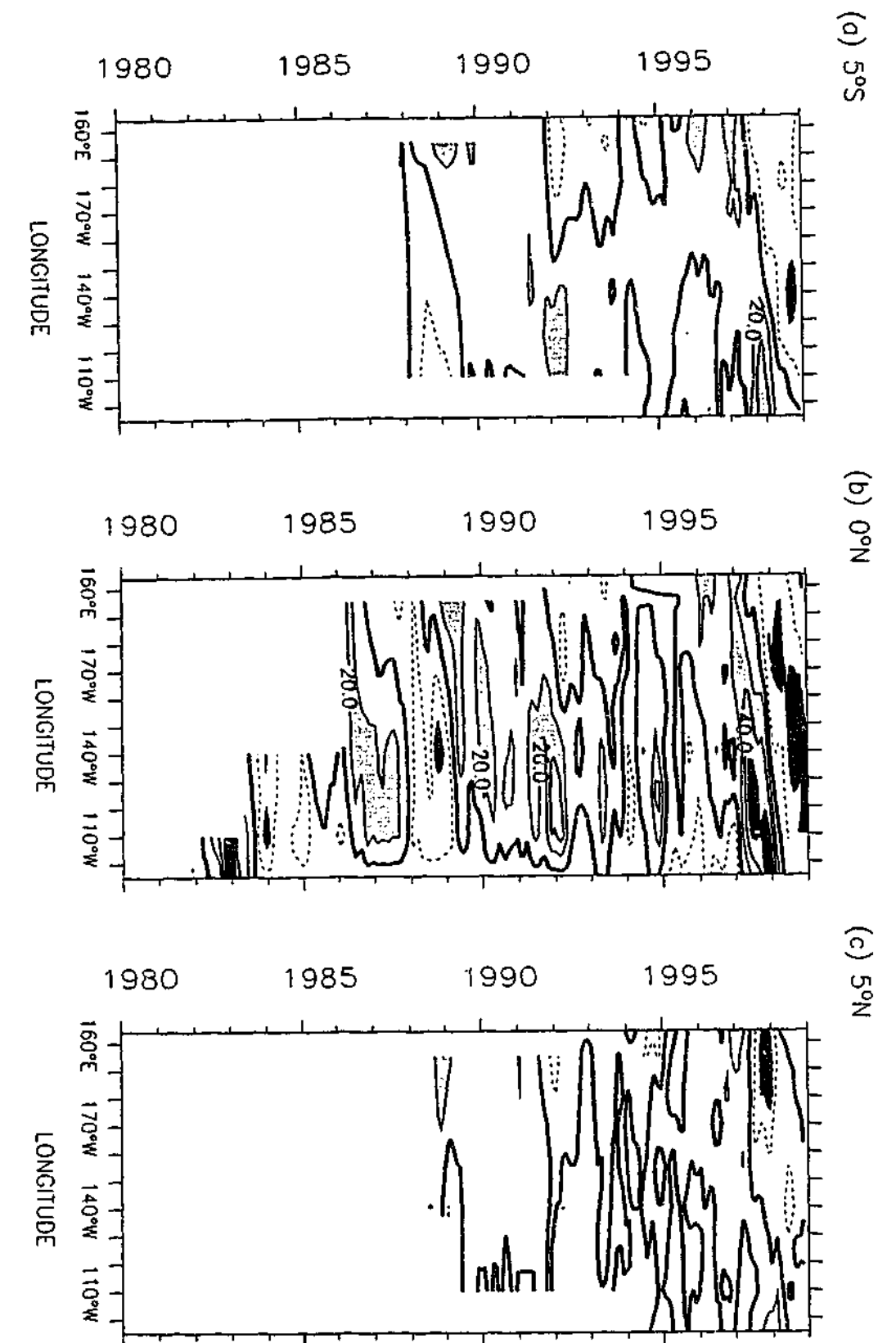


Figure 2.3: Variations in the depth of the 20-degree isotherm along (a) 5°S, (b) 0°N, and (c) 5°N are plotted in terms of anomalies about the climatological annual cycle. Positive values indicating a deeper thermocline. The climatology is calculated from Levitus et al. [1994] observations, and is shown in figure 2.2. In addition, anomalies are also adjusted to have zero long term mean. The units are m, the contour interval is 20m, and negative anomalies have dashed contours. Anomalies less than -40m are shaded in black, and anomalies greater than 20m are lightly shaded. (The plots are constructed using data from the TAO/TRITON array [Yu and McPhaden, 1999b])

Godfrey [1994] chapter 8, and Philander [1990] chapter 2. There are also several observational accounts of annual and interannual variability of zonal currents in the literature [Reverdin et al., 1994; Frankignoul et al., 1996; Yu and McPhaden, 1999b;a].

### 2.3.1 Data

Measurements of ocean currents in the tropical Pacific are by no means extensive. This is due to two factors: the important role of ocean circulation on world climate has only recently been recognised, and the great expense of making observations in remote locations. The importance of the tropical Pacific only came with the recognition that ENSO is significant to world climate, and that the tropical Pacific plays a critical role in this phenomenon. This realisation resulted in significant efforts being made since the 1980s to observe the equatorial Pacific; such as the TAO array of moored buoys [Yu and McPhaden, 1999b], and the Global Drifter Program [World Climate Research Programme, 1995].

#### Measurement Quality

There are a variety of methods for measuring near-surface currents: directly using mechanical current meters (MCMs), and acoustic Doppler current profilers (ADCP); and indirectly from drifters (satellite tracked buoys), ship drift measurements, and from satellite surface height and surface wind data.

The most accurate and extensive observations of surface currents are provided by drifters with a drogue attached. These drifters are able to measure currents at the drogue depth to within a few  $\text{cms}^{-1}$  [Reverdin et al., 1994; Lagerloef et al., 1999; World Climate Research Programme, 1995]. The drogues, typically at a 15m depth, minimise drift due to surface waves and windage. However, although accurate, drifter measurements are sparse in the equatorial region, because of the strong meridional divergence of currents about the equator.

Surface current measurements are also provided by ship drift and satellite ob-

zonal current anomalies relative to the annual mean. However, this differs from common practice in ENSO modelling studies of defining anomalies with respect to the annual cycle. The latter definition is assumed in this study, unless otherwise stated. The annual mean for this data is estimated for the period October 1992 to September 1994. The data covers the period October 1992 to October 1999, and is on a  $0.5^\circ$  latitude by  $5^\circ$  longitude grid, spanning the tropical Pacific ( $29^\circ\text{S}$  to  $29^\circ\text{N}$ ,  $125^\circ\text{E}$  to  $75^\circ\text{W}$ ). The data are in 5-day bins.

To allow direct comparison with TAO data, monthly means, a monthly mean climatology, and monthly mean interannual anomalies were calculated from the 5-day data. The climatology was calculated for the period October 1992 to September 1999; it compares well with the TAO/TRITON [Yu and McPhaden, 1999b] and Reverdin et al. [1994] climatologies. Interannual zonal current anomalies were calculated by subtracting the monthly climatology from the monthly means. Statistically the TOPEX/Poseidon annual and interannual monthly mean zonal-current anomalies compare well with TAO/TRITON data (table 2.1). Correlations are high, but weaken towards the east; errors are reasonable, but increase in the east; and the magnitude of the variability is comparable.

### 2.3.2 Annual mean

#### Surface currents

There are three well defined surface currents in the equatorial Pacific: the SEC, the NECC, and the NEC. Observations in figure 2.6a show the NECC and SEC. The NECC is located between  $4^\circ\text{N}$  and  $10^\circ\text{N}$ , and is an eastward current driven by wind stress curl through Sverdrup dynamics. The SEC is a westward wind driven current that is located between  $10^\circ\text{S}$  and  $4^\circ\text{N}$ , and extends from the dateline into the eastern Pacific. The NEC is a relatively weak and broad current, located to the north of the NECC. Only its southern edge is visible on this figure.

The strength of the SEC varies significantly. It is strongest north of the equator, where it reaches speeds of  $0.4\text{ms}^{-1}$ . On the equator the SEC is weak, and in fact its

Table 2.1: Linear correlation coefficient, ratio of standard deviation, and rms difference between TOPEX/Poseidon inferred zonal current and TAO/TRITON zonal current observations on the equator. Statistics for anomalies with respect to the annual mean and with respect to the annual cycle are given. (This is for comparison purposes in chapter 5).

	Correlation coefficient	Ratio std-deviation TOPEX/TAO	rms difference ( $\text{ms}^{-1}$ )
<b>Anomalies w.r.t annual mean</b>			
165°E	0.89	1.1	0.16
140°W	0.71	1.3	0.2
110°W	0.64	1.2	0.3
<b>Anomalies w.r.t. annual cycle</b>			
165°E	0.85	1.3	0.18
140°W	0.57	1.1	0.15
110°W	0.52	1.0	0.26

direction varies seasonally. South of the equator the SEC strengthens, and speeds of  $0.3\text{ms}^{-1}$  are observed. The strength of the NECC is fairly uniform across the entire Pacific, with typical zonal speeds greater than  $0.2\text{ms}^{-1}$ .

Surface meridional flow, shown in figure 2.6b, is poleward divergent, with divergence centred slightly north of the equator. Surface meridional currents, which are determined primarily by Ekman dynamics, are significantly weaker than zonal currents. Maximum poleward velocities are only between  $0.05\text{--}0.1\text{ms}^{-1}$ . Poleward flow is strongest in the central and eastern Pacific, between  $2$  to  $4^\circ\text{S}$ , and  $2$  to  $4^\circ\text{N}$ , which is consistent with Ekman dynamics. This is because this is where zonal wind stress peaks.

In comparison, WOCE/TOGA drifter data [World Climate Research Programme, 1995] show similar annual mean structure, and similar mean meridional current strength. However, significant difference exist in the strength of mean zonal currents. The NECC and large areas of the SEC are 30% weaker in the WOCE/TOGA data. Also, the minimum in the SEC, along the equator, is less well pronounced.

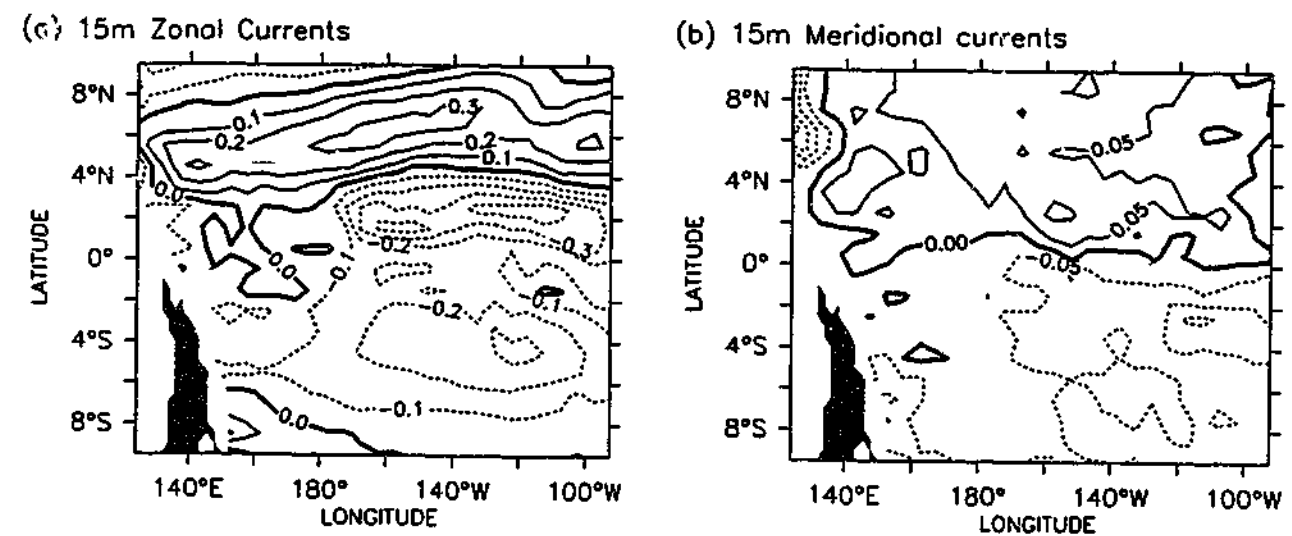


Figure 2.6: Annual mean surface (a) zonal currents, and (b) meridional currents. The units are  $ms^{-1}$ , and the contour intervals are  $0.1 ms^{-1}$  for zonal currents and  $0.05 ms^{-1}$  for meridional currents. Eastward and northward flow are shaded. (Plots constructed using data from the Reverdin et al. [1994] current climatology)

There are number of possible reasons for these differences, interannual variability is probably the most likely (The averaging period of the WOCE/TOGA data was 1988-1994, which was two years longer than the Reverdin et al. [1994] data, and included the El Niño events of the early 1990's). The explanation is not critical here, but it illustrates considerable uncertainties in the strength of mean surface zonal currents.

### Vertical structure

The equatorial current system is much more complex than surface observations would indicate. Figure 2.7a illustrates the meridional structure of zonal currents around  $160^{\circ}W$  to  $150^{\circ}W$ . At the surface the SEC and NECC are clearly seen. At lower levels the equatorial undercurrent (EUC), a core of eastward flow centred on the equator and strongly equatorially confined, is seen. The EUC is approximately 200m thick and 300km wide, and here is centred at a depth of 120m. The NECC is seen to extended well below the surface, and merges weakly with the EUC to the south.

The zonal structure of SEC and EUC are seen in figure 2.7b. The core of the

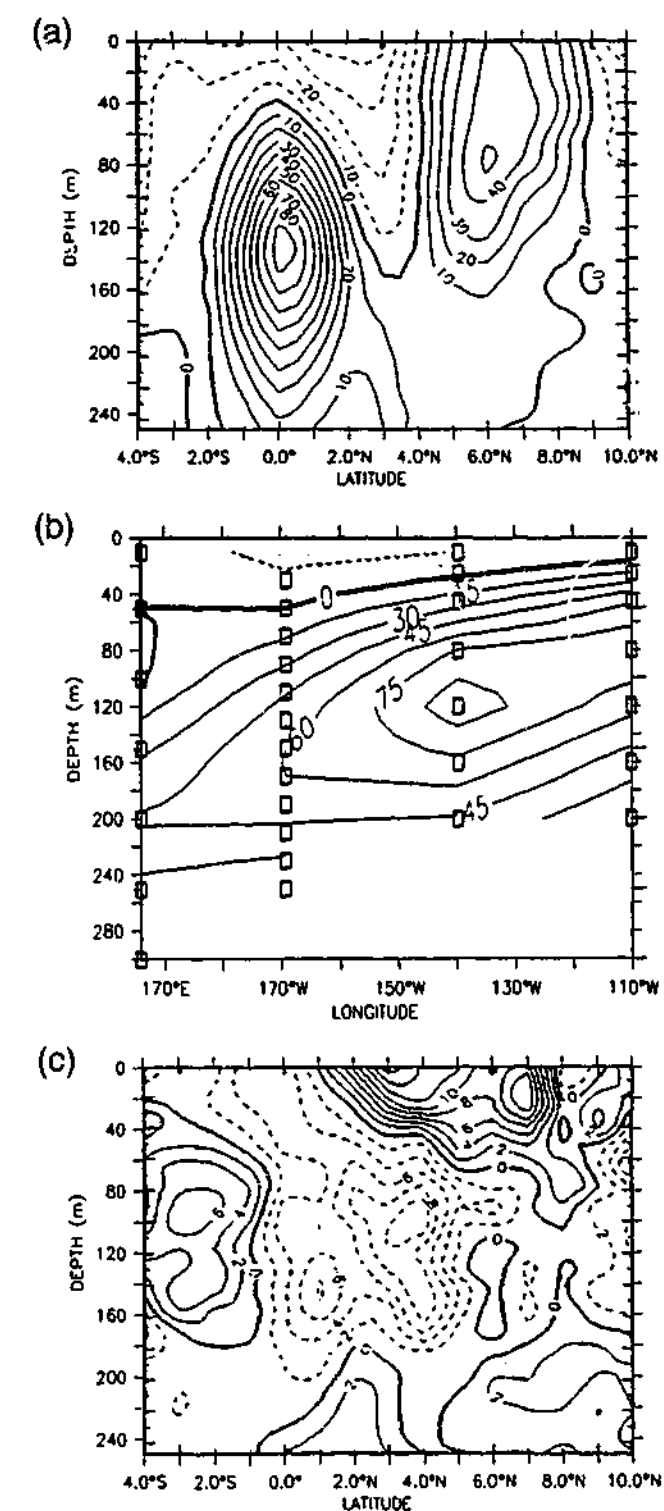


Figure 2.7: Observations of the annual mean structure of zonal and meridional currents. (a) The meridional structure of zonal currents in the eastern central Pacific, (b) the zonal structure of zonal currents along the equator, and (c) the meridional structure of meridional currents in the eastern central Pacific. Units are  $cms^{-1}$ , solid lines indicate positive flow, and dashed lines negative. (a) and (c) are taken from Johnson and Luther [1994] and were constructed using data between  $160^{\circ}W$ - $150^{\circ}W$  from the Hawaii-to-Tahiti shuttle experiment. (b) is taken from Yu and McPhaden [1999b] and is constructed using data from the TAO/TRITON array, boxes indicate measurement positions.

EUC rises from about 180m at 180°E to 80m at 110°W. The flow is strongest in the central eastern Pacific, where it averages speeds greater than  $0.9 \text{ ms}^{-1}$ . The SEC is less prominent, it is a shallow current that shoals towards the east.

Figure 2.7c, a cross equatorial section of the meridional currents, shows that below the surface, meridional currents remain significantly weaker than the zonal currents. The flow which at the surface is divergent about the equator, and at the level of the undercurrent convergent, can be characterised as two overturning cells with upwelling along the equator. This feature, which is seen in other data for the central and eastern Pacific, shall be referred to as the equatorial cell.

An important aspect of the TAO data, not represented in the above figures, is an estimate of the uncertainty due to interannual variability of the currents. With TAO data covering periods greater than seven years, estimates of the uncertainty due to interannual variability of the currents can be made. These estimates will now be described.

In figure 2.8a, b, and c annual mean zonal currents for the three locations of our data are shown. Error bars indicate the 95% confidence interval estimate for the annual mean, as estimated from the interannual variability of successive annual means, assuming the Student's *t* distribution. In the east, all features of the vertical structure are quite well represented. In the west, because of larger interannual variability and weaker mean currents, the vertical structure of currents is not so well resolved. The standard deviations, calculated from the distribution of annual means, are shown by dashed lines. They are typically of the order  $0.1 \text{ ms}^{-1}$  at all locations, indicating a significant amount of interannual variability in zonal currents.

In figures 2.8d, e, and f, annual mean meridional currents and their interannual variability are shown. The magnitude of interannual variability, typically  $0.03\text{--}0.04 \text{ ms}^{-1}$ , is smaller than that of zonal currents, but because meridional currents are much weaker, they are more significant. At certain levels, flow for different periods of time could easily be in opposite directions. Furthermore, comparison with other data sets shows the uncertainty estimates made here, in the strength and direc-

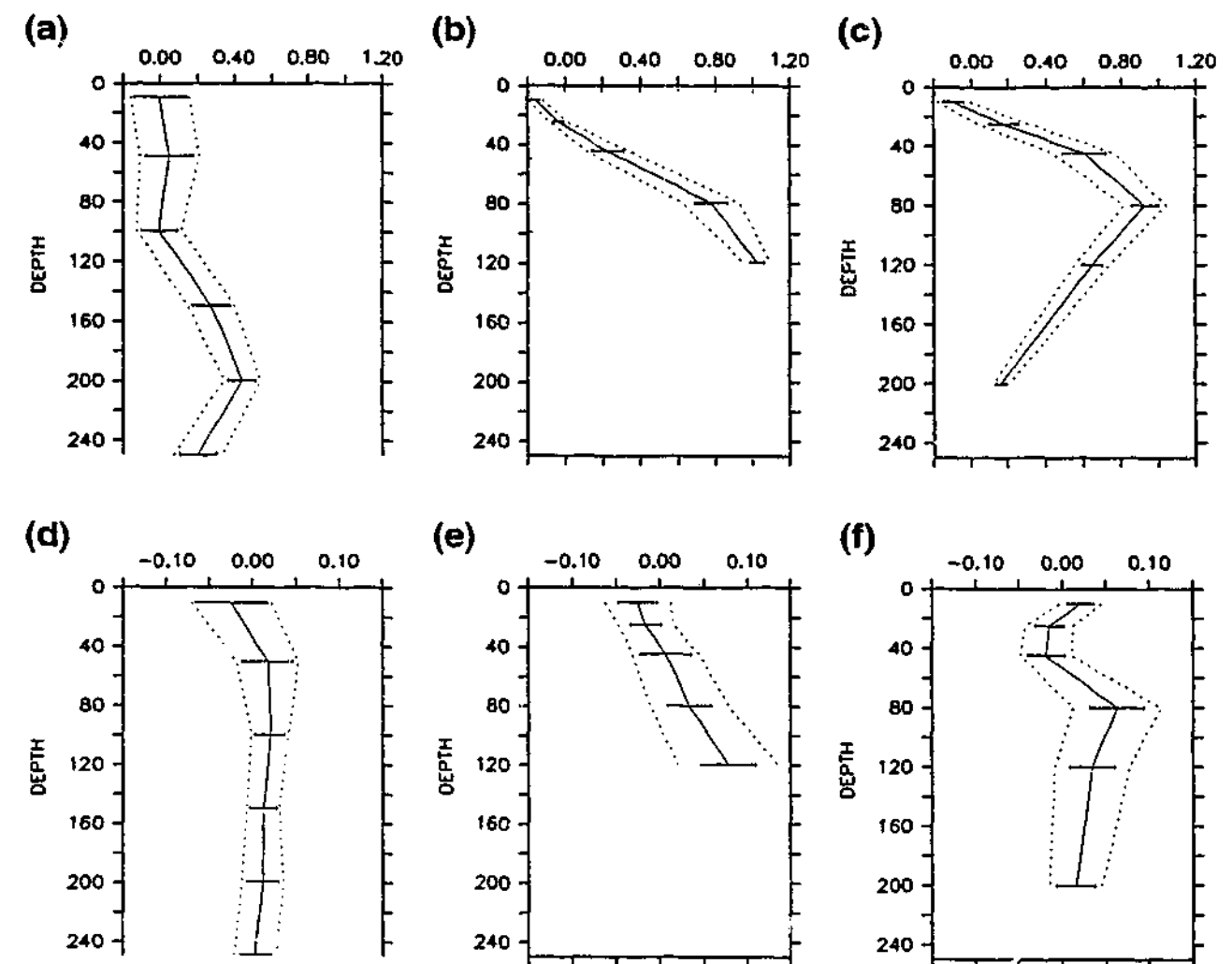


Figure 2.8: Annual mean zonal currents along the equator at (a) 165°E, (b) 140°W, and (c) 110°W. The units are  $\text{ms}^{-1}$ . Error bars indicate 95% confidence interval, as calculated from interannual variations in successive annual means, assuming the Student's *t* distribution. The dashed lines indicate 1-standard deviation about the annual mean. Lower panels (d), (e), and (f) are as in the upper panels, except for meridional velocity. (The data are from the TAO/TRITON array, and are detailed in Yu and McPhaden [1999b;a].)

tion of meridional currents on the equator, are underestimated. At 110°W, EPOCS data [Bryden and Brady, 1989], which covers an earlier period, shows southward flow across the undercurrent; TAO currents are northward. At 140W, a comparison between TIWE [Weisberg and Qiao, 2000] and TAO data for the same period shows errors of up to  $0.06 \text{ ms}^{-1}$  exist. In addition, NORPAX data [Bryden and Brady, 1989] shows the position of the equatorial cell can vary significantly over a few degrees of longitude. A precise definition of the equatorial cell, including its magnitude, is thus not possible with the available data. The data is only sufficient to show the presence of an equatorial cell in the central and eastern Pacific, with subsurface convergent

servations. Ship drift data, while potentially covering longer time periods, are of poorer quality than drifter data. They are subject to wind drift and are less well sampled (normally once daily). Also, most shipping routes perpendicularly cross equatorial currents, which smoothes the observations [Reverdin et al., 1994].

Satellite-inferred currents, while they provide the potential for high resolution current measurements, are not universally accurate. They are derived from satellite altimeter measurements, under the assumption of geostrophy. Satellite surface winds have also been used to include an estimate of the local wind-forced component (Ekman) of the flow, which is not in geostrophic balance, but can be significant [Lagerloef et al., 1999]. However, on the equator where classical geostrophic theory breaks down, and in regions where other terms also control surface currents, satellite-inferred currents will not be accurate (see chapter 5).

Experimental results show that satellite-inferred zonal current measurements correlate well with drifter data and in situ current measurements. Linear correlation coefficients with drifter data are of order 0.8 [Yu et al., 1995; Lagerloef et al., 1999]. Correlations with in situ moored current measurements vary between 0.9 and 0.49 [Lagerloef et al., 1999; Delcroix et al., 2000]. Correlations are consistently weaker on the equator in the east [Lagerloef et al., 1999; Delcroix et al., 2000]. A review of satellite measurements is presented in chapter 5, where reasons for the east-west differences are investigated. Meridional currents are significantly less well measured than zonal currents [Lagerloef et al., 1999].

MCMs and ADCPs provide the best means to observe subsurface currents. MCMs measure currents at fixed locations and levels, and have an accuracy between  $0.03$  and  $0.07\text{ms}^{-1}$  in magnitude, and between  $2$  and  $6^\circ$  in direction. ADCPs measure current profiles at fixed locations or from on board ships, and have an accuracy of  $\pm 0.05\text{ms}^{-1}$ ,  $\pm 2.5^\circ$ . These errors are estimated from comparison of co-located measurements, and are as quoted on the TAO home page (<http://www.cimel.noaa.gov/tao/>). Surface ADCP measurements from the TAO array are unreliable, because of sidelobe reflections in the upper 30m [Yu and McPhaden, 1999a], and because of interference with the acoustic signal by fish [Yu and McPhaden, 1999b].

### Data coverage and availability

Although drifters have been in use in the tropical Pacific since 1977, uniform measurements are only available from 1987, when drifters were standardised to measure currents at 15m. In 1994 there were over 180,000 days of drifts from 730 15m-drifters in the tropical Pacific [Reverdin et al., 1994]. These data are sufficient to determine the annual mean, and annual cycle of surface currents, and to get some idea of the interannual variability [Frankignoul et al., 1996]. Drifter data is available from MEDS (Marine Environmental Data Service), Canada (<http://www.meds-sdmm.dfo-mpo.gc.ca/>). Further details on drifter data can be found in the literature [Reverdin et al., 1994; World Climate Research Programme, 1995; Lagerloef et al., 1999].

Over the previous two decades, there have been a number of satellites equipped to measure sea level and surface wind speed. In particular surface height measurements have been made by Geosat (11/1985 to 8/1989), ERS-1/2 (7/1991 to present), and TOPEX/POSEIDON (8/1992 to present) satellites. These measurements have been used to calculate and study surface currents in the equatorial Pacific, for example Yu et al. [1995]; Picaut and Delcroix [1995]; Lagerloef et al. [1999], and Delcroix et al. [2000]. A more complete discussion of satellite observation, including measurements of surface wind speed, is given by McPhaden et al. [1998].

The most extensive set of current meter measurements in the Pacific are provided by the TAO/TRITON array of moored buoys. The array, illustrated in figure 2.4, consists of close to 70 moored buoys in the tropical Pacific. The TAO array, as it was previously known, was implemented by the TOGA (Tropical Ocean Global Atmosphere) program. It was primarily designed as an observing system for ENSO, with the goals of improved understanding and prediction of this phenomenon. As such, most of the buoys measure air temperature, relative humidity, wind velocity, and temperature in the upper 500m at 10 levels. Currents are only measured at 5 locations along the equator: 147°E, 165°E, 170°W, 140°W, and 110°W. Currents have also been measured at several other locations, but the measuring time periods

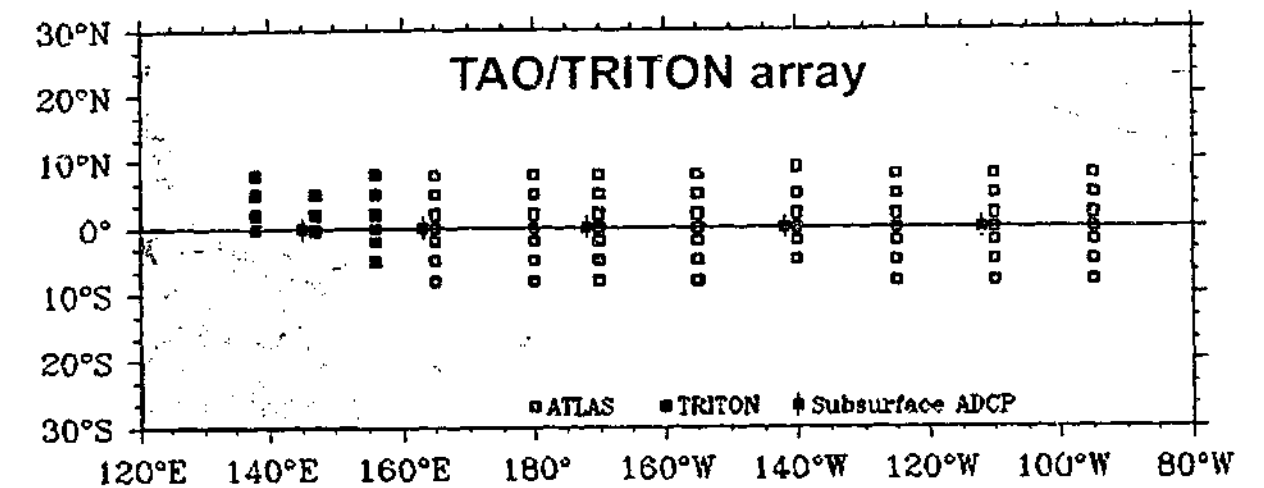


Figure 2.4: TOA/TRITON (Tropical Atmosphere Ocean/ Triangle Trans-Ocean Buoy Network) array of moored buoys in the tropical Pacific. (Figure taken from TAO homepage.)

are comparatively short.

TAO/TRITON current measurements are now made using upward facing ADCPs, and surface-mounted point Doppler current meters. Both provide measurements over the upper 250 to 300m, but point Doppler current meters only provide measurements at 4 to 5 levels. ADCP data is also only collected once yearly, whereas Doppler current meter data is available in near real time. Earlier measurements were mainly made with MCMs; these devices measured currents at 4 to 7 levels.

Current record length varies significantly, and records can have significant periods of missing data. The longest records are in the eastern Pacific, where measurements began in the early 1980s. A good summary of these aspects of the data, up to 1997, is given by Yu and McPhaden [1999a] (see also figure 2.5). TAO/TRITON array data is freely available from the NOAA/PMEL TAO homepage, which also provides comprehensive information on the TAO array. Extensive use of this information was made in the above summary.

There are various other relevant current data sets, which were collected through programs of shorter and more specific emphasis than the TOGA program: EPOCS (Equatorial Pacific Ocean Climate Study) [Bryden and Brady, 1989], NORPAX

(North Pacific Experiment) [Johnson and Luther, 1994], TIWE (Tropical Instability Wave Experiment) [Qiao and Weisberg, 1997], and Hawaii to Tahiti shuttle experiment [Johnson and Luther, 1994]. EPOCS, NORPAX, and TIWE consisted of arrays of 3 to 4 moored buoys straddling the equator, and thus not only measured zonal and meridional current, but also their divergence. The EPOCS array was located at  $110^{\circ}\text{W}$ , and collected data between January 1979 and October 1981. The NORPAX array was located at  $153^{\circ}\text{W}$ , and collected between April 1979 and June 1980. The TIWE was located at  $140^{\circ}\text{W}$ , and collected between May 1990 and June 1991. The Hawaii to Tahiti shuttle experiment consisted of a cruise that measured surface current profiles, along three longitudes ( $158^{\circ}\text{W}$ ,  $153^{\circ}\text{W}$ , and  $152^{\circ}\text{W}$ ), between  $10^{\circ}\text{N}$  and  $6^{\circ}\text{S}$ , over approximately the same period as the NORPAX experiment.

### Selected observations

In this study, extensive use will be made of data from the NORPAX-Hawaii to Tahiti shuttle experiment (as presented by Johnson and Luther [1994]), TAO/TRITON array, Reverdin drifter current climatology [Reverdin et al., 1994], and satellite-inferred currents from TOPEX/Poseidon sea level data [Delcroix et al., 2000]. Other current data are used, but only to complement these observations. The selected data are chosen because of their superior quality, coverage, and accuracy.

**NORPAX Hawaii to Tahiti shuttle data.** Data on the meridional structure of zonal and meridional currents in the equatorial Pacific are limited. The most highly referenced is the Hawaii to Tahiti shuttle data. It has been used for example by Lukas and Firing [1984] to show the EUC is in geostrophic balance, and by Bryden and Brady [1989] and Johnson and Luther [1994] to estimate the zonal momentum balance. Johnson and Luther [1994] combined these data with NORPAX data using a multi-linear regression. Their data is used below (in two figures from the paper) to illustrate the meridional structure of equatorial currents.

TAO/TRITON current data are used extensively throughout this thesis, because the data are located on the equator and are of a substantial time period (of

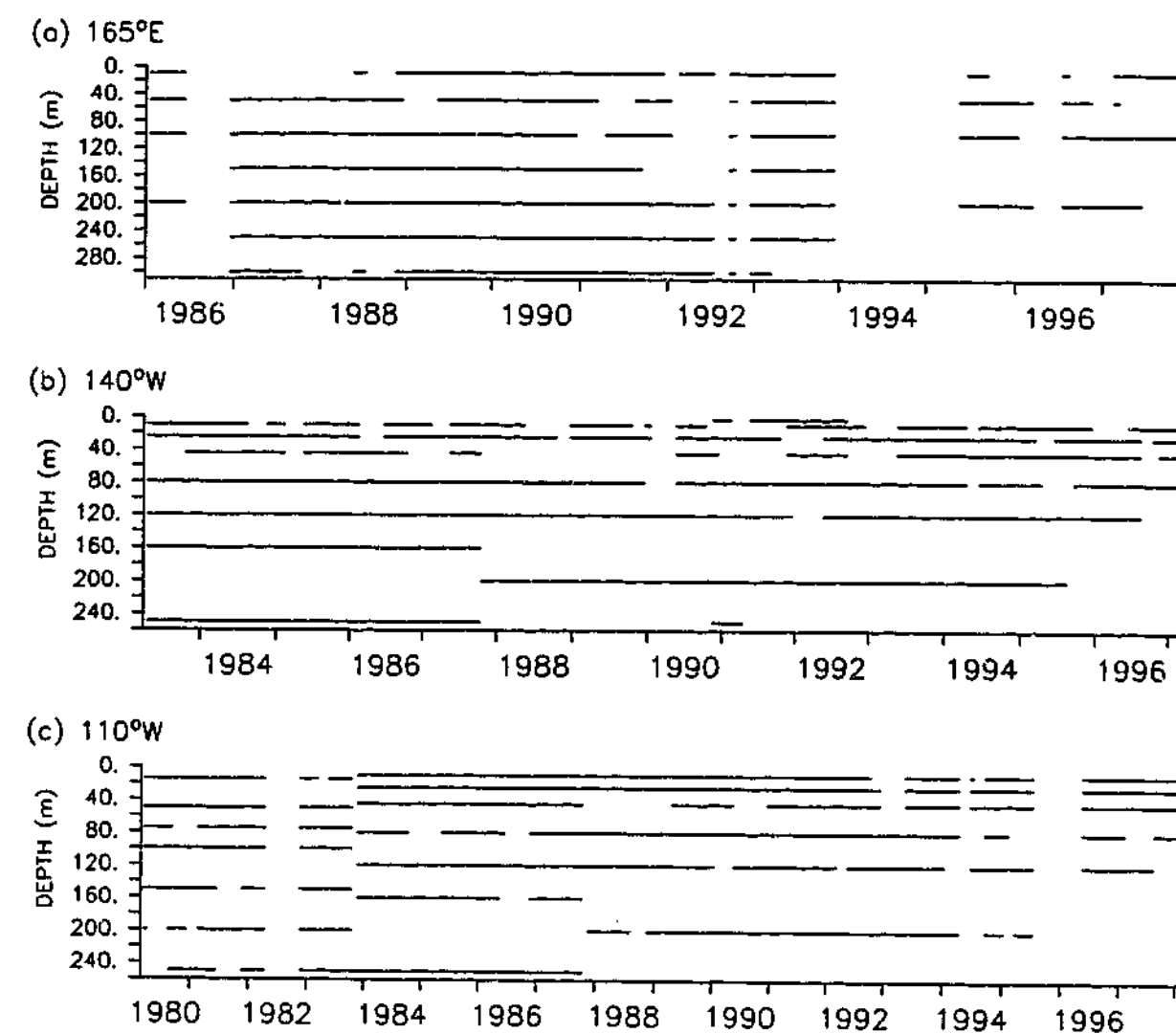


Figure 2.5: Summary of TAO/TRITON mechanical current meter data at (a)  $165^{\circ}\text{E}-0^{\circ}\text{N}$ , (b)  $140^{\circ}\text{W}-0^{\circ}\text{N}$ , and (c)  $110^{\circ}\text{W}-0^{\circ}\text{N}$ . Solid lines indicate levels and periods for which measurements are available.

the order 10 years). Only data from MCMs are selected, because of the problems with ADCP data, which were described above, and of most concern over the earlier period. Furthermore, only locations where data records are longer than seven years are considered:  $165^{\circ}\text{E}-0^{\circ}\text{N}$ ,  $140^{\circ}\text{W}-0^{\circ}\text{N}$ , and  $110^{\circ}\text{W}-0^{\circ}\text{N}$ . The temporal extent of the data at these locations is summarised in figure 2.5.

The zonal-current annual mean, annual cycle, and interannual anomalies presented here, were independently constructed from the raw daily data as follows. Monthly means were calculated by averaging the daily data over each month. The annual cycles was calculated from the monthly means, as described below. Annual mean currents were calculated by averaging the annual cycle, not by averaging over

all the data, as is common. This method for calculating the annual mean, reduces biases due to missing data. However, the quality and length of the TAO data is such that the long term mean does not differ significantly from the annual mean here. Interannual anomalies were simply calculated by subtracting the annual cycle from the full monthly mean data.

The climatological annual cycle was constructed as follows. Each climatological month was calculated as an average of the monthly averages for that calendar month. At each location, the averaging period for all levels was identical, and was never less than seven years. At 165°E it was from 12/87 to 11/93, at 140°W it was from 10/83 to 9/96, and at 110°W it was from 11/83 to 10/94. The levels where a climatology was calculated are indicated on figure 2.10. The climatology created here compares well to the climatology presented by Yu and McPhaden [1999b].

Time series representative of surface and subsurface zonal flow are also constructed from TAO data. These time series will be extensively used in chapter 5. Several techniques, which are described below, are employed to maximise the length of these time series.

At 165°E and 140°W, the vertical coherence of near surface velocity variations allow data from two levels to be combined as follows: where measurement at both levels exist an average is taken; and where measurements exist only at one level, that value is taken. The surface-layer current time series at 165°E is created using data from the 10m and 50m levels. At 140°W, the surface-layer current time series is created using data from the 10m and 25m levels.

At 110°W, the mixed layer is shallow, and vertical coherence of near surface current variations are not significant. Here, the surface-current time series consists of 10m currents post 1984. Prior to 1984, 15m current measurements are linearly extrapolated to the 10m level, using the average linear gradient between 10m and 25m for the later period. (The time periods referred to here are shown in figure 2.5c.)

The great vertical shear in subsurface zonal currents prevents the use of techniques similar to those above, for constructing subsurface time series. At 165°E,

currents at 100m are taken to represent subsurface flow. At 140°W, currents at 120m are taken to represent subsurface flow. At 110W, subsurface flow is represented by 75m currents for the earlier period, and 80m currents for the later period. The levels in the east correspond to the depth of the EUC core. (The time periods referred to here are shown in figure 2.5c.)

Reverdin 15m-current climatology are used to describe the annual mean and annual cycle of surface currents [Reverdin et al., 1994]. The current climatology is primarily constructed from drifter data between 20°S to 20°N, and 120°E to 80°W, over the period 1/1987 to 4/1992. TAO moored buoy data are also used, supplementing the drifter data on the equator. The Reverdin et al. [1994] current climatology is used in preference to drifter data alone, because drifter data are sparse in the equatorial region. However, the short data length may not be sufficient to fully resolve the annual cycle.

The data set is constructed by monthly averaging the daily averaged data in  $1^\circ \times 5^\circ$  latitude  $\times$  longitude boxes, and then least square fitting to a set of prescribed functions. The function fitting smoothes the data only in the zonal direction, and so retains the meridional structure. Temporally, only the mean, and annual and semi-annual harmonics are retained. The currents are in agreement with ship drift data, but because of the analysis procedure are unreliable near the coasts. Zonal currents are also unreliable near the date-line, because of limited sampling of interannual variability [Reverdin et al., 1994]

TOPEX/Poseidon zonal current anomalies are used in chapter 5. There, they are contrasted against in situ TAO/TRITON data, to illustrate non-linear contributions to interannual zonal current variability. The data were kindly provided by T. Delcroix and are described in Delcroix et al. [2000]. The calculation of zonal current anomalies from sea level data, and the gridding methods are described in Delcroix et al. [1994].

The TOPEX/Poseidon zonal current anomalies are anomalies relative to the annual mean. It is common in the literature on satellite-inferred currents to define

velocities of the order  $0.05\text{--}0.1\text{ ms}^{-1}$ , and similar surface divergent flow.

A similar comparison between data sets for zonal currents indicates the vertical structure of zonal currents is quite well resolved by the available data. In summary, data for both zonal and meridional currents shows a large amount of interannual variability exists. The uncertainty though, is only significant in the case of the meridional circulation. Of course, only the off-equatorial meridional currents are in general dynamically significant.

### 2.3.3 Annual cycle

As described above, TAO data is used to illustrate the vertical structure of the annual cycle of surface zonal currents; the Reverdin et al. [1994] current climatology is used to illustrate the zonal and meridional structure of surface currents. TAO data has been used previously to describe the annual cycle of these currents [Yu and McPhaden, 1999b;a]. This description differs by focusing on the annual cycle of the EUC, rather than the vertically averaged currents. Following Yu and McPhaden [1999b], the annual cycle will be described in terms of velocity anomalies, i.e., variations about the annual mean. The separation of the annual cycle from the annual mean gives a much clearer picture.

#### Surface

The annual variability of zonal currents along the equator, is strongest in the eastern Pacific, where it is characterised by strong westward phase propagation (figure 2.9a). In the east, the strong eastward surge that occurs between April and July is associated with the reversal of the SEC. A phenomenon that is referred to as the spring time reversal of the SEC, because it occurs in the boreal spring. Westward phase propagation weakens west of  $140^\circ\text{W}$ , and in the western Pacific there is even evidence of eastward phase propagation. These aspects of the annual cycle are discussed and explained by Yu and McPhaden [1999].

One aspect not discussed in the literature, but which is an important aspect of

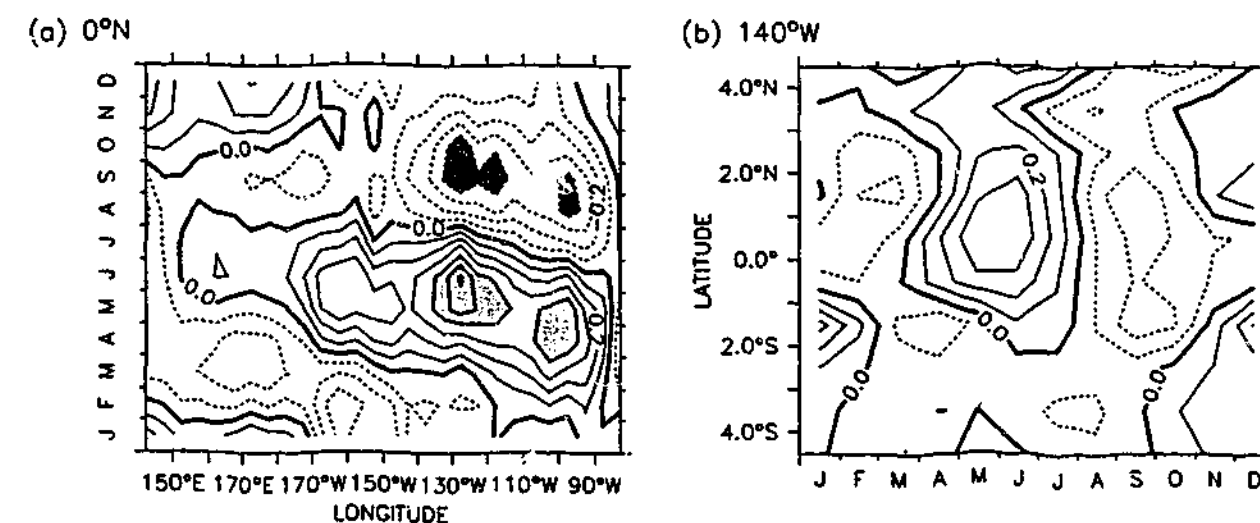


Figure 2.9: Annual cycle of zonal currents, (a) along the equator, and (b) about the equator at  $140^\circ\text{W}$  are shown in terms of anomalies about the annual mean. The units are  $\text{ms}^{-1}$ , and the contour interval is  $0.1\text{ms}^{-1}$ , with dashed contours indicating westward velocities. Eastward and westward velocities greater than  $0.4\text{ms}^{-1}$  have been shaded. (Data from the Reverdin et al. [1994] current climatology.)

the annual cycle, is the equatorially anti-symmetric nature of the annual cycle in the east. In the east, the currents (near the equator) in each hemisphere surge eastward during the spring and summer of that hemisphere, and thus tend to be out of phase across the equator. Although the northern annual cycle is much stronger than the southern, an anti-symmetric component in the annual cycle is seen in figure 2.9(b). In the west the annual cycle is completely symmetric about the equator.

#### Vertical structure

The annual cycle of zonal currents on the equator at  $165^\circ\text{E}$ ,  $140^\circ\text{W}$ , and  $110^\circ\text{W}$  are shown in figure 2.10. The annual mean vertical structure is shown in the right panels as it indicates the level and strength of the SEC and the EUC. In addition, the depth of the EUC is marked on the velocity anomaly plots with a horizontal dashed line. The vertical scale differs between the plots because of missing data. Fortunately at all locations data extends to the depth of the EUC.

The annual cycle at all three locations has a very similar structure. First, the eastward surge in currents that occurs at the surface, between April and July, extends to the depth of the undercurrent. This is referred to here as the spring time

surge (STS), because it occurs in the boreal spring. Second, the phase of the STS is fairly depth independent. However, the westward phase propagation of the STS is less evident with depth, and at the level of the EUC the westward phase speed is close to zero. Third, the STS has largest amplitude approximately 60m above the EUC core. Comparing the annual mean structure to the annual cycle shows, as stated above, that the eastward STS is strong enough to cause an eastward current at the surface.

Figure 2.10 shows the annual cycle in the undercurrent, including the eastward STS, is relatively weak compared to the annual cycle above. In figure 2.11 the annual cycle of the EUC is illustrated more clearly. At all locations annual variations are between 10% and 20% of the annual mean. Error bars show the eastward surge is significant, but westward phase propagation is not; the surge occurs at all locations around April to May.

### 2.3.4 Interannual variability

The monthly mean zonal current and interannual zonal current anomalies for TAO/TRITON data on the equator at 165°E, 140°W, and 110°W are shown in figures 2.12, 2.13, and 2.14, respectively. The monthly data (upper panels) clearly shows that the largest variations in zonal currents occur somewhere between the surface and the EUC core. Eastward velocities stronger than those in the EUC core are observed at this level. At these times the EUC is said to surface.

The monthly mean data reveal a large amount of interannual variability. As with annual variability, TAO data has also been used to document interannual variability [Yu and McPhaden, 1999a]. These authors show that at low frequencies (periods longer than a year) depth integrated zonal momentum is almost in Sverdrup balance, i.e., depth integrated zonal currents are balanced by wind stress. The account presented here differs from Yu and McPhaden's; it separates surface and subsurface motion, and is focused on describing seasonal current variability.

The time period covered by the data includes the 1982-83, 1986-87, 1991-92, 1993,

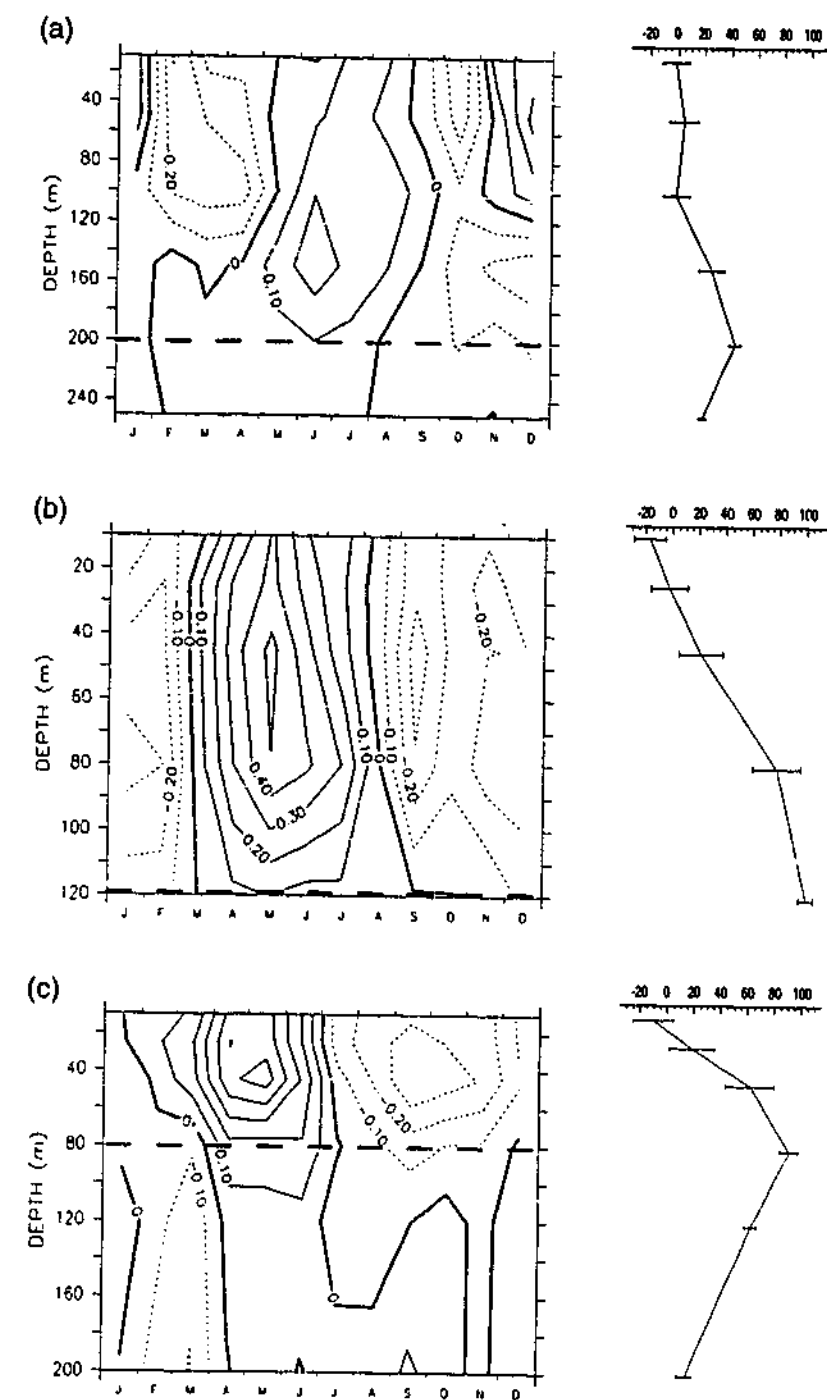


Figure 2.10: The annual cycle of zonal currents at (a) 165°E, (b) 140°W, and (c) 110°W calculated from TAO data; the data are detailed in Yu and McPhaden [1999b;a]. Panels on the left show the annual cycle of zonal currents in terms of velocity anomalies ( $\text{ms}^{-1}$ ). Dashed horizontal lines mark the depth of the undercurrent core on each plot. Panels on the right show the annual mean vertical structure of zonal currents ( $\text{cms}^{-1}$ ) at the three locations. Horizontal bars indicate 95% confidence interval calculated using the Student's t-distribution. The position of the bars also corresponds to measurement depths. Note, due to missing data, the vertical scales between plots differs.

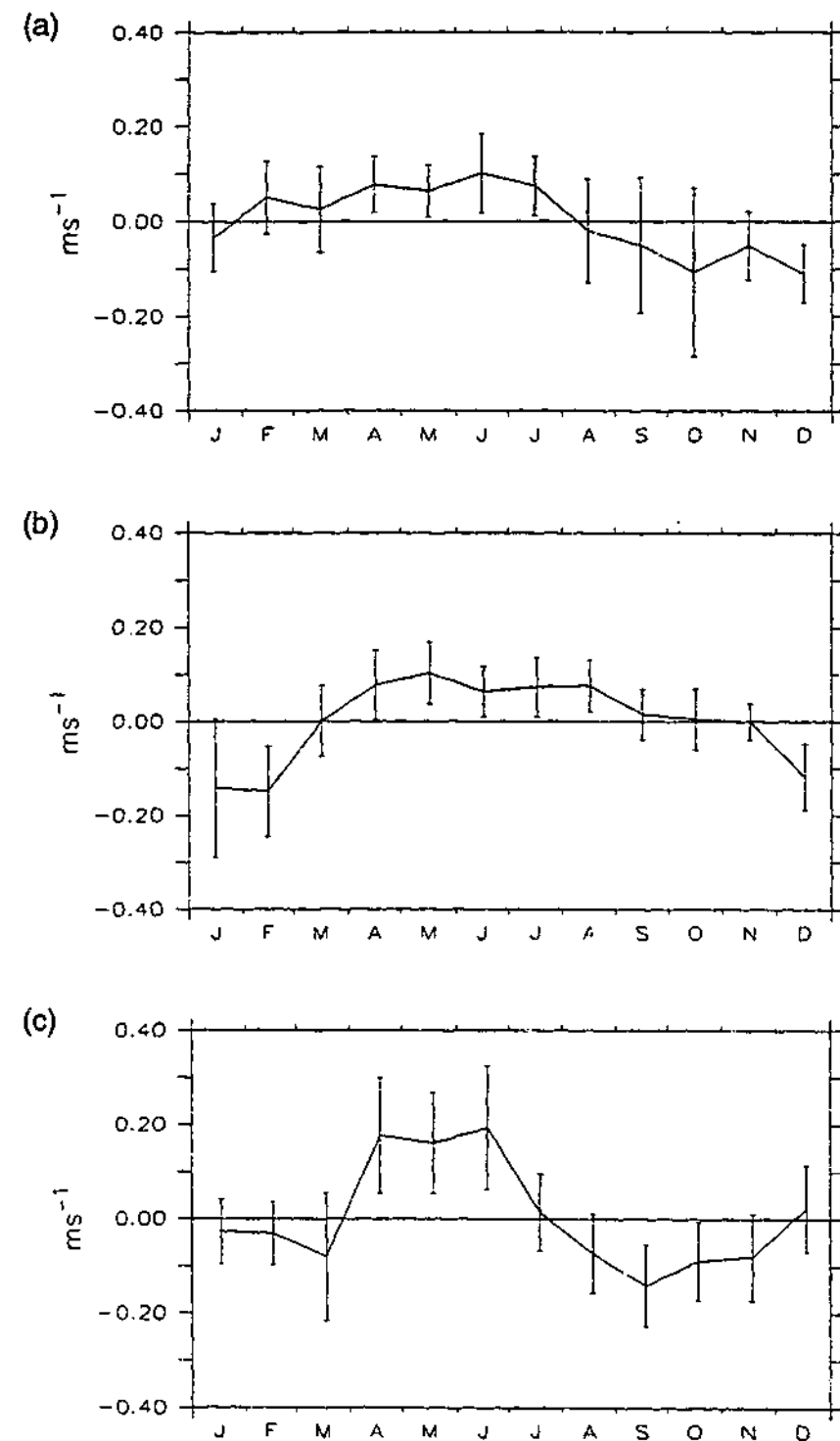


Figure 2.11: The annual cycle of zonal velocity anomaly ( $\text{ms}^{-1}$ ) at (a)  $165^{\circ}\text{E}, 0^{\circ}\text{N}$ , at 200m; (b)  $140^{\circ}\text{W}, 0^{\circ}\text{N}$ , at 120m; and (c)  $110^{\circ}\text{W}, 0^{\circ}\text{N}$ , at 80m. The depth at each location corresponds to the depth of the EUC core, hence these plots illustrate the annual cycle of the EUC. Vertical bars indicate the 90% confidence interval, calculated from the interannual variability of the data using a Student's *t*-distribution. (The data are from the TAO/TRITON array, and are detailed in Yu and McPhaden [1999b;a].)

1994-95, and 1997-98 El Niño events; and the 1988-89 La Niña events. However, missing data and varying record lengths, means these ENSO events are not captured at all three longitudes, and unfortunately, data records for the strong 1982-83 and 1997-98 El Niño events are incomplete.

The data, although limited, does illustrate features consistent with modelling and theoretical studies [Philander, 1990], and with earlier observational work [Gill, 1983]. The generally accepted picture is that during El Niño events, the surface currents surge eastward, cancelling the zonal pressure gradient (by transporting water from the west to the east), and eventually resulting in the disappearance of the EUC. Conversely, during La Niña events the surface currents surge westward, reinstating the zonal pressure gradient; eventually resulting in a stronger EUC, that slopes up more strongly toward the east.

At the surface, the strongest positive anomalies occur in 1983 and 1997, and are clearly associated with the corresponding strong El Niño events. During 1986 and through the early 1990's, positive zonal current anomalies are also evident, but the weakness of these anomalies, relative to the overall inter-annual variability, makes it hard to relate them to the El Niño events. Strong subsurface negative anomalies are also seen during El Niño events. At  $110^{\circ}\text{W}$  the negative anomalies in early 1983 and 1997 indicate the disappearance of the EUC. Significant negative anomalies also occur at  $140^{\circ}\text{W}$  in 1983. The picture for the 1986-87 event is less clear: The anomalies are weak, and their phase is not clearly related to the El Niño event. Similarly for the El Niño events of the early 1990's, there is little consistent behaviour in the anomalies. These differences are likely related to the different character of the 1982-83 and 1997-98 events, which were much stronger.

Only one La Niña event occurred during the data period, in 1988-89. During this event, the undercurrent is seen to surface, but the surfacing is not notably stronger than in other years. In the case of surface flow, only at  $165^{\circ}\text{E}$  are negative anomalies seen during the 1988 La Niña event. At the other two locations there are no significant surface anomalies. Thus, it is hard to relate zonal current anomalies to La Niña events.

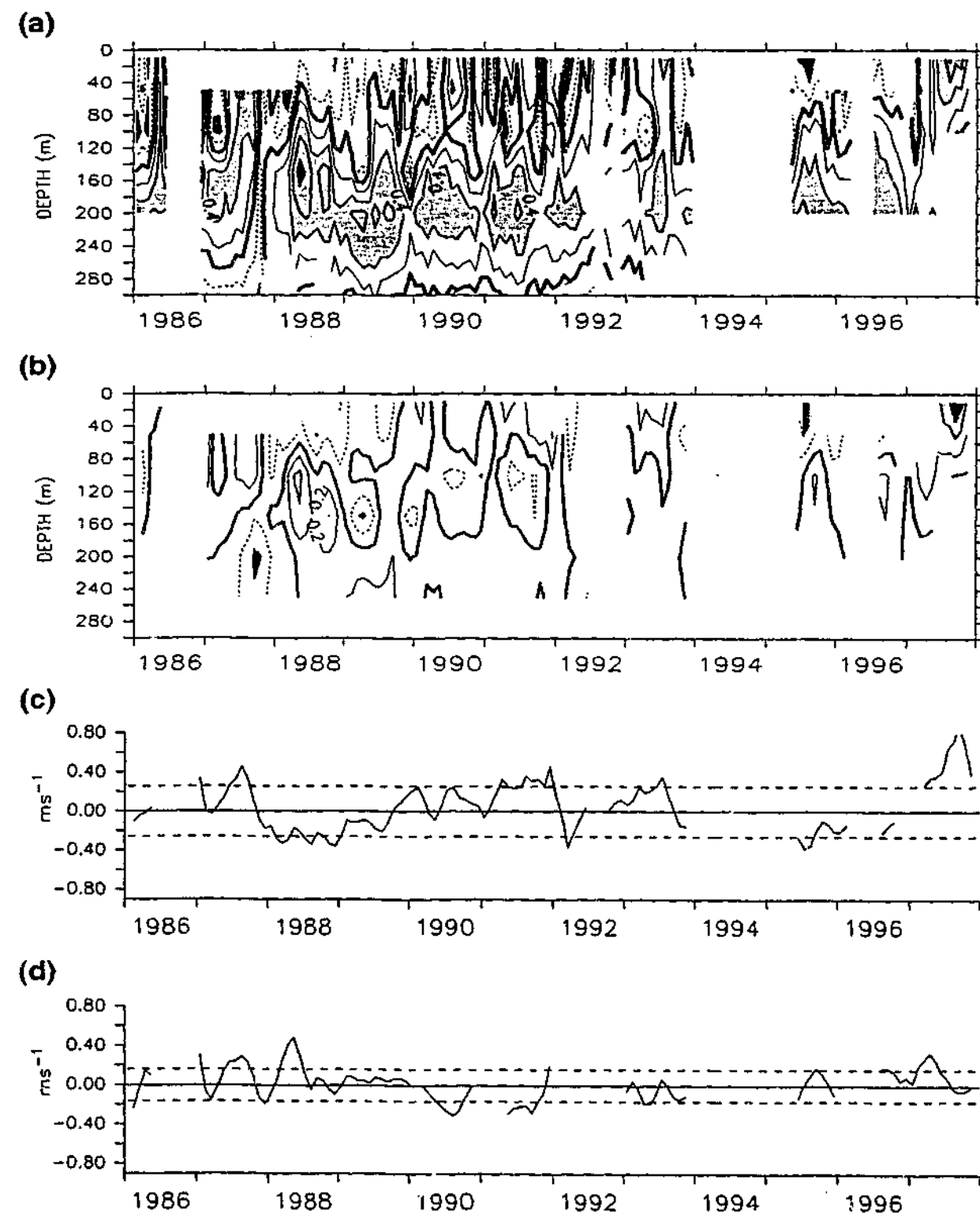


Figure 2.12: (a) Monthly mean zonal currents, (b) interannual zonal current anomalies, and time series of (c) surface and (d) subsurface zonal current anomalies at  $165^{\circ}\text{E}-0^{\circ}\text{N}$ . In (a) and (b) linear interpolation has been used to fill missing points, but only where data exists at both adjacent levels. In (c) and (d) a 3-month running mean has been applied to the data. The units are  $\text{ms}^{-1}$ . The contour interval in both (a) and (b) is  $0.2 \text{ ms}^{-1}$ , with a thick solid line for the zero contour, and dashed contours for negative values. In (c) and (d) dashed horizontal lines mark one standard deviation about zero. (The data are from the TAO/TRITON array, and are detailed in Yu and McPhaden [1999b;a].)

An interesting aspect of the interannual variability of zonal currents, which is revealed by the TAO/TRITON data, is the presence of coherent pulses between the three locations. During 1992 a non-dispersive pulse is seen to cross the Pacific. The monthly data are unable to precisely resolve the phase speed of this pulse, but it takes of the order a month to cross the equatorial Pacific. Thus, it is almost certainly a first baroclinic mode Kelvin wave. In late 1986 another weaker pulse is also seen.

To investigate the basin wide extent of zonal velocity anomalies, linear correlation coefficients were calculated for all combinations of surface and subsurface data. Focusing on seasonal variability, a three-month running mean was first applied to the data. Surface currents at  $110^{\circ}\text{W}$  and  $140^{\circ}\text{W}$  were quite well correlated, with a linear correlation coefficient ( $r$ ) of 0.5, but not well correlated with surface currents at  $165^{\circ}\text{E}$  ( $r=0.2$ ). Indeed overlaying the time series for  $110^{\circ}\text{W}$  and  $140^{\circ}\text{W}$  shows all the larger fluctuations are well matched.

In figure 2.15, TOPEX/Poseidon inferred zonal current anomalies on the equator are presented. The TOPEX/Poseidon data illustrates a much stronger relationship between ENSO and zonal current variability. However, while geostrophic currents compare well to in-situ TAO/TRITON measurements in the central Pacific, the correspondence in the east is significantly poorer (see chapter 5).

During the strong El Niño event of 1997-98 positive zonal current anomalies extend across the Pacific. Basin wide positive anomalies also occur during the 1993 and 1994-95 El Niño events. In addition, during the 1998-99 La Niña event strong negative zonal current anomalies extend across the basin. The strong relationship between geostrophic derived currents and ENSO variability is not altogether surprising, given the strong relationship between ENSO and sea-level variability. At least in the central Pacific, where zonal current variability is primarily geostrophic (See discussion in chapter 5), TOPEX/Poseidon data support the classical picture of zonal current variability associated with ENSO. In summary, the limited TAO/TRITON data prevents a complete description of the nature of interannual variability of zonal currents, and the zonal current behaviour during ENSO events. However, the data clearly illustrates that during strong El Niño events, surface currents surge eastward,

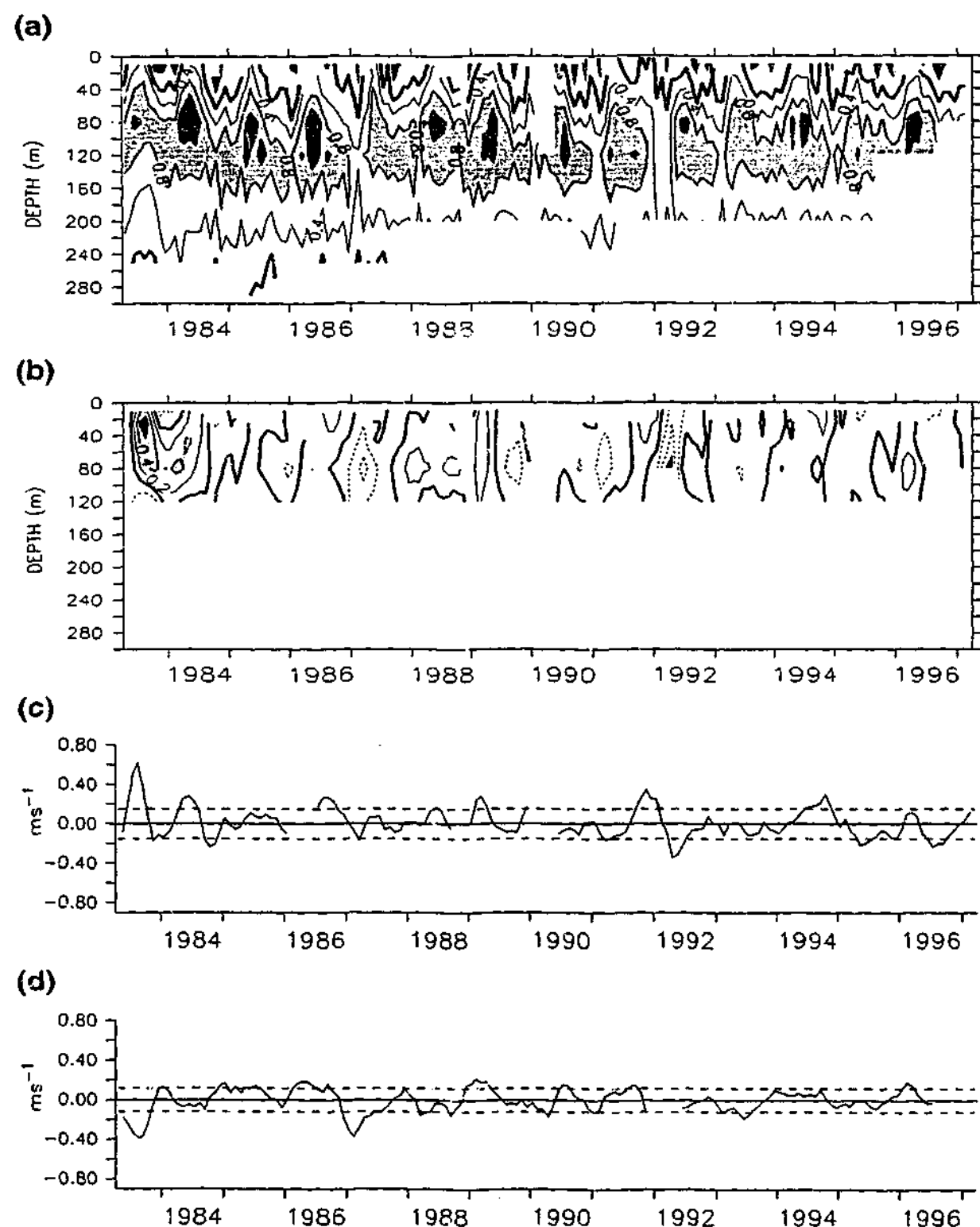


Figure 2.13: (a) Monthly mean zonal currents, (b) interannual zonal current anomalies, and time series of (c) surface and (d) subsurface zonal current anomalies at  $140^{\circ}\text{W}-0^{\circ}\text{N}$ . In (a) and (b) linear interpolation has been used to fill missing points, but only where data exists at adjacent levels. In (c) and (d) a 3-month running mean has been applied to the data. The units are  $\text{ms}^{-1}$ . The contour interval in (a) is  $0.4 \text{ ms}^{-1}$  and in (b) is  $0.2 \text{ ms}^{-1}$ , with a thick solid line for the zero contour, and dashed contours for negative values. In (c) and (d) dashed horizontal lines mark one standard deviation about zero. (The data are from the TAO/TRITON array, and are detailed in Yu and McPhaden [1999b;a].)

and the undercurrent weakens, even disappearing. Also, surface positive anomalies are strongest in the west, and subsurface negative anomalies are strongest in the east. TOPEX/Poseidon derived currents show a stronger relationship to ENSO, but this data is only reliable in the central Pacific.

## 2.4 Vertical velocity

In the equatorial oceans, upwelling primarily occurs along the equator, where it links the surface divergent Ekman flow, with the subsurface convergent geostrophic flow. Upwelling is very important in regulating SST [Philander, 1990], and in fact its signature is most strongly seen in the equatorial cold tongues of the Atlantic and Pacific oceans. However, upwelling is too weak to be measured directly with present instruments, and it is the least well known component of the equatorial circulation. A review of upwelling estimates is presented below. It is primarily taken from the more complete reviews of Weisberg and Qiao [2000] and Poulain [1993].

To date, all observational upwelling estimates have been made by calculating the divergence of horizontal currents, and then using mass continuity to infer vertical velocity. In particular, vertical velocity at the base of the mixed layer has been calculated using drifter data [Poulain, 1993]. Also, vertical velocity profiles have been calculated using data from moored buoy arrays [Weisberg and Qiao, 2000]). Another method has been to calculate area averaged vertical velocity profiles using linear dynamics, and hydrographic and surface wind data [Bryden and Brady, 1985].

Due to poor data quality, estimates of the vertical velocity profiles are problematic, and major differences exist between the estimates. However, all estimates indicate that upwelling is strongest between the EUC core and the surface, and has a maximum mean value of the order  $2-3 \times 10^{-5} \text{ ms}^{-1}$ .

The observational work of Poulain [1993], which is based on 12 years of surface drifter data, suggest upwelling is an order of magnitude stronger than the estimates made from vertical velocity profiles. Poulain, through a careful treatment of the

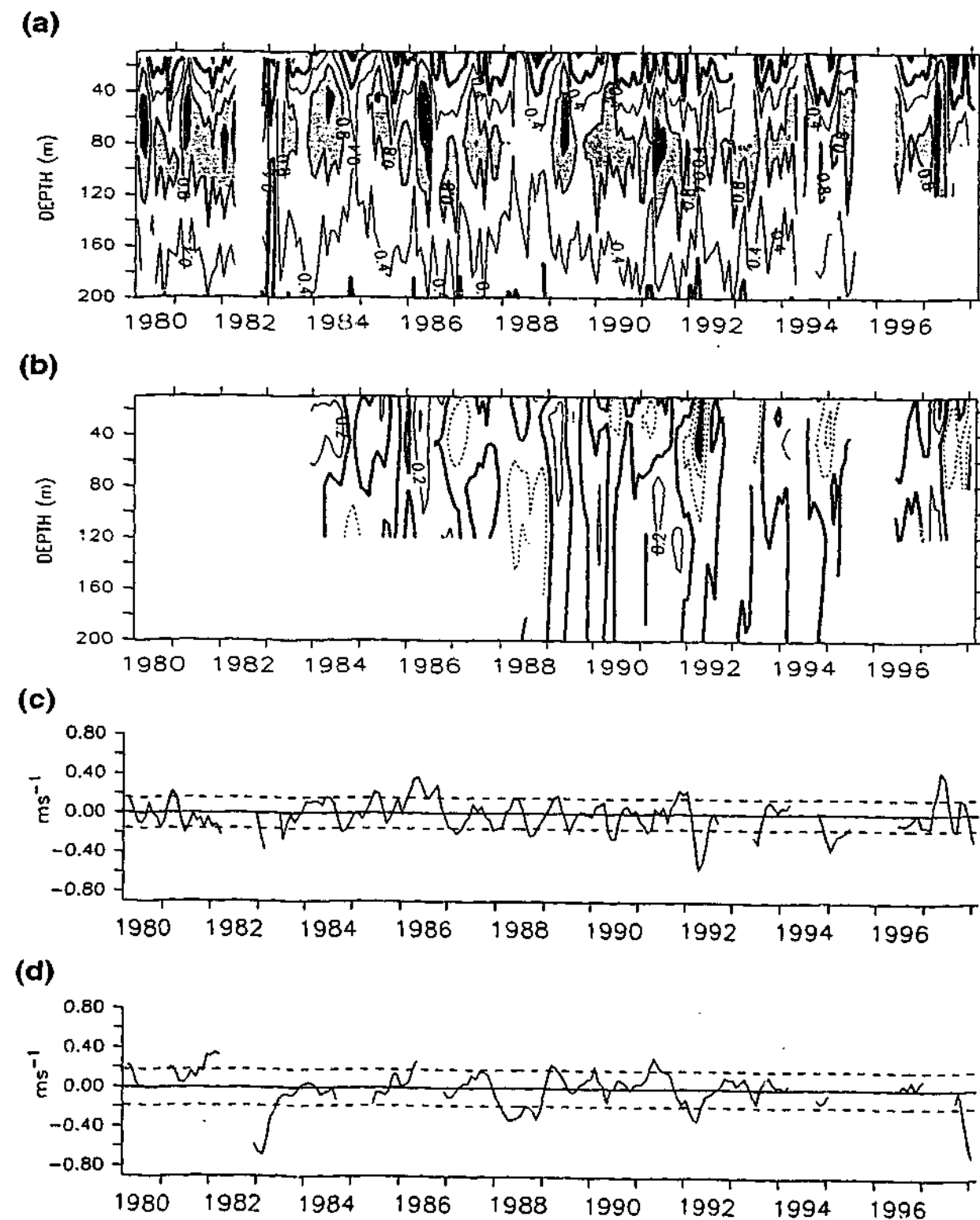


Figure 2.14: Monthly mean currents and anomalies as in-figure 2.13 except for 110°W-0°N.

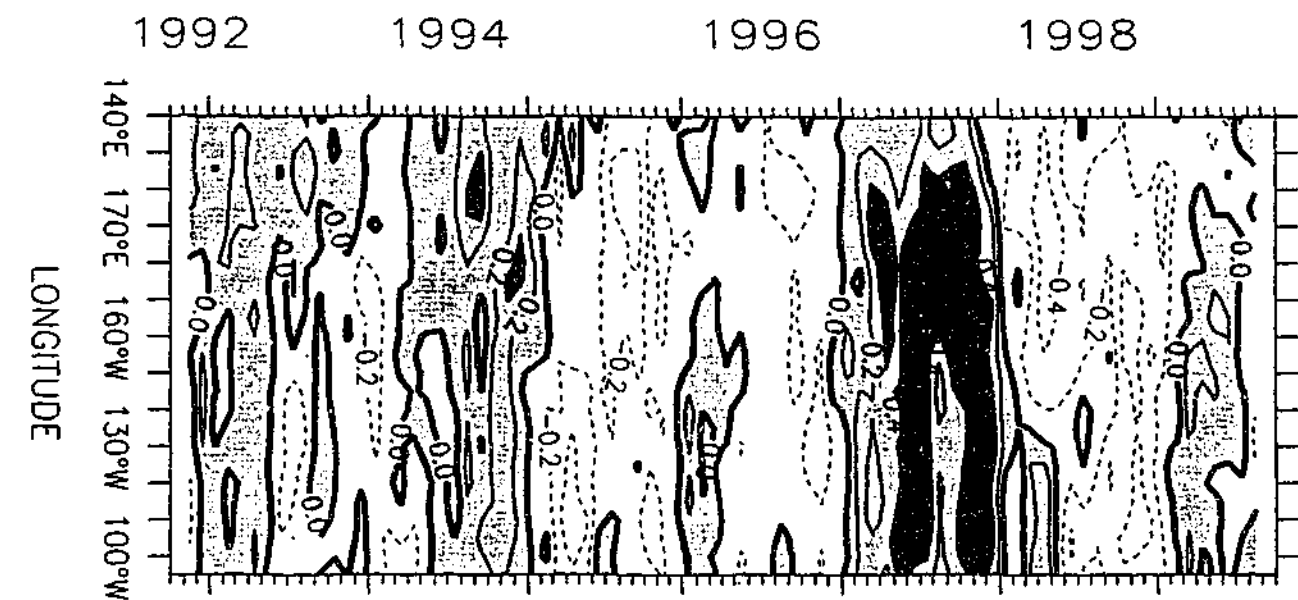


Figure 2.15: TOPEX/Poseidon inferred zonal current anomalies on the equator. The units are  $ms^{-1}$ , the contour interval is  $0.2 ms^{-1}$ , and positive anomalies are shaded. The data are from Delcroix et al. [2000]. Details on the data are described in the main text.

drifter observations, resolves longitudinally averaged meridional currents on a 0.05 degree latitude grid. His results indicate that maximum meridional divergence occurs within a 20km band centred on the equator, and has an annual mean magnitude of  $3$  to  $4 \times 10^{-6} s^{-1}$ ; equivalent to an upwelling velocity of  $1.5$  to  $2 \times 10^{-4} ms^{-1}$  at 50m. Meridional divergence and upwelling are thus too strongly equatorially confined to be resolved by moored buoy arrays or other area averaged techniques. Upon area averaging his estimates are consistent with previous estimates, calculated on coarser meridional grids.

Lack of data has prevented any significant descriptions of annual, interannual, or intra-annual variability of vertical velocity. Poulain [1993] presents an annual cycle for surface meridional divergence that is roughly in phase with zonal wind stress. However, the data are subject to large uncertainties. Although this relationship would be consistent with upwelling being driven by surface Ekman flow off the equator, his results are not conclusive, and in fact Reverdin et al. [1994] data would indicate a completely opposite relationship. Clearly large uncertainties exist.

On intra-annual time scales, vertical velocity is seen to be highly variable [Weisberg

and Qiao, 2000]. ENSO modelling studies would indicate that there is also a large amount of interannual variability [Philander, 1990].

Another approach to estimating vertical velocity has been to use numerical ocean models [Philander et al., 1987], but numerical models are of little use in resolving specific issues related to meridional circulation, because of the strong sensitivity of meridional currents to the formulation of vertical diffusion [Weisberg and Qiao, 2000; World Climate Research Programme, 1995].

## 2.5 Sea Surface Temperature

SST is one of the more important climate variables. It is also the most well record variable in the equatorial Pacific ocean. SST records are long, spatially extensive, and of high quality. This is primarily because SST is easily measured, and SST varies smoothly over large spatial scales. (See McPhaden et al. [1998] for a discussion of SST data.) The primary purpose of this section is to introduce observations of interannual SST variability. The SST annual mean and the annual cycle are also discussed.

### 2.5.1 Data

There are several available data sets. For example, the Climate Analysis Center (CAC) analysis (see Harrison et al. [1990]), the Comprehensive Ocean Atmosphere Data Set (COADS) [Slutz et al., 1985], and the Reynolds and Smith [1994] SST analysis. The different data sets have slightly different temporal and spatial resolution, and are constructed from slightly different observations. The most recent data is of high quality [McPhaden et al., 1998], and although there are significant disagreements between data sets for earlier periods, there is overall agreement between the data sets [Harrison et al., 1990].

One of the most widely used data set in ENSO modelling applications is the CAC analysis. For example, it has been used by Zebiak and Cane [1987]: Bat-

tisti [1988]; Kleeman [1993]; Dewitte [2000], and Shu and Clarke [2000]. However, this product was discontinued in 1995, and replaced with an optimal interpolated product [Reynolds and Smith, 1994]. This product is used here.

The Reynolds and Smith [1994] optimal interpolated SST fields are constructed from ship, buoy, and bias corrected satellite data. The data is on a global  $1^\circ$  grid and extends from Nov-1981 to the present. SST anomalies are calculated relative to the Reynolds and Smith [1995] SST climatology. This climatology is derived from monthly optimal interpolated SST analyses, adjusted to a base period of 1950 to 1979. These data are from IGOSS NMC and were obtained from the IRI/LDEO climate library (<http://ingrid.ldeo.columbia.edu/>).

### 2.5.2 Annual mean

Figure 2.16a illustrates annual mean SST in the equatorial Pacific. In the west, the western Pacific warm pool is seen: A large body of water with SST greater than  $28^\circ\text{C}$ . Within the warm pool horizontal temperature gradients are weak, and the maximum SST is  $29^\circ\text{C}$ . East of the warm pool, temperatures drop significantly, and at the South American coast SST is around  $20^\circ\text{C}$ . The warm pool, and the associated convection above, are important components of the global atmospheric circulation. Movements of the eastern edge of the warm pool are associated with interannual movements in convection, and are linked to the ENSO phenomenon [Fu et al., 1986]. Understanding SST variability in this region is the focus of this study. There are two other prominent features seen in the annual mean SST pattern: a band of warm waters north of the equator; and a band of cooler water along the equator, east of the warm pool (the equatorial cold tongue). The warm water north of the equator is associated with the NECC and the Inter-tropical Convergence Zone. The equatorial cold tongue, is associated with strong equatorial upwelling. Indeed, the annual mean SST pattern, equatorial currents, and atmospheric circulation are all strongly linked [Philander, 1990].

The annual mean thermal structure along the equator is shown in figure 2.16b.

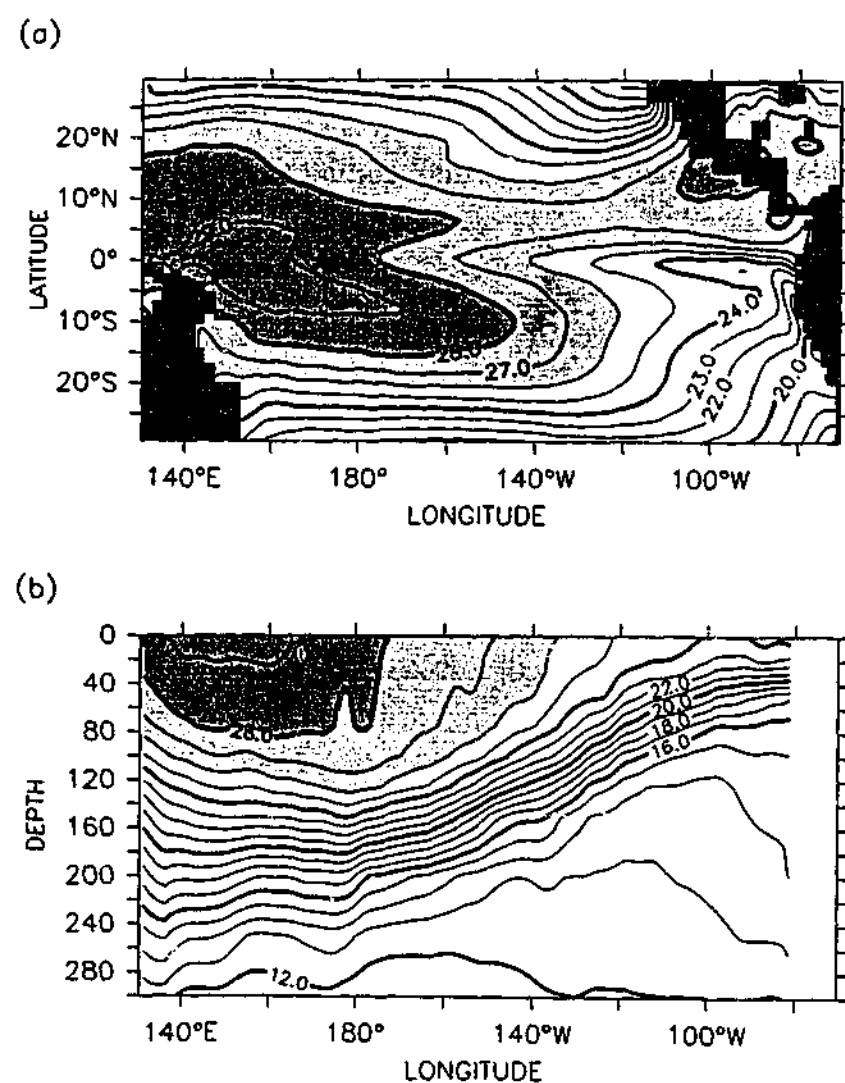


Figure 2.16: (a) Annual mean SST in the equatorial Pacific, and (b) an annual-mean temperature section along the equator. Units are  $^{\circ}\text{C}$ . (Data in (a) are from Reynolds and Smith [1995] SST climatology, and in (b) from Levitus [1982])

Two important features are illustrated. First, vertical temperature gradients in the western Pacific warm pool are weak. The warm pool extends well below the surface, and is a large reservoir of thermal energy. The second feature is the equatorial thermocline, which is the region of sharp temperature gradient below the surface. Its centre is marked by the twenty degree isotherm.

The thermocline is linked to many features of the equatorial Pacific. The strong horizontal gradients in surface temperature east of the warm pool are associated with the eastward surfacing of thermocline. The thermocline marks the position of the EUC, and its eastward slope is a dynamical response to the surface trade winds. In the east, vertical movements of the thermocline are associated with in-

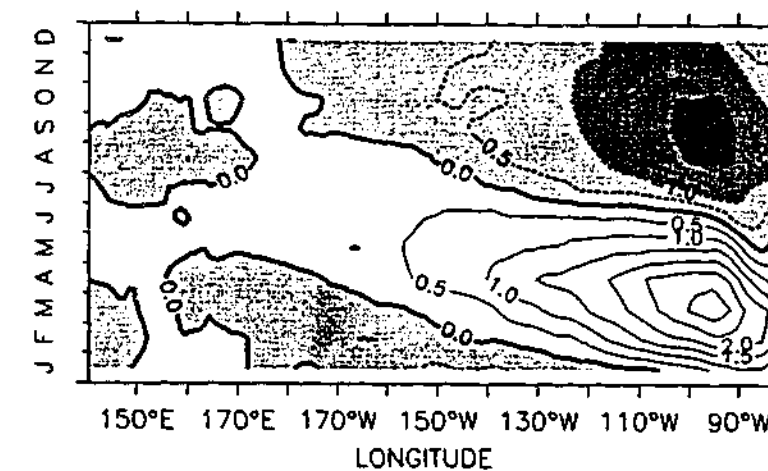


Figure 2.17: The annual cycle of SST along the equator in the Pacific. Anomalies about the annual mean are plotted in units of  $^{\circ}\text{C}$ . (Data are from Reynolds and Smith [1995] SST climatology)

terannual variability in temperature [Wang and McPhaden, 2000], and the ENSO phenomenon [Philander, 1990].

### 2.5.3 Annual cycle

The annual cycle of SST along the equator is shown in figure 2.17. It bears much similarity to the annual cycle of zonal currents and zonal wind stress [Yu and McPhaden, 1999b]. Variability is strong in the east, where SST can vary by  $5^{\circ}\text{C}$ , and weak in the west. In the east the phase of the annual cycle propagates westward, closely resembles that of zonal currents (see figure 2.9). This figure clearly illustrates that annual variability is confined to the eastern Pacific.

### 2.5.4 Interannual variability

Interannual SST variations in the equatorial Pacific between January 1982 and December 1999 are shown in figure 2.18. Large positive anomalies in 1982-83 and 1997-98, and weaker positive anomalies in 1986-87, 1991-92, 1993, and 1994-95, mark the El Niño events of the period. Large negative anomalies in 1988-89 and 1998-99 mark the La Niña events. The strong SST variability with a 3 to 5 year period, illustrated by the figure, is one of the most striking signatures of the ENSO

phenomenon[Philander, 1990].

Figure 2.18 shows that, like annual variability, interannual SST variability is strongest in the east. It also shows that interannual variability is stronger than annual variability. Interannual anomalies vary between  $-2^{\circ}$  and  $5^{\circ}$  in magnitude.

The zonal structure of interannual SST anomalies is different to that of the annual anomalies (figure 2.17). The interannual anomalies extend further across the Pacific, with strong anomalies occurring at the dateline. The latter indicate movements in the eastern edge of the western Pacific warm pool.

Observationally, SST rarely drop below  $20^{\circ}\text{C}$  or rise above  $29^{\circ}\text{C}$ . These observational limits are apparent during El Niño and La Niña events. During El Niño,  $28^{\circ}$  waters extend across the Pacific, and during La Niña SST isotherms contract westward, but SST does not drop significantly below  $20^{\circ}\text{C}$ . These observational limits are visible in the different zonal structure of negative and positive anomalies. Negative anomalies tend to be strongest in the central Pacific, and positive anomalies tend to be strongest in the eastern Pacific. The different zonal structure simply reflects the background zonal temperature gradient.

## 2.6 Concluding Remarks

This chapter forms the observational basis of the thesis. Observations relevant to modelling interannual variability of zonal currents and SST were presented. The main focus was on the MCM data from the TAO/TRITON array of moored buoys [Yu and McPhaden, 1999b]. These data are relatively new, of high quality, and of a long enough period to investigate interannual variability. The remainder of the thesis is a modelling study of zonal currents, and their role in SST variability. The TAO/TRITON data is central in this investigation.

Other current data, and thermocline depth measurements were also described in this chapter. The additional current data complement the TAO data, providing greater spatial coverage. Thermocline depth measurements are used in chapter 6, to

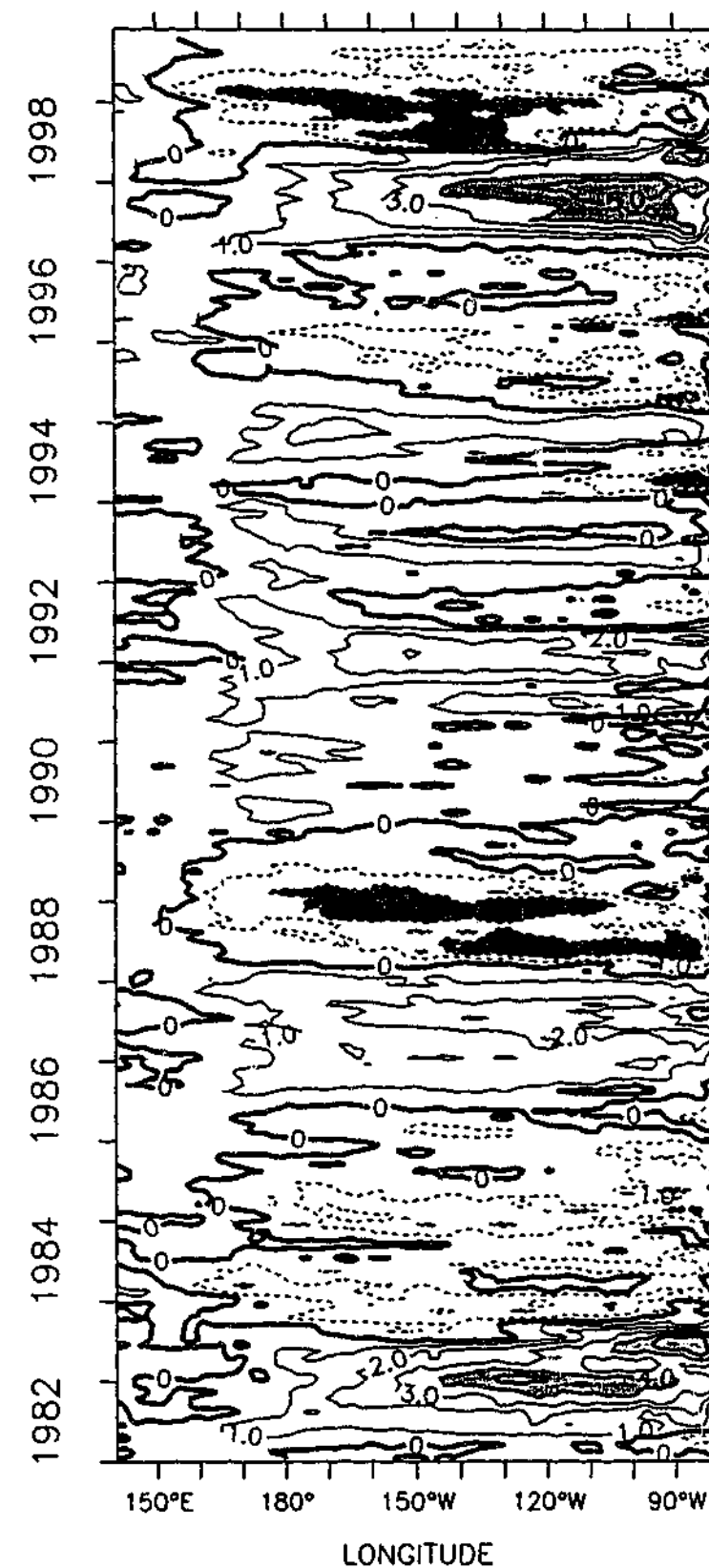


Figure 2.18: Interannual SST anomalies along the equator in the Pacific. Units are  $^{\circ}\text{C}$ . The contour interval is  $1^{\circ}\text{C}$ ; and positive anomalies greater than  $2^{\circ}$ , and negative anomalies less than  $-2^{\circ}\text{C}$  are shade. (Data are from Reynolds and Smith [1994], and anomalies are relative to the Reynolds and Smith [1995] SST climatology)

develop the SST component of the ICM. Throughout the thesis there is an emphasis on using observations to assess model performance. Thus, a survey of the available data was also given.

## Chapter 3

# Dynamical Ocean Model

### 3.1 Introduction

The main tool used in this study for investigating the dynamics of zonal currents, and the importance of zonal advection in controlling SST, is an intermediate complexity ocean model. In this chapter, the dynamical component of the ocean model is formulated and a careful description of its annual mean simulation is given. Simulation of annual and interannual zonal current variability is described in the following two chapters. The thermodynamic model component is presented in chapter 6.

The dynamical ocean model consists of a linear and a non-linear component. The linear component is basically a McCreary [1981] type modal model, extended to a horizontally-varying background stratification. It is the dominant component, largely determining the structure and magnitude of the solution. The non-linear component is a highly simplified model of the residual non-linear momentum equations. It provides important corrections to the solution where the linear assumption breaks down. It is this novel treatment that allows the importance of linear and non-linear terms to be determined, and a number of basic mechanisms controlling annual and inter-annual variability of zonal currents to be explained.

The model's design is motivated as follows. Firstly, a large amount of observational evidence and experimental results exists, that show linear dynamics, generally associated only with the low order baroclinic modes, can successfully explain

many features of the equatorial Pacific ocean [McCreary, 1981; Yu and McPhaden, 1999b;a; Cane, 1984]. Secondly, there are regions where non-linearity is important; for example, in the momentum balance of surface zonal currents [Wascogne, 1989], and the annual cycle of the EUC (to be shown in the next chapter). Thirdly, horizontal variations in stratification are important, having a significant effect on the wind projection onto baroclinic modes, and hence the solution [Dewitte et al., 1999]. Thus the model is relatively simple, but able to accurately model many aspects of equatorial dynamics.

The structure of this chapter is as follows. First, the mathematical formulation and physical justification of the dynamical ocean model will be presented. In section 3.3, the implementation of the model is described. Details of the model's domain, grids, and parameter values are given. In section 3.4, the model's annual mean simulation is described and the annual mean zonal momentum balance is discussed. Finally, in section 3.5, mode convergence properties are presented to show that the design of the linear component is appropriate.

A discussion of the model's sensitivity, to parameter choice and design, is deferred to the next chapter, so that it can be discussed in the context of the full simulation. These sensitivity studies indicate the model is robust over a reasonable parameter range. The results presented in this chapter and the next clearly show the model is able to capture the basic dynamics of the equatorial Pacific.

## 3.2 Model formulation

In outline, the derivation of the model equations is as follows. First, the equations governing large-scale equatorial flow are presented. The model is derived from these equations, and for completeness all the basic assumptions are stated. The splitting into linear and non-linear components is described in section 3.2.2. It is clearly shown that these equations are an exact representation of the full equations. The individual formulations of the linear and non-linear components are given in sections 3.2.3 and 3.2.4 respectively. Careful attention is paid to the approximations, particularly those

associated with features new to intermediate complexity modelling.

### 3.2.1 Dynamical equations of motion

The model is derived from equations describing wind-induced dynamical perturbations about a resting background state. The influence of thermodynamics on dynamics is neglected. This assumption, which is common to ICMs, is demonstrated to hold on annual and interannual time scales. For example, annual mean currents and horizontal variations in stratification and pressure are largely dynamically determined [McCreary, 1981] (Also see results in section 3.4). The annual cycle of surface zonal currents is also determined dynamically [Yu and McPhaden, 1999b]. The negligible influence of thermodynamics on dynamics is also illustrated by the success of ICMs at modelling annual and interannual SST variability [Seager et al., 1988; Blumenthal and Cane, 1989].

Assuming isentropic and incompressible flow, neglecting viscous and diffusive effects, and making the hydrostatic and Boussinesq assumptions, the equations describing perturbations about a background resting state are

$$\begin{aligned} \frac{Du}{Dt} - fv &= -p_x + \nu_h \nabla_h^2 u + (\nu_v u_z)_z, \\ \frac{Dv}{Dt} + fu &= -p_y + \nu_h \nabla_h^2 v + (\nu_v v_z)_z, \\ p_z + \rho g &= 0, \\ \nabla \cdot \mathbf{u} &= 0, \\ \rho_t + \bar{\rho}^{-1} \mathbf{u} \cdot \nabla (\bar{\rho} + \bar{\rho} \rho) &= \kappa_h \nabla_h^2 \rho + (\kappa_v \rho)_{zz}, \end{aligned} \quad (3.1)$$

where  $\frac{D}{Dt} = \frac{\partial}{\partial t} + \mathbf{u} \cdot \nabla$  is the material derivative;  $\mathbf{u} = (u, v, w)$  is the velocity specified in east, west, and vertical directions;  $f$  is the Coriolis parameter;  $\nu_h$  and  $\nu_v$  are the horizontal and vertical eddy diffusivities for momentum; and  $\kappa_h$  and  $\kappa_v$  are the horizontal and vertical eddy diffusivities for heat. Pressure and density are expressed as kinematic pressure and specific gravity, i.e.,  $p = \frac{p}{\bar{\rho}}$  and  $\rho = \frac{\rho}{\bar{\rho}}$ , where  $\bar{\rho}$  is the mean background density profile. The mean background density is horizontally uniform

by requirement of the steady state. In this equation and throughout the thesis, independent variable subscripts on dependent variables denote partial derivatives.

The first three equations are the standard momentum equations, with horizontal and vertical eddy mixing included. The fourth equation is conservation of mass for an incompressible fluid. The fifth equation is a form of the equation of state, with eddy mixing included. It is straightforward to derive these equations from the full equations of motion, by simply expanding about a resting state. The full equations of motion, excluding eddy mixing, are presented in Gill [1982] section 4.10.

The appropriate boundary conditions for equations 3.1 are

at the surface ( $z = 0$ ),

$$\begin{aligned}\nu_v u_z &= \tau^x, \\ \nu_v v_z &= \tau^y, \\ \kappa \rho &= 0, \\ \frac{D\eta}{Dt} &= 0,\end{aligned}$$

at the bottom ( $z = -H$ ),

$$\begin{aligned}\nu_v u_z &= 0, \\ \nu_v v_z &= 0, \\ \kappa \rho &= 0, \\ w &= 0,\end{aligned}$$

and at lateral boundaries, no slip:

$$\underline{\mathbf{u}} = \mathbf{0}, \quad (3.2)$$

$\tau^x$  and  $\tau^y$  are the zonal and meridional surface wind stress,  $\eta$  is the free surface, and  $H$  is the depth of the ocean. Following McCreary [1981],  $\kappa \rho = 0$  at the upper and lower boundaries, i.e., density does not vary on these surfaces. As density anomalies are created only by advection, this is appropriate.

### 3.2.2 Linear and Non-linear components

Recognising the importance of linear dynamics and the ability of baroclinic models to simulate the dynamics of the equatorial Pacific, equations 3.1 and boundary conditions 3.2, are expressed as the sum of a linear component, and a residual non-linear component. The splitting of the equations into linear and non-linear components, which allows the linear component to be treated in greater detail, is described first. The separate treatments of the individual components follows.

Let the solution of equations 3.1, satisfying BCs 3.2 be written as two components:

$$\begin{aligned}\underline{\mathbf{u}} &= \underline{\mathbf{u}}^l + \underline{\mathbf{u}}^{nl} \\ &= (u^l, v^l, w^l) + (u^{nl}, v^{nl}, w^{nl}) \\ p &= p^l + p^{nl} \\ \rho &= \rho^l + \rho^{nl},\end{aligned} \quad (3.3)$$

where superscripts  $l$  and  $nl$  indicate the linear and non-linear components respectively.

Let the linear component be defined as the solution to the linearised equations of motion, satisfying the full BCs 3.2,

$$\begin{aligned}u_t^l - f v^l &= -p_x^l + \nu_h \nabla_h^2 u^l + (\nu_v u_z^l)_z \\ v_t^l + f u^l &= -p_y^l + \nu_h \nabla_h^2 v^l + (\nu_v v_z^l)_z \\ p_z^l + \rho^l g &= 0 \\ \nabla \cdot \underline{\mathbf{u}}^l &= 0 \\ \rho_t^l - \frac{w^l}{g} N^2 &= \kappa_h \nabla_h^2 \rho^l + (\kappa \rho^l)_{zz},\end{aligned} \quad (3.4)$$

where  $N^2 = -g\bar{\rho}^{-1}\bar{\rho}_z$  is the background Brunt-Väisälä frequency. These equations are obtained by linearisation of equations 3.1, neglecting horizontal advection

of mean horizontal density gradients. Neglect of these terms, which is standard in linear models, is not easily justified, but given the results presented in this thesis, does not seem a significant issue. (See discussion in section 3.2.4)

The non-linear component is defined as a perturbation about our linear state. It is obtained by substituting definitions 3.3 into equations 3.1, and using equations 3.4 and BCs 3.2. The resulting set of equations, which are referred to as the residual non-linear equations, are

$$\begin{aligned}
 u_t^{nl} + \underline{\mathbf{u}} \cdot \nabla u - f v^{nl} &= -p_x^{nl} + \nu_h \nabla_h^2 (u^{nl}) + (\nu_v u_z^{nl})_z, \\
 v_t^{nl} + \underline{\mathbf{u}} \cdot \nabla v + f u^{nl} &= -p_y^{nl} + \nu_h \nabla_h^2 (v^{nl}) + (\nu_v v_z^{nl})_z, \\
 p_z^{nl} + \rho^{nl} g &= 0 \\
 \nabla \cdot \underline{\mathbf{u}}^{nl} &= 0, \\
 \rho_t^{nl} + \frac{1}{\bar{\rho}} (\underline{\mathbf{u}}^{nl} \cdot \nabla \bar{\rho} + u^l \bar{\rho}_x + v^l \bar{\rho}_y) \\
 + \underline{\mathbf{u}} \cdot \nabla \rho &= \kappa_h \nabla_h^2 \rho^{nl} + (\kappa \rho^{nl})_{zz}. \quad (3.5)
 \end{aligned}$$

Care must be taken in distinguishing the total velocity,  $\underline{\mathbf{u}}$  ( $= \underline{\mathbf{u}}^l + \underline{\mathbf{u}}^{nl}$ ); the non-linear velocity,  $\underline{\mathbf{u}}^{nl}$ ; the total zonal velocity component,  $u$  ( $= u^l + u^{nl}$ ); and the non-linear zonal velocity component,  $u^{nl}$ . Although the non-linear equations shall be given a highly simplified treatment, they are expressed completely to show the separation into linear and non-linear components, in itself, does not involve approximations.

The boundary conditions on the non-linear residual equations, which are similarly obtained as a residual of the full boundary conditions 3.2, are the zero boundary conditions,

at the top and bottom ( $z = 0, -H$ ),

$$\begin{aligned}
 \nu_v u_z &= 0, \\
 \nu_v v_z &= 0,
 \end{aligned}$$

$$\kappa \rho = 0,$$

$$w = 0,$$

and at lateral boundary, no slip:

$$\underline{\mathbf{u}} = \underline{\mathbf{0}}. \quad (3.6)$$

### 3.2.3 Linear component

The linear component consists of a ten baroclinic mode model plus two surface layers. The ten baroclinic mode model simulates the first ten baroclinic modes. The surface layers simulate the combined effect of baroclinic modes 11 to 30. They are governed by Ekman dynamics, and simulate the ocean's local response to wind forcing. Similar formulations have been used by other authors [Zebiak and Cane, 1987; Blumenthal and Cane, 1989].

A ten mode solution ensures zonal velocity and pressure fields are converged (section 3.5). A contribution for modes 11 to 30 is included, because these modes contribute significantly to the meridional circulation. A complete discussion of the approximations and background for this formulation is now given. A full derivation follows.

#### Background

Separation into baroclinic modes is allowed when the hydrostatic approximation holds, vertical mixing can be ignored, and the background stratification is horizontally uniform. As equations 3.4 include vertical mixing, and the background stratification is to be taken as the observed annual-mean horizontally-varying stratification (the reasons for this are explained below), expressing the solution in terms of baroclinic modes requires certain assumptions:

- Vertical eddy mixing coefficients for both heat,  $\kappa_v$ , and momentum,  $\nu_v$ , are inversely proportional to the square of Brunt-Väisälä frequency,  $N^2$ .

- Horizontal variations in stratification do not result in significant mode mixing (scattering among the modes).

This parameterisation of vertical mixing results in a mode dependent damping that is inversely proportional to the mode's shallow water speed squared. Thus, mode damping increases with mode number. The parameterisation was first applied by McCreary [1981] in a model of the EUC, and has since been applied in a variety of applications [Minobe and Takeuchi, 1995; Yu and McPhaden, 1999b; Shu and Clarke, 2000]. Other forms of mode dependent damping that also damp higher modes more strongly, have been used to simulate the effects of vertical mixing [Blumenthal and Cane, 1989; Dewitte, 2000]. The variety of formulations indicate an insensitivity of zonal currents and pressure to the form of vertical mixing. Thus, the McCreary parameterisation is sufficiently accurate to model those aspects of equatorial dynamics studied here.

There are two reasons for choosing the observed annual mean stratification (as opposed to a horizontally uniform) to express the linear solution in terms of baroclinic modes. The first reason is that wind projection onto the modes is more realistic, because the wind projection coefficients vary spatially. The latter refer to the mode dependent coefficients,  $\psi_n(0)/(\int_{-H}^0 \psi_n^2 dz)$ , that result from the vertical eddy mixing term, when the momentum equations are separated into baroclinic modes, with wind stress matching surface boundary conditions, i.e.,

$$(\nu_v u_z)_z \rightarrow \frac{\tau^x \psi_n(0)}{\int_{-H}^0 \psi_n^2 dz} - r_n u_x$$

where  $\psi_n$  is the  $n$ th baroclinic mode,  $\psi_n(0)$  is the surface value of the  $n$ th baroclinic mode,  $r_n$  is mode dependent damping, and  $u_n$  is the zonal velocity coefficient of the  $n$ th baroclinic mode. These terms are further described below. The wind projection coefficients determine how strongly the individual modes are forced, hence affects the solution strongly.

The second reason is that the vertical structure of the solution resembles observations more closely, because the vertical structure functions vary horizontally. If mode mixing is neglected, there are no other differences between this solution and

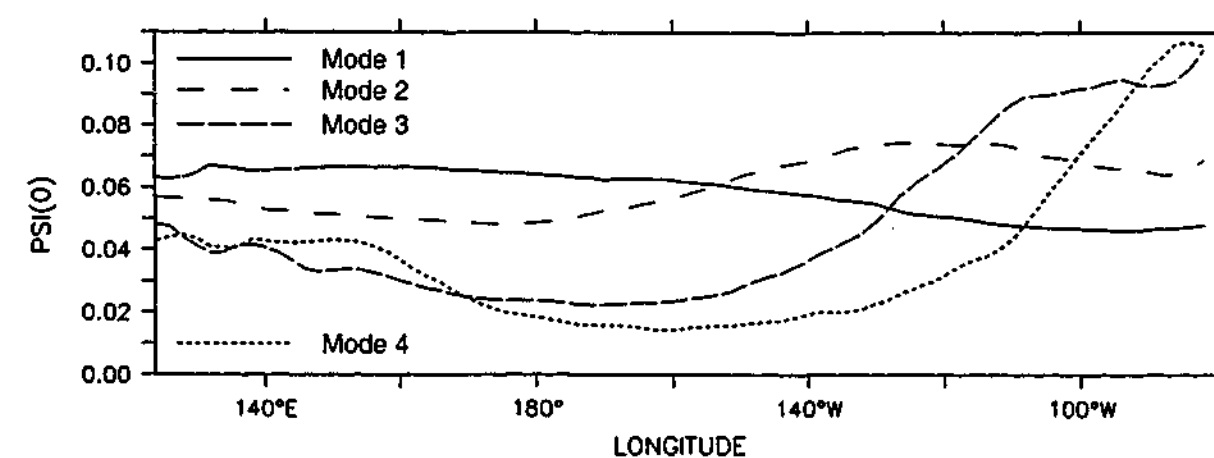


Figure 3.1: Wind-projection coefficients along the equator in the Pacific for the first four baroclinic modes. The wind-projections coefficients determine how strongly the individual modes are forced, see main text for details. (Calculated using Levitus [1982] data)

that obtained with a horizontally-uniform stratification. In particular, horizontal variations in background density do not result in horizontal variations in pressure.

The formulation of the linear component does not conflict with the full equations (3.1), which were derived by assuming a resting background state (with horizontally-uniform stratification). This is because, in the full equations, horizontal variations in background density cause horizontal variations in pressure, but in the linear model there is no such influence. Thus, the linear component can be used to simulate annual mean currents and pressure (as well as linear perturbations about the annual mean stratification, pressure, and currents).

The ocean's response to wind forcing is better represented in this formulation for following reasons. First, observed stratification is found to vary more in space than in time [Dewitte et al., 1999]. Second, these spatial variations result in significant spatial variations in the wind-projection coefficients [Dewitte et al., 1999] (Also see figure 3.1). Third, for low order modes, shallow water speeds, which control mode adjustment time and damping, vary significantly from mode to mode. It follows that the oceans response should be better represented with the observed annual-mean stratification, instead of a horizontally-uniform stratification, since the wind forcing, and the ensuing adjustment will be better represented. Clearly, if the characteristic

horizontal length scale for density is large compared to the horizontal scales of motion, mode mixing will be negligible. However, for the observed stratification it is not clear that this holds. Instead, to demonstrate mode mixing is indeed negligible, a number of sensitivity experiments were performed with a linear model that solves equations 3.4 in finite difference, i.e., there is no separation into baroclinic modes (section 4.4). The results suggest the primary effect of stratification is to modify the vertical structure of propagating modes to match that of the local modes, and that mode mixing due to the observed stratification is insignificant. These results strongly support the calculation of baroclinic modes from the observed stratification. They also explain why the structure of the solution is improved by using annual mean stratification.

There are of course factors other than dynamics that influence horizontal variations in the density. For example, vertical mixing (an idealised representation is used here), thermodynamic effects, and advective density terms. However, the linear model's realistic representation of annual mean currents and dynamic height (section 3.4), suggests these effects are small.

### Separation of the linear equations

Let the solution to equations 3.4 be expressed as a linear sum of vertical modes as follows,

$$\begin{aligned} u &= \sum_{n=1}^N u_n \psi_n, & v &= \sum_{n=1}^N v_n \psi_n, & p &= \sum_{n=1}^N p_n \psi_n \\ w &= \sum_{n=1}^N w_n \int_{-H}^z \psi_n dz, & \rho &= \sum_{n=1}^N \rho_n \psi_{nz}, \end{aligned} \quad (3.7)$$

where the vertical modes,  $\psi_n$ , are defined by the following vertical structure equation,

$$(N^{-2} \psi_{nz})_z = -c_n^{-2} \psi_n, \quad (3.8)$$

and satisfy upper and lower boundary conditions,

$$\begin{aligned} N^{-2} \psi_{nz} + g^{-1} \psi_n &= 0 & ; z &= 0 \\ \psi_{nz} &= 0 & ; z &= -H. \end{aligned} \quad (3.9)$$

Equations 3.8 and 3.9 constitute a Sturm-Liouville problem. The solutions (vertical modes) are infinite in number and form a complete orthonormal set. Associated

with each vertical mode is an eigenvalue,  $c_n$ , which is the mode's shallow water speed. Due to  $N^2$  being a function of  $x$ ,  $y$ , and  $z$ , the modes and the shallow water speeds are horizontally-varying. As standard, let the modes be ordered in terms of decreasing shallow water speed, labelling beginning at 0. The first mode,  $\psi_0$ , is the barotropic mode. Stratification is not important for this mode, it also has by far the greatest shallow water speed. The other modes,  $\psi_1, \psi_2, \dots$ , are the baroclinic modes. For a good discussion on vertical modes see Gill [1982] chapter 6.

The barotropic mode, because of its large length scale, 3000km, and short time scale, 4hrs, is not important to equatorial dynamics [Moore and Philander, 1977]. Thus it is ignored, and the sums in equation 3.7 all begin at  $n = 1$ .

The equations governing the expansion coefficients are obtained by substituting definitions 3.7 into equations 3.4, giving

$$\begin{aligned} u_{nt} + R_n^u - f v_n + p_{nx} + M_n^u &= \tau_n^x + \nu_h \nabla_h^2 u_n, \\ v_{nt} + R_n^v + f u_n + p_{ny} + M_n^v &= \tau_n^y + \nu_h \nabla_h^2 v_n, \\ c_n^{-2} (p_{nt} + R_n^p) + u_{nx} + v_{ny} + M_n^p &= 0, \\ w_n &= c_n^{-2} (p_{nt} + R_n^p), \\ \rho_n &= -g^{-1} p_n, \end{aligned} \quad (3.10)$$

where the forcing terms are given by

$$\begin{aligned} \tau_n^x &= \frac{\tau^x \psi_n(0)}{D_n}, \\ \tau_n^y &= \frac{\tau^y \psi_n(0)}{D_n}, \end{aligned} \quad (3.11)$$

the damping terms,  $R$ , are given by

$$\begin{aligned} R_n^u &= -\sum_{i=1}^N u_i \frac{1}{D_n} \int_{-H}^0 (\nu \psi_{nz})_z \psi_i dz, \\ R_n^v &= -\sum_{i=1}^N v_i \frac{1}{D_n} \int_{-H}^0 (\nu \psi_{nz})_z \psi_i dz, \\ R_n^p &= -\sum_{i=1}^N p_i \frac{c_n^2}{D_n} \int_{-H}^0 \frac{(\kappa \psi_{nz})_{zz} \psi_i}{N^2} dz, \end{aligned} \quad (3.12)$$

and the mode mixing terms,  $M$ , are given by

$$\begin{aligned} M_n^v &= \sum_{i=1}^N p_i \frac{1}{D_n} \int_{-H}^0 \psi_{ix} \psi_n dz, \\ M_n^u &= \sum_{i=1}^N p_i \frac{1}{D_n} \int_{-H}^0 \psi_{iy} \psi_n dz, \\ M_n^p &= -\sum_{i=1}^N \left( u_i \frac{1}{D_n} \int_{-H}^0 \psi_{ix} \psi_n dz + v_i \frac{1}{D_n} \int_{-H}^0 \psi_{iy} \psi_n dz \right), \end{aligned} \quad (3.13)$$

with

$$D_n = \int_{-H}^0 \psi_n^2 dz.$$

In the above equations, upper and lower boundary conditions are all incorporated. In particular, the stress boundary conditions are incorporated through the  $\tau$  forcing terms. Boundary conditions on the free surface,  $\eta$ , and vertical velocity at the bottom are automatically satisfied by the upper and lower boundary conditions on the vertical structure functions (equations 3.9).

Equations 3.10 clearly show that because of horizontally-varying stratification, and vertical mixing, the linear equations 3.4 are in general not separable. Mode mixing terms,  $M$ , and damping terms,  $R$ , result. Mode mixing terms express how a disturbance associated with one mode will project onto other modes, when it propagates through a region of horizontally-varying stratification. The damping terms arise from the inclusion of vertical mixing.

As discussed above, mode mixing is assumed negligible, i.e.,  $M = 0$ . Horizontal variations in shallow water speed are also neglected. Modal shallow water speed can vary significantly across the Pacific and Atlantic oceans [Picaut and Sombardier, 1993], but since these variations primarily only effect the dispersion of the modes, the solution should be minimally affected.

The vertical mixing coefficients are assumed inversely proportional to the square of the Brunt-Väisälä frequency. Only this form of vertical mixing affects only the amplitudes of the modes, and not their vertical structure. The damping terms can then be simplified as follows. Following McCreary [1981], the coefficients for vertical

mixing of heat and momentum are chosen to be identical,

$$\nu_v = \kappa_v = \frac{A}{N^2}. \quad (3.14)$$

The coefficient of proportionality,  $A$ , shall be referred to as the vertical diffusion parameter. The damping terms then reduce to

$$\begin{aligned} R_n^u &= r_n u_n, \\ R_n^v &= r_n v_n, \\ R_n^p &= r_n p_n, \end{aligned}$$

where

$$r_n = \frac{A}{c_n^2}. \quad (3.15)$$

Under these three assumptions, the model equations simplify to,

$$\begin{aligned} u_{nt} + r_n u_n - f v_n + p_{nx} &= \tau_n^x + \nu_h \nabla_h^2 u_n, \\ v_{nt} + r_n v_n + f u_n + p_{ny} &= \tau_n^y + \nu_h \nabla_h^2 v_n, \\ c_n^{-2} (p_{nt} + r_n p_n) + u_{nx} + v_{ny} &= 0, \\ w_n &= c_n^{-2} (p_{nt} + r_n p_n), \\ \rho_n &= -g^{-1} p_n. \end{aligned} \quad (3.16)$$

These equations in appearance are identical to the McCreary [1981] model. The only difference is that now the vertical structure functions vary horizontally. In effect, the horizontally-varying stratification is allowed to influence the vertical structure (and wind-projection coefficients) only and not the modal shallow water speeds,  $c_n$ .

The linear components 10 baroclinic modes are modelled as above.

### Two layer treatment of high order modes

Although a ten mode truncation accurately represents large-scale pressure and zonal velocity, meridional velocity and upwelling are primarily determined by high order modes,  $n > 10$  (See section 3.5). However, the vertical structure of high order

modes is sensitive to stratification, which at these scales is not well resolved by the observations. Also, given the known sensitivity of meridional velocity and upwelling to the specification of vertical mixing [Weisberg and Qiao, 2000; World Climate Research Programme, 1995], the representation of the meridional circulation by these modes becomes questionable. The two surface layer model for high order modes simplifies (coarsens the resolution of) the model without any loss of physical justification.

The flow within the model's two surface layers are governed by frictional Ekman equations. A simplification that can be made, because the high order modes are strongly damped. The use of a surface frictional Ekman layer to model the ocean's local response to winds is quite common [Zebiak and Cane, 1987; Blumenthal and Cane, 1989]. However, the choice of parameter values varies, and is quite arbitrary. The derivation below shows that modelling the local response to wind stress in terms of frictional Ekman layers is appropriate, and provides a self-consistent set of parameters.

Unlike other modelling studies, which use a single surface layer to model surface flow, I choose to use two surface layers. The surface layers cover the upper 125 meters and are divided by the mixed layer depth. The use of two surface layers is in recognition that accurate simulation of the equatorial cell is important to modelling of non-linearities; the layering providing a rough division between surface poleward flow, and subsurface equatorward flow. (The mixed layer is defined in section 3.3)

**Simplifying assumptions.** Three simplifying assumptions apply to the higher order modes: the pressure contribution is negligible, the modes are in steady state with respect to monthly forcing, and horizontal eddy mixing terms become negligible. It is an observational fact that the contribution of higher order modes to the pressure field is small [Cane, 1984; Blumenthal and Cane, 1989; Yu and McPhaden, 1999b] (also see section 3.5). The increase of mode damping with mode number (equation 3.15) ensure that for large enough mode number,  $n \geq N_E$ , the other two conditions hold. The validity of these approximations is covered in sec-

tion 3.5, where the mode convergence properties of the solution are described.

These approximations reduce equations 3.16 to

$$\tau_n u_n - f v_n = \tau_n^x, \quad (3.17)$$

$$\tau_n v_n + f u_n = \tau_n^y, \quad (3.18)$$

$$w_n + u_{nx} + v_{ny} = 0. \quad (3.19)$$

Consistent with the neglect of pressure, the density anomaly is also neglected. These equations are exactly those describing a wind-forced frictional Ekman layer. The solution to which can be expressed in the following matrix form

$$\begin{pmatrix} u_n \\ v_n \end{pmatrix} = \underline{\underline{A}}_n \cdot \begin{pmatrix} \tau_n^x \\ \tau_n^y \end{pmatrix}, \quad (3.20)$$

where

$$\underline{\underline{A}}_n = \frac{1}{(\tau_n^2 + f^2)} \begin{pmatrix} \tau_n & f \\ -f & \tau_n \end{pmatrix}.$$

Vertical velocity is obtained directly from equation 3.19.

**Layer-average velocities** are obtained by vertical integration of equations 3.20 over the surface layers. Defining the upper layer to extend from the surface to the mixed layer depth,  $-H_1$ , and the lower layer to extend from  $-H_1$  to depth  $-H_2$ , where both  $H_1$  and  $H_2$  are free to vary spatially. Then, from definitions 3.7, the transport in the surface layer,  $\underline{\underline{U}}_{H_1}$ , is given by

$$\underline{\underline{U}}_{H_1} = \begin{pmatrix} U_{H_1} \\ V_{H_1} \end{pmatrix} = \int_{-H_1}^0 \sum_{n \geq N_E}^N \begin{pmatrix} u_n \\ v_n \end{pmatrix} \psi_n(z) dz$$

Using equation 3.20 this simplifies to

$$\underline{\underline{U}}_{H_1} = \underline{\underline{A}}_{H_1} \cdot \underline{\underline{\tau}}, \quad (3.21)$$

where

$$\underline{\underline{A}}_E = \sum_{n \geq N_E}^N \frac{\psi_n(0)}{D_n} \int_{-H_1}^0 \psi_n(z) dz \underline{\underline{A}}_n, \quad (3.22)$$

$$\underline{\underline{\tau}} = \begin{pmatrix} \tau_x \\ \tau_y \end{pmatrix}.$$

Similarly one obtains for the lower layer

$$\underline{U}_{H_2} = \underline{A}_{H_2} \cdot \underline{\tau}, \quad (3.23)$$

where

$$\underline{A}_{H_2} = \sum_{n \geq N_E}^N \frac{\psi_n(0)}{D_n} \int_{-H_2}^{-H_1} \psi_n(z) dz \underline{A}_n. \quad (3.24)$$

Subscripts  $H_1$ , and  $H_2$  are used to indicate the upper and lower layers respectively.

The average velocity in each layer is simply obtained by dividing by the layer thickness

$$\begin{aligned} \underline{u}_{H_1} &= \frac{1}{H_1} \underline{U}_{H_1} \\ \underline{u}_{H_2} &= \frac{1}{(H_2 - H_1)} \underline{U}_{H_2}. \end{aligned}$$

The vertical velocity at the base of the surface layer is taken as the divergence of the Ekman transport, assuming  $w = 0$  at the surface:

$$w_{H_1} = \nabla \cdot (\underline{A}_{H_1} \cdot \underline{\tau}), \quad (3.25)$$

As  $H_1$  is permitted to vary, this is not the vertical velocity, but the velocity normal to our mixed layer. However, this definition is more appropriate as it conserves volume.

These equations are identical to those of a surface frictional Ekman layer, and the parameters are derived from the full equations (3.16), so treatment of the high order modes as frictional Ekman layers is appropriate.

The linear component's two surface layers are formed from modes 11 to 30, using the formulation set out above.

### 3.2.4 Non-linear component

The main purpose of the non-linear component of the model is to provide a second order correction to the linear equations for neglected non-linearity. Consistent with

this purpose, the equations are simplified and formulated into two surface layers. The layers are chosen identical to those used for modelling the high order modes, so that the SEC, EUC, and the equatorial cell are broadly resolved.

The formulation of the non-linear equations is based on the neglect of non-linear density, pressure, and meridional velocity perturbations. The justification for neglecting these terms will be given first. The resulting simplified zonal momentum and continuity equations are then vertically integrated, giving a set of coupled equations for non-linear zonal velocity in the two surface layers, and vertical velocity at the mixed-layer depth.

#### Neglected terms

Linear models are able to reproduce many aspects of the equatorial circulation: pressure fields are realistic; density perturbation fields are reasonable, except at the surface; most major zonal currents are fairly well represented; and meridional currents have realistic structure and magnitude (see section 3.4). The only major breakdown in the linear solution is the representation of the annual mean SEC (section 3.4), and associated density anomalies. (Non-linearity is also important in the annual cycle of the EUC, chapter 4.)

The simulation of the SEC by linear models is in general too intense. Early studies suggested weak vertical mixing to be responsible [McCreary, 1981; McPhaden, 1981]. However, scale analysis of the equations of motion shows non-linear terms in the zonal momentum balance are not negligible; see discussion below. Model results presented in section 3.4 show neglected non-linear terms are the dominant process controlling the magnitude of the SEC, not vertical mixing.

Equation 3.5 and boundary conditions 3.6 describe the terms neglected by the linear component. The magnitudes of these terms are estimated in appendix A; a summary is presented in table 3.1. These results are now used to simplify these equations, to retain only the dominant terms. Being simplified, the model is better able to illustrate dominant mechanisms.

Table 3.1: Magnitudes of advective terms in the zonal and meridional momentum equations, and the density equation. (See appendix A for details)

	Zonal			Meridional			Density		
	$u \frac{\partial u}{\partial x}$	$v \frac{\partial u}{\partial y}$	$w \frac{\partial u}{\partial z} \dagger$	$u \frac{\partial v}{\partial x}$	$v \frac{\partial v}{\partial y}$	$w \frac{\partial v}{\partial z} \dagger$	$u \frac{\partial \rho}{\partial x}$	$v \frac{\partial \rho}{\partial y}$	$w \frac{\partial \rho}{\partial z} \dagger$
Surface	$10^{-9}$	$10^{-7}$	$10^{-7}$ ( $10^{-6}$ )	$10^{-9} \ddagger$	$10^{-8} \ddagger$	$10^{-7} \ddagger$	$10^{-8}$	$10^{-7}$	$10^{-6}$ ( $10^{-5}$ )
EUC ( $\approx 120m$ )	$10^{-7}$	$10^{-7}$	$10^{-7}$ ( $10^{-6}$ )	?	$10^{-8}$	$10^{-7} \ddagger$	$10^{-7}$	$10^{-7}$	$10^{-6}$ ( $10^{-5}$ )

† Estimates based on Poulain [1993] vertical velocity are bracketed. Estimates using more conservative vertical velocity values are un-bracketed.

‡ These terms are difficult to estimate, and the values given are upper bounds.

? This term can not be estimated from observations.

Advective terms in the zonal momentum equation are of the order  $10^{-7}$ . The Coriolis term vanishes on the equator, and the zonal pressure gradient is largely balanced by wind-stress. However, the balance is not exact [Wascogne, 1989; Johnson and Luther, 1994; Qiao and Weisberg, 1997]. Observational estimates of the zonal pressure gradient term,  $\frac{1}{\rho} \frac{\partial p}{\partial x}$ , are of the order  $5 \times 10^{-7}$  [Johnson and Luther, 1994; Qiao and Weisberg, 1997]. Thus, non-linear advective terms are potentially important, and are retained in this formulation. The horizontal and vertical diffusion terms are also retained.

In the case of the meridional momentum equation, observations show that the meridional pressure gradient vanishes on the equator, and zonal current are in geostrophic balance. Zonal currents calculated using the meridionally differentiated form of the geostrophic balance compare well to observations [Lukas and Firing, 1984; Yu et al., 1995]. The meridionally differentiated form of the geostrophic balance must be used on the equator, because the Coriolis force vanishes (see chapter 5).

As the meridional pressure gradient and the Coriolis terms are in balance, the non-linear terms must either vanish, or cancel. Advective terms in the meridional momentum equation are at least an order of magnitude smaller than the advective

terms in the zonal momentum equation (table 3.1). Thus, these terms are considered negligible, and hence the non-linear correction to meridional velocity is neglected. However, as described in chapter 5, there is evidence that this is not a good assumption in the eastern Pacific. None the less, for expedience these terms are neglected.

The vertical advection term is at least an order of magnitude greater than the other advective terms in the density equation. Results from linear models, which retain the linearised vertical advective term,  $w \frac{\partial \rho}{\partial z}$ , clearly illustrate the importance of this term. In particular, to first order, linear models are able to reproduce the equatorial pressure field (section 3.4). In addition, the realistic magnitude of the EUC in these models indicates the baroclinic pressure field is roughly correct, both zonally and meridionally (section 3.4). These results indicate that perturbations in pressure resulting from the other advective terms in the density equation are negligible. Thus, perturbation density and pressure are neglected. Further justification of the neglect of these terms is difficult, but it is standard to do so [Moore and Philander, 1977; McCreary, 1981].

Applying these assumptions, equations 3.5 are reduced to

$$\begin{aligned} u_t^{nl} + \mathbf{u} \cdot \nabla(u) &= \nu_h \nabla_h^2(u^{nl}) + (\nu_v u_z^{nl})_z, \\ \nabla \cdot \mathbf{u}^{nl} &= 0, \end{aligned} \quad (3.26)$$

where, as before,

$$\mathbf{u} = \mathbf{u}^l + \mathbf{u}^{nl},$$

but now, with the contribution of  $v^{nl}$  neglected,  $\mathbf{u}^{nl}$  becomes

$$\mathbf{u}^{nl} = (u^{nl}, 0, w^{nl})$$

It is important to note that these equations are not forced through boundary conditions, but through linear velocities, i.e., terms from the linear component.

### Layer average velocity

To provide a correction for neglected non-linear terms on the SEC and the EUC, the highly simplified equations 3.26 are integrated across the two surface layers, used to represent the high order modes. Non-linear terms are found to cancel on vertical integration [Qiao and Weisberg, 1997; Yu and McPhaden, 1999a]. Thus, integration into layers, also ensures that the neglect of other non-linear effects, for example in the density equation, will be even less significant.

The equations governing non-linear zonal velocity in the two surface layers and the vertical velocity at the mixed layer depth, obtained by integrating equations 3.26 over both layers, are

$$\begin{aligned}
 \frac{\partial}{\partial t}(\Delta H_1 u^{nl(1)}) &= -\frac{\partial}{\partial x}(\Delta H_1 u^{(1)} u^{(1)}) - \frac{\partial}{\partial y}(\Delta H_1 u^{(1)} v^{l(1)}) - \\
 &\quad (u^{(1)} w M(w) + u^{(2)} w M(-w)) + \\
 &\quad \nu_h \nabla_h \cdot \Delta H_1 \nabla_h u^{nl(1)} + 2\nu_v \left( \frac{u^{nl(2)} - u^{nl(1)}}{\Delta H_1 + \Delta H_2} \right), \\
 \frac{\partial}{\partial t}(\Delta H_2 u^{nl(2)}) &= -\frac{\partial}{\partial x}(\Delta H_2 u^{(2)} u^{(2)}) - \frac{\partial}{\partial y}(\Delta H_2 u^{(2)} v^{l(2)}) + \\
 &\quad (u^{(1)} w M(w) + u^{(2)} w M(-w)) + \\
 &\quad \nu_h \nabla_h \cdot \Delta H_2 \nabla_h u^{nl(2)} + 2\nu_v \left( \frac{u^{nl(1)} - u^{nl(2)}}{\Delta H_1 + \Delta H_2} \right), \\
 w^{nl} &= -\frac{\partial}{\partial x}(\Delta H_1 u^{nl(1)}), \tag{3.27}
 \end{aligned}$$

where the superscripts (1) and (2) indicate velocities in the upper and lower layers respectively.  $\Delta H_1 (= H_1)$  and  $\Delta H_2 (= H_2 - H_1)$  are the thickness of the surface and lower layers,  $M$  is the Heaviside function, i.e.,

$$M(x) = \begin{cases} 1 & ; \text{if } x \geq 0 \\ 0 & ; \text{if } x < 0 \end{cases}$$

$u (= u^{nl} + u^l)$  is the total zonal velocity, and  $w (= w^l + w^{nl})$  is the total vertical velocity at the base of the mixed layer.

### 3.3 Implementation

#### 3.3.1 Grids, Integration, and Parameter values

The model spans the Pacific and Atlantic oceans. (Only results from the Pacific basin are included in this study.) Its domain extends from 124°W to 30°E, and from 33.5°S to 33.5°N. An Arakawa c-grid is used with 2 degree zonal grid spacing, and a stretched meridional grid, with 0.5 degree grid spacing within 10 degrees of the equator, extending to 3 degrees at the boundaries. A realistic representation of land is also included (figure 3.2).

Vertically a 5500m flat bottom ocean is assumed. The vertical grid on which the linear component is expressed has 33 levels. The grid spacing, with 8 levels in the surface 125m, focuses on resolving surface dynamics. The two layers used to simulate non-linear effects and high order baroclinic modes cover the upper 125m, and are divided by the mixed layer depth.

The model is integrated using a standard leapfrog scheme, with a time step of 5000s, and filtering every 60 time steps. Open northern and southern boundary conditions are applied by both linear and non-linear components.

The coefficients for horizontal diffusion of heat and momentum are assumed equal, and are identical for both the linear and non-linear components. The zonal coefficients are  $2.5 \times 10^4 m^2 s^{-1}$ . The meridional coefficients are  $2.5 \times 10^3 m^2 s^{-1}$  in the interior, but increase linearly over the outer 7 grid points to a value of  $1.275 \times 10^5 m^2 s^{-1}$ . The vertical diffusion parameter is taken as  $1 \times 10^{-7} m^2 s^{-3}$ , which gives equivalent values for the coefficient of vertical diffusion of 6 to  $4 \times 10^{-2} m^2 s^{-1}$  in the mixed layer and  $3 \times 10^{-4} m^2 s^{-1}$  in the EUC core. It was chosen to match surface observation by Peters et al. [1988] of 3 to  $6 \times 10^{-2} m^2 s^{-1}$ . The coefficient of vertical diffusion in the non-linear model is  $1 \times 10^{-3} m^2 s^{-1}$ . Sensitivity studies indicate these parameter values are appropriate (section 4.4).

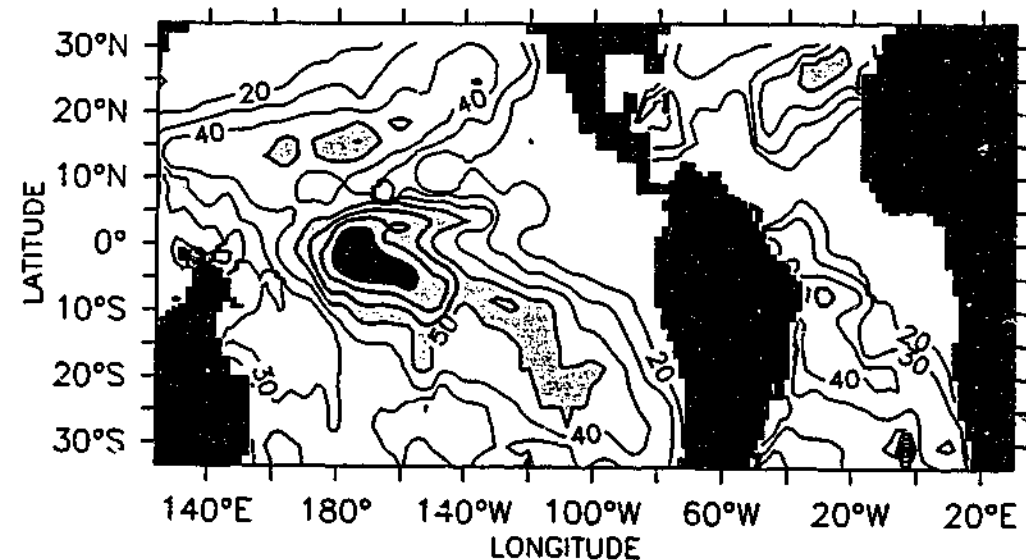


Figure 3.2: The model's mixed layer depth, calculated from Levitus [1982] data as described in the text, is contoured with an interval of 10m. Light and dark shading indicates mixed layers greater than 50m and 80m respectively. The model's land sea mask is also shown, filled in black.

### 3.3.2 Mixed layer

The mixed layer is defined on a stability criterion; effectively as surface water with  $N^2 < 6.5 \times 10^{-6} s^{-2}$ . However, to maintain a smooth and finite depth mixed layer, the mixed layer depth is actually defined as the depth above the  $N^2$  thermocline maximum where the profile first drops below  $6.5 \times 10^{-5} s^{-1}$ . This definition excludes the barrier layers of the western Pacific. A minimum mixed-layer depth of 10m is imposed. A maximum depth of 50m is imposed in the subductive regions of the south eastern Pacific, and north eastern Atlantic, where the  $N^2$  is always less than  $6.5 \times 10^{-5} s^{-1}$ . In addition, the model's mixed layer depth is estimated to within 0.2m, via cubic spline interpolation of the  $N^2$  profile. A smooth mixed-layer depth is important to maintaining smooth vertical velocity at the base of the mixed layer. The model's mixed layer, shown in figure 3.2, is calculated from Levitus [1982] annual mean temperature and salinity data.

Table 3.2: Shallow water speeds for the model's first ten baroclinic modes, calculated using stratification at  $180^\circ E, 0^\circ N$ . (Stratification calculated from Levitus [1982] data.)

Mode No.	1	2	3	4	5	6	7	8	9	10
$c(m s^{-1})$	2.96	1.84	1.13	0.82	0.66	0.57	0.47	0.41	0.38	0.35

### 3.3.3 Calculation of the vertical modes

The vertical modes and shallow water speeds are calculated from Levitus [1982] annual mean salinity and temperature observations as follows.

The Levitus [1982] data are first smoothed and interpolated onto the model grid. A density profile is then calculated at each grid point, using a two step scheme to solve the UNESCO (1981) equation of state (as specified in Gill [1982], Appendix 3). In the first step, pressure is estimated from the hydrostatic equation using the density estimate from the previous step. In the second, density is then re-estimated using the Levitus data, estimated pressure, and the equation of state. The scheme is initialised using a constant density of  $1 \times 10^3 kg m^{-3}$ . It converges rapidly, and only five iterations are required to produce a realistic density field. A profile of Brunt Väisälä frequency squared is then calculated using the following equation, which can be derived from Gill [1982],

$$N^2 = g(\rho^{-1} \frac{\partial \rho}{\partial z} - \frac{g}{c_s^2}). \quad (3.28)$$

$c_s$  is the speed of sound, which was calculated from a regression relation derived from Gill [1982]. In addition a minimum  $N^2$  value of  $1 \times 10^{-8} s^{-2}$  is imposed, which ensures numerical stability of the vertical-mode eigen value problem.

The vertical modes and shallow water speeds are then calculated as an eigenvector solution to the matrix finite-difference representation of  $\frac{\partial}{\partial z} N^{-2} \frac{\partial}{\partial z}$ . Vertical modes are calculated at each grid point. The shallow water speeds used for integration and damping of the model equations are horizontally-uniform and taken from the density profile at  $180^\circ E, 0^\circ N$ . The shallow water speeds for the first 10 modes are listed in table 3.2.

### 3.4 Simulation of the annual mean

The model is an anomaly model, simulating dynamical perturbations about a resting state. A description of the annual mean simulation is presented below to support the model's approximations, by illustrating that the model dynamics are behaving correctly. The description concentrates on the simulation of equatorial currents, as these are of most interest to the study.

The annual mean discussed here is obtained from the final year of a ten year model run, forced from rest with the Hellerman and Rosenstein [1983] climatological wind stress, reduced in magnitude by 20%. The 20% reduction is in line with revised estimates that indicate the Hellerman and Rosenstein winds over estimate the stress by 20 to 25% in the tropics [Harrison, 1989]. The model is almost spun up after three years, and by ten years the annual cycle shows no year to year variations. The model's sensitivity to wind stress is covered in section 4.4.

#### 3.4.1 Stratification

The model's annual mean stratification cannot be discussed, since the model assumes the annual mean stratification. Instead, to clearly show that annual mean horizontal variations in stratification are primarily dynamically determined, results from a model run with stratification set to that at 180°E, 0°N are discussed. The magnitude of currents and surface dynamic height are very similar to those of the full model. However, the spatial structure is quite different. In particular the EUC does not rise towards the east.

Figure 3.3 shows both the linear model's simulation of annual mean density perturbation, and the observed variations in density relative to the stratification at 180°E, 0°N. The strength of the density perturbations in the east are very realistic, but the vertical position of the anomaly is too deep, and there is no eastward rise. This is as expected: Perturbations in stratification do not influence the vertical structure of modes. The modelled density anomaly is also vertically too confined;

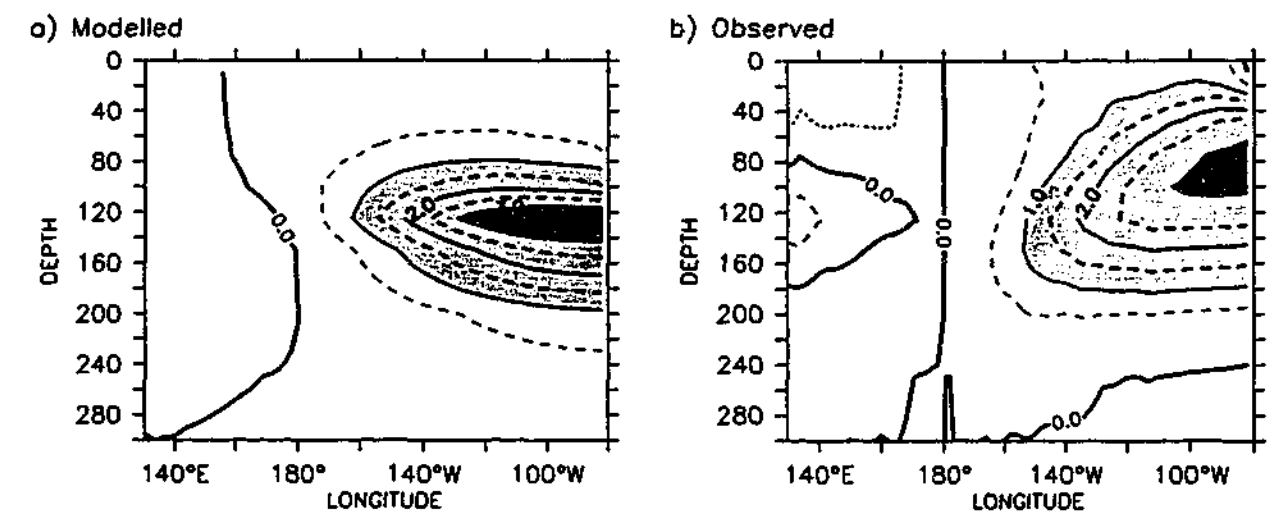


Figure 3.3: Comparison between (a) modelled annual mean zonal variations in density along the equator, relative to the stratification at 180°E, 0°N, and (b) observed variations. The units are  $\text{Kg m}^{-3}$ . Modelled results are generated using a linear 10 baroclinic mode model, with horizontal stratification taken from 180°E, 0°N, and forced by annual mean Hellerman and Rosenstein [1983] wind stress. The stratification is calculated from Levitus [1982] data.

idealised vertical mixing, and the neglect of thermodynamic and advective terms in the density equation make this hardly surprising. In the west, density variations appear not to be dynamically determined, but are small.

The model's representation of meridional variations in stratification (not shown), is reasonably realistic in the vicinity of the EUC, but poor at the surface and in the region of the NECC. These features are seen in the model's representation of dynamic height and the NECC. The overall realistic representation of horizontal variations in stratification is consistent with the model's realistic current and pressure fields, and shows equatorial dynamics are primarily baroclinic.

#### 3.4.2 Dynamic height

In figure 3.4, the modelled annual mean dynamic height is shown. Comparison to observations (figure 2.1) shows the model captures most features well. The structure is accurate, with the northern and southern equatorial gyres, and the equatorial troughs and ridges in dynamic height all well placed. The east-west gradient along

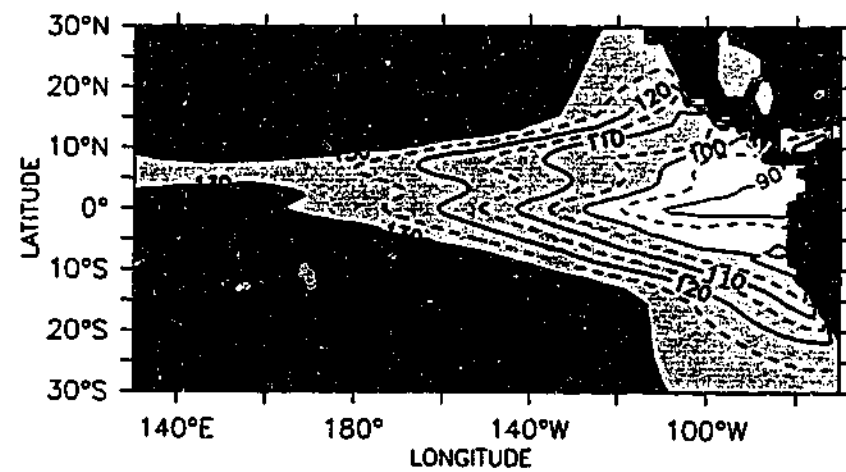


Figure 3.4: Modelled annual mean dynamic height anomaly relative to 5500m for the Pacific. To facilitate direct comparison with the observations in figure 2.1, the units are Dynamic centimetres ( $10m^2s^{-2}$ ), and a constant offset has been added.

the equator is also accurate. The model is less able to simulate the east-west gradient across subtropical gyres, and the meridional gradients across the major zonal currents. These gradients are all weaker than observed, indicating the currents are too weak. The results on the equator are consistent with depth integrated zonal momentum balance being between zonal pressure gradient and wind stress [Johnson and Luther, 1994; Qiao and Weisberg, 1997; Wascogne, 1989]. Accurate representation of dynamic height is as expected. It simply indicates the model is able to simulate Sverdrup balance.

### 3.4.3 Currents

The model is able to realistically capture the large scale features of the equatorial circulation both in terms of magnitude and structure.

#### Surface

Figure 3.5a shows the model is able to capture the structure of surface zonal currents. The SEC has realistic magnitude, and agreeing with observations (figure 2.6a), flow is at a minimum on the equator, and at a maximum north-east of the equator. In the east, currents have realistic magnitude but, in the west, they are westward-biased. The NECC is also too weak; Yu et al. [2000] have attributed this problem, which is

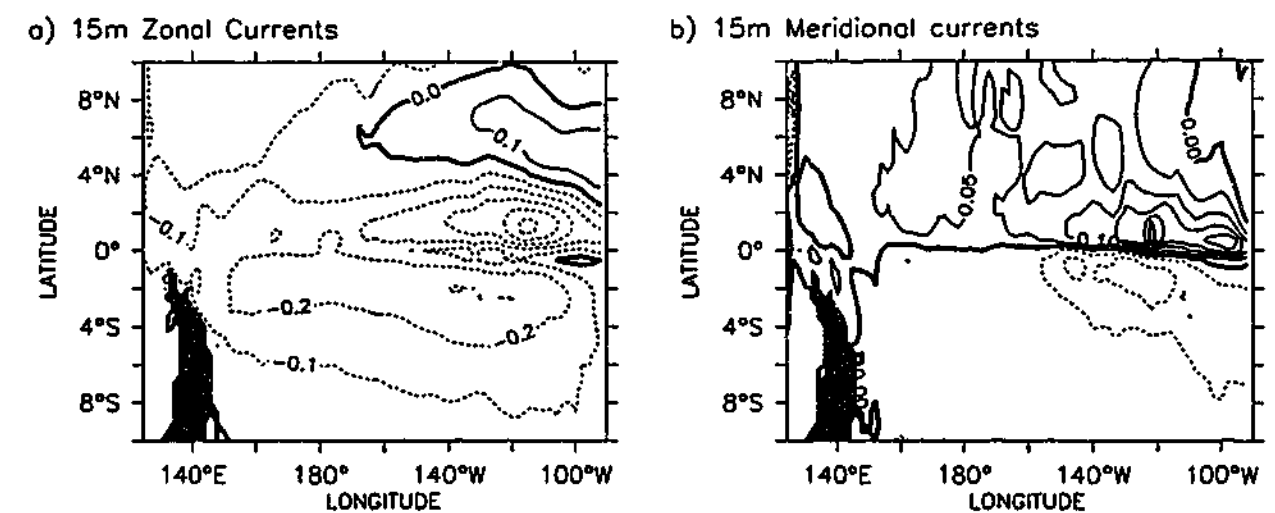


Figure 3.5: Modelled (a) annual mean surface zonal currents, and (b) meridional currents. Units are  $ms^{-1}$ , and the contour intervals are  $0.1ms^{-1}$  for zonal currents, and  $0.05ms^{-1}$  for meridional currents. Eastward and northward flow has been shaded. Currents were generated using re-scaled Hellerman and Rosenstein [1983] wind stress. ( These plots can be compared directly to the observations presented in figure 2.6.)

common to many models, to be due to inaccuracies in the wind field. Thus, a large component of our models poor simulation of the NECC is likely due to inaccuracies in the wind field, and is not an indication of poor dynamics.

The model is able to capture the poleward divergence of surface meridional flow with realistic magnitude, except north-east of the equator, where the currents are approximately 8 times too strong (figure 3.5b). The latter problem is associated with the surface layer approximations, and is discussed in section 3.5. A minor, but noticeable difference, is seen in the centre of meridional divergence, but as discussed in chapter 2, observations of the position of the equatorial cell may not be accurate, due to large interannual variability.

### Vertical structure

Figure 3.6 illustrates the vertical structure of the SEC, EUC, and the equatorial cell. The model's zonal currents are shown in figures 3.6a, and 3.6b. Discontinuity above the EUC, most apparent in figure 3.6b, is due to the differing resolutions of linear and non-linear model components. The SEC, EUC, and the NECC are all captured. The depth and eastward rise of the EUC are realistic. It is a little stronger than the observations, and vertically too narrow, but its meridional structure is quite accurate. The magnitude and width of the SEC compares well to observations, but is vertically too deep. The NECC is well positioned, but, as in figure 3.5a, is much weaker than observed.

The model's meridional circulation between  $160^{\circ}\text{E}$  and  $100^{\circ}\text{W}$ , consists of a well defined equatorial cell, centred roughly about the equator. Consistent with subsurface flow being geostrophic, the subsurface branch is weak outside of this longitude region: Zonal pressure gradient is only significant between  $160^{\circ}\text{E}$  and  $100^{\circ}\text{W}$ . The model's meridional circulation at  $152^{\circ}\text{W}$  is seen in figure 3.6c. As can be seen from figure 2.7c, it has realistic magnitude and appropriate structure. The cross equatorial southward flow, seen in the observations, that extends from the surface down to  $160\text{m}$  is not present. However, as discussed in section 2.3.2, the structure of the equatorial cell is not well defined by observations.

### Vertical velocity

Due to the lack of observations, and the focus on SST simulation, only vertical velocity at the depth of the model's mixed layer is considered. Figure 3.7 shows the model's vertical velocity has realistic structure and magnitude. In agreement with Poulain [1993] vertical velocity is strongest in the central eastern Pacific, and confined to a few tens of kilometers about the equator. Maximum model upwelling is around  $9 \times 10^{-4} \text{ms}^{-1}$ . This value is somewhat weaker than Poulain's estimate of  $1.5\text{--}2 \times 10^{-4} \text{ms}^{-1}$  at  $50\text{m}$ , but significantly stronger than most model estimates. However, upwelling averaged between  $1^{\circ}\text{S}$  and  $1^{\circ}\text{N}$ , has peak magnitude

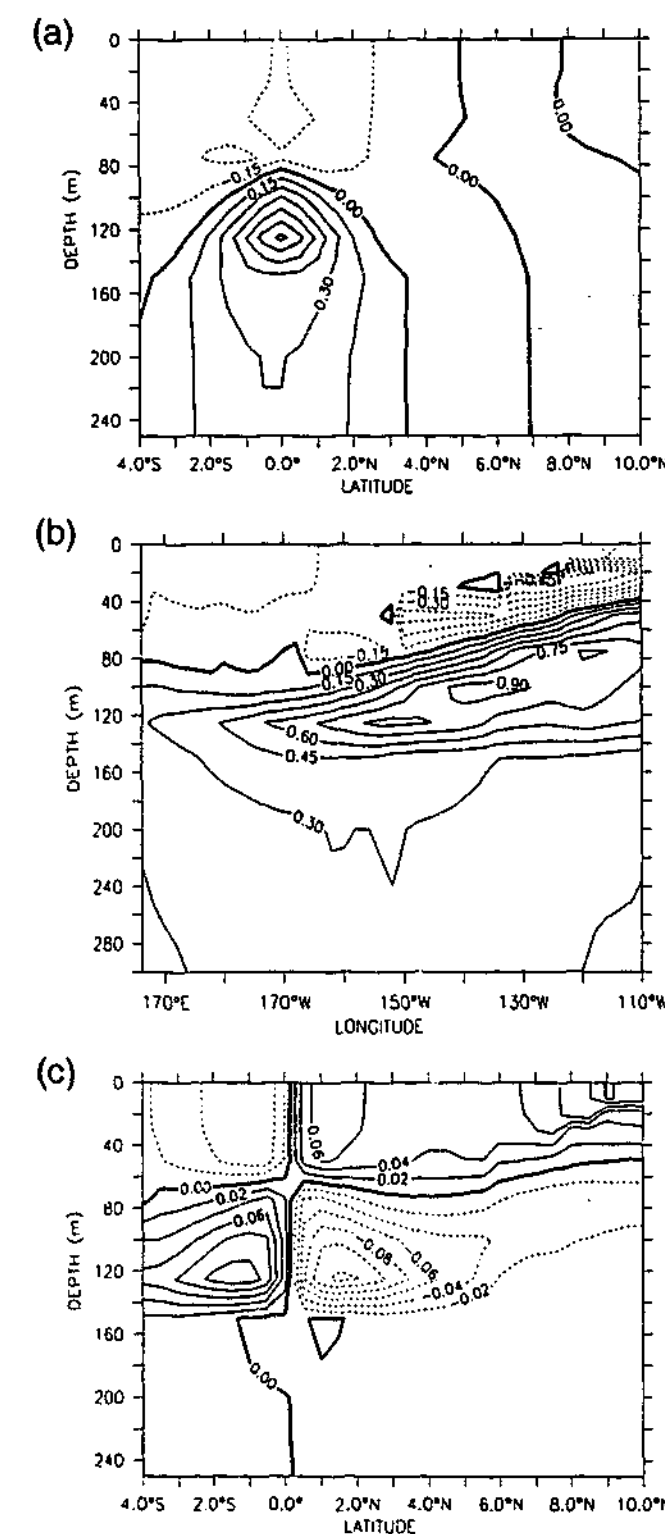


Figure 3.6: The annual mean structure of the model's zonal and meridional currents. (a) The meridional structure of zonal currents at  $154^{\circ}\text{W}$ , (b) the zonal structure of zonal currents along the equator, and (c) the meridional structure of meridional currents at  $154^{\circ}\text{W}$ . Units are  $\text{ms}^{-1}$ , the contour interval for zonal currents is  $0.15\text{ms}^{-1}$ , and for meridional currents  $0.02\text{ms}^{-1}$ . Shading shows eastward and northward flow. Currents generated using re-scaled Hellerman and Rosenstein [1983] wind stress. (These plots can be compared directly to the observations presented in figure 2.7.)

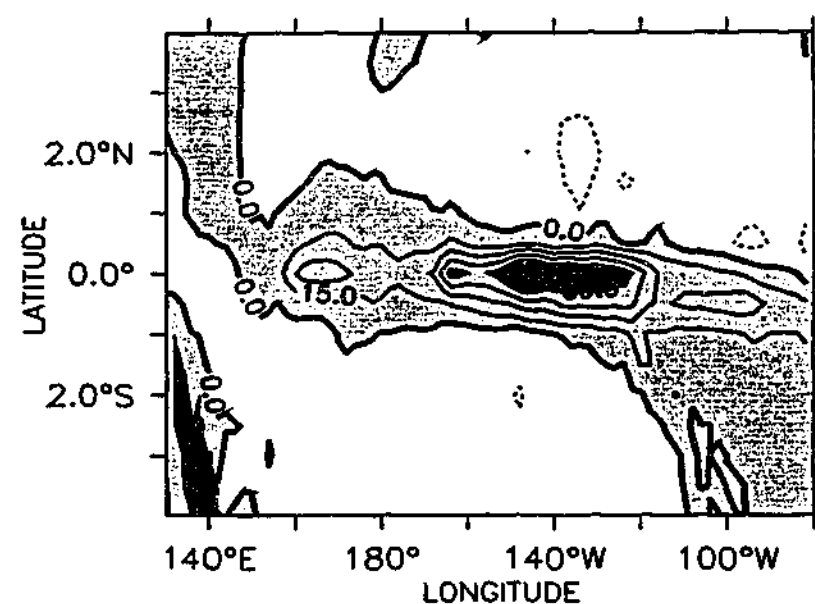


Figure 3.7: Annual mean vertical velocity at the base of the mixed layer. Units are  $\times 10^{-6} \text{ms}^{-1}$ , with contours every  $15 \times 10^{-6} \text{ms}^{-1}$ . Dark shading shows velocities greater than  $60 \times 10^{-6} \text{ms}^{-1}$ . These currents were generated using re-scaled Hellerman and Rosenstein [1983] wind stress.

of  $4 \times 10^{-5} \text{ms}^{-1}$ , which is in agreement with most estimates (section 2.3.2).

#### 3.4.4 Important terms in the annual mean zonal momentum balance

A qualitative description of the annual mean zonal momentum balance is now given. It illustrates the model dynamics are behaving correctly, which is important, as the model is used in the simulation of interannual current anomalies, and data for interannual current anomalies is poor. A detailed description is not appropriate as model non-linearities are highly simplified.

As expected, the linear component of the model dominates the solution. Consistent with McCreary [1981], the magnitude of the EUC and its vertical, meridional, and zonal structure are due to linear dynamics. Non-linearity is most important in the surface layers, where it gives the SEC realistic magnitude and structure, but it is also important in the lower layer in the east, where mean meridional advection of zonal momentum shifts the EUC core south of the equator. The latter is seen in many GCMs [Wascogne, 1989; Yu et al., 1997].

The ability of linear dynamics to accurately model the annual mean EUC is consistent with observational [Lukas and Firing, 1984; Johnson and Luther, 1994; Qiao and Weisberg, 1997] and modelling [Wascogne, 1989] studies. These studies indicate that, in the annual mean, the EUC is in approximate geostrophic balance and non-linear terms act only to perturb the vertical and meridional structure. Model non-linearity in the EUC is indeed consistent with this, but as non-linearity is only represented by two layers, it primarily affects only the magnitude of the currents. As a result the EUC is not vertically stretched, and the SEC is too deep (figure 3.6).

The annual mean non-linear zonal velocity in the upper layer is shown in figure 3.8a. The strong eastward peak, centred on the equator, clearly indicates the importance of non-linearity to the surface zonal momentum balance (ZMB). The peak counters stronger westward linear currents, to produce the model's realistic SEC, as seen in figure 3.5a. These features, hidden in the full model fields, are as expected. Strong westward linear currents occur because the linear component is only able to produce the balance between zonal pressure gradient (ZPG) and vertical stress divergence. As this is the dominant balance in the surface layers [Qiao and Weisberg, 1997], the ZPG is realistic (figure 3.4). However, as vertical stress divergence is represented by Rayleigh friction ( $r_n u$ ), strong westward surface currents result. The strong non-linear contribution is consistent with non-linear terms modifying vertical stress divergence profile [Qiao and Weisberg, 1997].

In figure 3.8b-f the model's ZMB in the surface layers is clearly illustrated. All terms except zonal advection of zonal momentum are significant. The mean meridional circulation determines surface non-linear velocity. Vertical advection transports eastward momentum from the EUC to the surface layers, and meridional advection removes surface westward zonal momentum from the equator. Horizontal diffusion is important on the equator, and also opposes the westward surface flow. Vertical diffusion is clearly also very important, and indicates a modification of the vertical stress divergence profile. This picture agrees with observational and modelling studies, except that horizontal diffusion replaces the role of meridional eddy

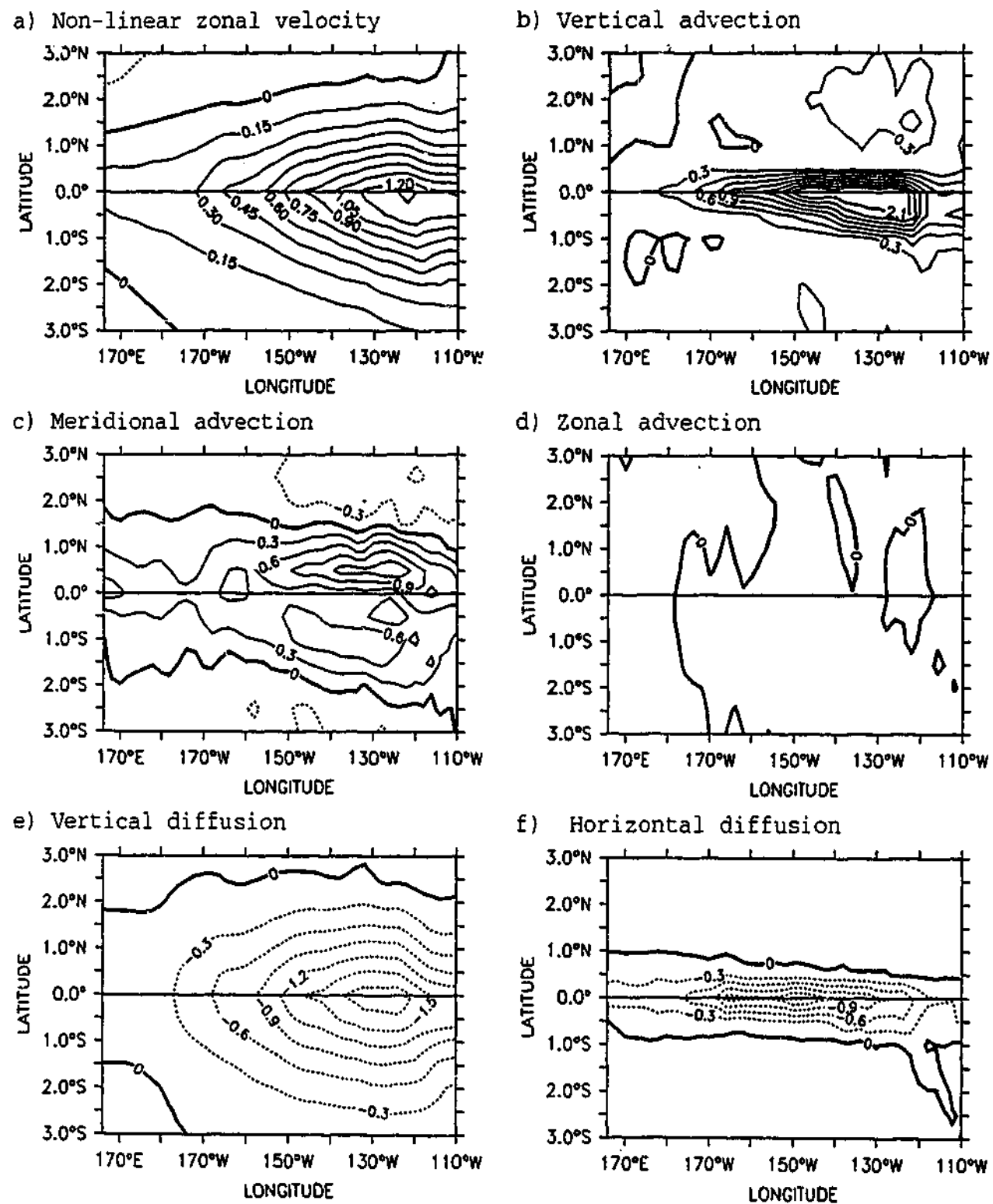


Figure 3.8: (a) Annual mean surface non-linear zonal currents are plotted in units of  $ms^{-1}$ , with a contour interval of  $0.15ms^{-1}$ . The non-linear modifications to the surface ZMB are plotted in b-f. The terms plotted refer to the five terms on the LHS of equation 3.27. Note the advective terms in this equation are in flux divergence form. The non-linear tendencies are 12 month averages of monthly means. The monthly means were calculated from data at each time step. The units are  $10^{-5}m^2s^{-2}$ , and the contour interval is  $0.3 \times 10^{-5}m^2s^{-2}$ . All terms except zonal advection of zonal momentum are significant. (Hellerman and Rosenstein [1983] wind stress was used to force the model.)

advection [Qiao and Weisberg, 1997; Wascogne, 1989]. The latter is not surprising as meridional eddy advection is primarily due to tropical instability waves [Qiao and Weisberg, 1997], which are not represented in our model.

### 3.5 Modal convergence

In this section, a modal decomposition of the annual mean dynamics is performed. The decomposition illustrates that a modal solution is an appropriate and simple way to accurately model many aspects of the large scale circulation in the equatorial Pacific. Understanding the baroclinic break down of the currents is also important, as it reveals which dynamics are locally driven, and which are due to larger scale adjustments in the winds.

The results show that modelled zonal velocity, and pressure are determined by the first ten modes, and that meridional velocity, and equatorial upwelling are predominately determined by high order modes. The two layer representation of modes 11 to 30 is also shown to satisfactorily capture the contribution of these modes.

These results provide further experimental justification for the design of the linear component, and, in fact, determined the final structure of the model. This may seem surprising given the primary purpose of the model is to simulate interannual variability. However, accurate representation of the annual mean implies, to a certain degree, that annual and interannual variability are also captured. Also, the annual mean state is more precisely known and straight forward to diagnose. Modal decomposition of annual and interannual variability will be discussed in the next two chapters.

The results presented in this section were generated using annual mean Hellerman and Rosenstein [1983] wind-stress, re-scaled as described above. The model parameters are as in section 3.3. Sensitivity of the modal convergence to model parameters was not extensively investigated. However, the sensitivity of the model as a whole indicates that mode convergence properties are sensitive to parameter

choice (section 4.4). These effects are most pronounced for vertical diffusion. Increased vertical diffusion favouring the low order modes as expected. This effect is important for meridional and vertical velocity and is mentioned below.

The discussion below focuses on baroclinic mode convergence, which refers to the point where addition of higher modes adds no significant information to the solution. It is discussed because it allows an optimal truncation point to be determined. However, it is important to realise that scales of motion that are not essentially linear, or dynamically determined, can not be represented by the model at any truncation.

There have been a number of studies on baroclinic mode decomposition of equatorial dynamics. These will be referenced in the following chapters because their focus is on annual and interannual dynamics. Poor simulation of annual mean surface zonal currents by linear models is no doubt a major reason for no modal decomposition studies of the annual mean circulation. However, by clearly separating linear and non-linear effects, a modal decomposition of the annual mean becomes readily interpretable.

**Pressure.** Figure 3.9a, and b show clearly that equatorial surface and subsurface pressure are effectively determined by the first three baroclinic modes. Interestingly, the first mode is most important in the central Pacific but, in the east and west, the second mode becomes dominant. This is due to differences in stratification. Three mode convergence is a feature of the entire equatorial region. This is illustrated for surface pressure in figure 3.9c and d, where the contributions of the first three modes, and the residual contributions from higher order modes are plotted. Convergence is achieved everywhere except along the equator in the eastern Pacific, where the equatorial trough is too weak. The latter is more pronounced in the full model fields, constructed from 10 modes (figure 3.4).

The higher order convergence along the equator is primarily due to modes 6 and 7. Their contributions are quite localised, and do not feature in figure 3.9a,

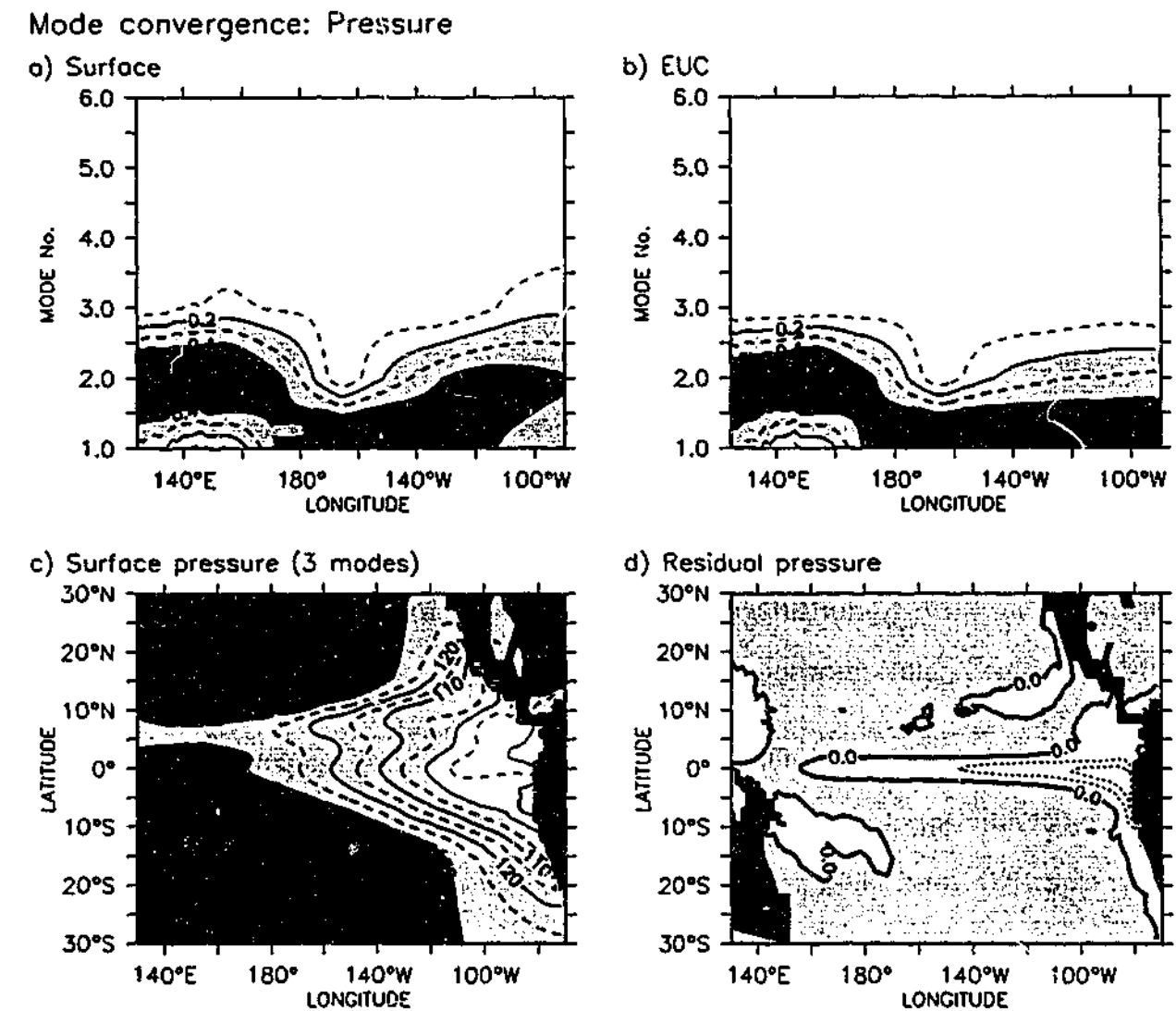


Figure 3.9: (a) relative mode contribution averaged between 5°S and 5°N, and over the upper 20m. The relative mode contribution of the  $n$ th mode is defined as the absolute value of the  $n$ th modes contribution to the full field, divided by the sum of the absolute values of all the modal contributions. It has a value between 0 and 1, with larger values indicating a greater modal contribution. The contour interval is 0.1 units. (b) the same as (a) except averaged between 70–130m, corresponding roughly to the EUC. (c) annual mean surface pressure, shown as dynamic height, as constructed from the first three baroclinic modes. The units are dyn cm, and the contour interval is 10 dyn cm. (d) the residual pressure due modes 4–30, contours are 2 dyn cm. In both (c) and (d), land is filled in black. (Data generated using rescaled Hellerman and Rosenstein [1983] wind stress)

or b, which presents latitude average results. As further discussed below, these modes are associated strongly with zonal velocity in the EUC. Given that the EUC is in approximate geostrophic balance [Lukas and Firing, 1984], it is consistent that pressure variations associated with these modes are important on the equator.

**Zonal velocity.** Zonal currents have effectively converged with the seven baroclinic modes. The zonal, meridional, and vertical structure of the undercurrent is accurately depicted by these modes. Surface currents are unrealistic, but this is due to the importance of non-linearity (section 3.4.4), not poor modal resolution. Figure 3.10a and b show that in the west and central Pacific surface and subsurface currents are mainly determined by the first three baroclinic modes. In the east modes 4 to 7 become increasingly important. This is most apparent for subsurface currents. In fact, the magnitude and structure of the EUC are effectively determined by modes 6 and 7 (not shown).

Figure 3.10a and b also show that modal power is not concentrated in a few select modes, but spread over many modes: Individual mode contributions are never greater than 0.3, and the sum of the first 10 modes is clearly not 1. Modes 11 to 30 make a 20 to 30% contribution, but since these modes have a large amount of vertical structure, they mainly represent fine details of the currents. Figure 3.10c and d show that 10 baroclinic modes realistically capture the EUC, and that the contribution of modes 11 to 30 is primarily to raise the EUC, and is not important to the overall structure.

**Meridional velocity.** The picture of mode contribution is very different to that of zonal velocity and pressure. All 30 of the model's baroclinic modes are important, and high order modes are much more significant (figures 3.11a and b). As surface meridional currents are primarily Ekman driven, high order modes feature strongly in the surface layers of central eastern Pacific, where zonal winds are strongest. Subsurface equatorward flow is primarily geostrophic, and hence is not controlled to the same degree by high order modes.

### Mode convergence: Zonal velocity

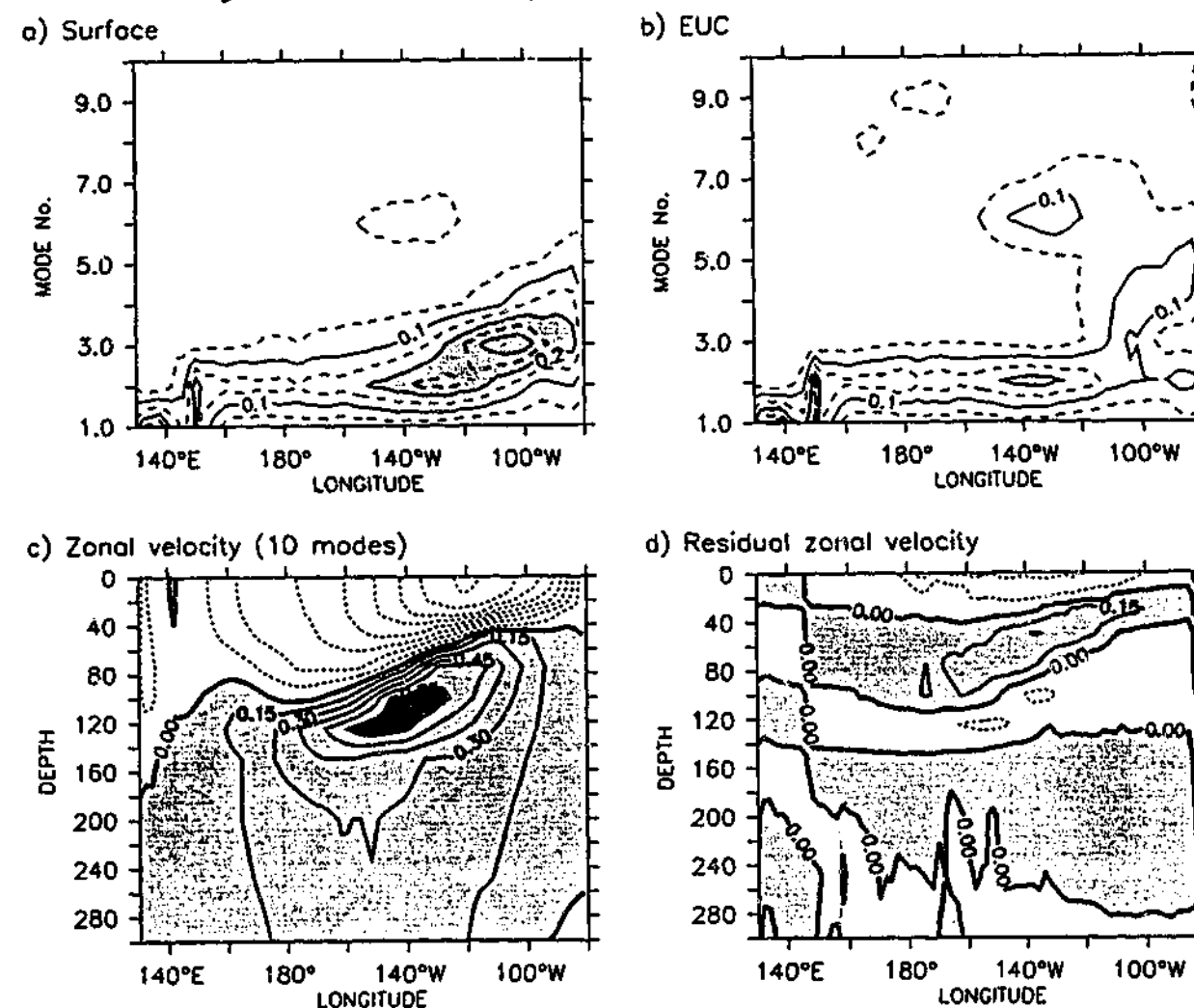


Figure 3.10: (a) and (b) are as in figure 3.9, but for zonal velocity, and the contour interval is changed to 0.05. (c) Zonal currents along the equator as constructed from the first 10 baroclinic modes. The EUC is realistically captured. (d) The residual contribution of modes 11-30. These modes primarily perturb the vertical structure. Zonal velocity is in  $ms^{-1}$ , and the contour interval is  $0.15ms^{-1}$ . (Data generated using rescaled Hellerman and Rosenstein [1983] wind stress)

## Mode convergence: Meridional velocity

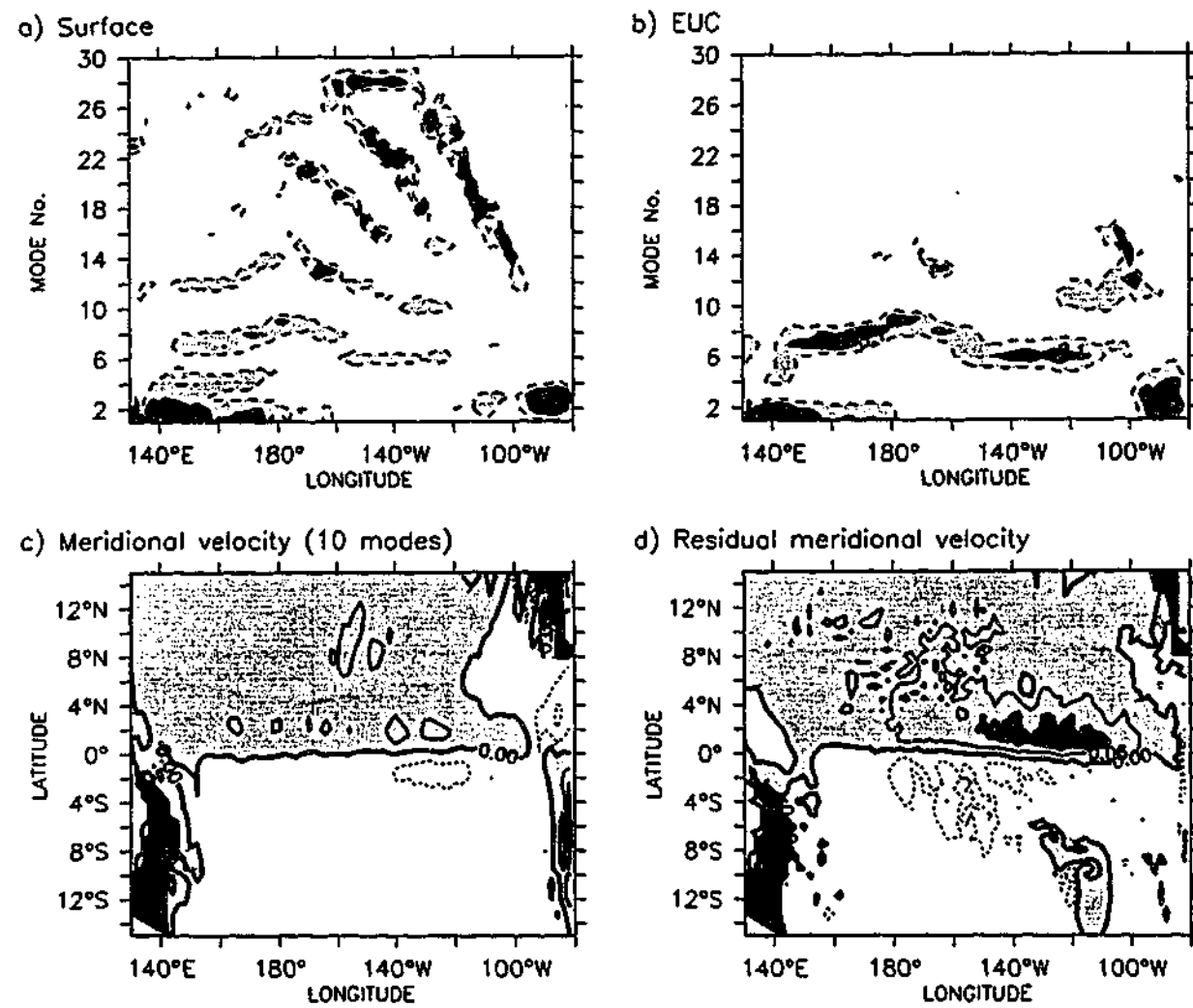


Figure 3.11: (a) and (b), similar to panels (a) and (b) of figures 3.9 and 3.10, show the relative mode contribution for surface and subsurface meridional velocity. However, as meridional flow is symmetric about the equator, the averaging is only between 0–5°N (a similar pattern is obtained averaging between 0–5°S). Contour spacing is 0.05 units, and dark shading indicates contributions greater than 0.1. (c) a ten mode representation of surface meridional flow, and (d) the residual contribution of modes 11–30. Clearly Ekman divergence is controlled by high order modes. The units are  $ms^{-1}$ , and the contour interval is  $0.05ms^{-1}$ . Speeds greater than  $0.1ms^{-1}$  have the darkest shading. Land is shown in black. (Data generated using rescaled Hellerman and Rosenstein [1983] wind stress)

Figure 3.11c and d show that a 10 mode truncation only weakly captures the surface flow. Although this truncation seems adequate where the model's flow is weak, it is unable to capture the strong localised currents in the eastern Pacific. These strong currents are modelled only by high order modes. The modal breakdown of surface meridional currents is clearly very sensitive to longitude, with the contributions of higher order modes quite localised (figure 3.11a). This is also true meridionally (not shown). This sensitivity is due to spatial variations in the wind-projection coefficients, and results in quite noisy surface meridional currents. Given that the vertical resolution of these modes becomes unreliable (due to the limited resolution of the density profile), the large spatial variations in the wind-projection coefficients is likely unrealistic.

**Vertical velocity.** Since vertical velocity is primarily determined by divergence of surface Ekman currents, it is controlled by high order modes. The convergence properties of vertical velocity are thus quite similar to surface meridional velocity, and shall not be discussed further.

**Representation of modes 11 to 30.** The results above clearly show a contribution from modes 11 to 30 is required to model meridional and vertical velocity. In the model, these modes are represented within two surface layers. This representation has two advantages. First, meridional currents and upwelling are less noisy, since the sensitivity to spatial variations in the projection coefficients is less apparent. Second, the computational expense is significantly reduced. It will now be shown that the approximations made in these layers are valid.

In order to approximate modes 11 to 30 using Ekman dynamics, they must be in steady state, and horizontal diffusion and horizontal pressure gradients must be negligible. Results above clearly indicate that pressure contribution due to modes 11 to 30 is negligible. In fact pressure variations associated with these modes form less than 1% of the total horizontal surface pressure variations. Since mode dependent damping increases with mode number, the two remaining criteria will be met for

sufficiently high mode number. The Rayleigh damping time scale for mode 11 is 12 days, and thus modes 11 and greater are effectively in steady state with respect to monthly wind forcing.

Experimental results show that horizontal diffusion is not completely negligible in the dynamics of modes 11 to 20. Neglecting horizontal diffusion results in more intense poleward velocities in the east, and stronger and more equatorially trapped upwelling. These effects can be seen by comparing figure 3.11d with figure 3.12a, and figure 3.12b with figure 3.12c. Although weaker upwelling is consistent with most modelling and observational studies, it is not necessarily realistic. The model's intense and equatorially trapped upwelling fields are in agreement with Poulain [1993]. Also results from modelling studies are unreliable, as upwelling is highly sensitive to vertical diffusion (see discussion in section 4.3).

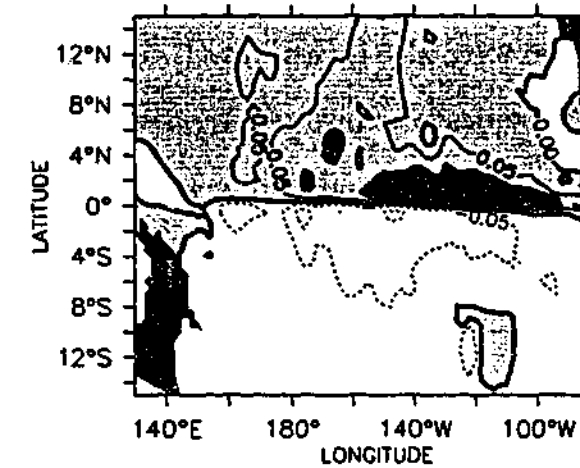
Calculations with Ekman dynamics and full vertical structure functions were compared to the simplified two layer treatment. The main results are as follows. Vertical integration into layers cancels the contribution of high order modes to zonal velocity (not shown). Meridional circulation is realistically captured by two layers, except in the east, where the two-layer-model's surface currents are too strong (not shown). Upwelling currents were nearly identical (compare figure 3.12d to figure 3.12b). Thus, the two layer representation simulates Ekman dynamics well. The steady-state Ekman representation though does not correspond fully to the dynamical representation, because of neglected horizontal diffusion.

### 3.6 Summary

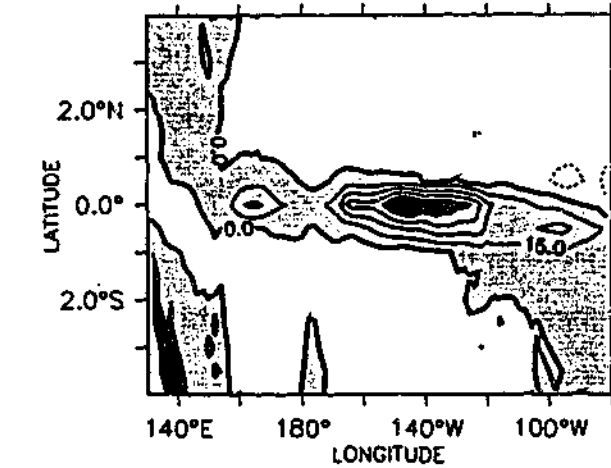
In this chapter the dynamical component of an ICM of the tropical Pacific ocean was formulated. The model consists of a linear and non-linear component. The linear component solves the linearised equation of motion in terms of baroclinic modes, and is adapted from McCreary [1981]. The non-linear component is a highly simplified treatment of the residual non-linear equations.

#### Representations of modes 11--30

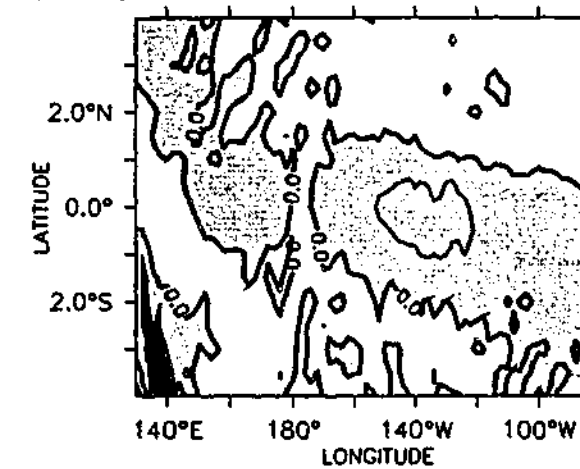
a) V, Diagnostic



b) W, Diagnostic



c) W, Dynamical



d) W, Ekman

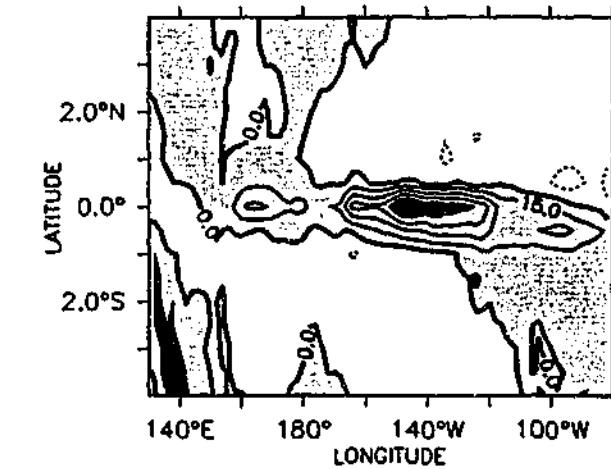


Figure 3.12: (a) annual mean surface (15m) meridional currents constructed from modes 11-30. The individual modal contributions are calculated using Ekman dynamics and the full vertical structure functions of each mode. Units are  $ms^{-1}$ , and the contour interval is  $0.05ms^{-1}$ . (b) annual mean vertical velocity at the depth of the model's mixed layer, constructed from modes 11-30 in (a). Units are  $\times 10^{-5}ms^{-1}$ , with contours every  $15 \times 10^{-5}ms^{-1}$ . (c) vertical velocity contribution of modes 11-30 calculated with the full dynamical equations. (d) as in (b) and (c), except calculated using the model's two layer representation for modes 11-30. (Data generated using re-scaled Hellerman and Rosenstein [1983] wind stress)

The model's annual mean simulation was described in detail, and shown to compare well with the observations. The linear component determines the structure of pressure, zonal and meridional currents, and vertical velocity. The non-linear component's contribution is only significant in the SEC, where it is responsible for the model's realistic simulation.

The modal convergence properties of the model were also investigated. The main results are as follows. A 10-mode truncation provides a converged representation of zonal currents and pressure. The simulation of meridional and vertical velocity requires modes 11 to 30. The model's two-layer representation of these modes is reasonable. The reason behind the different and distinctive modal convergence properties was not investigated.

## Chapter 4

# Annual cycle of zonal currents

### 4.1 Introduction

Understanding the dynamics of the equatorial Pacific is important to world climate. The climate's sensitivity to sea surface temperature in this region is well accepted. On interannual time scales the strong air-sea interaction is a dominant driving force for the El Niño Southern Oscillation [Philander, 1990]. On longer time scales the role of the air-sea interaction and how it may change under global warming scenarios is not well understood, and is an active area of research. The equatorial undercurrent (EUC), a strong eastward subsurface jet, transports water into a region where the air-sea interaction is important. As much of this water originates in the extra-tropics [McCreary and Lu, 1994], the EUC may play an important role in both decadal variability [Gu and Philander, 1997], and in determining the climate's response to global warming [Cai and Whetton, 2000]. Together with the necessary reliance of climate and climate change studies on complex models, it is important to understand and accurately model the dynamics of the EUC.

In the past, currents have not contributed significantly to model testing and mechanism analysis, because of the limited amount of data. Now though, as described in chapter 2, measurements from several moored buoys in the Pacific are providing sufficient data to give an accurate picture of the annual cycle of zonal currents on the equator, over the upper 200m [Yu and McPhaden, 1999a]. Many

interesting features have been revealed, perhaps the most striking is an eastward surge which extends from the surface to the core of the EUC that occurs around April to July when the trade winds are weak. At the surface the surge is strong enough to cause the reversal of the westward south equatorial current (SEC). The observational and modelling work of Yu and McPhaden [1999b;a] has been successful in explaining this phenomenon. The surge is due to the unbalanced eastward pressure gradient that occurs when the winds are weak, and the zonal structure is determined by linear wave dynamics.

The penetration of the eastward surge into the EUC is not easily understood. For one, it is well accepted that the trade winds drive the EUC not directly, but through the eastward pressure gradient they create [Philander, 1990]. Second, observational [Johnson and Luther, 1994; Qiao and Weisberg, 1997] and modelling studies [Wascogne, 1989] both indicate that wind stress is not important in the momentum balance of the EUC. Third, observational work on the parameterisation of vertical mixing [Peters et al., 1988] shows that short term wind stress variability does not penetrate to the EUC core. All these would suggest that the slackening of the winds could only indirectly effect the annual cycle of the EUC, either through non-linearity, or by altering the pressure gradient; however any relaxation in the gradient of the thermocline (caused by the slackening of the winds) would weaken rather than strengthen the EUC.

Non-linear models are able to realistically reproduce the annual cycle of the EUC [Yu et al., 1997]. Similar studies with linear models do not exist. In this chapter, the simple model that was formulated in the previous chapter, is used to systematically decompose the observations of zonal currents along the equator into linear and non-linear effects, focusing on the annual cycle of the EUC. The results presented here indicate that the annual cycle of the EUC is not a linear effect, but set up by weak non-linearity due to mean advection by the meridional circulation.

The purpose of this chapter is both to present an explanation of the annual cycle of EUC, and to document the model's accurate simulation of the annual cycle of zonal currents. The model is able to simulate surface variations well, but as these

have been thoroughly discussed in the literature [Yu and McPhaden, 1999b;a], they will not be discussed in detail. Instead, the focus of this chapter is on the vertical structure of the annual cycle, and in particular the annual cycle of the EUC. The meridional structure of the annual cycle is also explained, as this is closely related to the annual cycle of the EUC. These aspects of the annual cycle of zonal currents have not been explained in the literature. The results have been submitted to the *Journal of Geophysical Research Oceans*.

This chapter serves to further demonstrate that the model captures the important dynamics of the equatorial currents. The model's simulation of interannual variability shall be discussed in the next chapter. The structure of the remainder of this chapter is as follows. The model's annual cycle is presented in section 4.2, with linear and non-linear contributions clearly described. The model's realistic representation of the annual mean and annual cycle gives us confidence in the description it provides, and in the following section a detailed analysis is given to explain the underlying mechanism for the annual cycle of the EUC in the model. In section 4.4 important sensitivity studies that indicate the robustness of the model are summarised. Last, a summary is presented.

## 4.2 Annual cycle

The annual cycle discussed here is obtained from the final year of a ten year model run, of which the annual mean was described in the previous chapter. The annual cycle is generated using Hellerman and Rosenstein [1983] climatological wind stress, reduced in magnitude by 20%. The model parameter values and the model run are described fully in the previous chapter. As in chapter 2, the annual cycle will be discussed in terms of velocity anomalies about the annual mean.

The annual cycle of zonal currents along the equator, and about the equator at 140°W are shown in figure 4.1. Comparison with the observations (figure 2.9) shows both, westward phase propagation of the spring time surge (STS), and the equatorial anti-symmetric nature of the annual cycle are well captured. However,

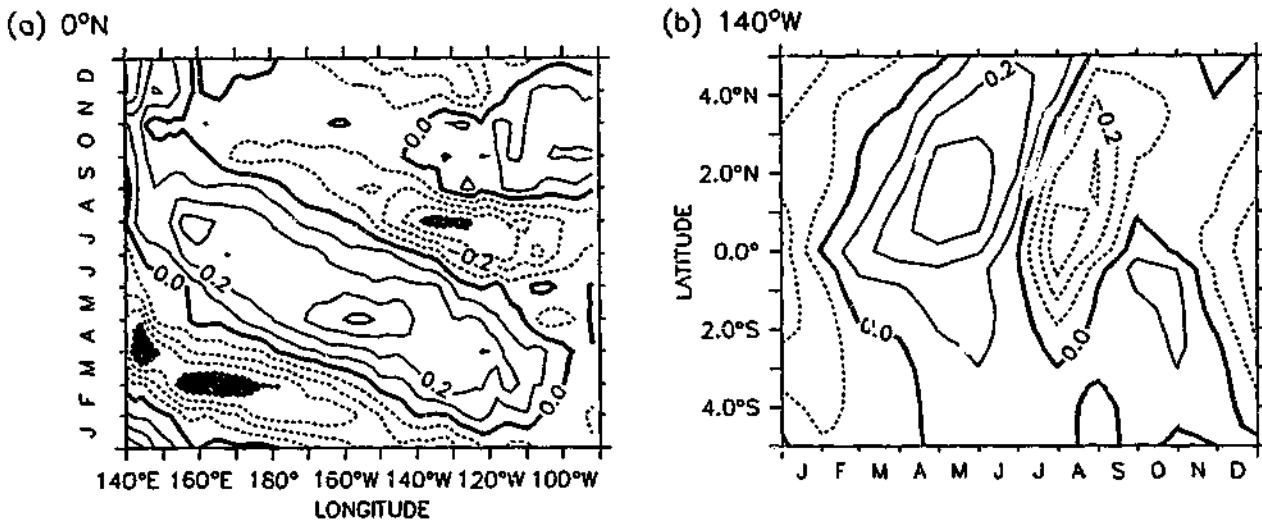


Figure 4.1: Annual cycle of 15m modelled zonal currents, (a) along the equator, and (b) about the equator at 140w are shown in terms of velocity anomalies. The units are  $ms^{-1}$ , and the contour interval is  $0.1ms^{-1}$ , with dashed contours indicating westward velocities. Eastward and westward velocities greater than  $0.4ms^{-1}$  have been shaded. . The annual cycle is generated using Hellerman and Rosenstein [1983] climatological wind stress. (This figure can be directly compared with figure 2.9)

westward phase propagation is a little faster than observed, and the annual cycle in the east (west) is weaker (stronger) than observed.

Consistent with previous work [Yu and McPhaden, 1999b], the magnitude and phase of the annual cycle of surface zonal currents are determined by linear dynamics. In general, the non-linear component degrades the solution. Weakening it in the west and strengthening it in the east, but not effecting the phase significantly. However, at  $140^{\circ}W$  the non-linear component acts appropriately, reducing the magnitude of the linear annual cycle (figure 4.1b ).

In figure 4.2 the vertical structure of the annual cycle of modelled zonal currents, on the equator, are plotted for the locations and depths of the observations. As with surface currents, the model is able to simulate the annual cycle of zonal currents well: The STS at all three locations has realistic magnitude and phase, but towards the east becomes surface trapped.

For flow above the EUC, the contributions from linear and non-linear components are as for surface flow, and were described above. In the EUC the situation is quite different. At  $140^{\circ}W$  certain aspects of the annual cycle are well modelled, in

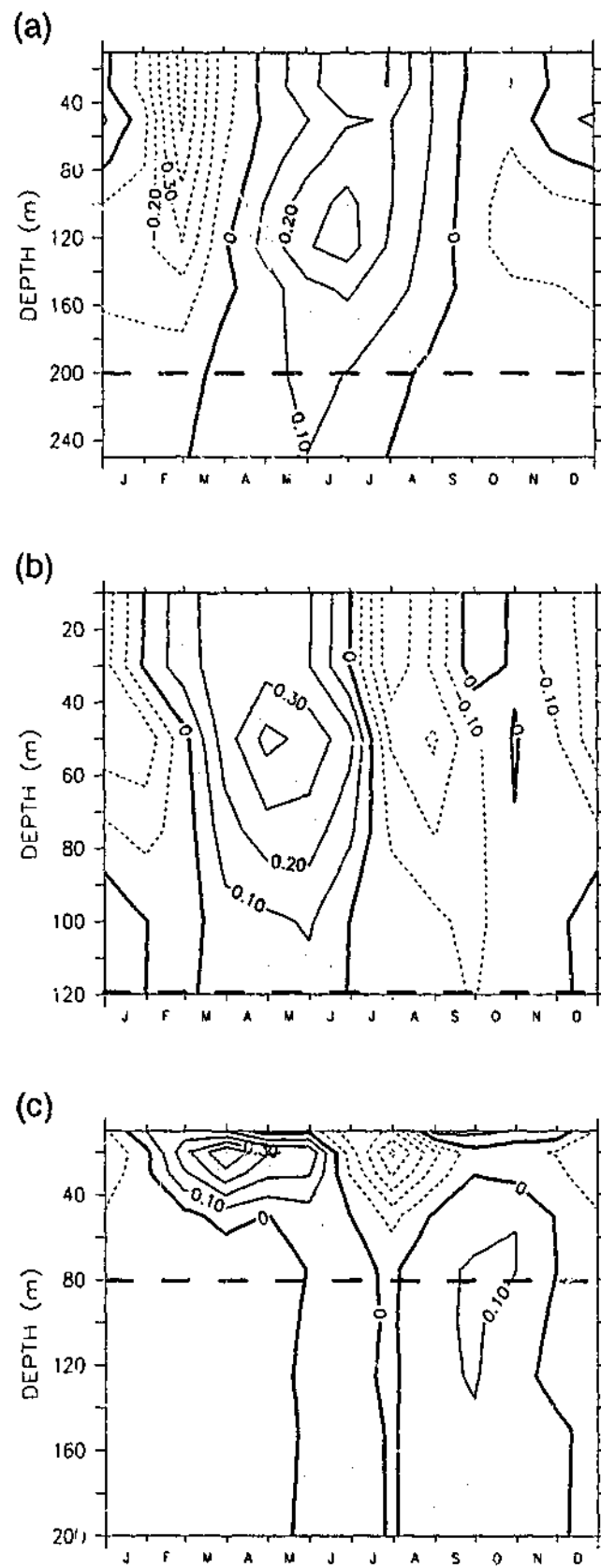


Figure 4.2: The vertical structure of the annual cycle of modelled zonal currents on the equator at  $165^\circ\text{E}$ ,  $140^\circ\text{W}$ , and  $110^\circ\text{W}$  are plotted in terms of velocity anomalies ( $\text{ms}^{-1}$ ). The dashed horizontal lines indicate the depths of the undercurrent. The model's annual cycle was generated using Hellerman and Rosenstein [1983] climatological wind stress. ( This figure may be compared directly with the observations presented in figure 2.10.)

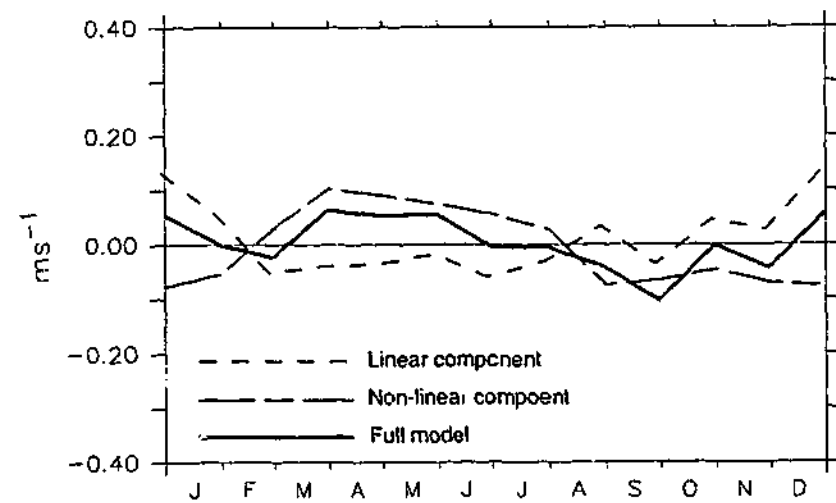


Figure 4.3: The annual cycle of modelled zonal currents in the EUC on the equator at 140°W, and 120m (solid) is decomposed into contributions from the linear (short dashed) and non-linear (long and short dashed) model components. Velocity anomalies are plotted in  $\text{ms}^{-1}$ . Comparison with figure 2.11b clearly illustrates the inability of linear dynamics to model the annual cycle of the EUC, and the accurate correcting behaviour of the non-linear component.

particular the STS, but here the linear component, hence linear dynamics, cannot simulate the annual cycle. It is the non-linear component that is responsible for the correct features. This is strongly highlighted in figure 4.3.

Perhaps the greatest insight into the annual cycle of the EUC is given by the meridional structure of the annual cycle of zonal currents, which shows the STS is a feature of the northern hemisphere (figure 4.1b). Figure 4.4 illustrates the case for the EUC at 140°W and 110°W. In both cases, a strong eastward surge in zonal currents that is centred approximately at 2°N, occurs at the time of the observed STS in EUC. Decomposition into linear and non-linear components shows all prominent features, including the off equatorial STS, are due to linear dynamics; non-linearity acts primarily as a meridional distortion of the linear features. In the next section it will be demonstrated that the dominant non-linear effect is mean meridional advection, and that the modelled STS in the EUC at 140°W is due to this distortion. At 110°W the meridional distortion is significantly weaker, and there is no STS in the EUC. Consistently though, the STS north of the equator is a strong feature. As fully discussed in the next section, the weakness of non-linearity is

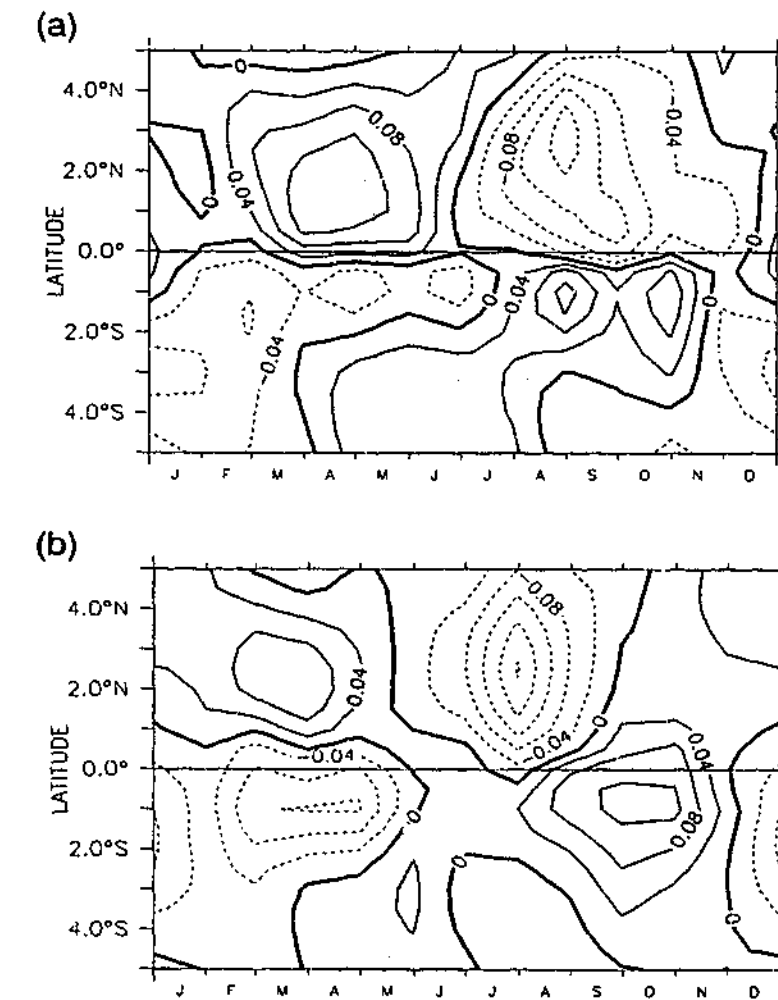


Figure 4.4: The meridional structure of the annual cycle of modelled zonal currents at the level of the EUC. (a) 140°W at 120m; and (b) 110°W at 80m. Velocity anomalies are plotted in  $\text{ms}^{-1}$ . Note the strong surge in zonal currents north of the equator that occurs in the boreal spring. At 140°W the spring time surge in the EUC is clearly associated with the surge to the north.

explained by the model's weak equatorial cell at 110°W, which surface observations indicate to be less realistic (section 3.4).

In brief summary, linear dynamics are accurate in simulating the annual cycle of zonal currents at all three locations, and at all levels, except in the EUC. Off the equator it would also seem that linear dynamics are dominant, even at the level of the EUC. In the EUC, non-linearity is able to correct the *linear* annual cycle.

### 4.3 Analysis and Discussion

The ability of linear dynamics to simulate the annual cycle of equatorial surface zonal currents and depth integrated (surface to 200m) zonal momentum has been covered by Yu and McPhaden [1999b;a]. Here, taking advantage of the model's ability to accurately simulate the vertical structure of the annual cycle of zonal currents, I focus only on explaining the annual cycle of the EUC. Detailed analysis described here shows that mean meridional advection of the northern annual cycle of zonal currents is the dominant and driving non-linearity. Also, the dynamics of the anti-symmetric annual cycle, which determines the annual cycle in the EUC, are easily understood in terms of equatorial wave dynamics.

#### 4.3.1 Non-linearity

Figure 4.5, the annual cycle of non-linear tendencies at  $140^\circ\text{W}$  in the EUC, clearly identifies the terms responsible for producing the non-linear component's correcting behaviour. Local acceleration,  $\frac{\partial u}{\partial t}$ , is close to zero for most of the year, corresponding to periods of fairly constant non-linear zonal velocity, i.e., the non-linear component's velocity. Two periods of non-zero local acceleration, one in February and another in August, are responsible for sharp changes in non-linear velocity, and determine the character of the annual cycle. Meridional advection,  $\frac{\partial vu}{\partial y}$ , and vertical advection,  $\frac{\partial wu}{\partial z}$ , are by far the strongest terms. The annual cycle of meridional advection would explain the STS, strongly peaking in May. Vertical advection counters the annual cycle of meridional advection, and in May almost alone cancels its effect. Together these two terms determine the structure of local acceleration, and hence non-linear zonal velocity. All other tendency terms are of similar magnitude and fairly weak.

The non-linear component's appearance of simply extending the northern linear annual cycle to the equator, and the similarity in phase between meridional advection and northern zonal currents, strongly suggests that mean meridional advection is important. To determine the role of the mean flow in determining non-linearity, an

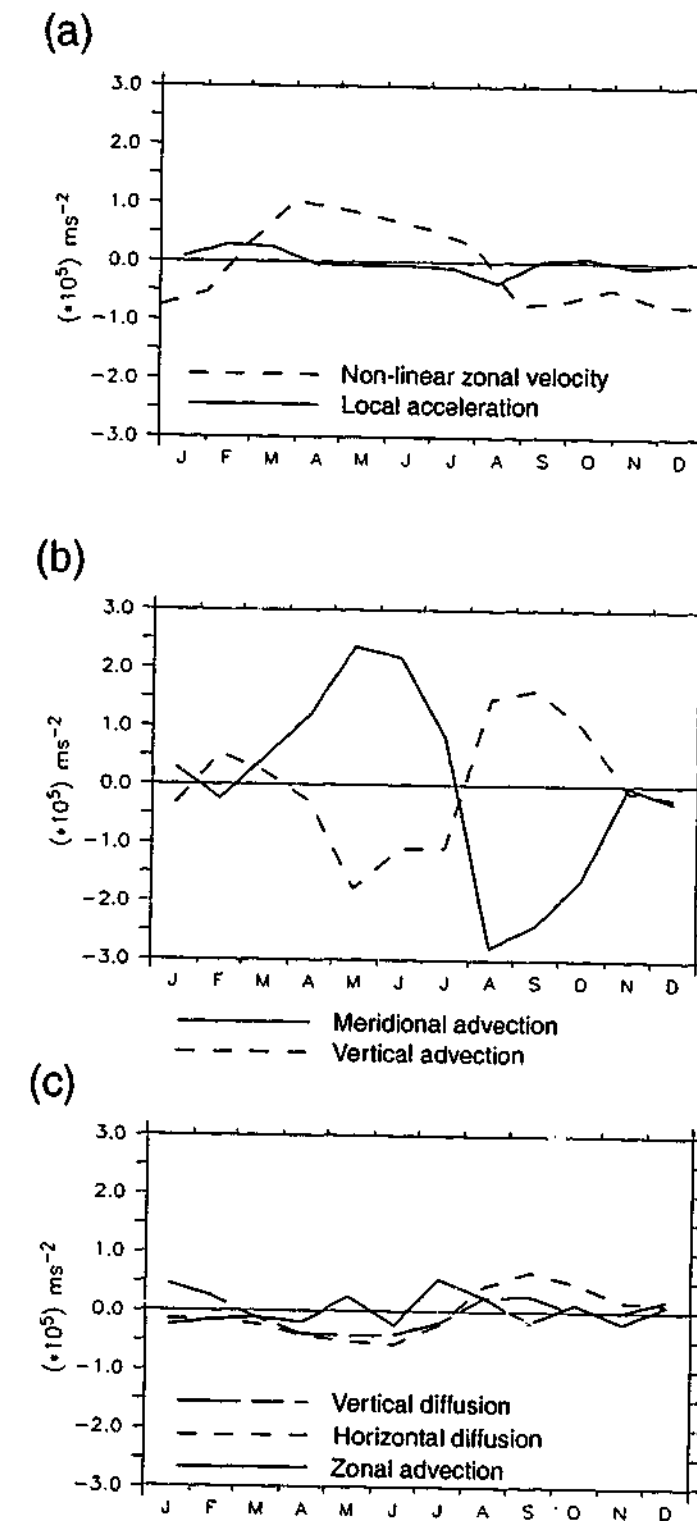


Figure 4.5: The annual cycle of the non-linear component's tendency terms at  $140^\circ\text{W}$ ,  $0^\circ\text{N}$  in the lower layer. (a) local acceleration (solid), and the non-linear component's zonal velocity anomaly (dashed and in  $\text{ms}^{-1}$ ); (b) meridional advection (solid), and vertical advection (dashed); and (c) zonal advection (solid), horizontal diffusion (short dashed), and vertical diffusion (long and short dashed). The terms plotted are anomalies about the annual mean, and in units of  $10^{-5} \text{ ms}^{-2}$ .

anomaly form of model was constructed. Using a model generated background state and Hellerman and Rosenstein [1983] wind stress anomalies for forcing, the anomaly model fields were nearly identical to the full model's anomaly fields.

In anomaly form the meridional advection and vertical advection terms are:

$$\frac{\partial w \bar{u}}{\partial y} + \frac{\partial \bar{w} u'}{\partial y} + \frac{\partial w' u'}{\partial y},$$

$$\frac{\partial w \bar{u}}{\partial z} + \frac{\partial \bar{w} u'}{\partial z} + \frac{\partial w' u'}{\partial z},$$

a                      b                      c                      d

where  $\bar{\quad}$  and  $\prime$  terms represent mean and anomaly quantities respectively. The last terms in both equations (anomaly products) were found to be insignificant and are not discussed. Term *a* represents meridional advection of mean zonal momentum, *b* mean meridional advection of zonal momentum, *c* vertical advection of mean zonal momentum, and *d* mean vertical advection of zonal momentum.

Terms *a*, *b*, *c*, and *d* are plotted in figure 4.6 for the EUC at 140°W. The annual cycle of both meridional and vertical advection is primarily determined by advection of anomalous zonal velocity by the mean equatorial cell, i.e., terms *b* and *d*. Annual variations in the strength of the equatorial cell, terms *a* and *c*, are not significant. The effects of non-linearity on the meridional structure are then easily interpreted as being due to mean meridional advection. Given the circulating direction of the equatorial cell it is also clear that meridional advection is the driving term, and that vertical advection is a reactive response, i.e., a surge in the EUC necessarily results in increased mean vertical advection (term *d*).

Another important observation is that on the equator the annual cycle in the northern hemisphere is seen to dominate. There are two clear reasons for this: the northern branch of the meridional cell is stronger (figure 3.6c), and annual variations in zonal currents are stronger in the north than in the south (figure 4.4a).

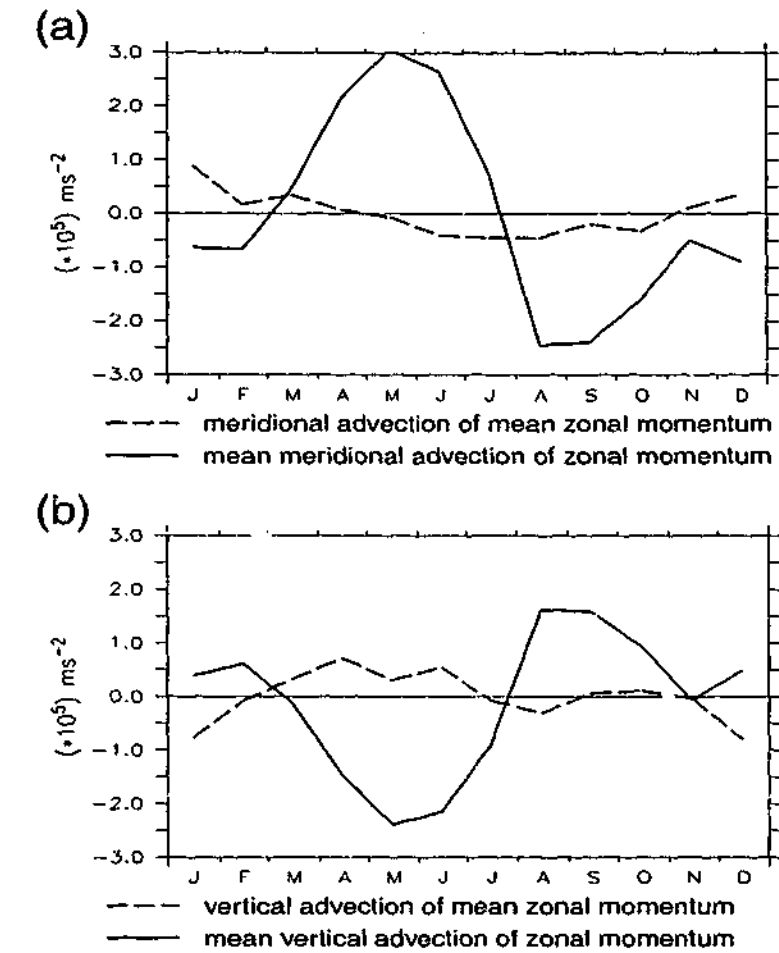


Figure 4.6: The annual cycle of the non-linear component's advective tendency terms (shown in figure 4.5b) are decomposed into anomaly terms. (a) mean meridional advection of zonal momentum (solid) and meridional advection of mean zonal momentum (dashed); (b) mean vertical advection of zonal momentum (solid) and vertical advection of mean zonal momentum (dashed). See the text for definitions. The terms plotted are anomalies about the annual mean, and in units of  $10^{-5} \text{ ms}^{-2}$ .

### 4.3.2 Linearity and the Meridional Structure of the Annual Cycle

Observations show the meridional structure of the annual cycle of surface zonal currents in the eastern equatorial Pacific is anti-symmetric about the equator (figure 2.9b). (In the west variations are equatorially symmetric.) At the surface the model matches the observations closely (figure 4.1). There are no observation with depth, but the model shows this feature extends to the depth of the EUC, where through non-linearity it is able to explain the STS in the EUC. As already stated, linear dynamics determines the meridional structure of the annual cycle of zonal currents, non-linearity only acts as a meridionally distortion. Thus, the meridional

structure may be interpreted in terms of baroclinic modes. It is found that the off equatorial anti-symmetric component is effectively only due to modes 1 and 2, and the equatorial symmetric component (particularly the incorrect January surge) is due to modes 6 and 7.

Modes 6 and 7 have short damping scales, 17 and 9 degrees respectively for Kelvin waves, and hence are locally forced. The surface zonal currents associated with these modes are positively correlated to zonal wind forcing directly to the west. In the EUC the correlation becomes negative, due to the vertical structure of these modes. The linear model's behaviour is as expected, the EUC is strongest (weakest) when the equatorial trades are strongest (weakest). Interestingly, elsewhere these modes behave appropriately: they almost solely determine the magnitude, and vertical and zonal structure of the EUC; and contribute significantly to the annual cycle of zonal currents at 165°E. This inconsistency suggests the linear component's failure in simulating the annual cycle of the EUC is due to the break down of linear assumptions, not the use of a modal solution, or poor choice of parameters. Sensitivity studies, described in section 4.4, support this.

Yu and McPhaden [1999b;a] show that baroclinic modes 1 and 2 explain a different balance, one between local acceleration, wind stress, and zonal pressure gradient; and that this balance is primarily determined by the Kelvin and first Rossby waves of these baroclinic modes. These waves being equatorially symmetric cannot explain the anti-symmetric nature of the annual cycle. To determine which aspects of the linear dynamics and wind forcing are responsible for producing an equatorially anti-symmetric response, a simple meridional mode model of these baroclinic modes was constructed; essentially that of Gill and Clarke [1974]. The model covered the equatorial Pacific (125°E-89°W by 29°S-29°N), and was forced with observed zonal winds [Hellerman and Rosenstein, 1983]; the effect of meridional winds are weak and not significant here. The spatially constant wind projection coefficients were calculated as basin averages of those used in our main model. Eastern and western boundary reflections were included.

On the equator the model agreed with Yu and McPhaden [1999b], showing the

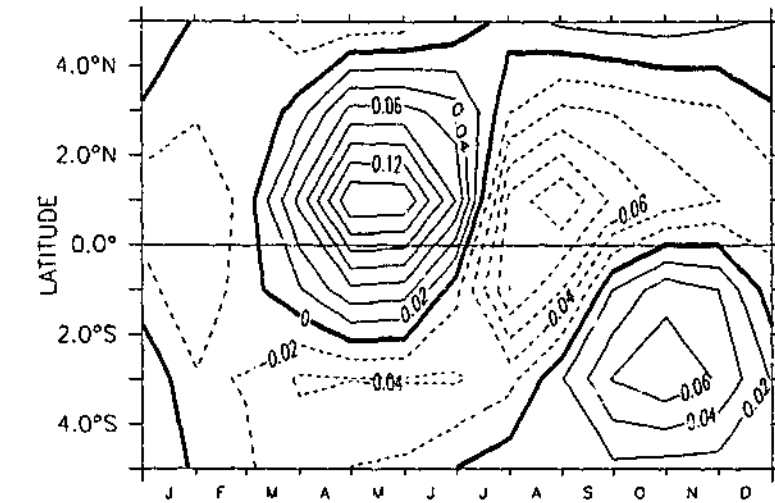


Figure 4.7: The meridional structure of the annual cycle of zonal currents at 140°W, 120m (the depth of the EUC) generated by a meridional mode model [Gill and Clarke, 1974]. The model consists of the first two baroclinic modes and their Kelvin and first and second Rossby waves. Velocity anomalies are plotted in  $\text{ms}^{-1}$  with a contour interval of  $0.02 \text{ ms}^{-1}$ . This simple linear model captures the meridional structure of the annual cycle shown in figure 4.6.

annual cycle of surface zonal currents is dominated by the Kelvin and first Rossby waves. In addition, it showed the equatorially anti-symmetric behaviour is primarily due to the second meridional Rossby wave, with significant contributions from both baroclinic modes. Figure 4.7 shows the meridional structure of the annual cycle of zonal currents at 140°W, at the depth of the EUC, constructed from the first two baroclinic modes and their Kelvin, and first and second Rossby waves. Comparison with figure 4.4a shows the off equatorial structure is accurately captured in both phase and amplitude.

The second meridional mode Rossby wave is forced by equatorially anti-symmetric variations in zonal wind stress, meridional winds being neglected (See Gill [1982]). For the first and second baroclinic modes these variations are between 10°S and 10°N. As the trade winds are strongest in the winter hemisphere, seasonal variations in wind stress in these regions are out of phase across the equator. Though this is true in both the east and west, only in the east do these variations project significantly onto the forcing functions of the second mode Rossby waves, explaining why in the full model the anti-symmetric response is only seen in the east. The

east-west asymmetry is most likely due to the east-west slope of the Intertropical Convergence Zone (ITCZ). In the east the seasonal variations in wind stress, which are associated with the north-south movement of the ITCZ, are further north, and thus better able to force the second meridional mode Rossby wave.

The results presented here demonstrate that the balance between zonal pressure gradient, local acceleration, and wind stress holds off the equator. The anti-symmetric annual cycle appears simply a response to seasonal variations in the trade winds, which are out of phase across the equator.

#### 4.3.3 Difficulties Simulating Non-Linearity

At 110°W the model is unable to simulate the annual cycle in the EUC. Consistent with the picture at 140°W, linear dynamics show a STS north of the equator, and incorrect behaviour in the EUC (figure 4.4b). Here though the non-linear correction is weak over the whole year. Analysis shows that mean meridional advection is weak, hence the off equatorial structure is unable to influence the annual cycle on the equator, and the mechanism described above is not active. Mean meridional advection at 110°W is weak for two reasons: first and most significant, the model's meridional circulation is much weaker here than at 140°W; second, the meridional structure of the annual cycle is also weaker here.

As discussed in section 2.3.2, observations of the meridional circulation are limited, and insufficient to determine whether the model's meridional circulation at the level of the undercurrent is less realistic at 110°W, but a comparison with Reverdin et al. [1994] 15m current climatology shows that the northern surface branch of the equatorial cell is less well modelled here (section 3.4). In fact, as described in the previous chapter, surface northward velocity, between the equator and 2°N, east of 140°W, is unrealistically strong. Poor modelling of the surface meridional flow would indicate the equatorial cell is less realistic. Meridional currents were found to depend crucially on the higher order baroclinic modes, which because they are strongly damped, are sensitive to both the precise spatial pattern of wind stress,

and also the vertical mixing formulation. The latter is consistent with other work [World Climate Research Programme, 1995]. The less than perfect representation in the model of the equatorial cell, therefore is likely a result of both inaccurate wind stress forcing and crude vertical mixing.

In the next section the meridional structure of the annual cycle of zonal currents, for which there are no observations, is shown to be highly sensitive to the representation of wind stress, and thus may not be accurately represented either. The clear modelled STS north of the equator, suggests the inability to model the annual cycle in the EUC at 110°W is due to poor modelling of both the equatorial cell, and the meridional structure of the annual cycle, not to a different mechanism.

Another issue that must be addressed is the incorrect response of non-linearity at the surface and in the western Pacific. An important observation is that in these regions the linear model is able to accurately reproduce the annual cycle. This would indicate that either the non-linear terms are negligible in these regions on the annual time scale, or that on the annual time scale they balance each other. Neither of these situations occurs in the annual mean. As the addition of non-linearity effects the model's simulation of the annual cycle, it would appear that non-linearity is not negligible. The second idea agrees with Wascogne [1989], who analysed the zonal momentum balance of the equatorial Atlantic using the Philander and Pacanowski [1984] model. In the annual cycle the following balance was found

$$vu_y + wu_z = -\frac{p_x}{\rho_0} + (\nu u_z)_z,$$

with all four terms varying in strength seasonally, but their sum remaining fairly constant. Note local acceleration is absent. Given the crudeness of our model, and the importance in our model of representing the mean equatorial cell correctly, it is not surprising that the model is unable to resolve this fine balance.

## 4.4 Sensitivity studies

This section presents, a brief summary of the extensive sensitivity studies that were performed to determine the robustness of the results presented in the previous sections. These experiments support the model findings, by demonstrating that the model parameters and layers are appropriate, the modal solution is consistent, and the important features of the mechanism for the annual cycle of the EUC are not wind field unique.

### 4.4.1 Diffusion Parameters

The model was tested to a wide range of vertical diffusion parameter values,  $0.5 - 6(\times 10^{-7})m^2s^{-3}$ . In agreement with other authors [Minobe and Takeuchi, 1995; Yu and McPhaden, 1999b], the vertical diffusion parameter affects the strength of the solution; increased damping leading to weaker zonal currents, and vice versa. In fact, this parameter is given a wide range of values in the literature. Typical values range between  $1.4 \times 10^{-7}m^2s^{-3}$  [Minobe and Takeuchi, 1995] to  $6 \times 10^{-7}m^2s^{-3}$  [Yu and McPhaden, 1999b]. (These values have been converted from e-fold damping values.) Such a wide range of values is easily attributed to the 20% differences in magnitude that exist among wind products. Our experiments clearly showed the model's parameter value is appropriate, and in addition that the annual cycle of the EUC remains unchanged, within the parameter range where the EUC is defined.

The model's sensitivity to the parameterisation of vertical diffusion was also tested, through independently specifying mode damping (as opposed to being inversely proportional to the square of the shallow water speeds). While both the annual mean and annual cycle of zonal currents could be significantly affected, the annual cycle of the EUC remained a robust feature.

To test the sensitivity of the non-linear component to vertical diffusion, the model was run with higher and lower values:  $\nu_v = 1. \times 10^{-2}$ , and  $1. \times 10^{-4}m^2s^{-1}$ . These experiments demonstrate that, although altering the contribution of vertical diffu-

sion to the zonal momentum balance affects modelled zonal currents, the changes do not result in more realistic simulations.

The model was tested to decreased and increased values of horizontal diffusion:  $\nu_h = 1. \times 10^2m^2s^{-1}$ , and  $3.5 \times 10^2m^2s^{-1}$ . Only the strength of mean zonal currents and upwelling were significantly affected, increasing diffusion severely weakening both. The other model features, including the annual cycle of the EUC, were completely robust.

### 4.4.2 Model Layers

To test the sensitivity of the results to the specification of the two surface layers, a variety of different configurations were implemented, in which the thickness and positions of the layers were altered. These included constant thickness layers; arbitrarily increasing and decreasing the depth of the upper layer; and changing the lower boundary of the lower layer to give lower layers of constant thickness. In all cases neither the annual mean currents or the annual cycle exhibited any significant sensitivity; clearly demonstrating the two layers are adequate in capturing the basic effects of the neglected processes, and that the model's simulation is not highly sensitive to their specification.

### 4.4.3 Mode Mixing

Scattering of modes due to horizontal variations in stratification (mode mixing) is neglected. As stated earlier, this can not be justified with scale arguments. To assess the neglect of mode mixing, we performed a number of numerical experiments using a finite difference model of equations 3.4, as opposed to a modal solution (The eddy coefficients for vertical diffusion of heat and momentum were taken to be inversely proportional to the square of Brunt Väisälä frequency, as in the modal model.) The model corresponded closely to the modal solution, producing similar results when forced with climatological winds; in particular the annual cycle of the EUC remained incorrect.

The experiments to measure mode mixing consisted of comparing the propagation of Kelvin wave pulses from the dateline to the eastern Pacific, through horizontally constant and horizontally varying stratifications. The horizontally varying stratification was that used to calculate the baroclinic modes, and the horizontally constant stratification was taken from 180°E, 0°N. Seven different Kelvin waves, corresponding closely to the first seven baroclinic modes, were tested; Zonally the Kelvin waves consisted of a 20 degree sinusoid hump centred on the dateline. In all cases, horizontal variations in stratification were found to slow the propagation of the waves and alter their vertical structure, but not to cause significant mode mixing. The most interesting result was that stratification modified the vertical structure of the modes to match those of the background stratification, strongly supporting our use of horizontally varying baroclinic modes. Mode mixing among higher order modes is not a significant issue here; these modes are strongly damped, and so do not contribute significantly to the adjustment process. Complete details on these experiments are presented in appendix A.

#### 4.4.4 Wind Forcing

The sensitivity of the results to different wind forcing was tested by using a climatology created primarily from the FSU winds [Stricherz et al., 1995] over the period 1979-1998 (NCEP re-analysis winds [Kalnay et al., 1996] were used over the Atlantic and at high latitudes not covered by FSU winds.) The zonal, meridional, and vertical structure of the annual mean currents did not differ significantly from that generated using Hellerman and Rosenstein [1983] wind stress, but the magnitude of the currents was up to 20% weaker. Such differences have been reported in the literature [Yu and McPhaden, 1999b].

The annual cycle along the equator was noticeably weaker, but the westward phase propagation and vertical structure of the annual cycle were identical. Significant differences occurred in the meridional structure of the annual cycle at the depth of the EUC. While the same off equatorial features important to the annual cycle of the EUC, described in section 4.3, are present, they are much weaker. As

a consequence the meridional distortion of non-linearity is not so apparent, and its effect on the annual cycle of EUC is weaker. This clearly suggests that correct representation of zonal wind stress is important to modelling the annual cycle of the EUC.

## 4.5 Summary

The annual cycle of zonal currents on the equator has a very definite structure. The most interesting feature, and unexplained, is an eastward spring time surge (STS) in the currents that extends from the surface to the EUC core. The surge occurs between April and July, and at the surface is strong enough to cause a reversal of the westward flowing SEC, known as the spring time reversal of the SEC.

The spring time reversal of the SEC, which has a very definite westward phase propagation, is explained by linear wave dynamics [Yu and McPhaden, 1999b]. The depth integrated momentum balance, which is dominated by the STS above the EUC, is a linear balance between local acceleration, wind stress, and zonal pressure gradient [Yu and McPhaden, 1999a]. Hence the STS above the EUC core is easily explained as due to an unbalanced pressure gradient that arises when the trade winds are weakest. Although it is part of the depth integrated zonal momentum balance, the STS of the EUC can not be explained so easily. Modelling [Wascogne, 1989] and observational [Johnson and Luther, 1994; Peters et al., 1988; Qiao and Weisberg, 1997] studies indicate that wind stress is not significant in the momentum balance; so a relaxation of the winds cannot directly effect the annual cycle within the undercurrent.

Here, using the simple model formulated in the previous chapter, a mechanism for the annual cycle of the EUC is presented. North of the equator, the annual cycle of zonal currents surges in spring, at the surface and at the depth of the undercurrent. The STS in the EUC and the full annual cycle are explained simply by mean advection by the meridional circulation, of the northern annual cycle onto the equator. The meridional structure of the annual cycle of zonal currents, from

the surface to the EUC, is equatorially anti-symmetric; this feature is also seen in observations of surface currents. Here it is shown, using linear wave dynamics, that this is a response to annual variations in trade winds, which are anti-symmetric about the equator. The balance between zonal pressure gradient, wind stress, and local acceleration that holds on the equator [Yu and McPhaden, 1999b] also holds off the equator. The second meridional Rossby wave, forced only in the eastern Pacific, is responsible for extending this balance, which is maintained on the equator by the Kelvin and first Rossby waves [Yu and McPhaden, 1999b], off the equator to produce the anti-symmetric response. The ability of mean meridional advection to advect the northern annual cycle onto the equator is demonstrated here.

The results presented in this chapter and the previous, clearly demonstrate the success of the model is due to the model's design, which takes advantage of the demonstrated success of linear dynamics in the equatorial region, yet includes a non-linear correction to zonal currents. As a result, the linear dynamics that determines the annual cycle of surface zonal currents [Yu and McPhaden, 1999a;b], and the annual mean strength and structure of the EUC [McCreary, 1981], are very well captured. In addition, the magnitude of SEC and the annual cycle of the EUC, which are due to non-linear effects, are also reasonably well represented. The demonstrated ability of the model gives confidence in the understandings it provides, and the simplicity of the model makes it an ideal tool for mechanism analysis.

The important findings of this work are that the annual cycle of zonal currents is explained largely by linear dynamics, with non-linearity only weakly distorting the linear picture: Only in the EUC does the distortion alone determine the annual cycle. This study suggests that to simulate the annual cycle of the EUC, ocean models must accurately represent non-linear terms. The shallow equatorial meridional overturning cell must also be realistically represented. Accurate representation of zonal wind stress is also important, since it is crucial to modelling the meridional structure of the annual cycle (and hence the annual cycle of the EUC).

The role of non-linearity in controlling interannual zonal current variations shall be discussed in the next chapter.

## Chapter 5

### Interannual variability of zonal currents

Displacement of the eastern edge of the warm pool in the equatorial western Pacific Ocean is linked to zonal movements in atmospheric convergence, and to interannual variability [Picaut and Delcroix, 1995; Picaut et al., 2001]. Also, modelling studies show that extra-tropical climate variations are more sensitive to the small sea surface temperature (SST) changes at the date line than to the larger SST changes in the east (See references in [Delcroix et al., 2000]). Interannual variations in SST at the date line are controlled primarily by zonal advection [Picaut and Delcroix, 1995; Frankignoul et al., 1996; Delcroix et al., 2000; Wang and McPhaden, 2000; Picaut et al., 2001]. In the east, upwelling of thermocline anomalies is more important, but zonal advection remains significant [Frankignoul et al., 1996; Wang and McPhaden, 2000]. For these reasons, it is important to understand the mechanisms controlling interannual variability of zonal currents, particularly in the central Pacific. This in turn will lead to more accurate modelling of zonal currents, and hence to better simulation of interannual SST variability and interannual climate variability [Picaut and Delcroix, 1995; Delcroix et al., 2000].

Understanding equatorial dynamics is also important for understanding the limitations of models, and of satellite-inferred surface currents. Non-linear advective momentum terms in the momentum equations are commonly neglected in intermediate complexity model (ICM) studies of interannual variability in the equatorial

Pacific (e.g., Zebiak and Cane [1987]; Battisti [1988]; Kleeman [1993]). Satellite-inferred currents are obtained from satellite sea-level measurements, using a modified form of geostrophy (e.g., [Lagerloef et al., 1999; Delcroix et al., 2000]). These data have been used to interpret ENSO dynamics [Picaut and Delcroix, 1995; Picaut et al., 2001]. However, while both linear model and satellite-inferred currents are realistic on the equator in the western and central Pacific, they are not so realistic on the equator in the east [Picaut et al., 2001]. Correlations of satellite-inferred currents with in-situ observations are weak. Many reasons have been suggested for the east-west discrepancies, but as yet no satisfactory explanation has been given.

In this chapter, the ocean model developed in chapter 3 is used to study the interannual variability of zonal currents in the equatorial Pacific. In particular, to investigate the possibility that the neglect of non-linear terms is responsible for the inaccurate linear-model and satellite-inferred currents in the eastern Pacific. The results suggest that this is indeed the case. The separate treatments of linear and non-linear contributions in the model make it an ideal tool for this investigation.

The remainder of the chapter is structured as follows. The next section presents a review of both the calculation of zonal currents on the equator using a modified form of the geostrophic balance, and the simulation of zonal currents. In section 5.2 the model's simulation of interannual zonal current variability is compared to observations. In the following section, analyses are given that describe the contributions of various baroclinic modes, explain the important non-linear terms, and explain the breakdown of the geostrophic assumptions. In section 5.4, sensitivity studies are described. A summary and discussion are presented in the final section.

Throughout this chapter, unless otherwise stated, the term zonal current anomaly refers to anomalies about the annual cycle. This follows the terminology used in modelling studies (e.g., Zebiak and Cane [1987]). However, in the literature on satellite-inferred currents, this term generally refers to anomalies about the annual mean. This point was made earlier, but is restated to ensure no misunderstanding.

## 5.1 Background

The following is a brief review of geostrophic calculated zonal currents on the equator, and the simulation of equatorial zonal currents.

### 5.1.1 Geostrophic calculated zonal currents

When local acceleration, frictional terms, and non-linear advective terms are all negligible, and the frictional wind-driven component of the flow is excluded, the momentum equations have a particularly simple form,

$$fu = -\rho^{-1}P_y, \quad (5.1)$$

known as geostrophic balance, where  $f$  is the Coriolis parameter,  $u$  is the zonal velocity,  $\rho$  is the water density, and  $P_y$  is the meridional pressure gradient. A similar equation holds for the meridional component of the flow.

Away from the equator and in the interior of the ocean, the above assumptions hold very well, and the flow is in geostrophic balance (e.g., Pond and Pickard [1983]). On the equator, even if the above assumptions hold, equation 5.1 is indeterminate, since the Coriolis parameter vanishes. However, by taking the meridional derivative of the above equation, the zonal flow on the equator can still be related to the pressure field,

$$\beta u = -\rho^{-1}P_{yy}, \quad (5.2)$$

where  $\beta = f_y$  is the beta parameter [Lukas and Firing, 1984]. Following common terminology, zonal currents calculated using equation 5.2 are referred to as geostrophic currents [Lukas and Firing, 1984; Picaut et al., 1989]. (This holds only for the zonal flow.)

Calculations using in-situ observations show that long-term mean, and monthly-mean variations in zonal currents are in approximate geostrophic balance on the equator [Lukas and Firing, 1984; Picaut et al., 1989]. Correlations between geostrophic calculated and observed monthly zonal current variability at 165°E, and at 110°W

were between 0.6 and 0.9. The weakest correlations were at 110°W at the surface [Picaut et al., 1989].

Although satellite sea-level measurements do not provide reliable absolute current measurements, because of systematic errors [Picaut et al., 1990; Yu et al., 1995; Picaut et al., 2001], they can be used to calculate zonal current variability (e.g., [Picaut et al., 1989; Delcroix et al., 1994; Yu et al., 1995; Lagerloef et al., 1999; Delcroix et al., 2000]). The agreement between satellite-inferred currents and in-situ observations depends on the averaging period, with monthly averaged data in closer agreement than 5-day averaged data (Picaut et al. [1989]; and Table 5.1).

On the equator in the central and western Pacific, there is good agreement between satellite-inferred currents and in-situ measurements (Table 5.1). In the east, correlations are consistently weaker and errors are substantially larger. The magnitude of satellite-inferred zonal current variability compares well with in-situ observations across the Pacific. Inclusion of an estimate of surface wind-driven Ekman currents does not improve the correlations [Lagerloef et al., 1999]. Satellite-inferred currents also compare well with drifter data in the western Pacific warm pool ( $r=0.92$ ) [Yu et al., 1995], and off the equator [Lagerloef et al., 1999]

The breakdown of geostrophy has been suggested as a reason for the deficiencies in satellite-inferred currents on the equator in the east [Delcroix et al., 1994; Lagerloef et al., 1999]. The high correlation ( $r=0.78$ , at 0°N-110°W) between satellite-inferred zonal currents and in-situ calculated geostrophic zonal currents is evidence of this [Delcroix et al., 1994]. So too is the observation that no east-west differences exist in the correlation between satellite-inferred and linear-model currents (Shu and Clarke [2000]; and section 5.3).

The errors associated with making the geostrophic assumption on the equator are discussed by Picaut et al. [1989]. They conclude that the neglect of frictional terms leads to underestimated wind-driven surface currents everywhere; that the local acceleration term only becomes important on time-scales less than 30 days, and that non-linear terms are at most 10% of the strength of the other terms. The

Table 5.1: Comparison between satellite-inferred zonal currents and TAO/TRITON observations Yu and McPhaden [1999b], as presented in the cited work. Statistics are for anomalies about the annual mean, except in Lagerloef et al. [1999] where full currents were estimated. Lagerloef et al. [1999] use 10-day averaged data, the other two work use 5-day averaged data. The last row corresponds to the monthly averaged TOPEX/Poseidon inferred zonal current [Delcroix et al., 2000], as described in section 2.3.

	Correlation coefficient			Standard error ( $\text{ms}^{-1}$ )†		
	165°E	140°W	110°W	165°E	140°W	110°W
<b>Geosat</b>						
Delcroix et al. [1994]	0.92	0.7	0.49	0.17	0.24	0.31
<b>TOPEX/Poseidon</b>						
Lagerloef et al. [1999]	0.72	0.53	0.22	0.25	0.24	0.27
Delcroix et al. [2000]	0.90	0.58	0.45	0.16	0.33	0.38
monthly mean ZCA	0.89	0.71	0.64	0.16	0.20	0.30

† standard errors are given as the standard root-mean-square difference, except for Lagerloef et al. [1999] data where they correspond to standard deviations of the difference.

latter is based on scale analysis. Results presented in this chapter indicate this assumption is not accurate for surface zonal flow in the east. Non-linear terms are important in the surface zonal momentum balance in the east.

### 5.1.2 Simulation of zonal currents

There are large differences in the ability of models to simulate surface zonal current variability on the equator (Table 5.2). The simulations of different models in the literature are not all comparable, because they are forced with different wind products, and simulation of zonal currents are sensitivity to wind forcing (section 5.4; Delcroix et al. [2000]). However, it is clear that linear-model currents become progressively less realistic toward the east, both in terms of correlation and amplitude. Also ocean general circulation models (OGCMs) and linear-models with more than a single baroclinic mode are comparable in the western Pacific, while in the east, the OGCM currents are more realistic, both in terms of correlation and amplitude.

Table 5.2: Comparison between modelled and observed (TAO/TRITON array [Yu and McPhaden, 1999b]) zonal currents on the equator, for several models of varying complexity. Dashes represents correlations that were not significant [Picaut et al., 2001]. Linear-1, Linear-3, and Linear-10 are baroclinic mode models of 1,3, and 10 modes, respectively; Linear-1 and Linear-10 include a surface frictional layer. GC [Gent and Cane, 1989] and OPA [Delecluse et al., 1993] are OGCMs. Linear-1, Linear-10, and GC are forced with FSU winds; Linear-3 is forced with satellite (ERS) winds; and OPA is forced with winds from a forced AGCM. (Statistics are from Delcroix et al. [2000], and Picaut et al. [2001])

	Corr. coef.			$\sigma_{\text{Model}}/\sigma_{\text{TAO}}$		
	165°E	140°W	110°W	165°E	140°W	110°W
linear-1	0.34	-	-	0.9	-	-
linear-3	0.59	0.25	0.4	1.2	0.9	0.65
linear-10	0.48	0.3	-	1.19	1.41	-
GC	0.6	0.41	0.47	1.16	1.15	1.09
OPA	0.39	0.35	0.54	1.13	1.19	1.15
	Rms difference ( $\text{ms}^{-1}$ )					
linear-3	0.38	0.46	0.4			

This last point is consistent with non-linear terms becoming significant in the east. The importance of non-linear terms on the equator in the east has been suggested by several authors (e.g., Shu and Clarke [2000]; Picaut et al. [2001]).

It is also apparent that the simulation of zonal currents by a linear model with three baroclinic modes is better than one with a single baroclinic mode. However, a model with ten baroclinic modes and a surface frictional Ekman layer is not better than a three baroclinic-mode model without a surface frictional Ekman layer. This is consistent with results presented later, and by Shu and Clarke [2000]. In fact, addition of high order modes results in unrealistically strong variability in the east. This behaviour is discussed in section 5.3.

The Shu and Clarke [2000] model warrants separate discussion. It is similar to the model developed in chapter 3, but it does not include a surface frictional layer

or use spatially-varying baroclinic modes. Also, currents are multiplied by a linear regression coefficient to account for neglected non-linearity, and to maintain realistic current magnitudes. Correlations between model (forced with FSU winds) and observed (TAO/TRITON) zonal current anomalies on the equator at 165°E, 170°W, 140°W, and 110°W are 0.8, 0.62, 0.6, and 0.36, respectively. The corresponding rms errors are 0.14, 0.18, 0.14, and 0.12  $\text{ms}^{-1}$ . The correlations and rms errors are good, but have been improved by smoothing the data with a double 5-month running mean filter.

In summary, on the equator in the western Pacific, both modelled and geostrophic derived currents match observed in-situ currents. Toward the east, linear model and geostrophic derived currents become less realistic. Both become poorly correlated to observations. Also, the magnitude of linear-model current variability is not realistic. The differences between OGCMs simulations in the east and in the west is less significant, implying non-linear terms become important in the eastern Pacific. The strong correlation between satellite-inferred currents and geostrophic currents calculated from in-situ data is also evidence of this assertion.

## 5.2 Modelled interannual zonal currents

Interannual variability of modelled zonal currents is now compared with TAO/TRITON in-situ data [Yu and McPhaden, 1999b] and TOPEX/Poseidon inferred currents [Delcroix et al., 2000]. Modelled zonal currents described here are generated using FSU research quality winds [Stricherz et al., 1995]. Wind stress was calculated using a drag coefficient of  $1.3 \times 10^{-3}$ , and air density of  $1.2 \text{ kgm}^{-3}$ . The wind data were provided by COAPS at FSU, from their website (<http://www.coaps.fsu.edu/WOCE/SAC/>). The wind stress was smoothed with a 1-2-1 space and time filter to reduce the amount of high frequency variability. It is not uncommon to smooth wind stress in studies of interannual variability (e.g., Kleeman [1993]). Sensitivity of model results to wind stress are described in section 5.4.

The discussion is on anomalies about the annual cycle, but statistics for the full

model currents are included in the tables to allow comparison with satellite-inferred currents and currents from other models (section 5.1). However, direct comparison should only be made with models forced with FSU winds (linear-1, linear-10, and GC; in table 5.2), since results are highly sensitive to wind forcing (section 5.4).

The full zonal current fields are generated using the full model (chapter 3), while modelled zonal current anomalies are generated using the anomaly version of the model (section 4.4). The monthly mean current climatology for the anomaly model was generated by forcing the full model for ten years with FSU monthly climatological wind stress [Stricherz et al., 1995]. Anomalies from the anomaly model were identical to anomalies calculated directly from the full model.

There can be problems in comparing anomalies calculated over different periods when the data lengths are short. In view of other uncertainties (e.g., in the wind forcing), this does not seem an important consideration and anomalies are calculated from the entire period of each data set.

#### a. General description

Modelled zonal current anomalies about the annual cycle on the equator at 165°E and 110°W are shown in figure 5.1. This figure can be compared with the TAO/TRITON observations presented in figures 2.12 and 2.14. The model's full currents are not shown, since the annual mean and annual cycle of modelled zonal currents were described in previous chapters, and because the visual comparison to observations is hampered by missing data. The only important thing not well illustrated by figure 5.1, is that because of the two-layer treatment of non-linearity, the model's undercurrent does not surface as in the observations. Modelled zonal current variability at 140°W is similar in character to that at 110°W, and not shown here.

Modelled interannual zonal current variability broadly agrees with observations and theory (section 2.3.4). During strong El Niño events the equatorial undercurrent (EUC) disappears; this occurs at 110°W in 1983 and is beginning to occur 1997-98 (figure 5.1b). In both cases, prior to the disappearance of the EUC in the east,

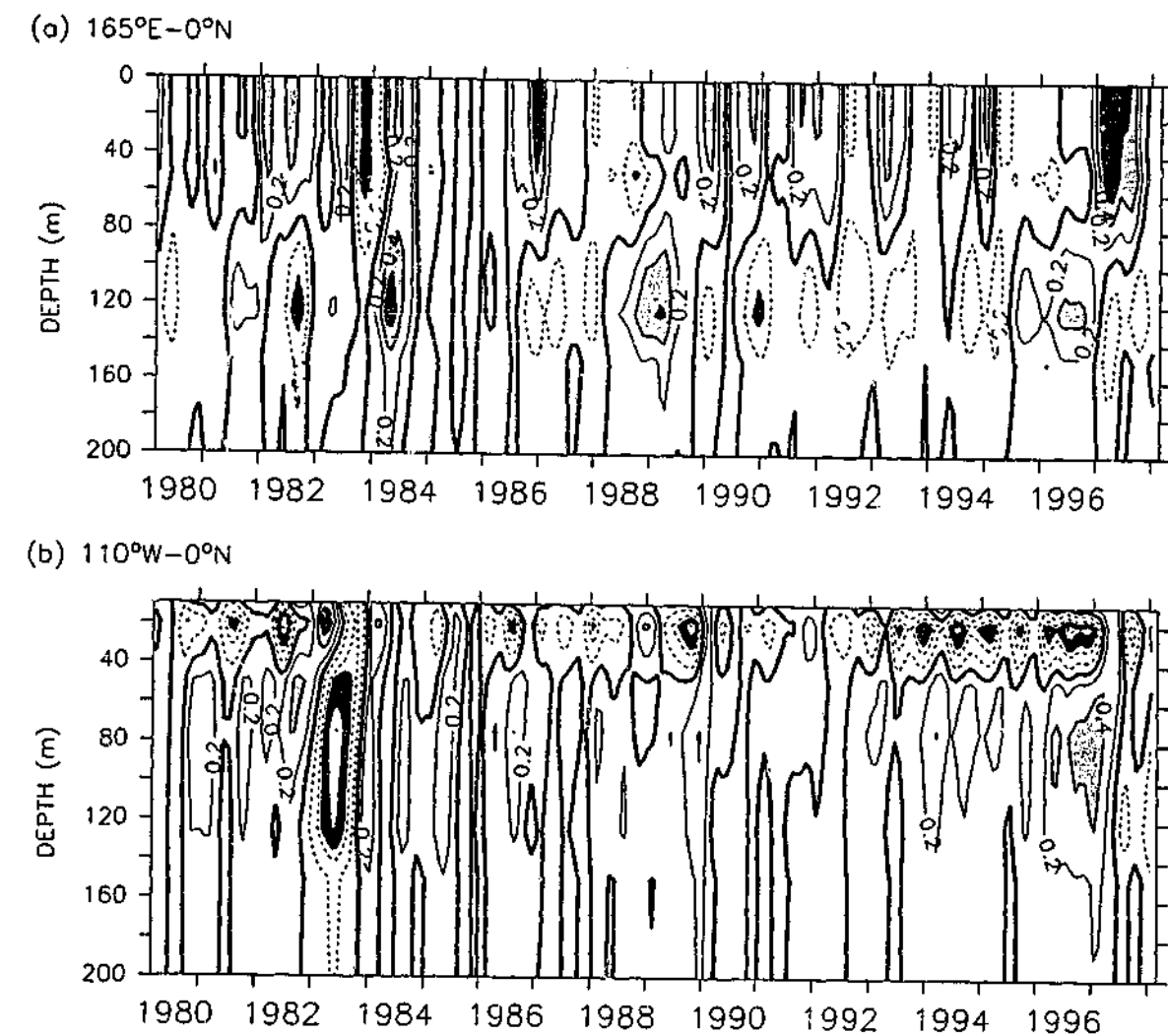


Figure 5.1: Modelled zonal current anomalies on the equator at (a) 165°E, and (b) 110°W. The units are  $\text{ms}^{-1}$ . The contour interval is  $0.2 \text{ ms}^{-1}$ , with a thick solid line for the zero contour, and dashed contours for negative values. These plots can be compared with TAO/TRITON observations [Yu and McPhaden, 1999b] in figures 2.12b and 2.14b. (Modelled currents are generated using FSU wind stress [Stricherz et al., 1995].)

surface currents in the west surge eastward (figure 5.1a). During the weaker El Niño events (1987, 1991-92, 1993, and 1994-95) this relationship is less apparent. In fact correlations between modelled zonal current variations in the undercurrent at 110°W and at the surface at 165°E are weak ( $r=0.06$ ). During the 1988-89 La Niña event, positive anomalies are observed in the undercurrent at 110°W (figure 5.1b); the situation is similar for the 1998-99 event (not shown). However, these positive anomalies are not stronger than those at other times; but this is not inconsistent with observations (section 2.3.4).

Modelled surface zonal current anomalies are shown in figure 5.2, for the same

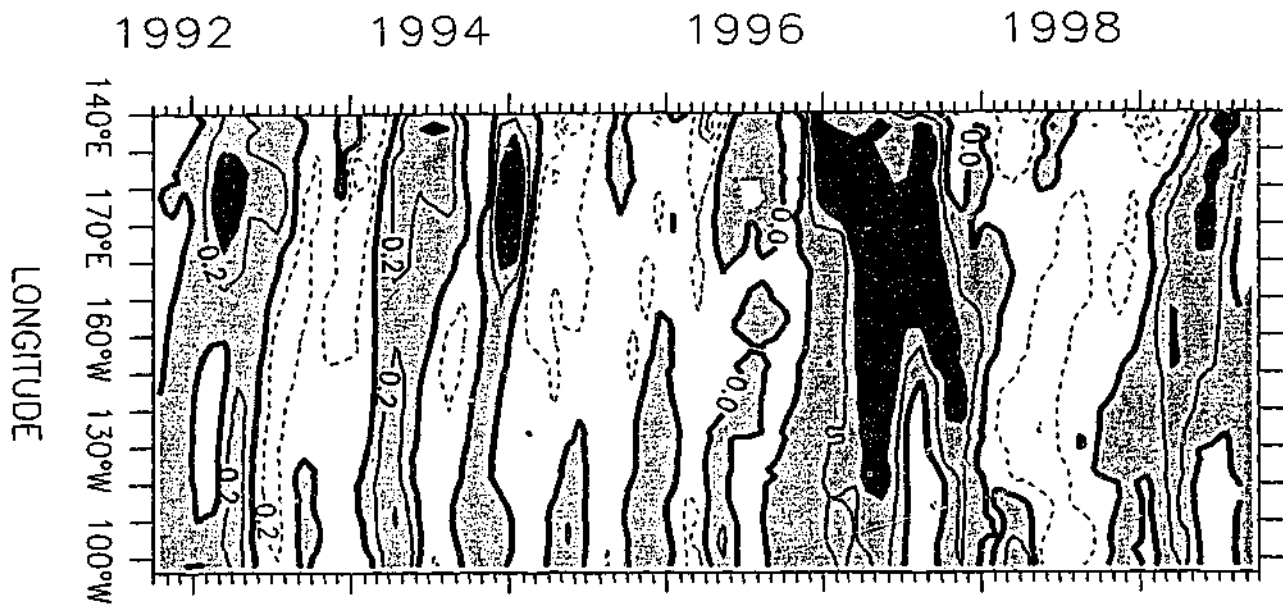


Figure 5.2: Modelled zonal current anomalies on the equator. The units are  $\text{ms}^{-1}$ , the contour interval is  $0.2 \text{ ms}^{-1}$ , and positive anomalies are shaded. This plot can be directly compared with the TOPEX/Poseidon [Delcroix et al., 2000] derived currents in figure 2.15. (Modelled currents are generated using FSU wind stress [Stricherz et al., 1995].)

period as the TOPEX/Poseidon derived currents (figure 2.15). There is remarkable agreement between the TOPEX/Poseidon and modelled currents (see correlation analysis in section 5.3). Periods of eastward and westward flow compare well, both in terms of phase and magnitude. The structure of the 1997-98 El Niño event is highly realistic, including the double peaked response in the east, and the eastward surge in the western Pacific early in 1997. The latter has important consequences for modelling SST in the early stages of this event (chapter 6).

A difference between model and TOPEX/Poseidon zonal current variability, is that in the model the variability does not extend as strongly into the east. Correlation between TOPEX/Poseidon-inferred and model zonal currents also weaken toward the east (section 5.3). This behaviour is due to non-linear terms in the model. It is argued that these terms are important in reality, and explain the less accurate satellite-inferred currents in the east (section 5.3).

Table 5.3: Comparison between modelled and observed surface zonal currents on the equator at 165°E, 140°W, and 110°W. Anomalies are with respect to the annual cycle. The observations are constructed from TAO/TRITON surface data [Yu and McPhaden, 1999b], as described in section 2.3.1. The 95% critical correlation coefficient was calculated following Davis [1976], but using the larger integral time scale of the two time series.

	165°E	140°W	110°W
<b>Zonal current</b>			
correlation coefficient	0.63	0.23	0.11
$\sigma_{\text{Model}}/\sigma_{\text{TAO}}$	0.86	0.86	0.82
rms difference ( $\text{ms}^{-1}$ )	0.3	0.33	0.41
95% critical cor. coeff.	0.38	0.27	0.23
<b>Zonal current anomalies</b>			
correlation coefficient	0.56	0.16	0.28
$\sigma_{\text{Model}}/\sigma_{\text{TAO}}$	0.81	0.8	0.71
rms difference	0.27	0.24	0.25
95% critical cor. coeff.	0.42	0.27	0.23

### Quantitative comparison

The qualitative agreement between model and observations, described above, is examined further by comparing modelled surface-layer and subsurface currents against time series constructed from TAO/TRITON observations [Yu and McPhaden, 1999b] on the equator at 165°E, 140°W, and 110°W (section 2.3.1). Table 5.3 and table 5.4 give statistical details of the comparison between modelled and observed surface-layer and subsurface zonal currents. The comparison against TOPEX/Poseidon surface currents [Delcroix et al., 2000] is described later.

At 165°E, modelled zonal currents compare well with the observations, having realistic magnitude and phase (figure 5.3a). At 110°W, although there are periods when modelled and observed currents are in phase, there are significant periods when they are out of phase (figure 5.3b). The magnitude of the variability is comparable to the observations. The east-west differences are reflected in the correlation coefficients

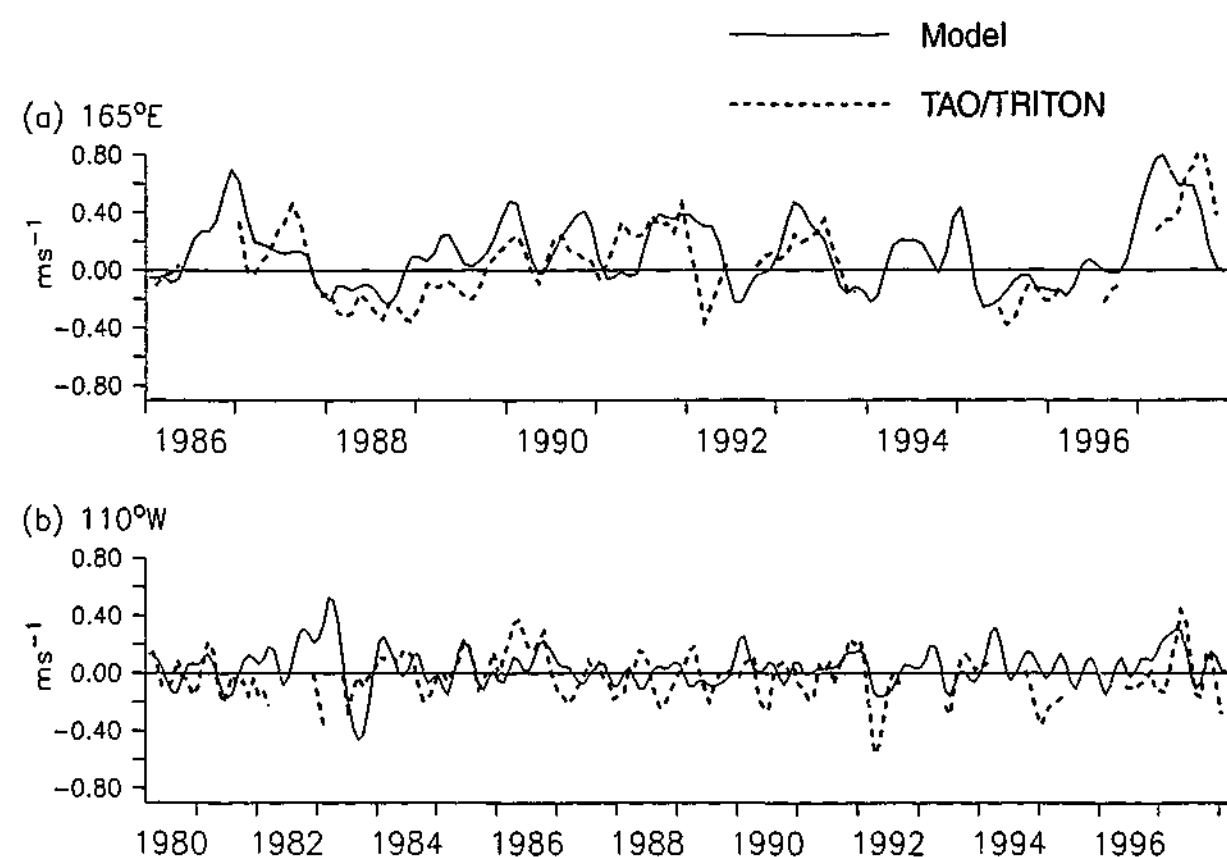


Figure 5.3: Modelled and observed surface zonal current anomalies at (a) 165°E, and (b) 110°W. A 3-month running mean filter has been applied to the time series. (Observations are constructed from TAO/TRITON array [Yu and McPhaden, 1999b], as described in section 2.3.1. Model currents are generated using FSU wind stress [Stricherz et al., 1995].)

listed in table 5.3. The weak correlations at 140°W are likely due to inaccuracies in the wind field; with NCEP stress the correlation is 0.4 (section 5.3).

The model compares well with the models forced with FSU winds listed in table 5.2 (linear-1, linear-10, and GC). Correlations with linear-3 currents appear significantly better, however, this model is forced with satellite surface winds (since the simulation was improved over the simulation with FSU forcing [Delcroix et al., 2000]). The magnitude of modelled currents are weaker than the OGCMs, but compare similarly well to the observations, and are better than the linear models forced with FSU winds. The correlation between modelled and observed zonal currents is as good as the best OGCM results in the west (table 5.2). In the east, like other models, the correlations decrease. The rms difference between modelled and observed current variability, while large, are better than the three-mode linear model

listed in table 5.2 (rms differences for the other models are not presented in the literature). The rms differences are also comparable to the rms differences between satellite and in-situ measurements (table 5.1).

The non-linear component of the model is responsible for limiting the magnitude of linear-model current variability, and reducing the large linear rms errors. The contributions of linear and non-linear components are described in see section 5.3.

The correlation and rms errors are significantly poorer than those of Shu and Clarke [2000] (described above). This is due to smoothing, as when the time series are smoothed with a 5-month running mean filter (similar to Shu and Clarke [2000]), the correlation coefficients are similar. The correlation coefficients between modelled and observed zonal current anomalies after smoothing on the equator at 165°E, 140°W, and 110°W are 0.72, 0.15, and 0.34, respectively. The corresponding rms errors are 0.18, 0.15, and 0.13  $\text{ms}^{-1}$ . The ratio of standard deviations also improve and are close to 1 at all three locations.

Subsurface model current variability at both 165°E and 110°W is of similar magnitude to the observations (figure 5.4). However, the phase of the anomalies, particularly in the east, does not match the observations well, even during the stronger El Niño events. Correlation coefficients between modelled and observed currents reflect these discrepancies (table 5.4). The weak correlations in the east and the large variability at 140°W may in part be due to inaccuracies of wind stress, and to over-simplified non-linearity (section 5.4).

In summary, surface zonal currents on the equator in the western Pacific (165°E) are well simulated. In the east, modelled and observed currents are weakly correlated. The magnitude of zonal current variability remains realistic across the Pacific. As was mentioned, and will be described next, the simple model shows that non-linear terms are important in the east.

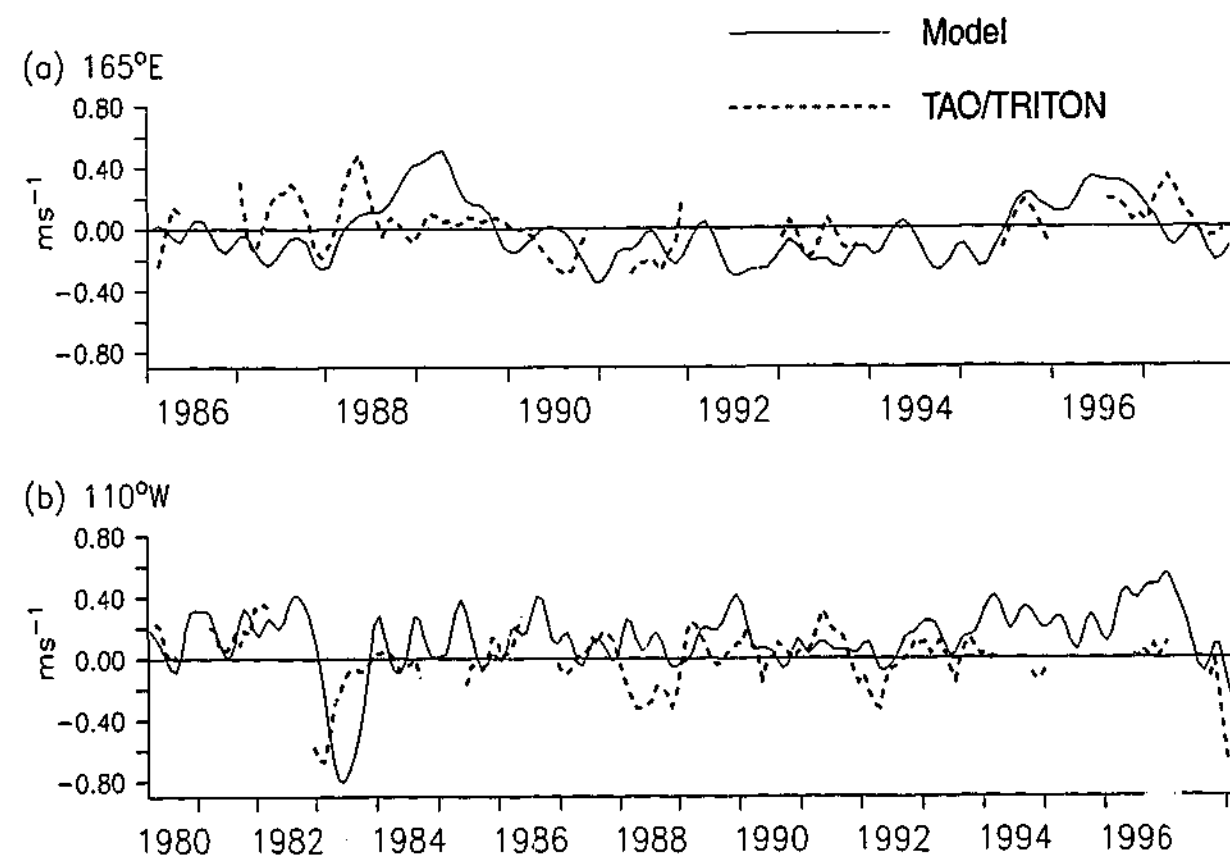


Figure 5.4: Modelled and observed subsurface interannual zonal current anomalies at (a) 165°E, and (b) 110°W. A 3-month running mean filter has been applied to the time series. (Observations are constructed from TAO/TRITON array [Yu and McPhaden, 1999b], as described in section 2.3.1. Model currents are generated using FSU wind stress [Stricherz et al., 1995].)

### 5.3 Analysis

The model's simulation of interannual zonal current variability is now analysed to investigate the underlying dynamics, and in particular, to determine the mechanisms limiting the magnitude of zonal current variability. The roles of baroclinic modes, and non-linearity are first discussed. Important non-linear terms are then described. Finally, the breakdown of linear and geostrophic assumptions in the east is investigated as the reason for the less accurate satellite-inferred and modelled currents there.

Table 5.4: Comparison between modelled and observed subsurface zonal currents on the equator at 165°E, 140°W, and 110°W. Anomalies are with respect to the annual cycle. The observations are constructed from TAO/TRITON surface data [Yu and McPhaden, 1999b], as described in section 2.3.1. The 95% critical correlation coefficient was calculated following Davis [1976], but using the larger integral time scale of the two time series.

	165°E	140°W	110°W
<b>Zonal current</b>			
correlation coefficient	0.4	0.2	0.13
$\sigma_{\text{Model}}/\sigma_{\text{TAO}}$	0.93	1.5	0.96
rms difference ( $m s^{-1}$ )	0.3	0.27	0.34
critical cor. coeff.	0.4	0.42	0.33
<b>Zonal current anomalies</b>			
correlation coefficient	0.18	0.43	0.29
$\sigma_{\text{Model}}/\sigma_{\text{TAO}}$	0.83	1.45	1
rms difference	0.28	0.22	0.3
critical cor. coeff.	0.55	0.42	0.36

#### 5.3.1 Baroclinic mode and non-linear contributions

Figure 5.5 shows the progressive effect, on the simulation of zonal currents on the equator, of increasing the number of baroclinic modes in the model, and then adding non-linearity. For surface currents, a linear model with two baroclinic modes simulates zonal currents most realistically. In the east, further addition of baroclinic modes results in unrealistically strong zonal current variability and large rms errors: At 110°W-0°N, variability in a model with 10-baroclinic modes is approximately twice as strong as the observed variability. For subsurface currents, the best correlations result from a model with 6 baroclinic modes. Unlike surface currents, the magnitude of subsurface zonal current variability is in general underestimated (except at 140°W). The model's two-surface layers, representing modes 11 to 30, only make a small contribution to zonal current variability.

The addition of non-linearity to the model reduces the unrealistically strong

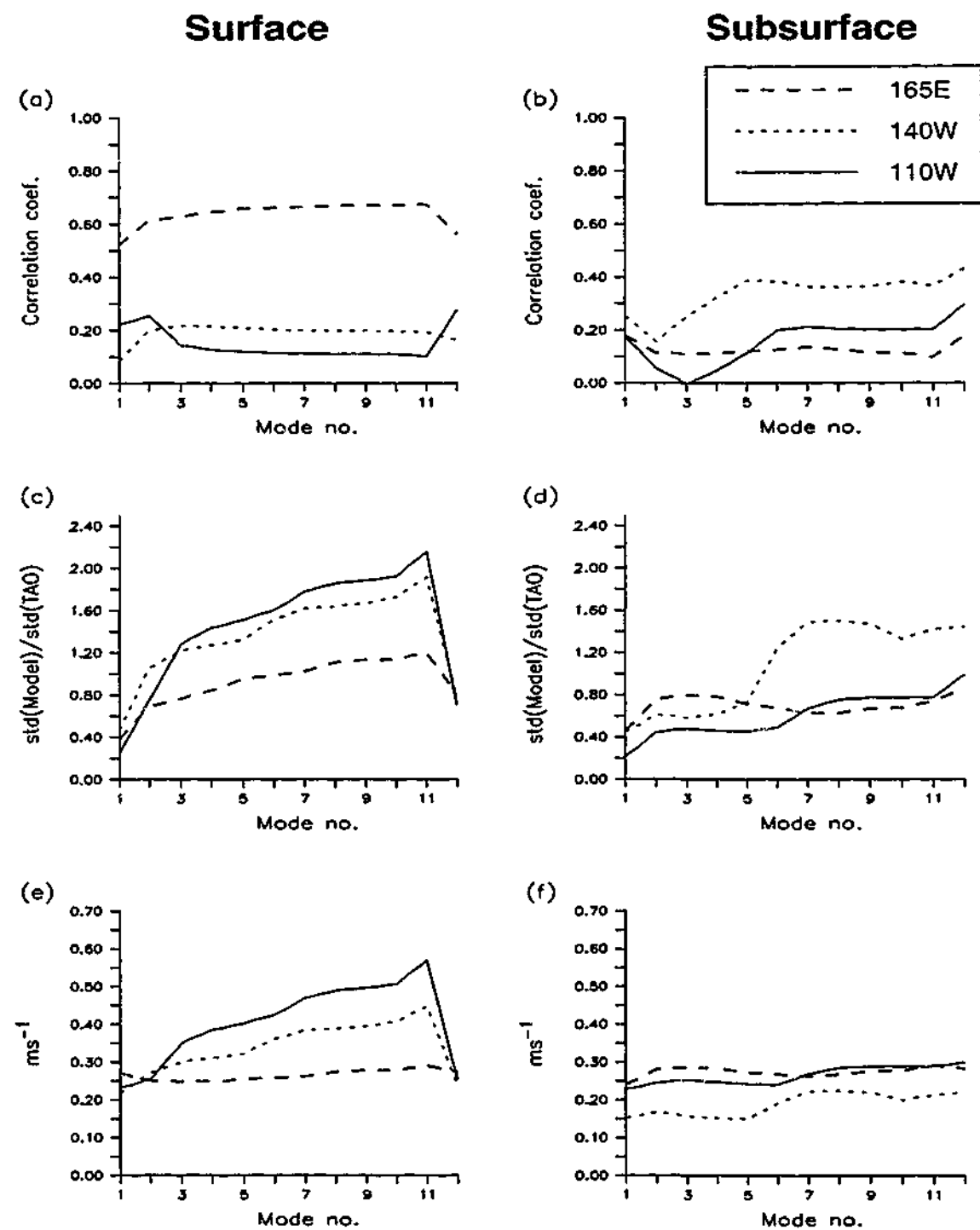


Figure 5.5: Comparison among models of increasing complexity in their ability to simulate surface (left panels) and subsurface (right panels) zonal current anomalies, on the equator at 165°E (long-dashed), 140°W (short-dashed), and 110°W (solid); correlation coefficient (upper panels), ratio of standard deviation (modelled to observed, middle panels), and rms differences (lower panels). The different models are indicated on the mode no. axis; tics 1–10 correspond to baroclinic mode models with 1–10 modes; tic 11 corresponds to the linear component of the model (10 baroclinic modes plus two surface frictional layers); and tic 12 is the full model (linear plus non-linear). (Observations are from the TAO/TRITON array [Yu and McPhaden, 1999b]; model currents are generated using FSU wind [Stricherz et al., 1995].)

surface zonal current variability and the large rms errors in the east (figure 5.5c and e); the correlation coefficients also improve. In the west and at lower layers the non-linear contribution is weak. The poor behaviour at 140°W is improved when NCEP stress are used to force the model (section 5.3). Unlike in figure 5.5c, in this simulation the addition of non-linearity improves the correlation.

The unrealistically strong variability of a ten baroclinic-mode model is likely due to the breakdown of linear dynamics. Firstly, the linear model simulates zonal current variability in the west well, which implies the modal formulation of the linear model is not at fault. Secondly, the addition of non-linearity significantly improves the magnitude of modelled zonal current variability. The addition of non-linearity does not significantly improve the correlation of model currents with observations, however, this is possibly due to the over-simplified formulation of non-linearity (section 5.4).

The model also does not simulate subsurface zonal current variability well. Two possible reasons for this are inaccuracies in wind stress, and an over-simplified treatment of non-linearity. Sensitivity studies support these ideas (section 5.4). Also, observations which show that the EUC undergoes large vertical movements (section 2.3.4), which indicates non-linearity is important.

### 5.3.2 Non-linear terms

The model's non-linear correction on the equator is now analysed in order to determine the role of non-linearity in limiting the magnitude surface zonal current variability in the east. This is further illustrated in figure 5.6, for 110°W–0°N. The unrealistically strong variability of the linear component drives interannual variability. The non-linear component behaves reactively. It is similar in strength, and opposes the linear component to produce variability of realistic magnitude. The behaviour at 140°W–0°N, and 165°E–0°N are similar. In the west though, non-linear contribution can at times be negligible.

The role of the individual non-linear terms in the surface-layer zonal momentum

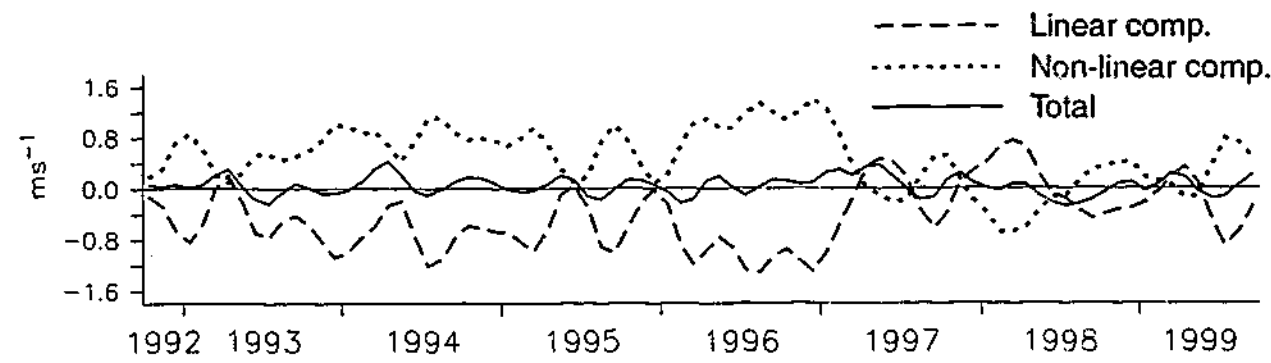


Figure 5.6: Modelled surface zonal current anomalies at 110°W-0°N (solid), with contributions from the linear (dashed) and non-linear (dotted) components shown. (Currents are generated using FSU wind stress [Stricherz et al., 1995].)

balance were checked at 165°E, 140°W, and 110°W on the equator. In figure 5.7 the non-linear tendency terms in the surface layer at 0°N-110°W are plotted. It is illustrative of the other two locations. Local acceleration is relatively weak, and close to zero most of the time. The non-linear zonal momentum balance is determined by advective terms of the equatorial cell, and horizontal and vertical diffusion. The sum of these terms, which individually are relatively large, determine the local acceleration, and hence variations in non-linear zonal velocity. Zonal advection of zonal momentum is weak in the east, and only slightly more important in the west.

Vertical advection is the driving non-linearity. This can be seen by comparing the vertical advective term with non-linear velocity (figure 5.7a and b). The meridional advective term is almost always 180° out of phase, and slightly lagging, the vertical advective term. The diffusive terms are, as expected, completely reactive, but they are highly significant.

As in the investigation of the annual cycle, the advective terms were decomposed into mean and anomaly contributions (section 4.3). However, the analysis does not aid interpretation of the dynamics, because, unlike in the annual cycle, both mean advection of anomaly terms, and anomaly advection of mean terms are important.

The action of non-linearity is similar to that in the annual mean (section 3.4.4). In the annual mean, the non-linear component's redistribution of zonal momentum

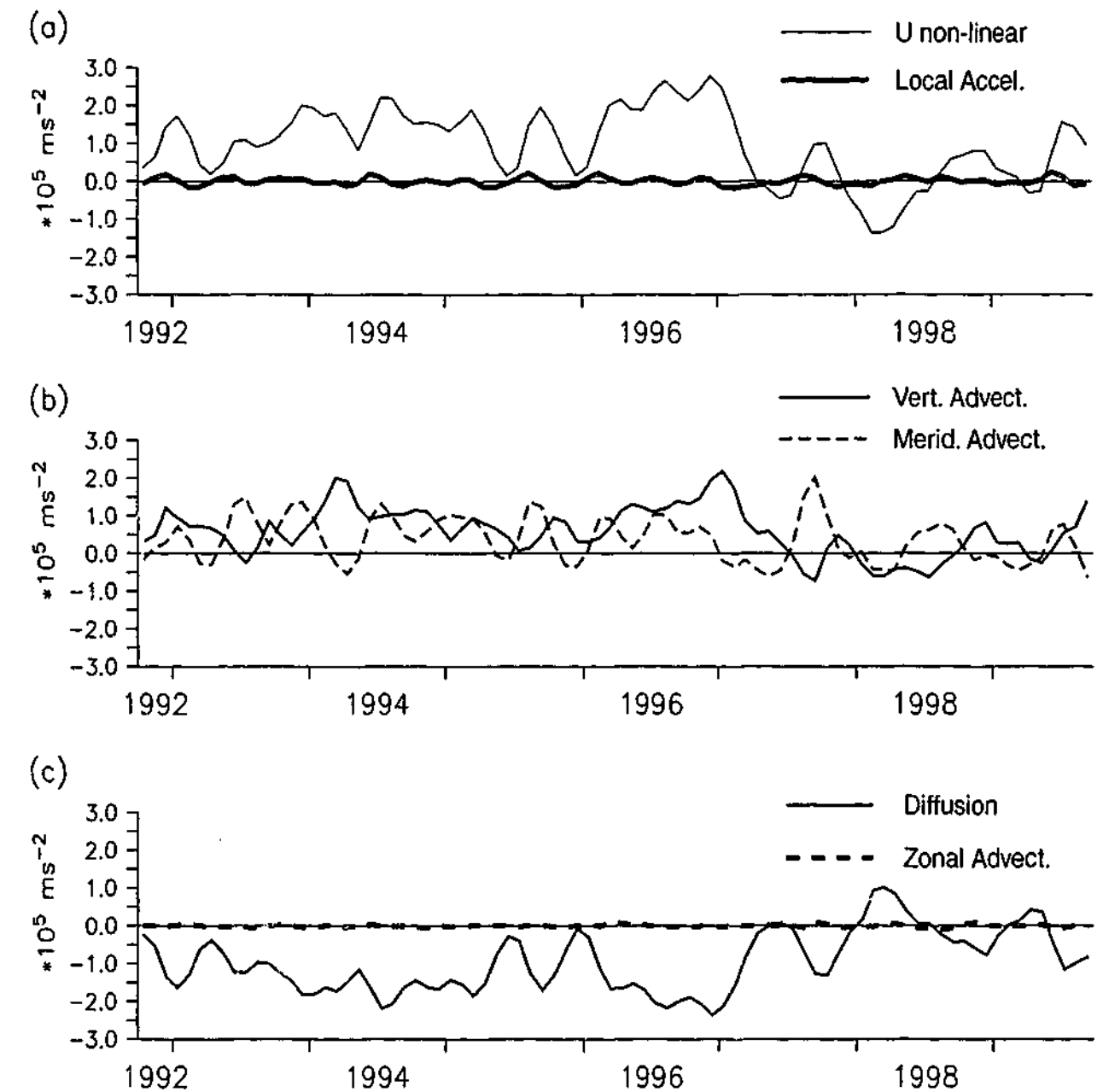


Figure 5.7: Non-linear tendency terms in the surface-layer zonal momentum balance at 110°W-0°N. (a) local acceleration (thick) and non-linear component zonal current anomaly (thin, and in units of  $\times 2\text{ms}^{-1}$ ). (b) vertical advection of zonal momentum (solid), and meridional advection of zonal momentum (dashed). (c) sum of vertical and horizontal diffusion of zonal momentum (solid), and zonal advection of zonal momentum (dashed). Tendencies are for zonal current anomalies generated with FSU wind [Stricherz et al., 1995]. (see section 4.3 for a full description of terms)

produces a south equatorial current (SEC) of realistic strength. Interannually, this balance adjusts to changes in the linear solution to maintain a SEC of realistic strength. This adjustment means the reaction of the currents in the east to changes in surface wind stress is not straight forward. In particular, the strong ENSO related variability in currents predicted by linear dynamics, evident at  $165^{\circ}\text{E}-0^{\circ}\text{N}$ , is not present in the east.

The simple model shows that non-linear terms in the surface zonal momentum balance associated with the meridional circulation are important in the east on the equator.

### 5.3.3 Geostrophic currents

Although geostrophic derived current are accurate in the western Pacific, they are not accurate in the east (see discussion in section 5.1). Several reasons have been suggested for this, but none have been accepted. In light of the findings above, the breakdown of the geostrophic assumption, due non-linear terms, is the likely explanation. In this section, it is illustrated that non-linear terms can indeed explain the less accurate geostrophic currents in the east.

Figure 5.8 compares TOPEX/Poseidon inferred currents [Delcroix et al., 2000] with TAO/TRITON in situ measurement [Yu and McPhaden, 1999b]. It illustrates the large discrepancies that occur in the east, between geostrophic calculated currents and in-situ data. Although the two data sets match each other relatively well, there are periods when they are out of phase, and large differences exist. For example, in the second half of 1997, TAO/TRITON currents indicate a period of strong negative anomalies. The TOPEX/Poseidon anomalies dip only weakly, and remain positive.

In figure 5.9, TOPEX/Poseidon derived currents [Delcroix et al., 2000] are compared with zonal currents from three models. The first model corresponds to geostrophic currents from the ICM (model-geostrophic); it only contains the meridional pressure gradient and Coriolis term. The second model is the linear component

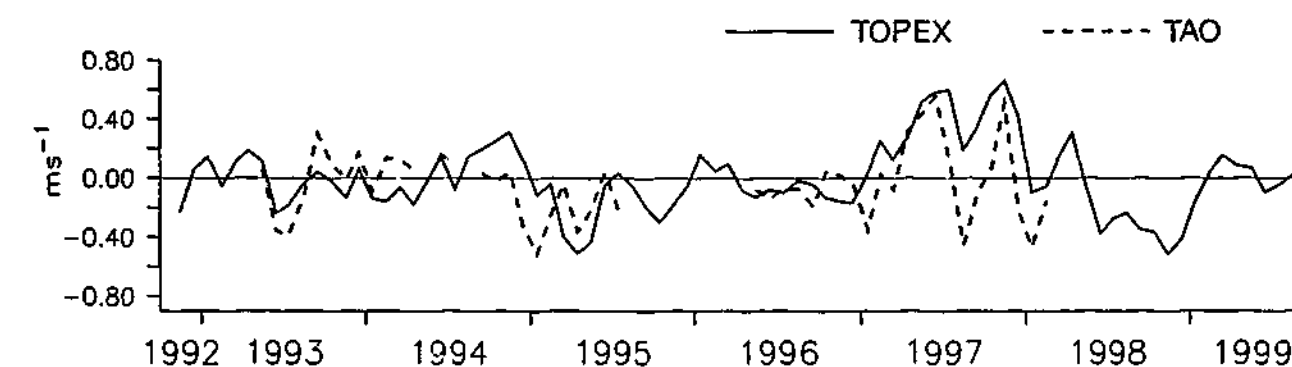


Figure 5.8: TOPEX/Poseidon derived [Delcroix et al., 2000] (solid), and TAO/TRITON [Yu and McPhaden, 1999b] in-situ (dashed) surface zonal current anomalies at  $110^{\circ}\text{W}-0^{\circ}\text{N}$ .

of the ICM (linear); in addition to the geostrophic terms, it contains local acceleration and diffusive terms. The third model is the ICM (non-linear); in addition to the linear model, it contains non-linear terms.

The model-geostrophic current were calculated from the ICM's surface pressure field, using the meridional derivative form of the geostrophic balance. The model pressure field was first smoothed, meridionally and zonally, to closely match the smoothing of TOPEX/Poseidon sea-level data [Delcroix et al., 2000].

In the central and western Pacific, the correlation between model and TOPEX/Poseidon data are similar for all the models (figure 5.9a). In the east the situation is quite different. The model-geostrophic currents remain highly correlated to the TOPEX/Poseidon data. Addition of diffusion and local acceleration weakens the correlation in the east, but the correlation still remain significant. On addition of non-linearity, the correlation in the east drop even more. Thus, the decrease in correlation between geostrophic-inferred and in-situ currents on the equator toward the east is consistent with the increasing importance of non-linear terms.

Figure 5.9b illustrates, again, how linear current variability is about twice as strong as the observations, and that the non-linear terms limit this variability to realistic magnitudes. The amplitude of model-geostrophic currents compares well to the TOPEX/Poseidon currents. However, this is due to the latitude smoothing of surface pressure. The amplitude of geostrophic current variations calculated from

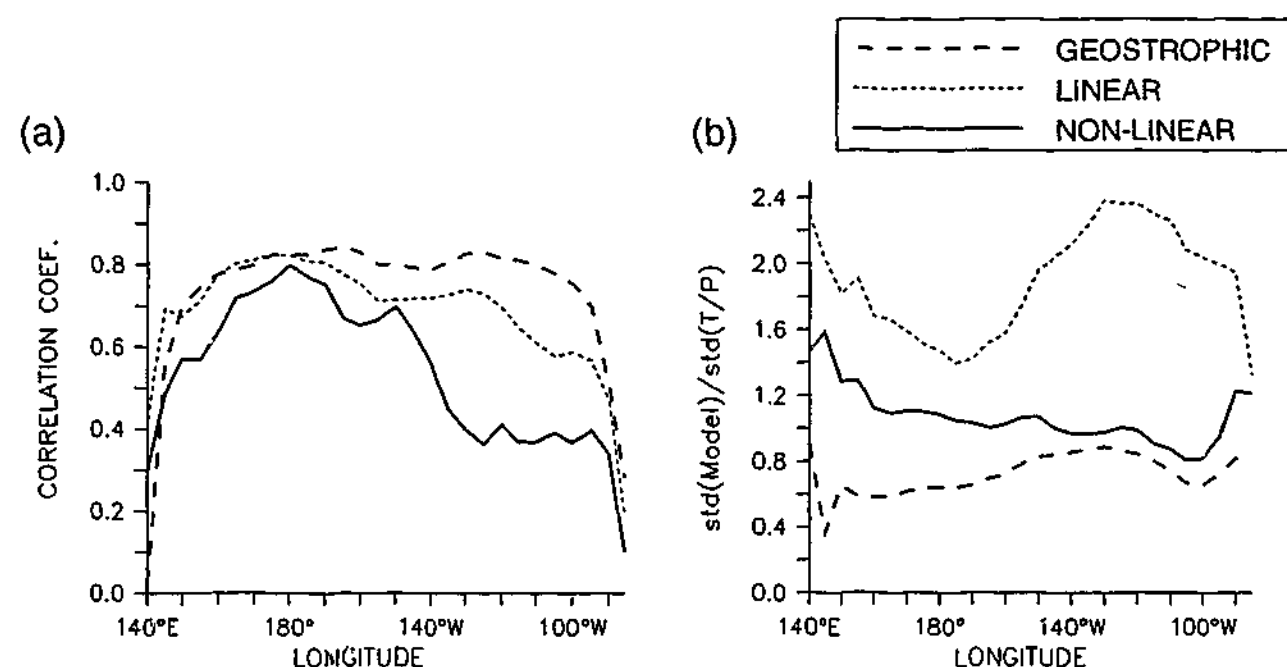


Figure 5.9: (a) Linear correlation between TOPEX/Poseidon inferred zonal current anomalies [Delcroix et al., 2000] and three models on the equator; anomalies are with respect to the annual mean. The non-linear model (solid) is the full model forced with FSU wind stress [Stricherz et al., 1995]; the linear model (dotted) is the linear component of the full model; the geostrophic model (dashed) corresponds to currents calculated from the full models surface pressure. (b) same as (a), except showing the ratio of standard deviations of modelled to TOPEX/Poseidon derived current variability.

unsmoothed pressure field are similar to that of linear currents. This shows that with latitude smoothing, geostrophic currents have similar magnitude to observations, even when non-linear terms are important.

The ability of the model to simulate surface pressure variability, and hence surface geostrophic currents, is not surprising. Surface pressure variations are controlled by low order baroclinic modes [Cane, 1984]. The result also suggest the reason why a two baroclinic mode model best represents the TOPEX/Poseidon data [Shu and Clarke, 2000], and why addition of high order modes does not improve the model simulation in the east: High order modes do not contribute significantly to the geostrophic balance, nor do they explain non-linear contributions.

## 5.4 Sensitivity studies

A number of sensitivity experiments were performed. These included forcing the model with NCEP re-analysis surface stress [Kalnay et al., 1996]; using a different background climatological circulation; varying the vertical diffusion parameter, shallow water speeds, and mixed-layer depth; and altering the frequency of forcing of the linear and non-linear components. The important results are that the non-linear mechanism controlling the magnitude of linear variability was robust. The model's sensitivity to wind stress makes it hard to determine model errors in the east, and to accurately model zonal current variability there. Poor model performance in the eastern Pacific relative to OGCMs is in part due to the model's over-simplified formulation of non-linearity. A summary of these experiments is now presented. In the following discussion, the model results presented above are referred to as the standard model.

### a. Wind stress

The models sensitivity to wind stress was tested by forcing the model with NCEP re-analysis surface stress [Kalnay et al., 1996]. The NCEP re-analysis data were provided by the NOAA-CIRES Climate Diagnostics Center, Boulder, Colorado, USA; from their web site (<http://www.cdc.noaa.gov/>).

Zonal current variability was 30 to 40% weaker, and significantly smoother than that of the standard model. Correlations between model and TAO/TRITON in-situ observations [Yu and McPhaden, 1999b] were significantly improved at the surface at 140°W-0°N ( $r=0.4$ , as opposed to 0.16), and at the lower layer at 110°W-0°N ( $r=0.49$ , as opposed to 0.11). Otherwise correlations remained similar. The non-linear mechanism remained the same; the reduced variability was due to weaker linear-model variability. These results are consistent with other modelling studies that indicate model results are sensitive to wind stress forcing (e.g., Chao et al. [1993]; Delcroix et al. [2000]). They indicate the difficulties involved in accurately simulating zonal current variability in the east, and determining model errors.

### b. Non-linearity

Although non-linearity corrects the unrealistically strong linear variability, and improves linear correlations, the model performs less well than OGCMs in the east. Two sensitivity experiments were performed to test if the poor model performance relative to OGCMs may be due to the crude formulation of non-linearity. In the first, wind stress was linearly interpolated to each time step, and the non-linear model forcing (i.e., the layer average linear fields) was updated each time step. In the standard model both linear and non-linear forcing fields are updated once monthly. In the second experiment, the anomaly model's background circulation was replaced with one generated by Hellerman and Rosenstein [1983] wind stress; otherwise the simulation was identical to the standard model.

A correlation analysis with in-situ TAO/TRITON observations [Yu and McPhaden, 1999b] was performed. In both experiments the representation of non-linearity was improved. In the first experiment, surface currents in the east were more strongly correlated with the observations (at 110°W,  $r=0.38$ ; as opposed to 0.11), but variability was weaker (ratio of model to observed standard deviations was 25% weaker in the east). In the second experiment, the amplitude of the variability was improved in the east (ratio of model to observed standard deviations was 1.); but correlations remained similar. Thus improving the model's depiction of non-linearity, either the formulation of non-linearity or the representation of the mean meridional circulation, can dramatically improve certain aspects of the simulation of zonal currents. This supports the notion that poor model behaviour in the east relative to OGCMs is due to poor depiction of non-linearity.

### c. Parameters

A number of experiments were performed to test model's sensitivity to key parameters, they are as follows. The model was run with decreased ( $A = 5. \times 10^{-8} \text{m}^2 \text{s}^{-3}$ ) and increased ( $A = 2. \times 10^{-8} \text{m}^2 \text{s}^{-3}$ ) vertical diffusion parameter. The model was run with shallow water speeds decreased to match Shu and Clarke [2000] (The shallow

water speeds of the first four modes were 2.74, 1.49, 0.97, and 0.71  $\text{ms}^{-1}$ ). Also, the model was run with a minimum mixed layer depth of 20m, as opposed to 10m in the standard model.

Simulated zonal currents were compared with TAO/TRITON in situ measurements [Yu and McPhaden, 1999b]. Correlations were similar or weaker to those of the standard model. Surface current variability in the east was significantly increased, elsewhere variability remained similar. The increased variability was due to either increased linear variability, or weakened non-linearity (due to weaker meridional circulation). In all cases though, non-linearity always acted to reduce linear current variability. The sensitivity of the magnitude of zonal current variability to parameter choice may explain some of the differences between observed and modelled variability.

## 5.5 Summary and discussion

In the western Pacific on the equator, satellite-inferred, linear-model, and OGCM surface zonal currents match in-situ observations well. Toward the east, satellite-inferred and linear-model currents become less well correlated to in-situ observations. Linear model variability also becomes too strong. These east-west differences are not present in OGCMs to the same extent, suggesting that non-linear terms may be important in the eastern Pacific.

The model developed in chapter 3 is used to investigate the process controlling interannual zonal current variability on the equator. In the western Pacific, the model simulates surface zonal currents well, both in terms of magnitude and correlation (table 5.3). In the east, the magnitude of modelled zonal current variability is similar to the observations (like OGCMs, but unlike linear models), but the correlation to observations are weak. The correlations are weaker than those of OGCMs, and comparable to those of linear models.

Investigation of the roles of baroclinic modes and non-linearity showed that in

the western Pacific, adding more baroclinic modes to the solution improved the simulation, but the improvements became marginal for high order modes. In the eastern Pacific, the behaviour was different. A linear model with two baroclinic modes best represented the surface zonal current variability. Further addition of baroclinic modes caused the solution to become unrealistically strong. Given that linear models realistically simulate zonal current variability in the west, the unrealistic variability of linear model currents in the east is probably due to the breakdown of linear assumptions.

Non-linear terms were found to correct the strength of linear-model surface variability. This was particularly important in the eastern Pacific, where the non-linear component was effective in halving the linear model's variability. The principal non-linear terms in the zonal momentum balance were meridional advection, vertical advection, horizontal diffusion, and vertical diffusion of zonal momentum. Vertical advection was the driving term. The interannual surface zonal current variability behaved as a slowly varying form of the annual mean zonal momentum balance. The non-linearity associated with the meridional circulation controlling the magnitude of the SEC.

On the equator, geostrophic currents calculated from the model's surface pressure field were in excellent agreement with satellite derived currents in both the eastern and western Pacific. Full model currents, which contain non-linear terms, agree less well. Thus, the importance of non-linearity in the east is consistent with satellite-inferred and linear model currents being less realistic there.

Although the model's simulation of zonal current variability improves on that of linear model's, in terms of correlation the model does not perform as well as OGCMs. However, sensitivity studies indicate this inconsistency is due to the simplified treatment of non-linear terms. The mechanism controlling non-linearity was robust to changes in wind forcing and parameter values. Sensitivity studies illustrated how inaccuracies in wind forcing, and uncertainties in parameter values may also contribute significantly to differences between modelled and observed zonal currents.

In summary, the importance of non-linearity in the eastern Pacific on the equator is demonstrated using a simple model. The model, which only includes a first order non-linear correction to the zonal momentum balance, indicates that non-linear terms associated with the meridional circulation can not be neglected in the east. The importance of these terms in the east is illustrated to be entirely consistent with the less realistic satellite-inferred and linear-model currents. It is a likely explanation for these problems, and suggests satellite-inferred currents in the east on the equator will only be accurate when these effects are taken into account.

The breakdown of geostrophy in the east implies the neglect of advective terms in the meridional momentum equation (section 3.2.4) is not completely justified. Following other authors, their neglect was based on scale arguments (see discussion in Picaut et al. [1989]). However, as there are large uncertainties in the magnitude of many of the meridional advective terms (appendix A), these arguments may well be flawed. From a practical perspective, given the Coriolis parameter vanishes on the equator, the neglected advective terms in the meridional momentum equation need not be large to account for large changes in zonal velocity. Thus, the surface meridional circulation, which is primarily in Ekman balance, need not be significantly affected.

It is beyond the scope of this study to investigate the implications of the neglect of non-linear terms on ENSO studies that are based on satellite data or linear models. An important assumption in these studies is non-linear effects do not significantly alter baroclinic mode propagation. The effect of non-linear terms on the propagation of baroclinic modes needs to be better understood, before the implications for ENSO studies can be addressed.

Finally, the results in this chapter show that zonal currents are well modelled in the warm-pool region. Thus the use of the model to investigate the role of zonal currents in controlling SST in the central Pacific is justified. This investigation is described in the next chapter.

## Chapter 6

# Modelling Sea Surface Temperature

The 1993, 1994/95, and 1997-98 El Niño events were poorly forecast by many models [Ji et al., 1996; Barnston et al., 1999], illustrating that large uncertainties still exist in our understanding of this phenomenon. In the earlier events, the weakness of the ENSO mode, which is captured in most models through the delayed oscillator mechanism [Battisti, 1988], seems to be the major reason for model failure [Kleeman and Moore, 1999; Goddard and Graham, 1997; Weisberg and Wang, 1997]. On the other hand, the 1997-98 event may have been significantly influenced by strong westerly wind anomalies at the date line, associated with the Madden-Julian oscillation [Van Oldenborgh, 2000; McPhaden and Yu, 1999]. This certainly limited the models, but even after the event was well underway, many model performed poorly [Barnston et al., 1999].

The role of sea surface temperature (SST) in ENSO is well accepted, and ocean models have been able to simulate many aspects of interannual SST variability [Stockdale et al., 1998]. SST variability in the models is controlled by zonal and meridional advection, and entrainment processes, but the importance of the different processes differs between models [Miller et al., 1993]. Observational studies have not been able to answer these questions, because of the large uncertainties that exist in measurements (e.g., Wang and McPhaden [2000]). The role of vertical advection in controlling SST, particularly in the eastern Pacific, is generally accepted [Kleeman,

1993; Shu and Clarke, 2000]. So too is the role of zonal currents in the central Pacific. Although the latter was recognised by Gill [1983], its significance to ENSO is only recently becoming recognised [Picaut and Delcroix, 1995; Delcroix et al., 2000; Picaut et al., 2001].

Clearly, there remain large uncertainties in both our understanding of ENSO, and of the mechanisms that control SST variations. In this chapter, the role of zonal currents in controlling SST is investigated with an ICM anomaly model. The model consists of the dynamical ocean model developed in chapter 3 and a SST component, which is developed here. The latter is similar to the SST component of other ICMs. The only significant difference is its parameterization of subsurface temperature, which is obtained from an inversion of the annual mean SST balance. The model, although simple, simulates currents and SST anomalies as well as the more complex ocean general circulation models (OGCMs).

The work here is most similar to Shu and Clarke [2000], in that they also develop a multi-baroclinic mode SST model. The simulation of SST in their model in the central and eastern Pacific is good, but their treatment of the SST component in comparison to the one here is highly simplified.

It is not the purpose of this chapter to analyse the full SST budget. Many such analyses have been performed (see e.g., Wang and McPhaden [2000]). Instead, the focus is on the direct contribution of zonal currents to SST anomalies (SSTa), and only in the western and central Pacific, during the 1990s. This is the region where zonal currents contribute the most to interannual variability [Wang and McPhaden, 2000], and where the atmosphere is most sensitive to SSTa [Fu et al., 1986]). The period was chosen, both because it was characterised by poor ENSO forecasts, and because accurate current data are available for model evaluation. The interesting results are that the improved zonal current simulation results in accurate modelling of SSTa in 1997. However, the 1993 and 1994/95 events were poorly simulated, indicating some other mechanism or mechanisms were active at this time.

The structure of this chapter is as follows. The SST component is first formulated.

The model's simulation is described in section 6.2, followed by a discussion of model sensitivities. In section 6.4, the mechanisms controlling SST variability in the model are described. This is followed by a discussion of the role of zonal currents in SST variability in the central Pacific, for the period 1992-1999. A summary is presented in the final section.

## 6.1 Model

The SST component of the model is now formulated. Features of the model different to traditional ICMs are given special attention. These include the simulation of thermocline depth anomalies, and the parameterization of subsurface temperature. Because the model incorporates a horizontally varying mixed layer, which is also a modification on traditional ICMs, the derivation is fairly complete.

### 6.1.1 Layer model for SST

The evolution equation of ocean temperature is

$$\frac{\partial T}{\partial t} + \nabla \cdot (\mathbf{u}T) = \frac{-1}{\rho_0 c_w} \frac{dQ}{dz} + \nabla \cdot (\kappa \nabla T), \quad (6.1)$$

where  $T$  is the ocean temperature field;  $\mathbf{u}$  is the velocity;  $Q$  is the downward irradiance or flux of heat across a horizontal surface;  $\rho$  is the ocean density field;  $c_w$  is the specific heat of sea water; and  $\kappa$  is the coefficient of diffusivity for sea water.

Defining the SST as the temperature of water in the ocean surface mixed-layer, and assuming temperature is vertically uniform within this layer, an evolution equation for SST can be obtained by integrating equation 6.1 over the surface mixed layer. Neglecting flux terms due to horizontal gradients in the mixed-layer depth, vertical integration gives

$$\frac{\partial HT_m}{\partial t} + \frac{\partial uHT_m}{\partial x} + \frac{\partial vHT_m}{\partial y} + w(H)T(H) = \frac{(Q(0) - Q(H))}{\rho_0 c_w} + \kappa_h \nabla_h \cdot (H \nabla_h T_m) + \kappa_v(H) \frac{\partial T}{\partial z} \Big|_H. \quad (6.2)$$

$T_m$  is the SST (from here on the subscript  $m$  is dropped);  $u$  and  $v$  are the eastward and northward velocity components respectively;  $H$  is the depth of the surface mixed-layer;  $w(H)$  is the vertical velocity at the base of the mixed layer, positive downward;  $Q(H)$  and  $Q(0)$  are the downward heat fluxes at the base of the mixed layer and at the surface, respectively;  $T(H)$  and  $\left.\frac{\partial T}{\partial z}\right|_H$  are, respectively, the temperature and the vertical temperature gradient at the base of the mixed-layer; and  $\kappa_h$  and  $\kappa_v$  are the coefficients for horizontal and vertical diffusivity respectively.

Using the equation for continuity, and using an upstream formulation for vertical advection of temperature, the left hand side of equation 6.2 can be expressed in a more familiar form:

$$H\left(\frac{\partial T}{\partial t} + u\frac{\partial T}{\partial x} + v\frac{\partial T}{\partial y}\right) - wT + w\{M(w)T + M(-w)T_e\}. \quad (6.3)$$

Explicitly, the definition for the entrainment velocity,  $w_e = -\left(\frac{\partial H}{\partial t} + \frac{\partial uH}{\partial x} + \frac{\partial vH}{\partial y}\right)$ , has been used; in the case of a constant depth mixed layer, the entrainment velocity equals the vertical velocity at the base of the mixed layer. The terms in the curly brackets represent vertical advection of temperature;  $M()$  is the Heaviside function, and is used to describe differences in upwelling and downwelling. For upwelling ( $w < 0$ ) water from the bottom layer of temperature  $T_e$  is transported into the surface layer, and conversely for downwelling, water of temperature  $T$  is removed from the surface layer.

Using equation 6.3, equation 6.2 reduces to

$$\begin{aligned} \frac{\partial T}{\partial t} + u\frac{\partial T}{\partial x} + v\frac{\partial T}{\partial y} + \\ \frac{wM(-w)}{H}(T_e - T) = \frac{(Q(0) - Q(H))}{\rho_0 c_w H} + \frac{\kappa_h}{H} \nabla_h \cdot (H \nabla_h T) + \\ \frac{2\kappa_v}{H(H + H_2)}(T_e - T), \end{aligned} \quad (6.4)$$

where  $\nabla_h = \left(\frac{\partial}{\partial x}, \frac{\partial}{\partial y}\right)$  is the horizontal divergence operator, and  $H_2$  is the depth of the second layer. The treatment of vertical diffusivity of temperature is analogous to the vertical diffusivity of momentum in the non-linear component of the model 3.2.4, and  $H_2$  is identical. Sensitivity to the strength of this term is discussed in section 6.3.

### 6.1.2 Anomaly equation

The equation for SSTa that is implemented in the SST component, follows from equation 6.4,

$$\begin{aligned} \frac{\partial T'}{\partial t} = & \underbrace{-w'\frac{\partial \bar{T}}{\partial x}}_{(1)} - \underbrace{-(\bar{u} + u')\frac{\partial T'}{\partial x}}_{(2)} - \underbrace{-v'\frac{\partial \bar{T}}{\partial y}}_{(3)} - \underbrace{-(\bar{v} + v')\frac{\partial T'}{\partial y}}_{(4)} \\ & - \underbrace{\{(\bar{w} + w')M(-\bar{w} - w') - \bar{w}M(-\bar{w})\} \frac{(\bar{T}_e - \bar{T})}{H}}_{(5)} \\ & - \underbrace{-(\bar{w} + w')M(-\bar{w} - w') \frac{(T'_e - T')}{H}}_{(6)} - \underbrace{-\alpha T'}_{(7)} \\ & + \underbrace{\frac{\kappa_h}{H} \nabla_h \cdot (H \nabla_h T')}_{(8)} + \underbrace{\frac{2\kappa_v}{H(H + H_2)}(T'_e - T')}_{(9)}, \end{aligned} \quad (6.5)$$

where primes indicate anomalies, and over-bars indicate climatological values. Terms 1 and 2 are anomalous zonal advection of mean SST, and zonal advection of anomalous SST, respectively. Terms 3 and 4 are anomalous meridional advection of mean SST, and meridional advection of anomalous SST, respectively. Term 5 is the anomalous entrainment of climatological subsurface temperature, and term 6 is the entrainment of anomalous subsurface temperature. Term 7 is a parameterization for anomalous heat flux, and terms 8 and 9 represent horizontal and vertical mixing, respectively.

Terms 1 to 7 are standard in the SST component of ICMs (e.g., Zebiak and Cane [1987]). The only difference is that here,  $H$  is horizontally varying. Terms 8 and 9 are normally neglected. Similar to other ICMs, subsurface temperature is parameterised in terms of thermocline depth. This is a major simplification that assumes subsurface temperature variability is adiabatic. It is probably the reason ICMs out perform OGCMs in the eastern Pacific [Miller et al., 1993]. The poor performance of OGCMs in the east is related to difficulties in simulating the mean thermal structure [Stockdale et al., 1998]. This assumption avoids these problems. The calculation of thermocline depth, and the parameterization of subsurface temperature and anomalous heat flux are described below.

The coefficient of horizontal diffusivity is  $2.5 \times 10^3 \text{ m}^2\text{s}^{-1}$  meridionally and  $2.5 \times$

$10^4 \text{ m}^2\text{s}^{-1}$  zonally. These values are similar to those of other models [Stockdale et al., 1993]. The coefficient for vertical diffusivity is  $10^{-4}\text{m}^2\text{s}^{-1}$ . Sensitivity to these choices are discussed in section 6.3.

#### a. Thermocline depth anomalies

There are a number of difficulties associated with the calculation of thermocline depth anomalies in a multi-mode model. The biggest difficulty is that the calculations are highly sensitive to mean thermocline depth [Dewitte, 2000]. This difficulty is further compounded when the vertical structure functions vary horizontally. The solution applied here is based on (1) the well known ability of modal models to simulate sea-level [Busalacchi and O'Brien, 1980; Cane, 1984], and (2) the inverse linear relation between sea-level and thermocline depth anomalies [Rebert et al., 1985]. Model thermocline depth anomalies ( $\delta z_{20}$ ) are given by

$$\delta z_{20} = 31.p[z = 0], \quad (6.6)$$

where  $p[z = 0]$  is the dynamic model's surface kinematic pressure (chapter 3). The proportionality coefficient is determined by linear regression of annual mean modelled sea-level against observed thermocline depth, as described in appendix B.

The model simulates annual and interannual anomalies well (figure 6.1). Linear correlation coefficients between observed and modelled thermocline depth interannual anomalies are greater than 0.7 along the equator (see appendix B). The simulation of thermocline depth anomalies is sensitive to wind stress (figure 6.1). In particular, note the large differences at  $110^\circ\text{W}-0^\circ\text{N}$  in 1996 between the simulations with FSU research quality winds [Stricherz et al., 1995], and NCEP surface stress [Kalnay et al., 1996] forcing. Appendix B provides further details on model simulations.

#### b. Parameterization of subsurface temperature

The accurate simulation of SST anomalies in ICMs is dependent on accurate representation of subsurface temperature,  $T_e$  [Dewitte and Perigaud, 1996]. The above

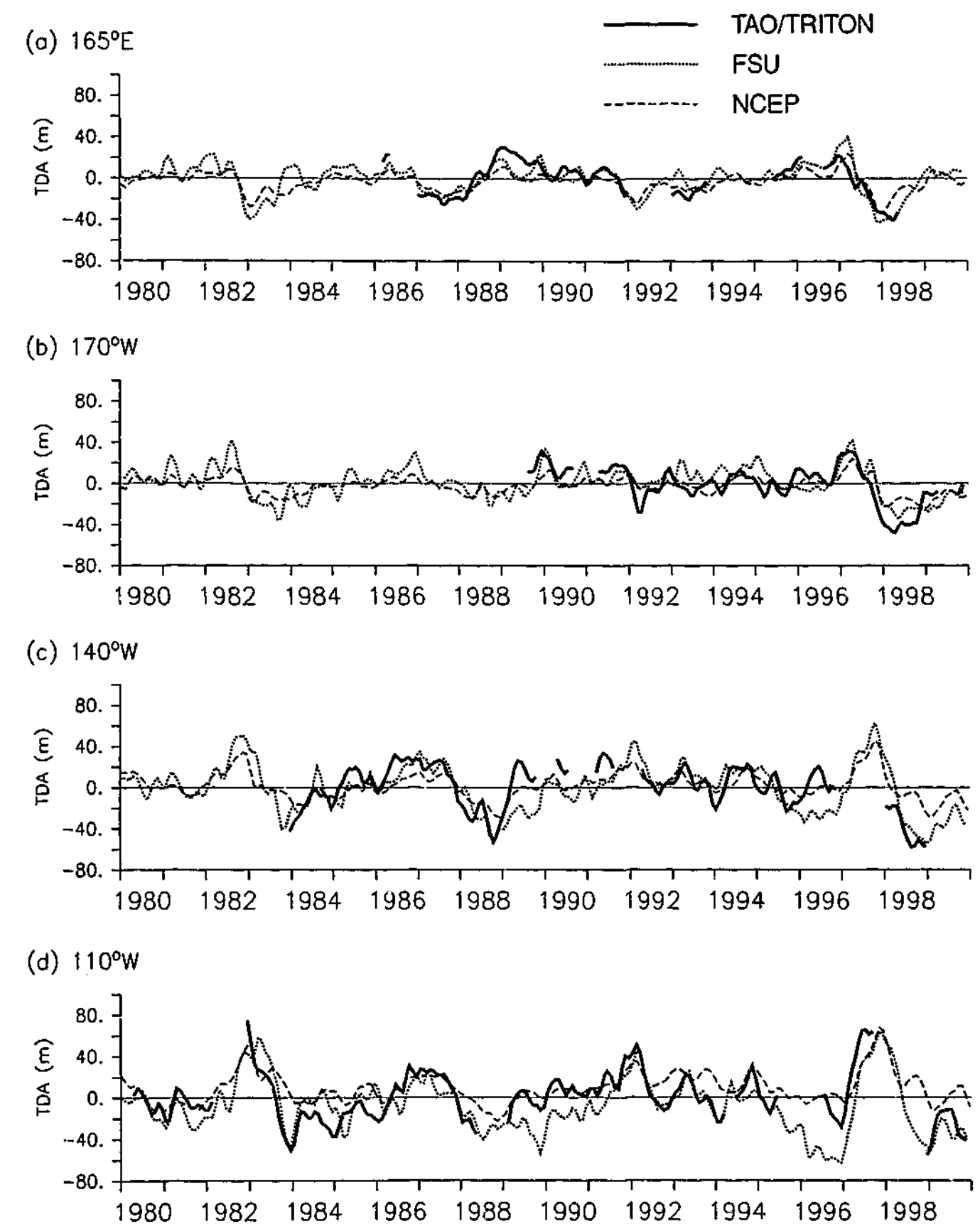


Figure 6.1: Modelled and observed interannual anomalies of 20-degree isotherm depth on the equator at (a)  $165^\circ\text{E}$ , (b)  $170^\circ\text{W}$ , (c)  $140^\circ\text{W}$ , and (d)  $110^\circ\text{W}$ . Dark solid line, TAO/TRITON observation (chapter 2); dotted line, FSU research quality winds [Stricherz et al., 1995], and dashed line, NCEP re-analysis surface stress [Kalnay et al., 1996].

formulation identifies  $T_e$  as the temperature of water entrained into the upper layer, from the subsurface layer. Determining  $T_e$  is not straight forward, since the subsurface layer is difficult to define.

There have been several definitions for  $T_e$ . The most common is to define  $T_e$  to lie "somewhere" between the water temperature at the surface and the temperature at the base of the models mixed layer [Zebiak and Cane, 1987; Seager et al., 1988; Dewitte, 2000]. The somewhere being defined by an entrainment efficiency parameter,  $\gamma$ , which represents mixed-layer depth variability. However,  $\gamma$  is a poorly defined parameter. It is arbitrarily chosen, and sometimes even omitted [Chen et al., 1995]. Formulations based on more physical arguments, which avoid an entrainment parameter also exist, however, they introduce other uncertainties, such as the specification of an entrainment depth [Wang et al., 1995].

There are also disagreements in the relation between  $T_e$  and thermocline depth. In more recent studies,  $T_e$ , is obtained as a fit to observations [Seager et al., 1988; Blumenthal and Cane, 1989; Dewitte and Perigaud, 1996; Dewitte, 2000]. Based on different data and fitting different relations, the parameterizations differ somewhat.

In an attempt to avoid these issues, a new parameterization for  $T_e$  was developed. The parameterization is based on the inversion of the annual mean temperature budget, using model currents, and observed SST, heat flux, and 20-degree isotherm depth ( $z_{20}$ ) measurements.  $T_e$  is the only undetermined quantity, and is inferred by closing the heat budget. The parameterization is obtained by fitting zonal variations in  $T_e$  and  $z_{20}$ , which match each other reasonably well (figure B.5b). Details on the parameterization are given in appendix B.

Anomalous subsurface temperature (in terms 6 and 9; equation 6.5) is calculated using the above parameterization as follows,  $T_e = T_e(z_{20}) - T_e(\overline{z_{20}})$ . The climatological subsurface temperature is not defined as  $T_e(\overline{z_{20}})$ . Instead  $(\overline{T_e} - \overline{T})$  itself is parameterised in terms of  $\overline{z_{20}}$ . This relation, which is derived in the same way as  $T_e(z_{20})$ , is not discussed. The results are insensitive to the formulation of this term (section 6.3).

### c. Anomalous heat flux

Heat flux is a poorly measured and highly uncertain quantity (e.g., see discussion in Seager et al. [1988]), and is normally parameterised in models. Thermal damping is the simplest parameterization [Haney, 1971], and most widely used among ICMs (e.g., Zebiak and Cane [1987]; Kleeman [1993]; Shu and Clarke [2000]). It is adopted here (term 7 in equation 6.5), because of its simplicity, its wide spread use, and because observations generally support this assumption [Wang and McPhaden, 2000].

The thermal damping parameterisation is based on latent heat being controlled by anomalous SST, through changes in evaporation and cloudiness [Barnett et al., 1991; Wang and McPhaden, 2000]. Both mechanism act to damp SST anomalies. East of the date line, observations support this assumption [Wang and McPhaden, 2000]. However, if wind speed are weak, evaporation need not be controlled by changes in SST, and hence, latent heat and net heat flux need not damp the SST anomalies. This may be the case near to and west of the date line [Wang and McPhaden, 2000]. Results presented here are consistent with anomalous heat flux acting as a forcing in the western and central Pacific during 1993, and 1994-95 (section 6.5).

The value for the thermal damping coefficient in the model is  $(100 \text{ days})^{-1}$ . Values in the literature vary from  $(125 \text{ days})^{-1}$  [Zebiak and Cane, 1987] to  $(40 \text{ days})^{-1}$  [Kleeman, 1993]. The value used here is in line with more recent studies [Dewitte, 2000; Shu and Clarke, 2000].

### 6.1.3 Implementation

The SST component is solved on the model's u-grid and uses an identical time step and leap frog scheme to the dynamical model component (see chapter 3). The model was run off-line, with model current and thermocline depth anomalies ingested every 5 days. An off-line simulation was adopted to allow more rapid model testing; 5-

day fields were deemed sufficiently accurate, given that they were generated by monthly mean winds. The model's climatological fields consisted of Reynolds and Smith [1995] SST, model currents generated using the FSU wind stress [Stricherz et al., 1995], and thermocline depth, constructed from mean Levitus [1982] data and model anomalies about the annual mean. The climatological fields were updated once monthly.

## 6.2 Simulation of SST anomalies

The simulation of SSTa using FSU research-quality winds [Stricherz et al., 1995] is described in this section, and analysed in following sections. Unless otherwise stated, discussion always refers to this simulation. In figure 6.2, the model's simulation of SSTa along the equator is shown, and can be directly compared to observations in figure 2.18.

The 1982-83, 1986-87, 1991-92, and 1997-98 El Niño events are all simulated; the 1986-87 and 1991-92 events albeit weakly. The 1993 and 1994-95 events are poorly modelled, however, this is a common problem among models [Ji et al., 1996; Latif et al., 1997]. The particularly good simulation in the western central Pacific of the 1997-98 event, and the poor simulations in the early 1990's are discussed in section 6.5.

The 1998-99 La Niña event is simulated. Negative anomalies are also visible in 1988-89. As described below, the strong negative anomalies in 1996 are due to inaccuracies in the FSU winds. There is also an overall negative bias in the eastern Pacific; this is not present in the NCEP simulation described below.

In the eastern and western Pacific the magnitude of positive and negative anomalies are similar to the observations. In the central Pacific the amplitude of variability is too weak: approximately 50% of the observed variability (figure 6.3b; table 6.1). In the east-central Pacific this most likely related to inaccuracies in the parameterization of subsurface temperature (section 6.3). In the west-central Pacific the weak

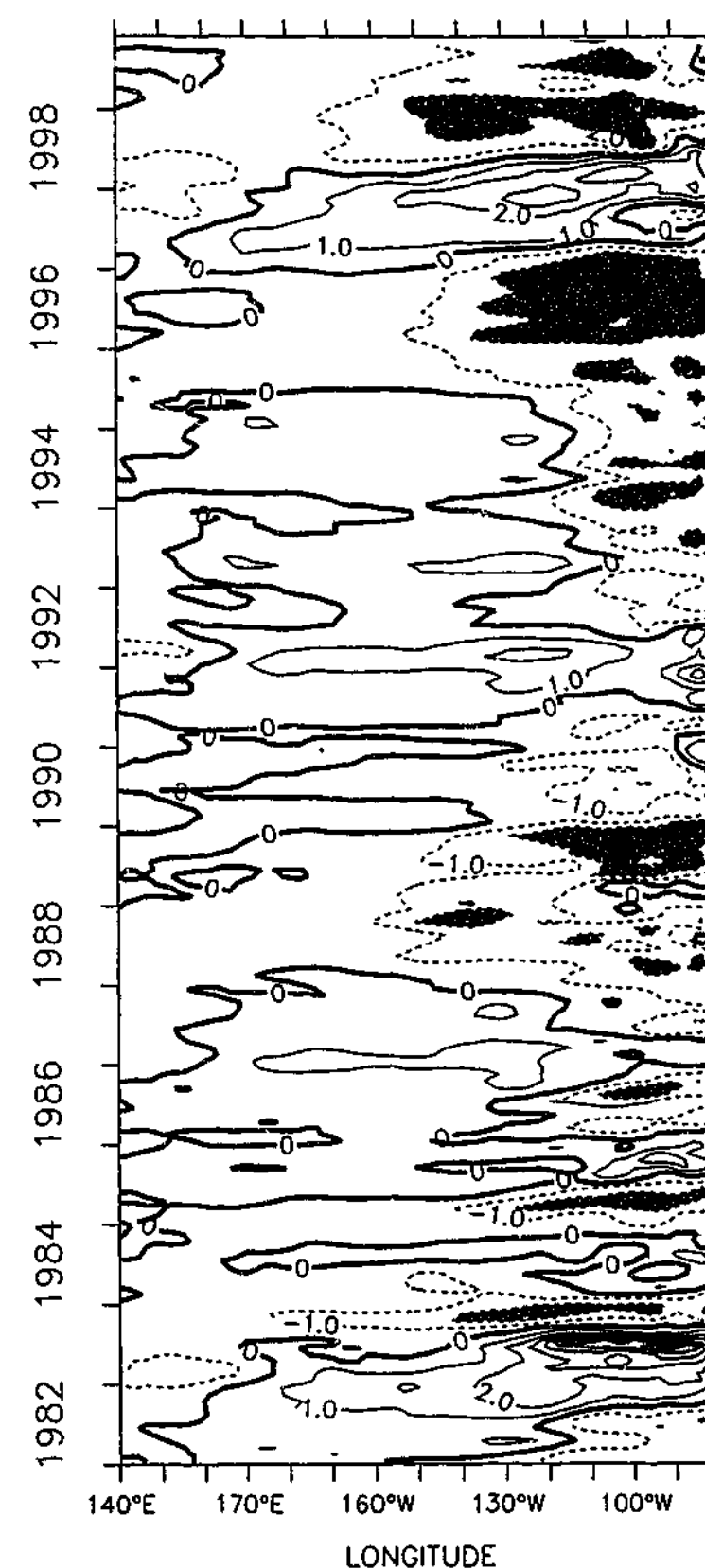


Figure 6.2: Modelled SSTa along the equator in the Pacific. Units are °C. The contour interval is 1°C; positive anomalies greater than 2°, and negative anomalies less than -2°C are shaded. (Model SSTa are generated with FSU wind stress [Stricherz et al., 1995].)

Table 6.1: Comparison between observed and modelled SST anomalies for the period 1/1982-11/1999. The model runs listed are FSU [Stricherz et al., 1995] and NCEP [Kalnay et al., 1996] wind forcing; FSU forcing with the Dewitte and Perigaud [1996] subsurface temperature parameterization (DP96); and FSU forcing with parameter values altered as shown.

	Nino4			Nino3		
	Corr. coef.	$\sigma_{Mod}/\sigma_{Obs}$	RMS dif. (°C)	Corr. coef.	$\sigma_{Mod}/\sigma_{Obs}$	RMS dif. (°C)
FSU	0.74	0.53	0.56	0.75	0.85	1.02
NCEP	0.74	0.31	0.58	0.76	0.51	0.80
$T_e$ DP96	0.76	0.66	0.52	0.79	1.63	1.55
$\alpha^{-1} = 200$ days	0.77	0.64	0.53	0.75	0.95	1.05
$\alpha^{-1} = 50$ days	0.69	0.37	0.61	0.74	0.71	0.99
$\kappa_h = 2.5 \times 10^2 \text{m}^2 \text{s}^{-1}$	0.74	0.54	0.56	0.75	0.86	1.02
$\kappa_h = 2.5 \times 10^4 \text{m}^2 \text{s}^{-1}$	0.71	0.43	0.61	0.75	0.78	1.02
$\kappa_v = 1. \times 10^{-3} \text{m}^2 \text{s}^{-1}$	0.58	0.43	0.64	0.81	0.87	0.92

variability is also related to the models poor behaviour in the early 1990s.

Correlations between modelled and observed SSTa are good, and root mean square errors are also reasonable. Along the equator in the central Pacific correlations are greater than 0.8 (figure 6.3a). For the NINO 4 SST index (SST averaged over 160°E-150°W, 5°S-5°N) and NINO 3 SST index (SST averaged over 150°W-90°W, 5°S-5°N) correlations are around 0.75 (table 6.1). These values compare well to OGCMs, which have correlations around 0.7 to 0.8, and are better than those of traditional ICM; for example, correlations for Zebiak and Cane [1987] model in the NINO4 and NINO3 region are around 0.5, and 0.6, respectively. (These statistics are from Miller et al. [1993] and were calculated for the period 1970-85 using COADS data, for which wind data may have been of poorer quality.)

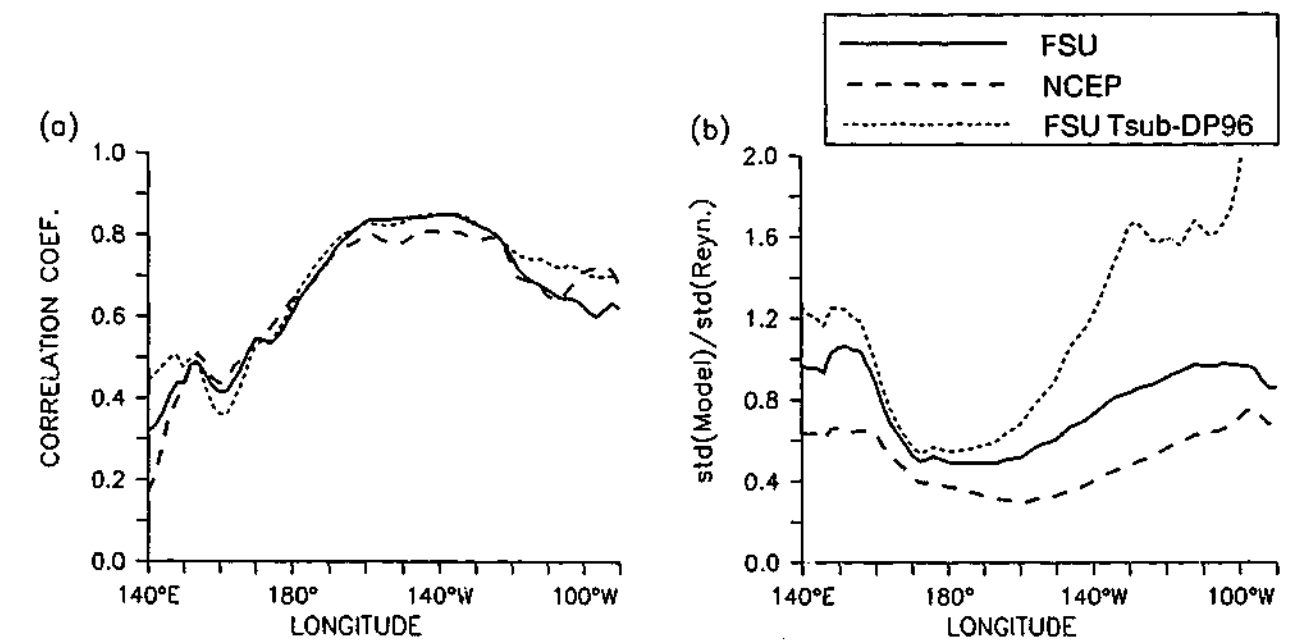


Figure 6.3: (a) Linear correlation between modelled and observed SSTa for three different model simulations: the standard model forced with FSU wind stress [Stricherz et al., 1995] (solid); the standard model forced with NCEP re-analysis surface stress [Kalnay et al., 1996] (dashed); and the standard model with Dewitte and Perigaud [1996] subsurface temperature parameterization and forced with FSU wind stress. (b) same as a, except showing the ratio of standard deviations of modelled to observed SSTa. (observations are from [Reynolds and Smith, 1994].)

### 6.3 Sensitivity studies

In summary of the previous section, the model simulates the phase of SSTa accurately over the equatorial Pacific. The main differences between model and observation are weak variability in the central Pacific, and a negative bias in the east. A number of sensitivity studies were performed to determine the model's robustness, and to ascertain reasons for these two problems. Summary statistics for the NINO4 and NINO3 regions are given in table 6.1. In brief, the model's sensitivity to wind stress indicate the negative bias in the east is related to inaccuracies in the FSU wind stress [Stricherz et al., 1995]. The sensitivity to the parameterization of subsurface temperature suggests the model's weak variability in the east-central Pacific is due to inaccuracies in the parameterization of subsurface temperature.

### a. Wind stress

To test model sensitivity to wind stress, the model was forced with NCEP re-analysis surface stress [Kalnay et al., 1996]; the simulation of SSTa on the equator is plotted in figure 6.4. The correlations between observed and model SSTa were indistinguishable from that of the FSU simulation (figure 6.3a; table 6.1).

There were two significant differences between the simulations. First, the NCEP simulation was significantly weaker than both the observations and the FSU simulation (figure 6.3b and table 6.1). This is consistent with the overall weak variability of the FSU simulation (see section 5.4 and appendix B). Second, there was a positive bias in NCEP simulation of SSTa variability in the eastern Pacific, in direct contrast to the FSU simulation.

Another difference that deserves mention is the simulation of SSTa in the east in 1996. In the NCEP simulation and in the observations this is a period of weak negative anomalies. In the FSU simulation there are strong negative SSTa, which are due to incorrectly simulated thermocline depth anomalies (See figure 6.1, and appendix B).

Inaccuracies in the wind forcing are clearly responsible for large model errors, most notably in the eastern Pacific. Similar problems in simulating SST have been noted by others [Hackett et al., 2001]. These types of uncertainties make it hard to identify model errors; they must also contribute to ENSO forecast errors.

### b. Subsurface temperature parameterization

Sensitivity to the parameterization of subsurface temperature was tested by running the model with the parameterization developed by Dewitte and Perigaud [1996]. Their parameterization is a zonally varying fit of the Zebiak and Cane [1987] parameterization to XBT data; it was shown to significantly improve the simulation of Zebiak and Cane [1987] model.

Correlation to observations on the whole were similar to those of the standard

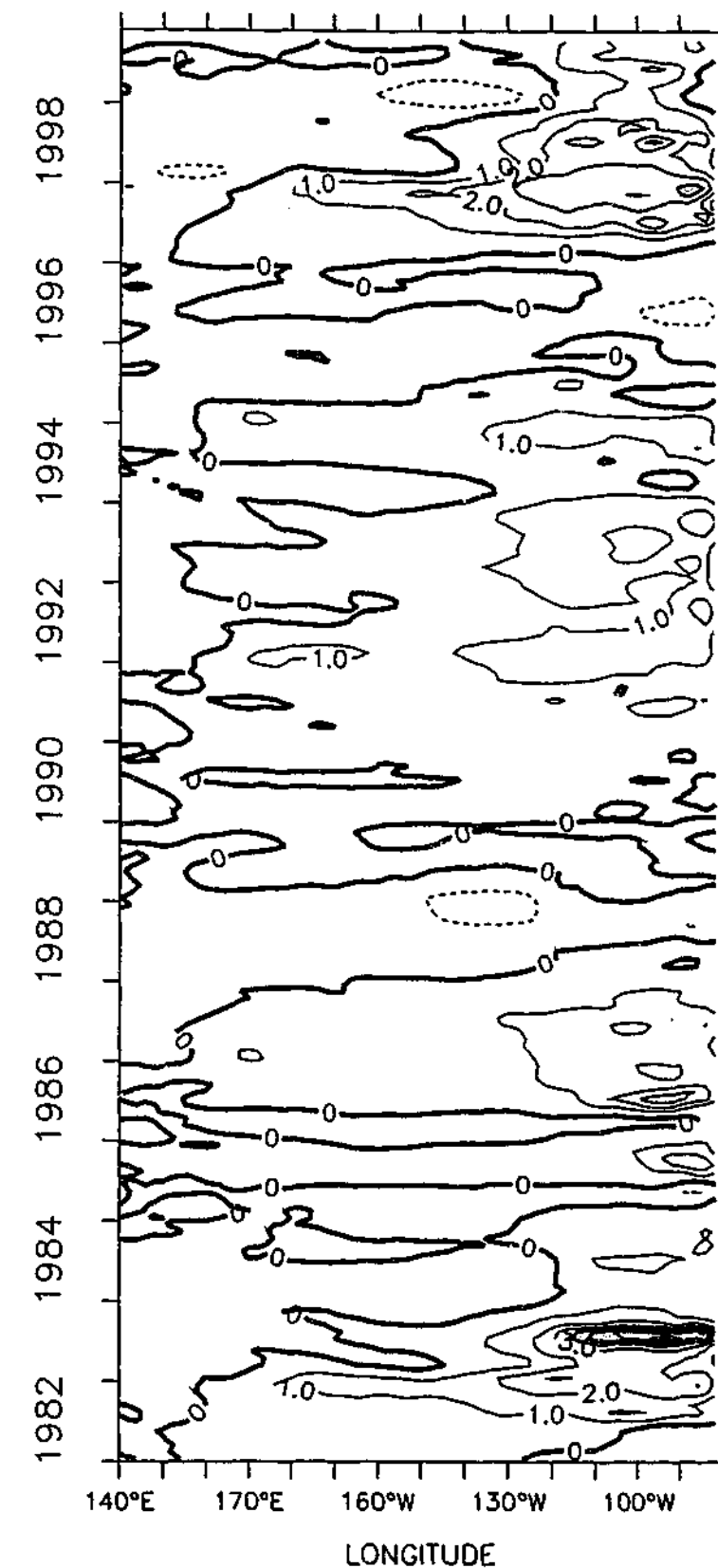


Figure 6.4: Modelled SSTa along the equator, generated with NCEP re-analysis surface stress [Kalnay et al., 1996]. Units are  $^{\circ}\text{C}$ . The contour interval is  $1^{\circ}\text{C}$ ; positive anomalies greater than  $2^{\circ}$ , and negative anomalies less than  $-2^{\circ}\text{C}$  are shade.

model (table 6.1, and figure 6.3). In the east-central Pacific, there was a significant improvement in the simulation, with the best simulation occurring around 150°W. Toward the east the variability became unrealistically strong (table 6.1, and figure 6.3). This problem is most likely due to differences in thermocline depth and mixed-layer depth between this model and that of Dewitte and Perigaud [1996]. The model's sensitivity in the east is expected, because in the east, modelled SSTa are determined by subsurface temperature variability (section 6.4).

This experiment demonstrates that the model's weak SST variability in the east-central Pacific could easily be due to inaccuracies in the parameterization of subsurface temperature.

### c. Other experiments

A number of other sensitivity experiments were performed, these included increasing and decreasing the thermal damping coefficient ( $\alpha = (50 \text{ days})^{-1}$ , and  $(200 \text{ days})^{-1}$ ), increasing the coefficient of vertical diffusivity ( $\kappa_v = 10^{-3} \text{ m}^2 \text{ s}^{-1}$ ), and increasing and decreasing the coefficient horizontal diffusivity by a factor of 10.

The greatest sensitivity was to increases in the coefficient of vertical diffusivity. This term links subsurface temperature anomalies to SSTa in regions where there is no upwelling. On the equator, SSTa are fairly insensitive; off the equator, SST variability can be significantly affected. In the NINO4 region, where zonal advection is the most important term in the SST budget, the solution is degraded (table 6.1). In the NINO3 region the solution is improved.

The magnitude of the SST variability was affected by changes in the value of the thermal damping coefficient, the smaller value,  $(200 \text{ days})^{-1}$ , slightly improving the solution. The converse occurred for the larger value,  $(50 \text{ days})^{-1}$ . The simulation of SSTa was minimally affected by changes in horizontal diffusion. The model was also found to be insensitive to changes in the formulation of the mean vertical temperature gradient (term 5 in equation 6.5). In particular replacing  $\bar{T}_e$  with observed temperature at the base of the mixed layer had a minimal effect on term

Table 6.2: Ratio of all tendencies to the entrainment tendency in the anomalous SST equation 6.5. (Tendencies are monthly averaged; model run with FSU wind Stricherz et al. [1995].)

		170°E	170°W	110°W	NINO4	NINO3
(5)+(6)	wTz	1.	1.	1.	1	1.
(1)+(2)	uTx	0.8	1.	0.3	2.4	1.6
(3)+(4)	vTy	0.3	0.1	0.6	0.9	2.8
(7)	$\alpha T'$	0.3	0.6	0.2	1.6	2.7
(8)	hdiff	0.7	0.6	0.4	0.1	0.2
(9)	vdiff	0.1	0.1	0.1	0.4	1.

5 in equation 6.5 in the central Pacific. These experiments indicate that model parameters are reasonably chosen.

## 6.4 SST budget

The model's simulation of SSTa in the central Pacific matches observations fairly well, and certainly improves on traditional ICM (section 6.2). The model's SST budget was analysed to identify the mechanisms responsible for these improvements. Analysis was performed on the equator in the western, central, and eastern Pacific, and for the NINO4 and NINO3 regions. A summary is now given; the terms referenced are those in equation 6.5. Table 6.2 shows the ratio of all tendencies to the entrainment tendency (terms 5 and 6); table 6.3 shows the correlation between each tendency and modelled SSTa; and figure 6.5 shows the driving terms in the SST budget on the equator, at locations in the western, central, and eastern Pacific.

In the western Pacific, zonal advection (terms 1 and 2) and entrainment are the most important tendencies in the model SST budget (figure 6.5a); entrainment is the stronger of the terms, and most highly correlated with SST changes. These two terms are balanced primarily by horizontal diffusion, and to lesser extent anomalous heat flux.

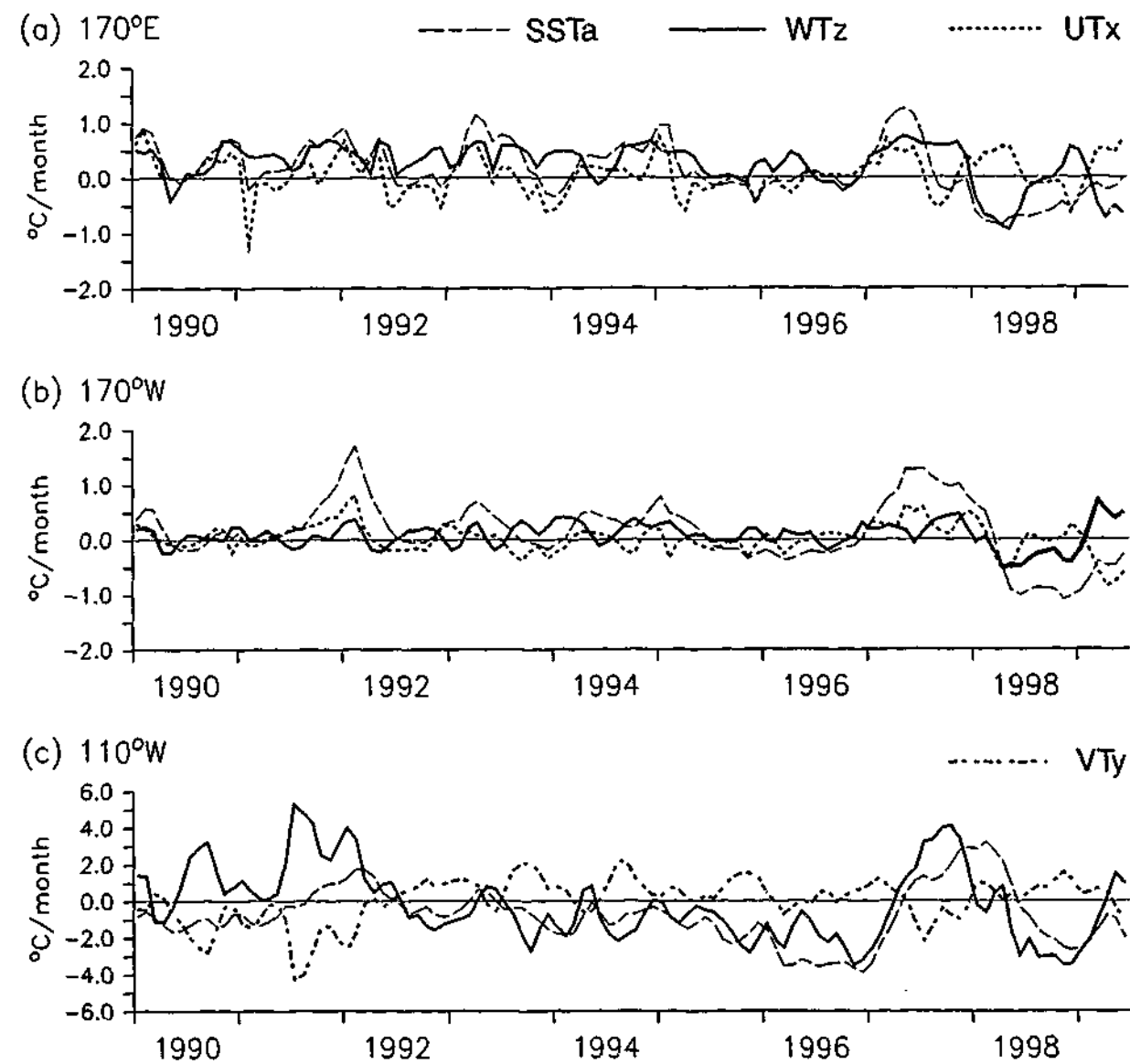


Figure 6.5: (a) zonal advection (dotted) and entrainment (solid) tendencies at  $170^{\circ}\text{E}-0^{\circ}\text{N}$ ; modelled SST anomaly (dashed) is overlaid. (b) same as a, except at  $170^{\circ}\text{W}-0^{\circ}\text{N}$ . (c) meridional advection (dashed-dotted) and entrainment (solid) tendencies at  $110^{\circ}\text{W}-0^{\circ}\text{N}$ ; modelled SST anomaly (dashed) is overlaid. Tendencies are in units of  $^{\circ}\text{C}/\text{month}$ , and SST anomaly in units of  $^{\circ}\text{C}$ . (See text for definitions of tendencies; the tendencies are monthly averaged and generated using FSU wind forcing [Stricherz et al., 1995].)

Table 6.3: Correlation between model SST anomaly and monthly averaged tendencies in the anomalous SST equation 6.5. (Model run with FSU wind Stricherz et al. [1995].)

		170°E	170°W	110°W	NINO4	NINO3
(5)+(6)	wTz	0.53	0.32	0.61	-0.44	0.50
(1)+(2)	uTx	0.42	0.64	0.15	0.83	0.38
(3)+(4)	vTy	0.24	0.27	-0.16	0.66	0.75
(7)	$\alpha T'$	-0.96	-0.98	-0.97	-0.98	-0.99
(8)	hdiff	-0.71	-0.44	-0.60	-0.83	-0.91
(9)	vdifff	-0.60	-0.59	-0.42	-0.64	0.10

In the central Pacific, like in the west, the most important tendencies are zonal advection and entrainment (figure 6.5b). Both terms are equally important, however, the high correlation ( $r=0.64$ ) between entrainment and modelled SSTA indicates this term drives the SST changes. These two terms are balanced by horizontal diffusion and anomalous heat flux, both terms of equal importance.

In the eastern Pacific, entrainment is the strongest term, followed by meridional advection (terms 3 and 4); these terms determine model SST variability (figure 6.5c). The entrainment tendency is well correlated with SST changes, and drives SST variations. This term is balanced primarily by the meridional advection tendency, and to a lesser extent by horizontal diffusion. The meridional flow advects the entrainment induced SSTA away from the equator. Thus, the meridional advection tendency opposes the entrainment tendency. The strength of the model's meridional flow in eastern Pacific (figure 3.5b) makes meridional advection an important term.

The zonal advection tendency in the western and central Pacific is due to anomalous advection of mean temperature (term 1); zonal advection of SSTA (term 2) is generally less significant. This is consistent with zonal advection being the driving term. Consistent with the meridional advection tendency being a responsive term, this term is dominated by meridional advection of anomalous temperature.

The entrainment tendency, is determined by both anomalous entrainment of

mean subsurface temperature (terms 5), and entrainment of anomalous subsurface temperature (term 6). Both terms are equally important along the equator. In the eastern and central Pacific, these terms are very strong and counter each other. The strength of both terms, makes it hard to determine the relative importance of thermocline induced SST changes (term 6) and Ekman induced SST changes (term 5) in the model. The close relation between subsurface temperature, which is controlled by thermocline depth variations, and modelled SST in the east implies the first is more important (figure 6.6c).

In the SST budget averaged over the NINO4 and NINO3 regions, the zonal and meridional advection tendencies, and the anomalous heat flux tendency became much more significant; entrainment and horizontal diffusion became less significant (tables 6.2, and 6.3). In the NINO4 region, SST changes were now driven by zonal advection, with anomalous heat flux closing the budget. In the NINO3 region, SSTa were now controlled by meridional advection, and to lesser extent zonal advection, anomalous heat flux again closing the budget. However, although meridional advection is the strongest term in the NINO3 budget, entrainment still drives SST changes: The direction of the mean meridional circulation (upwelling on the equator and poleward flow at the surface) means that meridional advection acts simply to spread equatorial anomalies induced by entrainment changes.

This picture fits with observational studies, which show entrainment is significant everywhere, but most important in the east, and anomalous zonal advection, relative to other processes, is most important in the central and western Pacific (e.g. Wang and McPhaden [2000]).

The zonal variations in the relative importance of these two mechanisms is illustrated by the strengthening of the relation between subsurface temperature and SST toward the east (figure 6.6). This is also consistent with the good performance in the east of traditional ICM (e.g., [Zebiak and Cane, 1987]), which focus on entrainment induced SST changes. In the west and central Pacific, where this mechanism is less important, these models simulate SSTa less well.

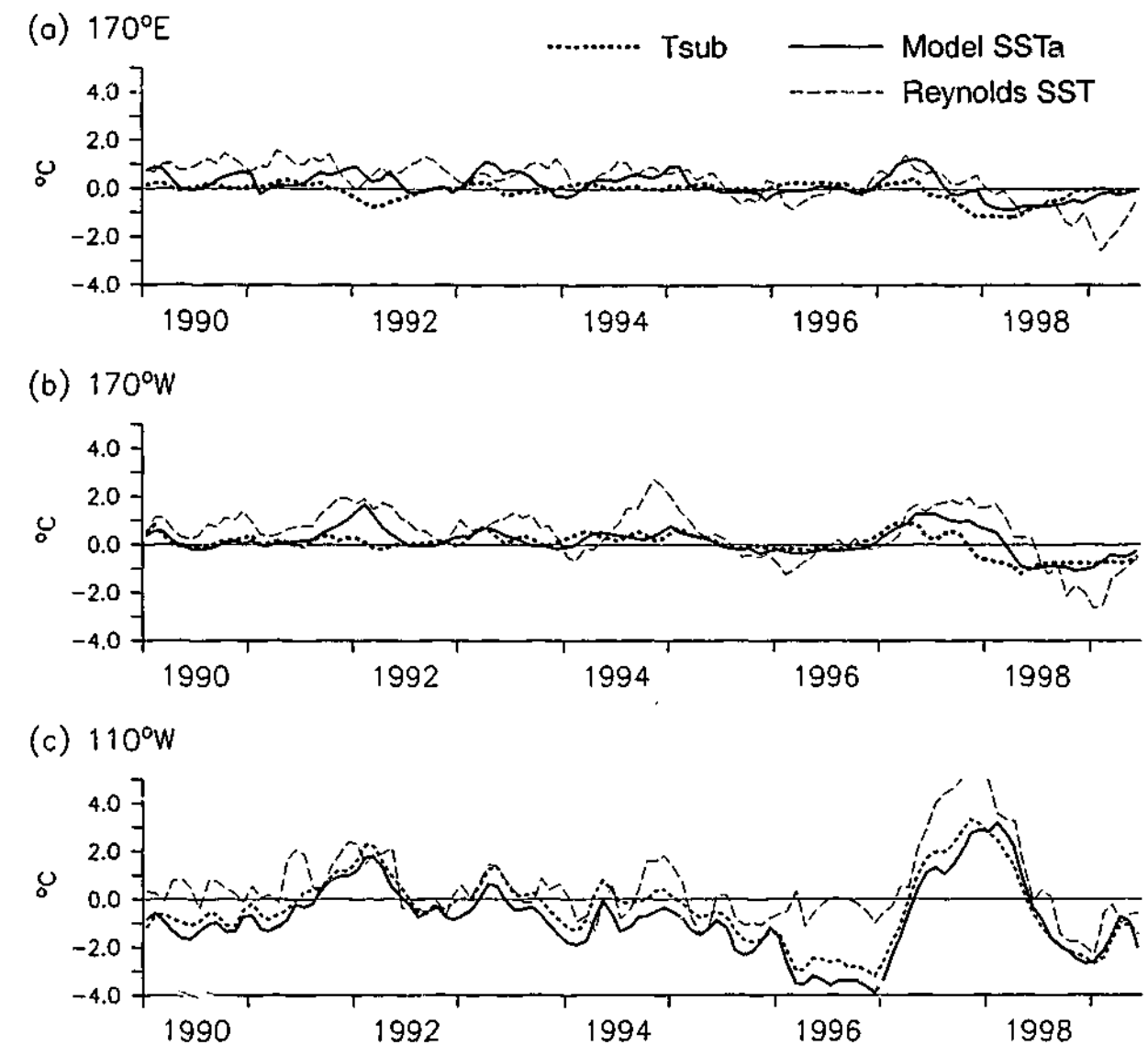


Figure 6.6: Modelled SST anomaly (solid), subsurface temperature (dotted), and observed Reynolds and Smith [1994] SST anomaly (dashed) on the equator at (a) 170°E, (b) 170°W, and (c) 110°W. (Model results are generated using FSU winds [Stricherz et al., 1995].)

In summary there are two mechanisms controlling SST variability in the model: anomalous zonal advection, and entrainment. Anomalous zonal advection and entrainment control SST in the west and central Pacific. Both terms are of equal importance. Entrainment controls SST in the east. Thus, the models improvements on traditional ICM in the central and western Pacific is probably due to more accurate simulation of zonal currents.

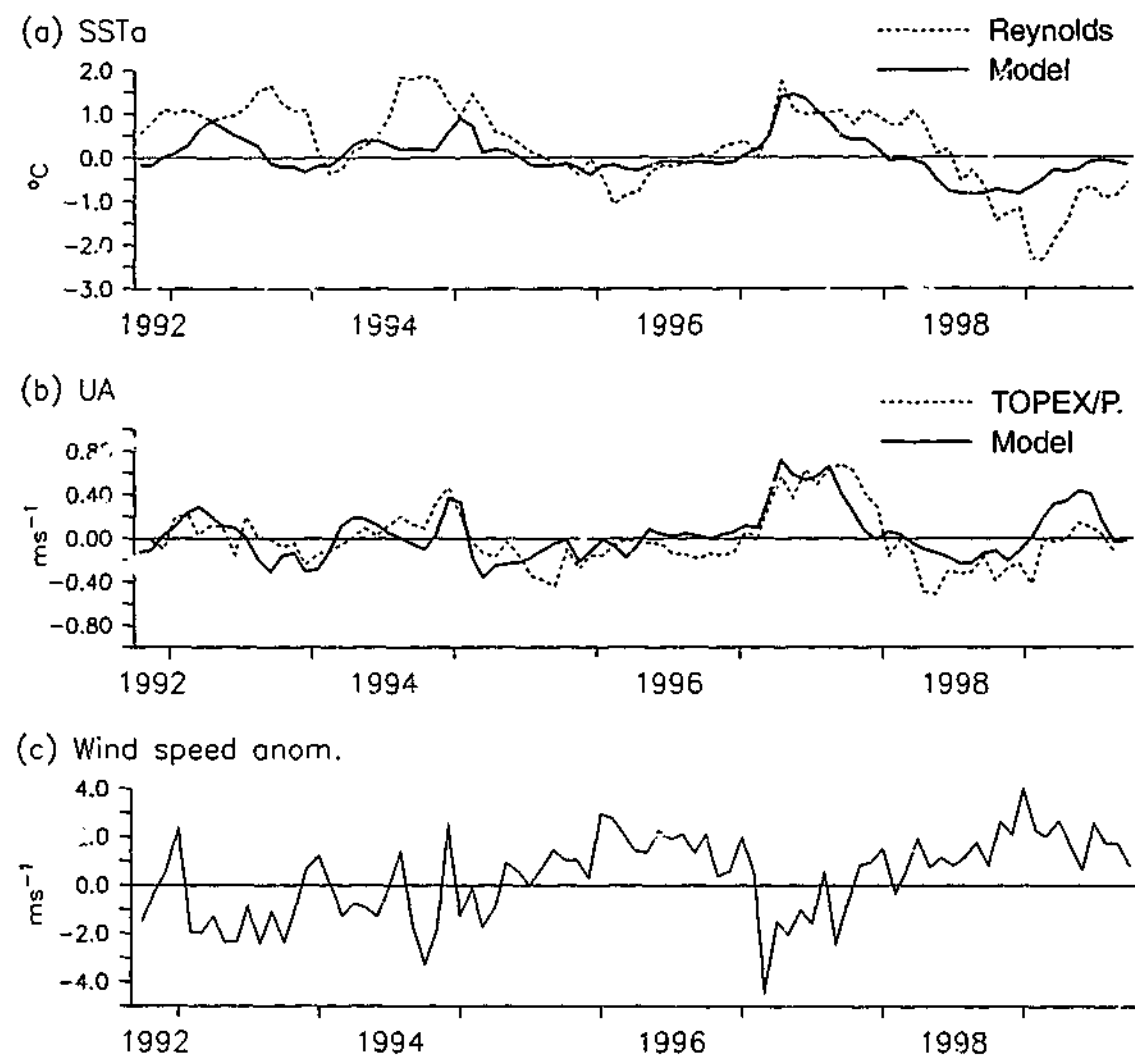


Figure 6.7: Model simulations and observations at  $180^{\circ}\text{W}-0^{\circ}\text{N}$ . (a) modelled (solid) and observed [Reynolds and Smith, 1994] (dotted) SST anomalies. (b) modelled zonal current anomalies (solid) and TOPEX/Poseidon inferred zonal current anomalies [Delcroix et al., 2000] (dotted). (c) FSU wind speed anomalies [Stricherz et al., 1995]. (Model results are generated using FSU wind stress.)

## 6.5 The 1990's

Anomalous zonal advection controls model SST variability in the central Pacific (section 6.4), and model zonal current variability in the central Pacific is accurate. Taking advantage of these two properties, the ICM will now be used to investigate the role of zonal currents in controlling SSTa in the central Pacific during the 1990s. Figure 6.7a, and b compare the models simulation of SSTa and zonal currents in the central Pacific between 9/1992 and 10/1999 with observations.

Of the three El Niño events that occurred during this period, the 1997-98 El

Niño event was the best simulated. The onset of the event is accurately captured. However, SSTa begin to decay immediately after the warming, whereas observed SSTa persist for almost a year. The simulation of zonal current anomalies for this period can hardly be faulted. Given that anomalous zonal advection of SST controls SST in the model at this longitude, it follows the accurate simulation of the initial warming is due only to accurate simulation of zonal currents. The decay of modelled SSTa is driven by anomalous heat flux and horizontal diffusion, and is less easy to explain, but perhaps as described below is due to failure of the model's heat-flux parameterization.

Unlike the 1997-98 event, the 1993 and 1994-95 events are very poorly simulated by the ICM (See figures 6.7a, 6.6a, and 6.6b). Modelled SSTa are insignificant compared to those observed, which at this longitude are as large as those in 1997. As in 1997, the models simulation of zonal currents is not at fault.

It is hard to identify a reason for the poor model behaviour in 1993 and 1994-95, but the following can be discounted. Inaccuracies in zonal wind stress are not significant, as indicated by the accurate simulation of zonal currents over this period. Entrainment processes can be discounted, as they are less important in the central and western Pacific, in both the model (section 6.4) and in the observations [Wang and McPhaden, 2000]. Likewise, meridional advection can be discounted, as it is not an important process in the western and west-central Pacific. Mixing terms are not significant in the model during these events, and thus cannot explain the weak anomalies either.

The only other term in the SST budget is the anomalous heat flux. Parameterising anomalous heat flux as thermal damping, as is done here, is a highly simplified treatment. As discussed in section 6.1, this assumption is based on wind speed changes being un-important. However, near to, and west of the date line, wind speed are weak and influence latent heat flux [Wang and McPhaden, 2000]. TAO/TRITON observations show there were sizable negative wind-speed anomalies (order  $2\text{ms}^{-1}$ ) over an extended period in 1993 and in late 1994. For illustrative purposes, figure 6.7c shows wind anomalies calculated from FSU pseudo stress, which

show anomalies similar to the TAO/TRITON daily data. Thus the likely explanation for poor SST simulations, given the excellence of the current simulation, is the poor parameterization of anomalous heat flux.

Supporting this explanation, other researchers have found that zonal advection was not an important mechanism controlling SST at 170°W-0°N, between 1988 and 1994 [Weisberg and Wang, 1997]. Also, forced ocean model results show that heat flux forcing associated with anomalous wind speed account for 40% of the persistent heat flux anomalies in the central Pacific during the early 1990s [Kleeman et al., 1996].

Thus it seems, while accurate zonal currents certainly improve SST simulation (e.g., the onset of the 1997 El Niño), other mechanisms are also active (e.g., in 1993 and 1994-95). One of these mechanisms is likely anomalous heat flux.

## 6.6 Discussion and summary

In this chapter the SST component of the ICM was developed, and combined with the dynamical ocean model, which was developed and tested in previous chapters. The SST component is similar to those of other ICMs (e.g., Zebiak and Cane [1987]), but includes a new parameterization of subsurface temperature. This parameterization, which is based on the inversion of annual mean SST budget, is more physically based than other parameterizations, as it avoids the use of an entrainment parameter.

When forced with FSU wind stress [Stricherz et al., 1995], the model's simulation of SSTa in the central and eastern Pacific is comparable with GCMs, and significantly better than traditional ICMs. Correlation between observed and simulated SSTa on the equator in the central and eastern Pacific are greater than 0.8. Averaged over the NINO3 and NINO4 regions correlations are around 0.75.

As in other studies, the simulation of SSTa is very sensitive to wind stress [Hackett et al., 2001]. In particular, when forced with NCEP surface stress [Kalnay et al.,

1996] the amplitude of the SSTa was significantly weaker. However the simulation of anomalies in the eastern Pacific was significantly improved over the FSU simulation. These errors make it hard to separate model errors from wind inaccuracies, especially in the eastern Pacific.

In the east-central Pacific, the model tends to underestimate the variability in SST. This appears related to inaccuracies in the model's parameterization of subsurface temperature (section 6.3). Overall though, given the highly simplified nature of the parameterization, it works well.

Two mechanisms control SST variability in the model: anomalous zonal advection, and entrainment. Anomalous zonal advection is important in the western and central Pacific. Entrainment is important across the Pacific, but most important in the eastern and east-central Pacific. This is consistent with other modelling studies (e.g., Shu and Clarke [2000]), and observational studies (e.g., Wang and McPhaden [2000]). It follows, that the improvement on traditional ICM (e.g., Zebiak and Cane [1987]) in the simulation of SST in the central Pacific is due to more realistic zonal current simulation.

The role of anomalous zonal currents in controlling SST has been recently emphasised [Picaut and Delcroix, 1995; Delcroix et al., 2000; Picaut et al., 2001]. With this in mind, the model's simulation of SST variability at the date line during 1990s was investigated. This period is of particular interest, given the failure of many forecast models to predict the 1993, 1994-95, and 1997-98 El Niño events. The model simulation of zonal currents for the whole period is accurate. In 1997, accurate simulation of zonal current anomalies is shown to be clearly important for getting the correct SST response. However, in 1993, and 1994-95, zonal current anomalies are weak, and as a result modelled SSTa are weak. It is suggested that anomalous heat flux was an important term during these events. Consistent with this, significant negative wind speed anomalies were observed at these times. This is also consistent with other studies [Kleeman et al., 1996; Weisberg and Wang, 1997]. The importance of anomalous heat flux in the western and central Pacific certainly deserves more attention.

In summary, the results presented here demonstrate that improving the simulation of zonal currents significantly improves the simulation of SSTa in the central and western Pacific. However, there are other mechanisms, probably anomalous heat flux, also controlling SST variability in this region. In relation to ENSO forecasts, poor simulation of zonal currents in the central and western Pacific, may have contributed to the failed 1997-98 El Niño forecasts in some models. On the other hand, accurate zonal current simulations would unlikely have improved forecasts of the 1993 and 1994-95 events.

## Chapter 7

### Concluding remarks and other work

This study was aimed at better understanding the dynamics of zonal currents, and their role in controlling SST variability. The background for this study was that SST variability in the central Pacific is now recognised as being important to ENSO, and that zonal advection is the dominant mechanism controlling SST variability in this region.

The dynamics of zonal current variability is not well understood, because of lack of data and a suitable analysis tool. Ocean general circulation models (OGCMs) are too complex to be useful for analysing zonal current variability, and intermediate complexity models (ICMs) aren't sufficiently realistic.

In this study an ICM is developed that better simulates zonal current variability. At all stages of model development, care was taken to test the model behaviour. The model as a result is able to simulate many aspects of the equatorial Pacific. The simplicity of the model allowed several interesting results to be obtained on the dynamics of zonal currents, and their role in controlling SST variability.

A description of the model, and a review of the main findings of this study, and how they have contributed to present understanding, are first given. This is followed by a discussion of further applications of the model and areas where the study could be expanded. A conclusion then summarise the study.

## 7.1 ICM

A major achievement of the study was the development of an ICM that improves on traditional ICMs in two important ways:

1. More realistic depiction of zonal currents
2. Realistic SST variability in the central Pacific

The focus of this study was on zonal currents; the realistic simulation of SST in the central Pacific largely follows. Improved zonal current simulation was achieved by

- Use of ten baroclinic modes, as opposed to one in traditional ICM [Zebiak and Cane, 1987]. Addition of higher modes produce a more realistic equatorial circulation [McCreary, 1981].
- Allowing the baroclinic modes to vary according to stratification, which produces a more realistic response to wind forcing, and a circulation with more realistic structure. Traditional ICMs maintain a horizontally constant stratification.
- Including a first order correction for non-linear terms in the zonal momentum balance. Non-linear terms can be important in the near-surface zonal momentum balance [Wascogne, 1989].

The model's simulation of the annual mean circulation was good, and although not demonstrated here, compared remarkably well to that of OGCMs (e.g., World Climate Research Programme [1995]). In particular, the equatorial undercurrent (EUC) and the south equatorial current (SEC) had highly realistic magnitude and structure. Realistic simulation of the EUC was due to the addition of high order modes; realistic simulation of the SEC was due to the inclusion of non-linear terms. Aspects of the model's interannual variability are discussed below.

The SST component of the model was similar in design to that of other ICMs (chapter 6). However, to address uncertainties in the parameterisation of subsurface temperature, a new parameterisation was developed. The parameterisation was based on an inversion of the annual-mean SST budget, using observed heat flux and thermocline depth measurements, and model currents. This parameterisation is more physically based than others [Zebiak and Cane, 1987; Dewitte, 2000], and avoids the use of an entrainment parameter. The parameterisation worked well.

The accurate representation of subsurface thermal variability in the eastern Pacific, and the better modelling of zonal currents in the western and central Pacific, resulted in realistic simulation of interannual SST variability across the equatorial Pacific. Linear correlations with observations for the variations of the NiNO3 and NiNO4 SST indices were approximately 0.75, and on the equator in the central-western Pacific correlations attained values in excess of 0.8.

## 7.2 Main findings

The addition of high order modes to ICMs has already been investigated by several authors [Shu and Clarke, 2000; Dewitte, 2000]. Thus, the most interesting results of this thesis arise from the investigation of non-linearity. The three main areas of research and the new findings are now summarised.

### 1. Annual cycle of the EUC

The annual cycle of the EUC is characterised by an eastward surge occurring between April and July (chapter 2). This surge cannot be understood in terms of linear dynamics, and has been poorly understood (e.g., Yu et al. [1997]). The model indicates that the annual cycle of the EUC is due to weak non-linearity, and in fact results from the equatorward advection, by the mean equatorial cell, of the linear annual-cycle north of the equator (chapter 4).

## 2. Geostrophic assumption on the equator

The model's simulation of interannual variability of surface zonal currents in the western Pacific was good, and compared well to simulations by OGCMs (chapter 5). Toward the east, the simulation deteriorated, and was less accurate than that of OGCMs. However, in one important aspect the solution remained more realistic than the simulation of linear-models: The magnitude of the variability was realistic; linear model solutions tend to overestimate the variability [Shu and Clarke, 2000].

Analysis of the model's simulation of interannual variability revealed that non-linear terms in the surface zonal-momentum balance, associated with the meridional circulation, are important on the equator in the eastern Pacific. These terms limit zonal current variability. The model's simplicity means that it does not perform as well as OGCMs, but it allows the importance of non-linearity to be demonstrated.

This finding has implications for both zonal currents calculated from satellite sea-level measurements, using modified-geostrophic assumptions, and linear modelling studies. The importance of non-linear terms in the eastern Pacific explains the less accurate linear-model and satellite-inferred currents in the east, relative to the west. The east-west differences have been commented on, but not explained before [Delcroix et al., 2000].

## 3. Mechanisms controlling SST variability

Analysis of the SST budget showed that the accurate simulation of SST in the eastern Pacific was due to accurate depiction of subsurface temperature and entrainment processes. In the central Pacific, SST was primarily driven by zonal advection. These results agree with observational work [Wang and McPhaden, 2000], and other modelling studies [Shu and Clarke, 2000]. In themselves they do not present interesting results.

The most interesting result was that zonal advection in the central Pacific is not always the dominant mechanism controlling SST variability. The simulation of

SST over the 1990s, a period characterised by poor ENSO forecasts [Ji et al., 1996; Barnston et al., 1999], was investigated. The simulation of zonal current was highly realistic, as shown by comparison with TOPEX/Poseidon inferred currents (which in this region compare well to in-situ measurements). The accurate simulation of zonal currents was instrumental in the accurate simulation of SST anomalies in the west at the early stages of the 1997-98 El Niño event. However, the model's SST simulation of the 1993, and 1994-95 El Niño events was poor. Another mechanism controlling SST was active during this period.

It was argued that anomalous heat flux may have been the dominant forcing in the central Pacific during 1993 and 1994-95, and produced the observed positive SST anomalies. The basis for this assertion was that (1) in the central Pacific, where surface winds are weak, anomalous heat flux may be controlled by wind speed changes, and not act as a thermal damping [Wang and McPhaden, 2000]. (2) there were large negative wind speed anomalies in the central Pacific during these times. Although additional evidence is required in support of this assertion, this is a significant result that merits further investigation.

## 7.3 Additional work, and other avenues of research

The model that was developed here is able to simulate the mean circulation, zonal current variability, and interannual SST variability in the tropical Pacific with a degree of veracity that in many respects is similar to an OGCM. The separation of dynamics from thermodynamics, and the decomposition of dynamics into baroclinic modes and non-linearity allows the contributions of the separate processes to be investigated. These properties of the model, together with its low complexity (running comfortably on a work-station) give the model many applications.

This study could have been extended in a number of ways, and some of these will be briefly discussed. Instead, the focus is on other applications of the model, which, because of the properties just described above, are of more interest.

### Additional work

The analysis of the annual cycle of the EUC and of interannual variability of surface zonal currents concentrated on assessing the model's performance in terms of observations. This approach is taken throughout the thesis. However, observation of many aspects of the equatorial ocean circulation and its variability are poor (chapter 2). Thus, a useful extension of this study, would be to compare the results here, with those of a high-resolution OGCM. OGCMs are able to accurately simulate the annual cycle of the EUC [Yu et al., 1997], and are also able to reasonably simulate the variability of surface zonal currents. An analysis of the fields in such a model would help clear up a number of uncertainties, introduced by lack of data, in the annual cycle of the EUC, and give more strength to the mechanism proposed here.

The study of interannual variability of zonal currents would also benefit from such an analysis. Firstly, it would be instructive to compare the currents calculated from the OGCM's surface pressure fields (using geostrophy), with the full OGCM currents. In fact, it is a little surprising that this has not been done, given the recent amount of research on satellite-inferred currents. Secondly, comparing the interannual zonal momentum balance in an OGCM with the one here may help answer questions on the significance of the neglected terms, in the density equation, and in the meridional momentum equation (chapter 3). This analysis might also suggest how the model's formulation of non-linearity might be improved in the eastern Pacific. On the other hand, such an analysis may be useful in pointing out deficiencies in OGCMs.

### Other avenues of research

Data assimilation in the ocean, compared to the atmosphere, is a relatively new area of research. Data assimilation is a very computer intensive process, because of the complexity of models needed to realistically represent the physical processes, and the number of calculation that need to be performed. The model here, being of considerably lower complexity than an OGCM, yet realistically simulating the ocean

circulation, might well form the basis of an accurate assimilation scheme. Such an assimilation scheme may well be a useful alternative to geostrophic zonal current estimates.

Perhaps the most obvious application is to develop a coupled ocean-atmosphere model for studying and prediction of ENSO. Accurately simulating interannual variability in SST across the Pacific, the model has the potential to perform as well as full coupled general circulation model (CGCM). Also, the simplicity of the model makes it a more useful tool for mechanism analysis than a CGCM.

The ocean model developed here encompasses the Pacific and Atlantic basins. Although results from the Atlantic were not discussed, the simulation of SST variability there is realistic (in itself it is a nice independent test of the model). In comparison to the Pacific, much less is known about the mechanisms controlling SST variability and the nature of coupled ocean-atmosphere modes in the Atlantic. With such a model, there is also the potential for studying inter-basin interactions; these are thought to be important in controlling variability in the Atlantic.

## 7.4 Summary

The goals of this thesis have been achieved. An ICM is developed that is useful in investigating the dynamics of zonal current variability. It is also able to simulate SST realistically across the equatorial Pacific. The simplicity of the model allows a number of interesting and significant results to be obtained. These included understanding the role of non-linearity in the annual cycle of the EUC and in the interannual variability of surface zonal currents, and also a demonstration that zonal advection is not the only mechanism controlling SST variability in the central Pacific.

The general implications of this study are that

1. Non-linear terms are important in the zonal momentum balance in the eastern Pacific, and thus need to be realistically represented for accurate depiction of

zonal currents there. However, accurate zonal current simulation is not critical to modelling SST variability in the east.

2. Other terms apart from zonal advection and entrainment, most likely anomalous heat flux, need to be better represented in the central Pacific, to ensure accurate simulation of SST variability.

Lastly, the model developed here, because of its simplicity, is an ideal tool for mechanism analysis. As a result, the model has a number of potentially useful applications, perhaps the most interesting is to develop a coupled ocean-atmosphere model encompassing the Atlantic and Pacific basins.

# Appendix A

## Approximations

In this appendix additional details on several of the approximations made in formulating the ocean model are given. In section A.1 experiments to assess the degree of mode mixing are described. Section A.2 presents a scale analysis of the zonal momentum equation.

### A.1 Stratification

In formulating the model it was assumed that mode mixing due to stratification was negligible. Though model results would indicate this assumption holds, it can not be justified using scale arguments. Instead careful experiments with a finite difference ocean model were performed to show that mode mixing is negligible. These experiments were summarised in section 4.4, but because the results are new and interesting, a more detailed account is given here.

Mode mixing in this context refers to the projection between modes that results when a disturbance propagates through a region of horizontally varying stratification. The projection between modes necessarily occurs because the vertical structure of the modes varies, and the modes at each location form a complete and orthonormal set.

The experiments here assess the degree of mode mixing by comparing the propagation of disturbance through regions with and without stratification. Only mode mixing among the first seven modes is considered here, since these modes control the adjustment process. The neglect of mode mixing for the higher order modes is not significant as these modes are strongly damped; also, their contribution are captured in Ekman layers.

The model used here is a finite difference model of the equations solved by the

modal model (equations 3.4). It was developed by Richard Kleeman, and solves the equations by removing the barotropic mode. To closely correspond to the modal model, the formulation for vertical viscosity is similar. In the important region of the EUC the coefficient of vertical viscosity is equal to  $\frac{A}{N^2}$ , with  $A = 1 \times 10^{-7} m^3 s^{-2}$ . For numerical stability reasons, values are limited at the surface to  $3 \times 10^{-3} m^2 s^{-2}$ , and at depth to  $1 \times 10^{-7} m^2 s^{-2}$ .

As a test of the model, its simulation of the annual cycle of zonal currents was compared with the modal model's. (The annual cycle was generated using Hellerman and Rosenstein [1983] wind stress.) Mean and annual variations of upper ocean zonal currents were very similar, but the EUC was too weak and broad. The annual cycle of the EUC, however, remained similar and incorrect. Reducing vertical diffusion to  $2.5 \times 10^{-8} m^3 s^{-2}$  results in a more realistic undercurrent, but annual mean and annual variations of surface currents are too strong. These differences point to different modelling of modes 6 and 7. These results, none the less, show the finite difference model is an adequate tool for testing mode mixing.

The experiments specifically consisted of modelling Kelvin waves propagating eastward from the date-line. In the zonal direction the kelvin waves were sinusoid humps, extending between  $170^\circ E$  and  $170^\circ W$  with a maximum at  $180^\circ E$ . Seven different vertical and meridional structures were used, each corresponding closely to one of the first seven baroclinic modes. The vertical structures were interpolated from the modal model, but being imperfect other baroclinic modes were introduced. So to clearly isolate the effects of stratification, the simulations were repeated using a horizontally constant stratification taken from  $180^\circ E, 0^\circ N$ . Thus, in total fourteen experiments were performed.

Analysis of the simulations showed scattering between the first seven modes is insignificant. To illustrate this figure A.1 shows the zonal velocity field after 120 days, for the experiment initialised with the seventh baroclinic mode. Apart from the seventh mode, modes 2, 5, 6, and two slower modes are excited. The presence of these modes with similar magnitude in both the experiments with and without stratification, illustrates mode mixing is insignificant. The predominant

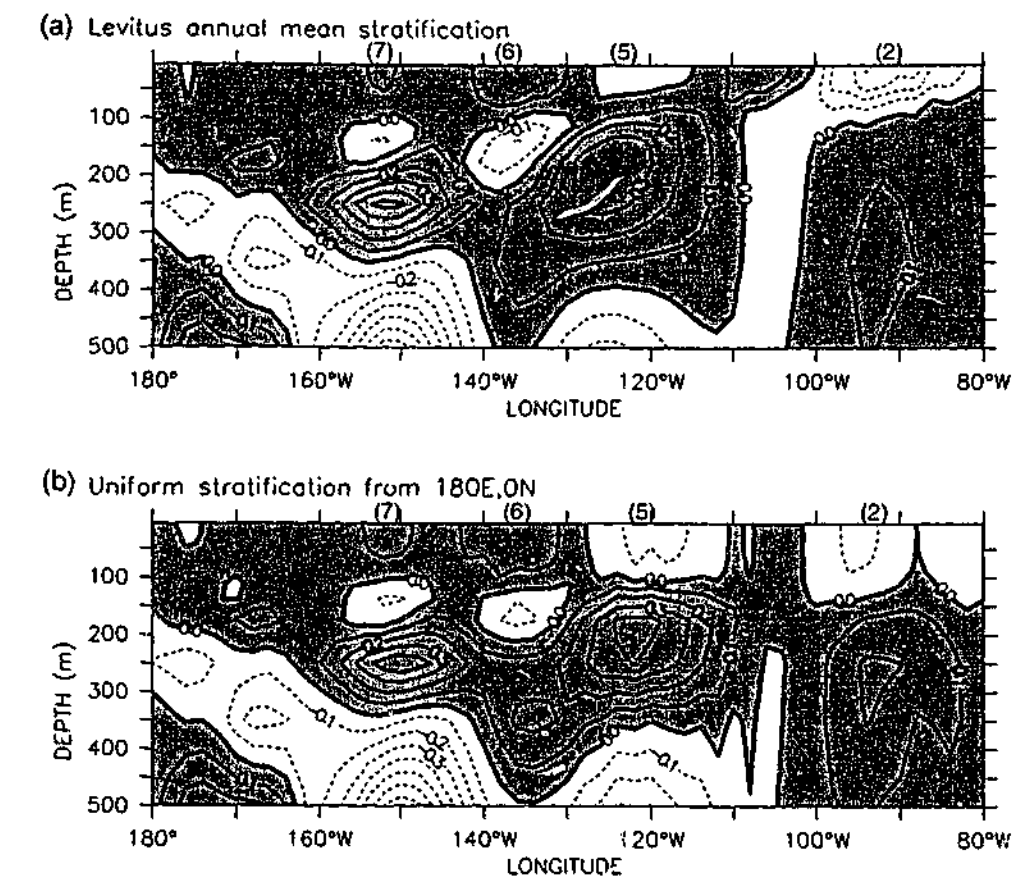


Figure A.1: The dispersion of a Kelvin wave pulse 120 days after initialisation at the date-line. The initial structure vertical structure resembled the seventh baroclinic mode. The plots show zonal velocity in m/s. In (a) the Kelvin wave has propagated through observed Levitus [1982] stratification, and in (b) through horizontally uniform stratification, which is identical to that at the dateline. After 120 days the seventh baroclinic mode has travelled to  $150^\circ W$ , and several other baroclinic modes are visible. The presence of all the modes in both (a) and (b) with similar amplitude indicates mode mixing is not significant. The positions of modes 2,5,6 and 7 are marked at the top of the plots. Note mode 2 has already reached the eastern boundary and been reflected.

effect of stratification is to slow the modes and alter their vertical structure. Hence the greatest differences occur in the east. The slowing of waves toward the east is consistent with the slower shallow water speeds there [Picaut and Sombardier, 1993].

Modification of the vertical structure presents a new and interesting result: The effect of stratification is to modify the modes to match the background stratification. This is in agreement with the treatment of modes by the modal model. This effect is illustrated for the second baroclinic mode in figure A.2, where the vertical structure of the modes after propagating to  $110^\circ W$  through constant and varying

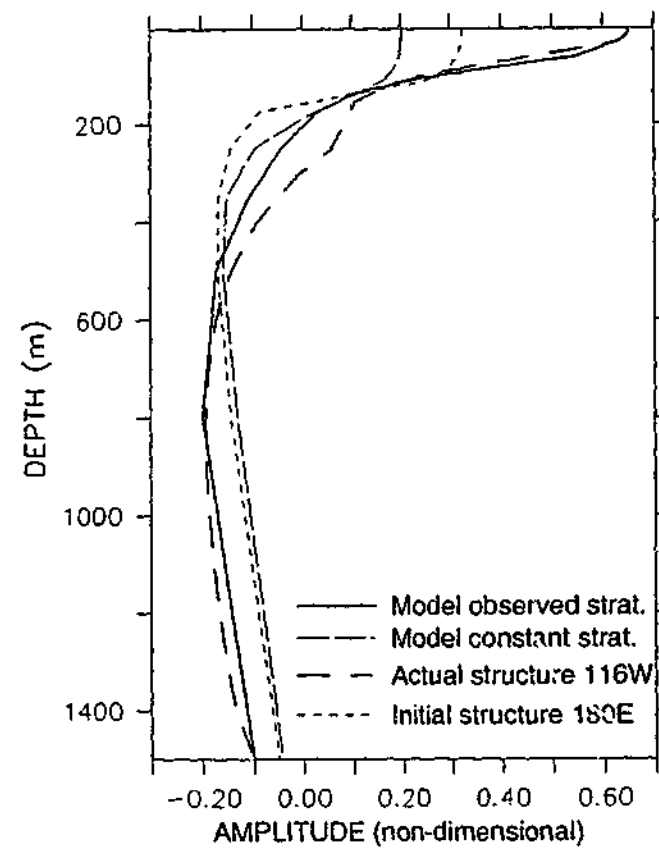


Figure A.2: The vertical structure of the second baroclinic mode after travelling to the eastern Pacific through observed (solid line) and horizontally uniform stratification (long dash with small gaps) as compared to the actual structure of the second baroclinic mode at  $116^{\circ}\text{W}$  (long dash with large gaps) and at  $180^{\circ}\text{E}$  (short dashed). In the case of uniform stratification the vertical structure remains similar to the initial structure, but with observed stratification the second mode is strongly modified, and resembles the local background structure.

stratification are compared to those calculated from the observed stratification at  $180^{\circ}\text{E}$  and  $116^{\circ}\text{W}$ . Quite clearly the vertical structure modified by varying stratification compares well to the background stratification at  $116^{\circ}\text{W}$ , and the vertical structure not modified by stratification remains similar to that at the date-line.

Modification of the baroclinic modes to match the background stratification is easily understood in terms of the layered modal model formulation [Lighthill, 1969]. In this formulation a baroclinic mode describes the linear relationship between the velocities in the different layers. The vertical structure of baroclinic modes changes with the thickness of the layers. Since the layers are simply a representation of the stratification, the vertical structure of modes alters to match the local stratification.

The layered formulations is also able to explain why the structure of annual mean simulation of the modal model used in this thesis is more realistic. In the continuous modal model formulation the vertical structure of the modes remains fixed McCreary [1981]. Whereas in the layered formulation the layer thickness is determined by the horizontal divergence of layer velocities. If the linear perturbation to stratification are large, as they are in the annual mean, the vertical structure of modes are significantly altered. Thus, the structure of the continuous modal model simulation of the annual mean is more realistic when the observed background stratification is used.

## A.2 Scale analysis of advective terms

A scale analysis of the advective terms in residual non-linear equations 3.5 using annual mean observations is presented here; the results are used to justify the neglect of terms in the residual non-linear equations.

### a. Horizontal advective terms at the surface

Zonal flow is westward and weak ( $0.15\text{ms}^{-1}$ ), with zonal and meridional gradients not more than  $0.15\text{ms}^{-1}$  in 60 degrees, and  $0.4\text{ms}^{-1}$  in 4 degrees respectively (figure 2.6 and 2.7).

Meridional velocities in the equatorial region are typically not greater than  $0.05\text{ms}^{-1}$ . Meridional gradients are at most  $0.05\text{ms}^{-1}$  in 0.5 degrees Poulain [1993]. Zonal gradients are hard to estimate, but are at most  $0.05\text{ms}^{-1}$  in 100 degrees (figure 2.6b). The estimates of the horizontal gradient, and the corresponding advective terms are most certainly upper bounds.

Zonal density gradients are of the order  $0.5\text{kgm}^{-3}$  in 80 degrees. Meridional gradients are of the order  $0.5\text{kgm}^{-3}$  in 4 degrees. (Figure A.3)



# Appendix B

## SST model development

In this appendix details on the calculation of thermocline depth and the parametrization of subsurface temperature are given.

### B.1 Thermocline depth anomalies

Determining thermocline (20-degree isotherm) depth anomalies is not straight forward in a multi-mode model. Unlike in a single mode model, the representation of the thermocline is not obvious. The most common method is to assume that isothermal and isopycnal surface are identical, and that perturbations are linear. From these the following relation can be derived,

$$\delta z = \frac{\delta \rho}{\frac{d\bar{\rho}}{dz}} = \frac{\frac{dp}{dz}}{g \frac{d\bar{\rho}}{dz}}, \quad (\text{B.1})$$

where  $\delta z$  is the thermocline depth anomaly.  $\delta \rho$ ,  $\frac{d\bar{\rho}}{dz}$ , and  $\frac{dp}{dz}$  are, respectively, the density anomaly, mean vertical density gradient, and vertical pressure gradient anomaly at the thermocline depth. The hydrostatic relation was used to represent the density anomaly in terms of the pressure anomaly (a variable directly simulated by the model). This method was used by Dewitte [2000], and Shu and Clarke [2000].

A major problems with this method is its sensitivity to the vertical structure functions, and the mean thermocline depth [Dewitte, 2000]. In the case of horizontally-uniform stratification this problem is less apparent, because realistic thermocline depth simulations are possible through careful choice mean thermocline depth [Shu and Clarke, 2000]. In the case of horizontally varying stratification, this type of tuning is non-trivial. Further, the most appropriate choice, which is to specify the mean horizontally varying thermocline depth from observation, results in a poor simulation: Thermocline depth anomalies are found to be half the amplitude of observed anomalies (not shown).

The problem with modelling thermocline perturbations is not due to inaccuracy of the linear approximation made in equation B.1. It is due to the model's poor simulation of large density anomalies (figure 3.3). Thus, this problem with modelling thermocline perturbations is due to the breakdown of linear assumptions in the model (see discussions in sections 3.4, and A.1).

A number of methods were tried to overcome this problem. These included, a quadratic approximation of equation B.1, a Lagrangian formulation using the models vertical velocity, and modelling perturbations to the vertical structure functions due to density perturbations. However, these were all unsatisfactory.

The solution was to use a regression relation between surface pressure and thermocline depth. The basis behind this relation are as follows. First, it is well accepted that modal models realistically simulate sea-level (a proxy for surface pressure) in the equatorial region [Busalacchi and O'Brien, 1981; Cane, 1984]. This was demonstrated for the model's annual mean simulation (section 3.4). Second, there is a strong observational relation between thermocline depth and sea-level in the tropics [Rebert et al., 1985; Philander, 1990].

The regression relation between surface pressure and thermocline depth was derived from annual mean data. Table B.1 lists regression coefficients. Thermocline depth observations are calculated from Levitus [1982] data (chapter 2). Model surface pressure was generated using Hellerman and Rosenstein [1983] re-scaled wind stress (chapter 3). The analysis was not performed for other wind data, but results are expected to remain robust as the annual mean surface pressure field is not strongly sensitive to wind stress.

Modelled surface pressure is well correlated to thermocline depth over the whole equatorial region (table B.1). The correlation is strongest close to the equator in the central and eastern Pacific. Based on these statistics, modelled thermocline depth ( $z_{20}$ ) is given by,

$$z_{20} = 178 + 31. * p(z = 0), \quad (\text{B.2})$$

where  $p$  is the kinematic pressure. This relation gives a good fit over over equatorial

Table B.1: Linear regression coefficient, and least square fit parameters between model surface kinematic pressure and annual mean 20-degree isotherm depth for a number of equatorial sectors. (Model data are generated from Hellerman and Rosenstein [1983] wind stress. 20-degree isotherm depth are calculated from Levitus [1982] data.)

	Cor. Coef.	Reg. Coef.	Intercept
140°E-82°W, 2°S-2°N	0.99	31.5	178.3
140°E-82°W, 5°S-5°N	0.93	31.1	173.3
124°E-82°W, 5°S-5°N	0.85	28.4	165.0

region, 10°S to 10°N, but breaks down at higher latitudes (figure B.1a). The fit is excellent along the equator (figure B.1b).

The annual cycle, which is well captured in both phase and amplitude, will not be discussed. Interannual thermocline depth variations are well simulated in the equatorial region (table B.2). Large positive and negative interannual anomalies are captured with realistic phase and amplitude (figure B.2). In terms of correlation and amplitude, the model simulates interannual anomalies well, over most of the equatorial region (figure B.3). The regression coefficient indicates modelled interannual anomalies are too strong (table B.2). This is due to the simulation of the weaker interannual variability, which is too strong. The largest thermocline depth anomalies are not overestimated (figure 6.1).

The simulation of interannual anomalies is highly sensitive to wind stress. Figure B.2, contrast simulations by FSU research quality winds [Stricherz et al., 1995], and NCEP re-analysis surface stress [Kalnay et al., 1996]. Apart from having overall weaker variability, the most apparent difference between NCEP and FSU simulations occurs in the eastern equatorial Pacific in 1996. FSU winds incorrectly simulate a strong negative anomaly, whereas the NCEP simulation remains realistic. In terms of correlation, the two simulations are similar (table B.2).

The good simulation of thermocline depth anomalies, which is due to the gravest

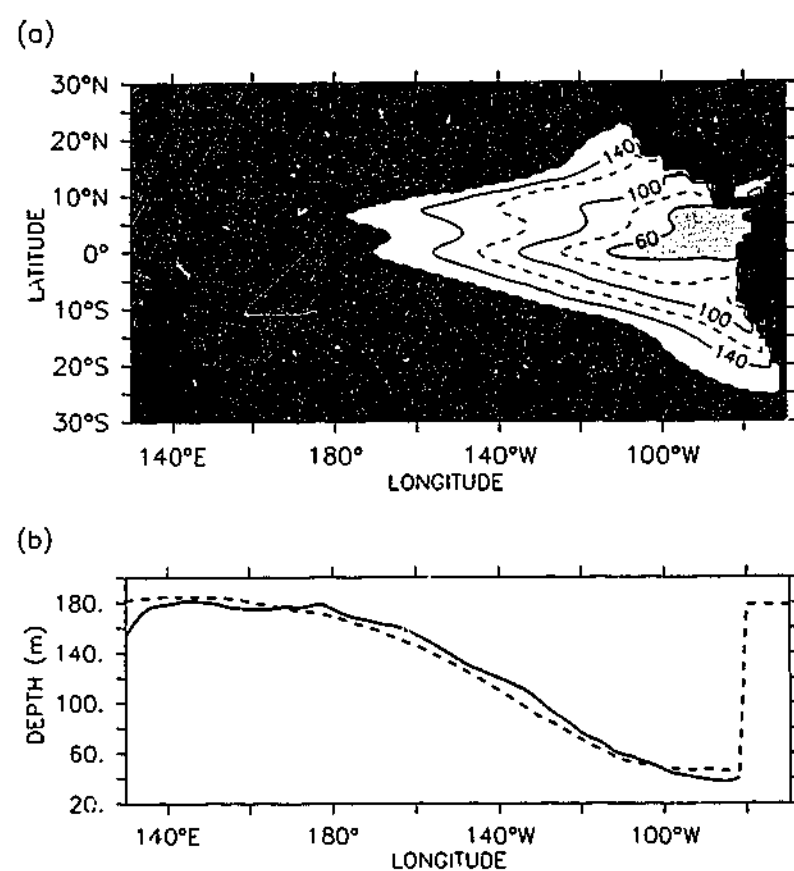


Figure B.1: (a) modelled annual mean 20-degree isotherm depth over the equatorial region. (b) modelled (dashed) and observed (solid) annual mean 20-degree isotherm depth along the equator. (Model results generated using Hellerman and Rosenstein [1983] re-scaled wind stress; observations from Levitus [1982])

Table B.2: Linear correlation and regression coefficients between observed and modelled 20-degree isotherm depth anomalies for the region 155°E-95°W, 5°S-5°N. The regression coefficients are calculated with the observations as the independent variable. Simulations for two wind products are shown. (Observations are from the TAO/TRITON array [Yu and McPhaden, 1999b].)

	Cor. Coef.	Reg. Coef.
FSU	0.65	0.60
NCEP	0.65	0.99

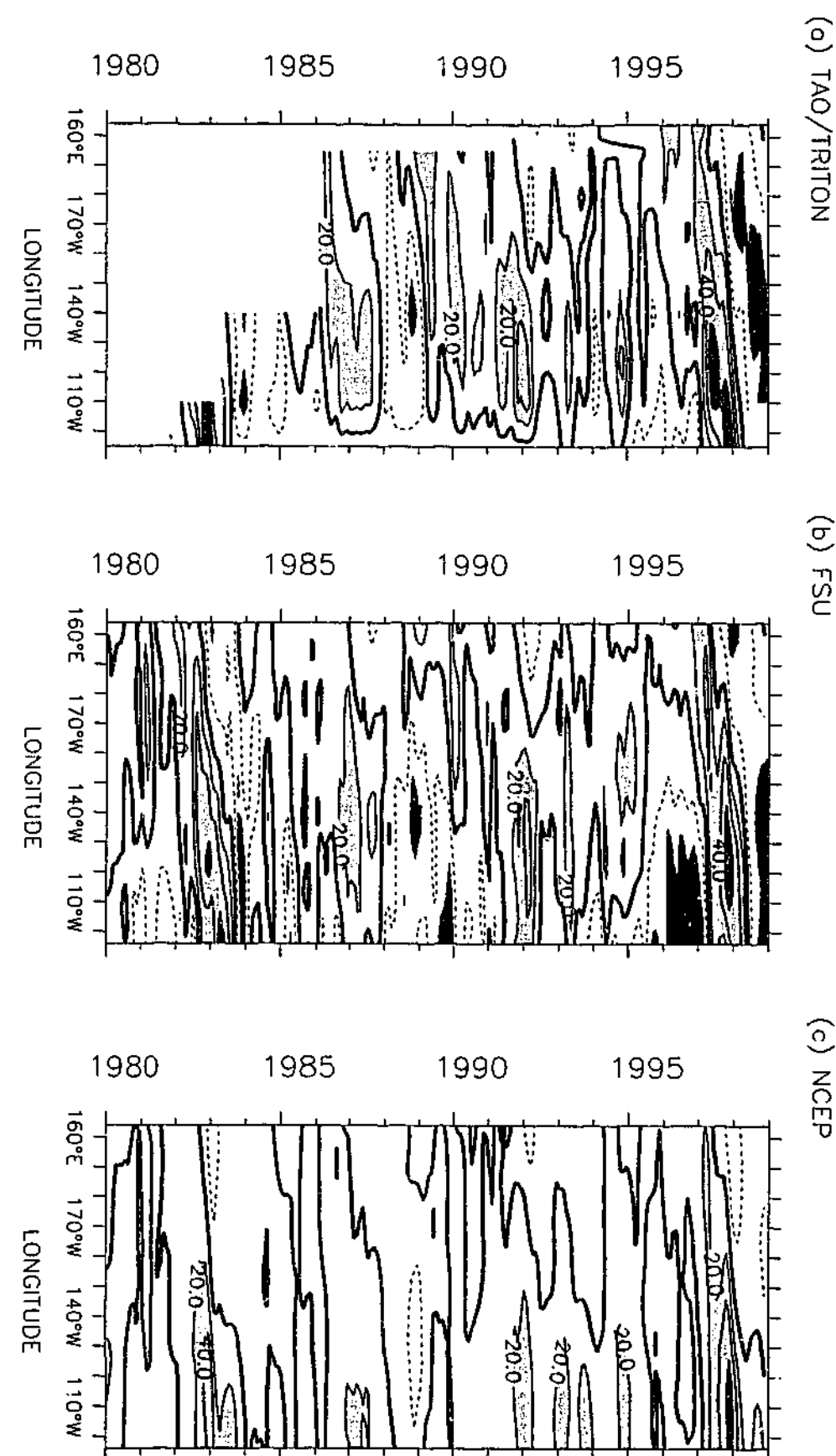


Figure B.2: Interannual 20-degree isotherm depth anomalies on the equator for (a) TAO/TRITON observation (chapter 2), (b) FSU research quality winds [Stricherz et al., 1995], and (c) NCEP re-analysis surface stress [Kalnay et al., 1996]. The units are m, the contour interval is 20 m, and negative anomalies have dashed contours. Anomalies less than -40 m are shaded in black, and anomalies greater than 20m are lightly shaded.

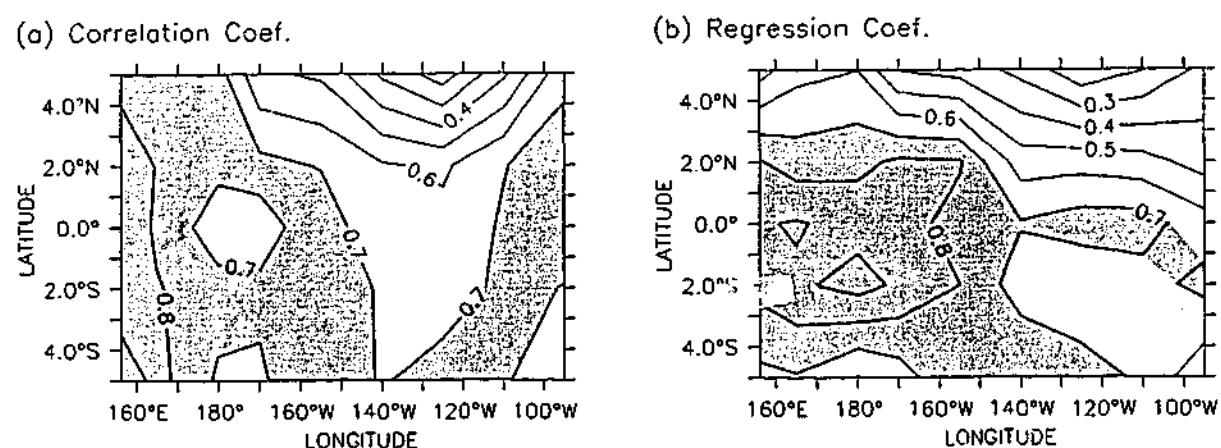


Figure B.3: (a) correlation coefficient between observed and model 20-degree isotherm depth anomalies. (b) regression coefficient between observed (independent variable) and modelled 20-degree isotherm depth anomalies. Anomalies are with respect the annual cycle. (Observations are from the TAO/TRITON array [Yu and McPhaden, 1999b]; modelled anomalies are generated using FSU wind stress [Stricherz et al., 1995].)

baroclinic modes, is consistent with previous work [Busalacchi and O'Brien, 1980; 1981; Cane, 1984; Shu and Clarke, 2000].

## B.2 Subsurface temperature parametrisation

The inversion of the annual-mean temperature budget to obtain parametrisation of subsurface temperature is described here. The parametrisation was used in chapter 6, and as discussed there was developed to side step problems with defining subsurface temperature.

The inversion is performed using annual mean data, because large uncertainties exist in monthly mean climatology and interannual surface heat flux observations [Seager et al., 1988]; the treatment is also simpler, as  $\frac{\partial T}{\partial t} = 0$ . Through inverting equation 6.4, subsurface temperature ( $T_e$ ) can be expressed as,

$$T_e = \alpha^{-1} SHT + T, \quad (\text{B.3})$$

where  $SHT$  denotes the surface heating term, and is given by

$$SHT = \underbrace{uH\frac{\partial T}{\partial x}}_1 + \underbrace{vH\frac{\partial T}{\partial y}}_2 - \underbrace{\frac{(Q(0)-Q(H))}{\rho_0 c_w H}}_3 - \underbrace{\frac{\kappa_h}{H} \frac{\partial}{\partial x} (H\frac{\partial T}{\partial x})}_4 - \underbrace{\frac{\kappa_h}{H} \frac{\partial}{\partial y} (H\frac{\partial T}{\partial y})}_5. \quad (\text{B.4})$$

$\alpha$  is a parameter that determines the strength of the coupling between  $T$  and  $T_e$ , and is given by

$$\alpha = \left( \frac{2\kappa_v}{H + H_2} - wM(-w) \right). \quad (\text{B.5})$$

In the inversion the following data and parameter values are used. Sensitivity to these choices are described below. Mixed-layer average currents, and vertical velocity at the base of mixed layer are obtained from a standard model run, forced with re-scaled Hellerman and Rosenstein [1983] wind stress (chapter 3). Mean SST is from the Reynolds and Smith [1995] climatology. Mean 20-degree isotherm depth are calculated from Levitus [1982]. The data are described in chapter 2.

Surface heat flux ( $Q(0)$ ) are from the NCEP re-analysis [Kalnay et al., 1996]. Heat flux at the base of the mixed layer ( $Q(H)$ ) are due to the penetration of short-wave (SW) radiation. They are estimated from the NCEP re-analysis, assuming 6% of the SW radiation entering the ocean penetrates through the mixed layer. This is a rough estimate, based on a 50 m deep mixed layer of typical sea water, and using data from Ivanoff [1977]. Penetration of SW radiation through the mixed layer depends strongly on the water properties, and on the depth of the mixed layer. Given the large uncertainties in these quantities in the tropical Pacific, a more in-depth treatment is inappropriate. See discussion by Ivanoff [1977], and Simonot and Treut [1986].

Values for other parameters are as follows,  $\kappa_h = 2.5 \times 10^3 \text{ms}^{-1}$ ,  $\kappa_v = 1. \times 10^{-4} \text{ms}^{-1}$ ,  $\rho_0 = 1000 \text{kgm}^{-3}$ ,  $c_w = 4000 \text{Jm}^{-3}$ , and  $(H + H_2) = 125 \text{m}$ .

In the western Pacific and off the equator (except east of 130°W), zonal (term 1) and meridional (term 2) advection are effective in balancing surface heat flux (term 3), and the SHT is small (figure B.4); terms refer to equation B.4. Horizontal diffusion (terms 4 and 5) makes a smaller contribution. Along the equator in the eastern Pacific, the SHT is strongly negative. This is due to strong negative surface heat flux that is not balanced by other horizontal terms (RHS equation B.4). This is where entrainment cooling is important, since upwelling is strong here, and the thermocline is shallowest. In the east, south of the equator, there are inconsistencies

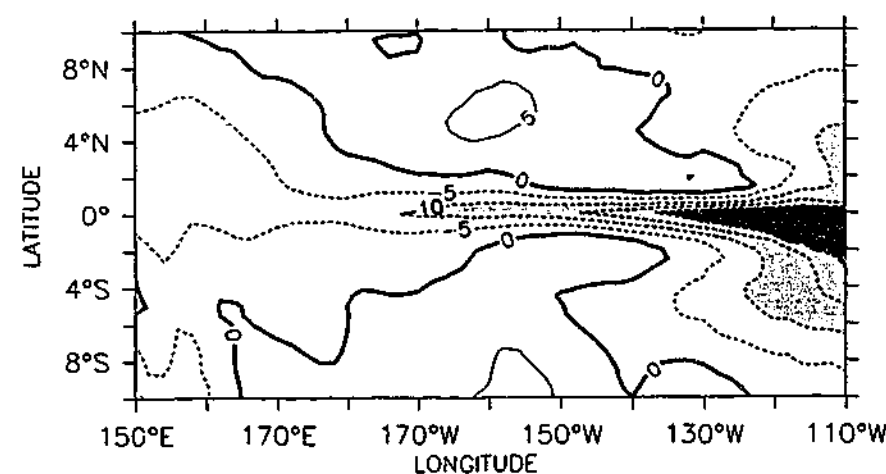


Figure B.4: The surface heating term (SHT) used in calculating the subsurface temperature parametrisation. Units are  $^{\circ}\text{Cms}^{-1}$ , and the contour interval is  $5^{\circ}\text{Cms}^{-1}$ ; negative contours are shaded. The SHT is calculated from model currents, Reynolds and Smith [1995] SST, and NCEP re-analysis surface flux data [Kalnay et al., 1996]. See main text for further details.

between the heat flux term and model terms: There is no upwelling to balance the negative values of the SHT.

Inversion of the SST equation over the whole equatorial region is not very revealing, because data points off the equator, where upwelling is weak or negative, introduce a large amount of variability. Calculations were thus limited to regions of upwelling. Even then the calculation are quite noisy (figure B.5a). The biggest problem though is that the  $T_e(z20)$  relation is too weak. A  $z20$  anomaly of 80 m would only result in a subsurface anomaly of  $4^{\circ}\text{C}$ . Observations suggest the subsurface anomaly should be closer to  $8^{\circ}\text{C}$  (See e.g., Neville Smiths subsurface temperature analysis, <http://www.bom.gov.au/bmrc/ocean/results/pastanal.htm>). Such a parametrisation, when implemented in the SST model (chapter 6), indeed resulted in too weak SST anomalies in the east.

The weak  $T_e(z20)$  relation is not due to poorly chosen parameters. The relationship was insensitive to variations in horizontal diffusivity, and to the replacement of model surface currents with observations [Reverdin et al., 1994]. This is not surprising as the balance on the equator is primarily between surface heat flux, and vertical velocity. The results were also insensitive to changes in the amount of penetrative heat flux, and to an order of magnitude increase in vertical diffusivity. One

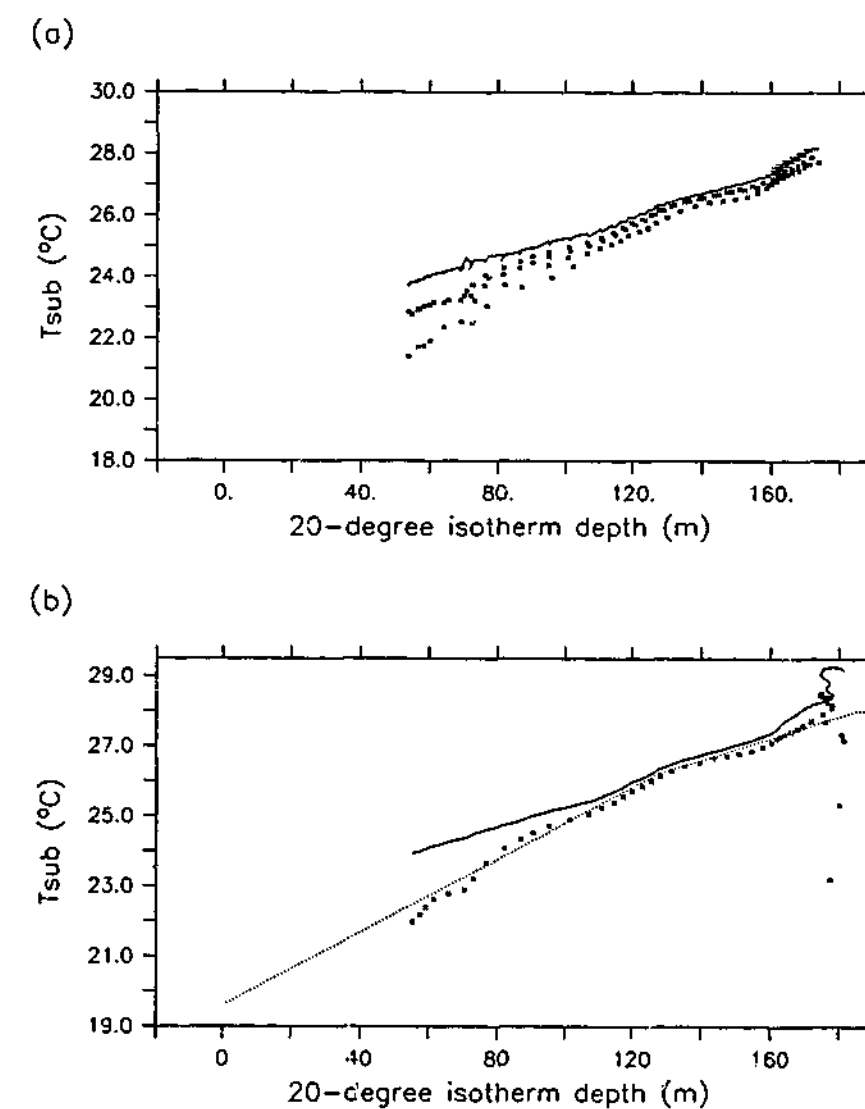


Figure B.5: (a) subsurface temperature ( $T_{\text{sub}}$ ) as a function of 20 degree isotherm depth.  $T_{\text{sub}}$  is calculated from the SHT data shown in figure B.4 and modelled vertical velocity. Corresponding mean SST data are overlaid, and joined by a thin line. Only upwelling data are plotted. (b) the same as a, except the data are averaged between  $1^{\circ}\text{S}$ - $1^{\circ}\text{N}$  prior to the inversion. The  $T_{\text{sub}}$  parametrisation used in the model is also overlaid (dotted line).

of the larger sensitivity is to SST data: Use of Levitus [1982] SST data produced subsurface temperatures similar in structure, but a degree cooler.

The weak  $T_e(z20)$  relation suggests an inconsistency between model vertical velocity fields, and the observed surface heat flux. Thus, one major concern is the equatorial confinement of upwelling (figure 3.7). To reduce these errors, the SHT and vertical velocity were averaged between 1°S and 1°N. The resulting curve is shown in figure B.5b. Shallow and deeper z20 variability are now different. The  $T_e(z20)$  relation for thermocline shallower than 130 m is now steeper, and more realistic. The response for deeper z20 variations is weak, which is consistent with deeper thermocline variability having less influence on SST changes (see e.g., Kleeman [1993]).

The parametrisation that is used in chapter 6, which is a straight line fit to the 1°S-1°N averaged data, is

$$T_e(z20) = \begin{cases} 19.6 & ; z20 \leq 0 \\ 19.6 + 0.052 \times z20 & ; 0 < z20 \leq 128 \\ 22.26 + 0.031 \times z20 & ; 128 < z20 \leq 185.2 \\ 28.0 & ; z20 > 185.2 \end{cases} \quad (\text{B.6})$$

where z20 depths are in meters. The parametrisation is shown in figure B.5b. The chosen high and low end extrapolations are the most straight forward. Other low end extrapolations were tried, but gave poor results. The accuracy of this parametrisation is discussed in chapter 6.

## Bibliography

- Barnett, T. P., M. Latif, E. Kirk, and E. Roeckner, On ENSO physics. *J. Climate*, 4:487-515, 1991.
- Barnston, A. G., M. H. Glantz, and Y. He, Predictive skill of statistical and dynamical climate models in sst forecasts during the 1997-98 El Niño episode and the 1998 La Niña onset. *Bull. Am. Meteorol. Soc.*, 80:217-243, 1999.
- Battisti, D. S, Dynamics and thermodynamics of a warming event in a coupled tropical atmosphere-ocean model. *J. Atmos. Sci.*, 45:2889-2919, 1988.
- Blumenthal, M. B., and M. Cane, Accounting for parameter uncertainties in model verification: An illustration with tropical sea surface temperature. *J. Phys. Oceanogr.*, 19:815-830, 1989.
- Bryden, H., and E. Brady, Diagnostic model of the three-dimensional circulation in the upper equatorial Pacific ocean. *J. Phys. Oceanogr.*, 15:1255-1273, 1985.
- Bryden, H., and E. Brady, Eddy momentum and heat fluxes and their effects on the circulation of the equatorial Pacific ocean. *J. Climate*, 47:55-79, 1989.
- Busalacchi, A. J., and J. J. O'Brien, The seasonal variability in a model of the tropical Pacific. *J. Phys. Oceanogr.*, 10:1929-1951, 1980.
- Busalacchi, A. J., and J. J. O'Brien, Interannual variability of the equatorial Pacific in the 1960's. *J. Geophys. Res.*, 86:10901-10907, 1981.
- Cai, W., and P. H. Whetton, Evidence for time-varying pattern of greenhouse warming in the Pacific ocean. *Geophys. Res. Lett.*, 27:2577-2580, 2000.
- Cane, M., Modeling sea level during el Niño. *J. Phys. Oceanogr.*, 14:1864-1874, 1984.
- Chao, Y., D. Halpern, and C. Perigaud, Sea surface height variability during 1986-1988 in the tropical Pacific ocean. *J. Geophys. Res.*, 98:6947-6959, 1993.
- Chen, Y.-Q., D. S. Battisti, and E. S. Sarachik, A new model for studying the tropical oceanic aspects of ENSO. *J. Phys. Oceanogr.*, 25:2065-2089, 1995.
- Davis, R. E., Predictability of sea surface temperature and sea level pressure anomalies over the north Pacific ocean. *J. Phys. Oceanogr.*, 6:249-266, 1976.
- Delcroix, T., Observed surface oceanic and atmospheric variability in the tropical Pacific at seasonal and ENSO timescales: A tentative overview. *J. Geophys. Res.*, 103:18611-18633, 1998.
- Delcroix, T., J. Boulanger, F. Masia, and C. Menkes, Geostat-derived sea level and surface current anomalies in the equatorial Pacific during the 1986-1989 El Niño and La Niña. *J. Geophys. Res.*, 99:25093-25107, 1994.

- Delcroix, T., B. Dewitte, Y. duPenhoat, F. Masia, and J. Picaut, Equatorial waves and warm pool displacements during the 1992-1998 El Niño Southern Oscillation events: Observations and modeling. *J. Geophys. Res.*, 105:26045-26062, 2000.
- Delecluse, P., G. Madec, M. Imbard, and C. Levy, OPA version 7, general circulation model reference manual. Internal Rep 93/05, LODYC, Paris, Francis, 140pp., 1993.
- Dewitte, B., Sensitivity of an intermediate ocean-atmosphere coupled model of the tropical Pacific to its oceanic vertical structure. *J. Climate*, 13:2363-2388, 2000.
- Dewitte, B., and C. Perigaud, El Niño-Laña events simulated with Cane and Zebiak's model and observed with satellite or in situ data. Part II: Model forced with observations. *J. Climate*, 9:1188-1207, 1996.
- Dewitte, B., G. Reverdin, and C. Maes, Vertical structure of an ogcm simulation of the equatorial Pacific ocean in 1985-94. *J. Phys. Oceanogr.*, 29:1542-1570, 1999.
- Frankignoul, C., F. Bonjean, and G. Reverdin, Interannual variability of surface currents in the tropical Pacific during 1987-1993. *J. Geophys. Res.*, 101:3629-3647, 1996.
- Fu, C., H. F. Diaz, and J. O. Fletcher, Characteristics of the response of sea surface temperature in the central Pacific associated with episodes of the Southern Oscillation. *Mon. Wea. Rev.*, 114:1716-1738, 1986.
- Gent, P., and M. Cane, A reduced gravity, primitive equation model of the upper equatorial ocean. *J. Comp. Phys.*, 81:444-480, 1989.
- Gill, A. E., *Atmosphere-Ocean Dynamics*. Academic Press, Inc., 1982.
- Gill, A. E., An estimation of sea-level and surface-currents during the 1972 El Niño and consequent thermal effects. *J. Phys. Oceanogr.*, 13:486-606, 1983.
- Gill, A. E., and A. J. Clarke, Wind-induced upwelling, coastal currents, and sea-level changes. *Deep-Sea Res.*, 21:325-345, 1974.
- Glantz, M. H., R. W. Katz, and N. Nicholls, editors, *Teleconnections linking world-wide climate anomalies: Scientific basis and societal impact*. Cambridge Univ. Press, New York, 1991.
- Goddard, L., and N. E. Graham, El Niño in the 1990s. *J. Geophys. Res.*, 102:10423-10436, 1997.
- Gu, D., and S. G. H. Philander, Interdecadal climate fluctuations that depend on exchanges between the tropics and the extratropics. *Science*, 275:805-807, 1997.
- Hackett, E. C., A. J. Busalacchi, and R. Murtugudde, A wind comparison study using an ocean general circulation model for the 1997-1998 El Niño. *J. Geophys. Res.*, 106:2345-2362, 2001.
- Haney, R. L., Surface thermal boundary condition for ocean circulation models. *J. Phys. Oceanogr.*, 1:241-248, 1971.
- Harrison, D. E., On climatological monthly mean wind stress and wind stress curl fields over the world ocean. *J. Climate*, 2:57-79, 1989.
- Harrison, D. E., B. S. Giese, and E. S. Sarachik, Mechanisms of SST change in the equatorial waveguide during the 1982-83 ENSO. *J. Climate*, 3:173-188, 1990.

- Hellerman, S., and M. Rosenstein, Normal monthly wind stress over the world ocean with error estimates. *J. Phys. Oceanogr.*, 13:1093-1104, 1983.
- Ivanoff, A., Oceanic absorption of solar energy. In E. B. Kraus, editor, *Modelling and prediction of the upper layers of the ocean*. Pergamon Press, 1977.
- Ji, M., A. Leetmaa, and V. E. Kousky, Coupled model predictions of ENSO during the 1980s and the 1990s at the National Centers for Environmental Prediction. *J. Climate*, 9:3105-3120, 1996.
- Johnson, E. S., and D. S. Luther, Mean zonal momentum balance in the upper and central equatorial Pacific ocean. *J. Geophys. Res.*, 99:7689-7705, 1994.
- Kalnay, E., et al., The NCEP/NCAR 40-year reanalysis project. *Bull. Am. Meteorol. Soc.*, 77:437-471, 1996.
- Kleeman, R., On the dependence of hindcast skill on ocean thermodynamics in a coupled ocean-atmosphere model. *J. Climate*, 11:2012-2033, 1993.
- Kleeman, R., R. Colman, N. Smith, and S. Power, A recent change in the mean state of the Pacific basin climate: Observational evidence and atmospheric and oceanic responses. *J. Geophys. Res.*, 101:20483-20499, 1996.
- Kleeman, R., and A. M. Moore, A new method for determining the reliability of dynamical ENSO predictions. *Mon. Wea. Rev.*, 127:694-705, 1999.
- Lagerloef, G. S., G. T. Mitchum, R. B. Lukas, and P. P. Niiler, Tropical Pacific near-surface currents estimated from altimeter, wind, and drifter data. *J. Geophys. Res.*, 104:23313-23326, 1999.
- Latif, M., et al., A review of the predictability and prediction of ENSO. *J. Geophys. Res.*, 103:14375-14393, 1998.
- Latif, M., R. Kleeman, and C. Eckert, Greenhouse warming, decadal variability, or El Niño? An attempt to understand the anomalous 1990s. *J. Climate*, 10:2221-2239, 1997.
- Levitus, S., Climatological atlas of the world ocean. Prof. paper 13, 173 pp., NOAA, U.S. Govt. Printing Office, 1982.
- Levitus, S., R. Burgett, and T. P. Boyer, *World Ocean Atlas, 1994*, volume 3 of *Salinity, NOAA Atlas NESDIS 3*. Natl. Oceanogr. Data Cent., Silver Springs, Md., 1994.
- Lighthill, M. J., Dynamic response of the Indian ocean to the onset of the southwest monsoon. *Philosophical Transactions of Royal Society(London)*, 265:45-93, 1969.
- Lukas, R., and E. Firing, The geostrophic balance of the Pacific equatorial undercurrent. *Deep-Sea Res.*, 31:61-66, 1984.
- McCreary, J. P., A linear stratified ocean model of the equatorial undercurrent. *Philosophical Transactions of Royal Society(London)*, 298:603-35, 1981.
- McCreary, J. P., and P. Lu, On the interaction between the subtropical and equatorial ocean circulation: Subtropical cell. *J. Phys. Oceanogr.*, 24:466-497, 1994.
- McPhaden, M. J., Continuously stratified models of the steady state equatorial ocean. *J. Phys. Oceanogr.*, 11:337-354, 1981.

- McPhaden, M. J. et al., The Tropical Ocean-Global Atmosphere observing system: A decade of progress. *J. Geophys. Res.*, 103:14169-14240, 1998.
- McPhaden, M. J., and X. Yu, Equatorial waves and the 1997-98 El Niño. *Geophys. Res. Lett.*, 26:2961-2964, 1999.
- Miller, A. J., T. P. Barnett, and N. E. Graham, A comparison of some tropical ocean models: Hindcast skill and El Niño evolution. *J. Phys. Oceanogr.*, 23:1567-1591, 1993.
- Minobe, S., and K. Takeuchi, Annual period equatorial waves in the Pacific ocean. *J. Geophys. Res.*, 100:18379-18392, 1995.
- D. W. Moore and S. G. H. Philander, Modeling of the tropical oceanic circulation correct reference. In *The Sea*, volume 6, pages 319-361. Wiley-Interscience, New York, 1977.
- Oldenborgh, G. J. V., What caused the onset of the 1997-98 El Niño? *Mon. Wea. Rev.*, 128:2601-2607, 2000.
- Peters, H., M. C. Gregg, and J. M. Toole, On the parameterisation of equatorial turbulence. *J. Geophys. Res.*, 93:1199-1218, 1988.
- Philander, S. G. H., *El Niño, La Niña, and the Southern Oscillation*. Academic Press, Inc., 1990.
- Philander, S. G. H., W. J. Hurlin, and A. D. Seigel, Simulation of the seasonal cycle of the tropical Pacific ocean. *J. Phys. Oceanogr.*, 17:1986-2002, 1987.
- Philander, S. G. H., and R. C. Pacanowski, Simulation of the seasonal cycle in the tropical atlantic ocean. *Geophys. Res. Lett.*, 11:802-804, 1984.
- Picaut, J., A. J. Busalacchi, M. J. McPhaden, and B. Camusat, Validation of the geostrophic method for estimating zonal currents at the equator from Geosat altimeter data. *J. Geophys. Res.*, 95:3015-3024, 1990.
- Picaut, P., and T. Delcroix, Equatorial wave sequence associated with warm pool displacements during the 1986-1989 El Niño-La Niña. *J. Geophys. Res.*, 100:18393-18408, 1995.
- Picaut, J., S. P. Hayes, and M. J. McPhaden, Use of geostrophic approximation to estimate time-varying zonal currents at the equator. *J. Geophys. Res.*, 94:3228-3236, 1989.
- Picaut, J., M. Ioualalen, T. Delcroix, F. Masia, R. Murtugudde, and J. Vialard, The oceanic zone of convergence on the eastern edge of the Pacific warm pool: A synthesis of results and implications for ENSO and biogeochemical phenomenon. *J. Geophys. Res.*, 106:2363-2386, 2001.
- Picaut, J., and L. Sombardier, Influence of density stratification and bottom depth on vertical mode structure functions in the tropical Pacific. *J. Geophys. Res.*, 98:14727-14737, 1993.
- Pond, S., and G. L. Pickard, *Introductory dynamical oceanography*. Butterworth-Heinemann, 2nd edition, 1983.
- Poulain, P.-M., Estimates of horizontal divergence and vertical velocity in the equatorial Pacific. *J. Phys. Oceanogr.*, 23:601-607, 1993.

- Qiao, L., and R. H. Weisberg, The zonal momentum balance of the equatorial undercurrent in the central Pacific. *J. Phys. Oceanogr.*, 27:1094-1119, 1997.
- Rebert, J. P., J. R. Donguy, G. Eldin, and K. Wyrtki, Relations between sea level, thermocline depth, heat content, and dynamic height in the tropical Pacific ocean. *J. Geophys. Res.*, 90:11719-11725, 1985.
- Reverdin, G., C. Frankignoul, E. Kestenare, and M. J. McPhaden, Seasonal variability in the surface currents of the equatorial Pacific. *J. Geophys. Res.*, 99:20323-20344, 1994.
- Reynolds, R. W., and T. M. Smith, Improved global sea surface temperature analyses. *J. Climate*, 7:929-948, 1994.
- Reynolds, R. W., and T. M. Smith, A high-resolution global sea surface temperature climatology. *J. Climate*, 8:1571-1583, 1995.
- Schopf, P. S., and M. J. Suarez, Vacillations in a coupled ocean-atmosphere model. *J. Atmos. Sci.*, 45:549-566, 1988.
- Seager, R., S. Zebiak, and M. A. Cane, A model of tropical Pacific sea surface temperature climatology. *J. Geophys. Res.*, 93:1265-1280, 1988.
- Shu, L., and A. J. Clarke, Using an ocean model to examine ENSO dynamics. *J. Phys. Oceanogr.*, submitted, 2000.
- Simonot, J., and H. L. Treut, A climatological field of mean optical properties of the world ocean. *J. Geophys. Res.*, 91:6642-6646, 1986.
- Slutz, R. J., S. Lubker, J. Hiscox, S. Woodruff, R. Jenne, P. Steurer, and J. Elms, Comprehensive Ocean-Atmosphere Data Set; Release 1. Technical report, Climate Research Program, Boulder, Colorado, 1985.
- Stockdale, T. N., A. J. Busalacchi, D. E. Harrison, and R. Seager, Ocean modeling for ENSO. *J. Geophys. Res.*, 103:14325-14355, 1998.
- Stockdale, T. N., et al., Intercomparison of tropical ocean gcms. Technical Report WMO/TD 545, 43 pp., World Meteorol. Organ., Geneva, 1993.
- Stricherz, J. N., D. M. Legler, and J. J. O'Brien, Toga pseudo-stress atlas 1985-1994. Volume II: Pacific Ocean, 173 pp., Florida State University, 1995.
- Tomeczak, M., and J. S. Godfrey, *Regional Oceanography: An introduction*. Pergamon, 1994.
- Wang, B., T. Li, and P. Chang, An intermediate model of the tropical Pacific ocean. *J. Phys. Oceanogr.*, 25:1599-1616, 1995.
- Wang, W., and M. J. McPhaden, The surface-layer heat balance in the equatorial Pacific ocean. Part II: Interannual variability. *J. Phys. Oceanogr.*, 30:2989-3008, 2000.
- Wascogne, W., Dynamical regimes of a fully nonlinear stratified model of the atlantic equatorial undercurrent. *J. Geophys. Res.*, 94:4801-4815, 1989.
- Weisberg, R. H., and L. Qiao, Equatorial upwelling in the central Pacific estimated from moored velocity profilers. *J. Phys. Oceanogr.*, 30:105-124, 2000.
- Weisberg, R. H., and C. Wang, Slow variability in the equatorial west-central Pacific in relation to ENSO. *J. Climate*, 10:1998-2017, 1997.

- World Climate Research Programme. Comparison of TOGA tropical Pacific ocean model simulations with the WOCE/TOGA surface velocity programme, drifter data set. *TOGA Numerical Experimentation Group Report 4/1995*, (Assembled by the Global Drifter Centre, Scripps institution of Oceanography), pp156., 1995.
- Yu, X., and M. J. McPhaden, Dynamical analysis of seasonal and interannual variability in the equatorial Pacific. *J. Phys. Oceanogr.*, 29:2350-2369, 1999a.
- Yu, X., and M. J. McPhaden, Seasonal variability in the equatorial Pacific. *J. Phys. Oceanogr.*, 29:925-947, 1999b.
- Yu, Y., W. J. Emery, and R. R. Leben, Satellite altimeter derived geostrophic currents in the western tropical Pacific during 1992-1993 and their validation with drifting buoy trajectories. *J. Geophys. Res.*, 100:25069-25085, 1995.
- Yu, Z., J. P. McCreary, W. S. Kessler, and K. A. Kelly, Influence of equatorial dynamics on the Pacific North Equatorial Countercurrent. *J. Phys. Oceanogr.*, in press, 2000.
- Yu, Z., P. S. Schopf, and J. P. McCreary, On the annual cycle of upper-ocean circulation in the eastern equatorial Pacific. *J. Phys. Oceanogr.*, 27:309-324, 1997.
- Zebiak, S. E., and M. A. Cane, A model El Niño-Southern Oscillation. *Mon. Wea. Rev.*, 115:2262-2278, 1987.